Ordered Patterns of Functional Oxide Nanostructures Grown from Chemical Solutions

JOSH MALOWNEY

Doctoral Thesis

Programa de Doctorat en Ciència de Materials

Supervised by Dr. Xavier Borrisé & Dr. Narcís Mestres

Tutor: Prof. Santiago Suriñach

Departament de Física

Facultat de Ciències

2012

Memòria presentada per aspirar al Grau de Doctor per

Josh Malowney

Vist i Plau…

Dr. Narcís Mestres Dr. Xavier Borrisé

Bellaterra, 4 de Juny de 2012

CONSEJO SUPERIOR
DE INVESTIGACIONES
CIENTÍFICAS

UAB
Universitat Autònoma
de Barcelona

El Dr. Xavier BORRISÉ I NOGUÉ del Institut Català de Nanotecnologia (ICN) i de l'Insitut de Microelectrònica de Barcelona (CNM) i el Dr. Narcís MESTRES ANDREU del Institut de Ciència de Materials de Barcelona (ICMAB-CSIC)

Certifiquen

Que el Sr. Josh Malowney, Master en Fìsica, va realitzar el treball d'investagació amb el títol: "Ordered Patterns of Functional Oxide Nanostructres Grown from Chemical Solutions". Aquest treball s'ha desenvolupat en el marc del programa de doctorat en Ciència de Materials del Departament de Física de la Universitat Autònoma de Barcelona

I perquè consti, signen el present certificat.

Dr. Xavier Borrisé i Nogué   Dr. Narcís Mestres i Andreu

Bellaterra 4 de Juny de 2012

To my Little Fish and my Little Little Fish

ACKNOWLEDGEMENTS

I would like to thank my advisors Xavier and Narcis, the Spanish government, and the Catalan government for giving me ideas, equipment, and funding to do this work. I would also like to thank everyone at both the ICMAB, ICN, and CNM for helping me both scientifically and bureaucratically. Special thanks to Albert for always helping me with the chemistry and to Jordi for making me all those lamellas. Thanks to all my friends for keeping my spirits up and to my family for supporting me.

I want to acknowledge Prof. Teresa Puig and Prof. Xavier Obradors for letting me be part of the Superconducting Materials and Large Scale Nanostructuration group at ICMAB-CSIC, and Prof. Juan Bausells for the hospitality that I have enjoyed at the Nanofabrication and Functional Properties of Nanostructures group of the IBM-CNM CSIC.

This work has been financed by the AGAUR grant resolution IUE/2681 and that this work has been possible thanks to the support of the project: “Materiales avanzados y NANOtecnologíaS para sistemas eléctricos, ELECTrónicos i magnetoelectrónicos innovadores” NANOSELECT (CSD2007-00041) from the program Consolider del Ministerio de Ciencia e Innovación in collaboration between the Institut de Ciència de Materials de Barcelona (ICMAB-CSIC) and the Institut de Microelectrònica de Barcelona (IMB-CSIC).

ABBREVIATIONS

AHD - Array of High Dosage

AFM - Atomic Force Microscopy

CSD - Chemical Solution Deposition

EBL - Electron Beam Lithography

EDX - Energy Dispersive X-ray Spectroscopy

EELS - Electron Energy Loss Spectroscopy

FIB - Focused Ion Beam

ICP - Inductively Coupled Plasma

ILD - Isolated Low Dosage

LAO - Lanthanum Aluminate

LSMO - $La_{0.7}Sr_{0.3}MnO_3$

NIL - Nanoimprint Lithography

PMMA - Poly (methyl methacrylate)

PVOH - Polyvinyl Alcohol

RIE - Reactive Ion Etcher

SCS - Single Crystal Substrate

SEM - Scanning Electron Microscopy

SQUID - Superconducting Quantum Interference Device

STO - Strontium Titanate

TEM - Transmission Electron Microscopy

YSZ - Yttrium Stabilized Zirconia

XPS - X-ray Photoelectron Spectroscopy

XRD - X-ray Diffraction

Summary & Motivation

Nanotechnology has been hailed as integral to solving the problems of future generations. By its very nature, it belongs not only to the unseeably small, but also the techniques relevant to its masterful manipulation. It is this manipulation that so much of current scientific research is centered and also the work herein. These studies of nano-techniques are as important to new devices as the instruments used to drive their existence into being. Much as tools such as hammer and nails can build a house, the correct technique, not the tool, is the defining ingredient in its construction.

The overarching technique in this work was lithography. The name lithography gets its name from rather ancient origins, being an amalgamation of the Greek words for stone and writing. The technique was to take a flat stone with very few defects and paint a design on it with hydrophobic oil. The stone was then dipped in a nitric acid solution to cause the non-painted areas to become hydrophilic. At the end, the stone possessed a design which was hydrophobic on a surface which was hydrophilic, thus allowing hydrophobic ink to be selectively placed with high precision and regularity onto paper. This two hundred years old technique lends little to the lithography of modern science except for the concept of fine pattern transfer.

To that end, two main instruments were used in the lithography process, several instruments were then employed to analyze those results, and a multitude of techniques were attempted during the optimization. Specifically, an electron beam and a nanoimprinter were the two instruments driving the lithography. Electron beam lithography (EBL) works by directing electrons to certain locations for certain periods of time on to an electron sensitive film which is then developed to reveal the design, essentially writing with electrons. Nanoimprint lithography (NIL) is the process of pressing a film with a stamp replete with nanoscale features and then removing excess material to reveal the design. Both forms of lithography have advantages and disadvantages with regards to their implementation in next generation devices. EBL takes days to finish writing an intricate circuit design onto a six inch wafer, however its ability to make inexpensive one-off devices is considerable compared to expensive large-scale photolithography masking techniques. NIL is seen as favorable to large-scale production due to its quick turn-around time of minutes, although the ability to control finer design elements is difficult.

The film used in the lithography process was that of mixture of metal salts, polymer, and water, called a precursor. The metal salts were initially lanthanum, strontium, and manganese nitrates then later lanthanum, strontium, and manganese acetates. The specific amount of metal salts introduced into the mixture yielded a film of $La_{0.7}Sr_{0.3}MnO_3$ (LSMO) when annealed in an oven. The conditions of the annealing were such that the organic species present in the film were released and the inorganic metals had sufficient thermal energy to form a LSMO crystal. The polymer used was polyvinyl alcohol (PVOH) due to its ability to harden under low heat, becoming water insoluble. This low heat came in the form of focused electrons and hot silicon molds. The mechanism responsible for the hardening of the PVOH is the due to physical cross-linking of the polymer chains. The reason why a polymer which can be hardened locally is important to the EBL procedure is that the water solubility of the film. With this ability, arrays can be made water insoluble and thus will remain after developing the film in water. The importance to the NIL procedure of having a polymer in the precursor is critical insomuch that without it, no pattern transfer can occur. A novelty of this work is the nanoimprinting of a PVOH based precursor film, which stands in contrast to the vast majority of NIL done on and PMMA [1-5].

LSMO was the oxide crystal used in this work due to its interesting physical properties. This perovskite mixed valence crystal has a Curie temperature of 370 K, the ability to change electrical resistance dramatically under applied magnetic field, high electrical conductivity at high temperatures, half metallicity for spin conduction, a highly anisotropic magnetic nature, and the ability to alter its physical properties when strained [6-14]. Current applications of LSMO are centered on solid oxide fuel cells, however many future applications have been imagined [15-17]. These include magnetic memory sites and components in spin transistors. This coupled with the explosion in new research regarding oxides and in particular multiferroics, drove the motivation to fabricate LSMO nanocrystals in a controlled and economic way [18-20].

The method in which the thin film was formed comes from taking a drop of precursor and placing it on top of a spinning substrate. This process is called spin coating and is an inexpensive method of forming thin films as opposed to other high cost vacuum methods. The substrates used in this work were single crystal substrates (SCS) by and large and silicon occasionally for optimization purposes. Specifically the SCS used were lanthanum aluminate (LAO), strontium titanate (STO), and yttrium stabilized zirconia (YSZ). These SCS allow for the growth of single crystalline epitaxial LSMO when its thin film precursor is annealed on top, this umbrella procedure being called chemical solution deposition (CSD). It must be stressed that this work was inspired by the electron beam experiments on silicon, but it was thought to create interesting functional nanostructures, oxide single crystal substrates would need to be used [21-23]. The unit cell of STO and LAO is very similar to that of LSMO, thus a contorted cube-on-cube growth occurs, however the unit cell of YSZ is very different to that of LSMO. These non-conventional substrates' negative attribute is their highly insulating nature which makes writing with electrons more difficult.

The instruments employed in the analysis of the results by lithography were principally the scanning electron microscope (SEM), the atomic force microscope (AFM), and the transmission electron microscope (TEM). The SEM was used first to detect that the lithography was successful and that nanostructures were made. The surface was then probed with an AFM to determine the morphology with nanometer precision. Finally, to observe the crystalline nature of the nanostructures, a thinned slice was analyzed with a TEM. Other instruments were also employed to confirm the metal stoichiometry being inductively coupled plasma (ICP), x-ray diffraction (XRD), x-ray photoelectric spectrometry (XPS), and electron energy loss spectrometry (EELS) .

Specifically regarding the structures formed in the electron beam lithography process, a morphological relationship was observed with dosage, distance between nearest neighbor (pitch), and the substrate used. Dosage here refers to amount of time in which a singular location was exposed with electrons, due to the current remaining constant; the larger the dosage, the wider the diameter of spot affected by electrons. When electrons initially were focused onto a single point on the precursor film, a nanosized depression was observed with AFM, called here a nanocavity. The film was then developed in water, the film was largely removed except for singular sites on the film which were irradiated with focused electrons, called here nanoislands. When the substrate with nanoislands was annealed at high heat for many hours, crystals were formed where the nanoislands were, called here nanodots.

If the dosage was low enough, only a small area would become a nanoisland and thus a small nanodot would form. Typically, the morphology of this nanoisland was round, however when purposefully made highly elliptical and sufficiently isolated, nanowires were seen to grow instead of nanodots when annealed. On the other end of the spectrum, when the dosage was sufficiently high, and surrounded by neighbors of appropriate distance, nanowires formed. These nanowires formed at the edge of the area that was irradiated and are orientated on the surface of the substrate. Both the nanodots and nanowires were made into cross-sectional lamellas so as to observe with TEM and EELS. It was noted that the nanostructures grew epitaxially on the surface of the single crystal substrate. However elemental analysis showed the oxide crystals to be devoid of manganese. The origin of this phenomenon is not entire understood, but was thought to lie with the electron radiation itself.

The reason for this hypothesis is that structures formed from nanoimprint lithography were observed to have epitaxial grown LSMO crystals with the correct amount of manganese. The nanostructures formed from NIL were as varied as those of EBL. The stamp used in this work was covered with nanoscale pillars, such that when pressed into the precursor film tiny depressions were formed. These depressions are called here

nanopores. These nanopores had depths less than that of the film, thus to remove the remaining film between the bottom of the nanopore and the top of the SCS, an etching step was performed. This etching was highly directional due to the applied field inside the reactive ion etcher (RIE). The anisotropic etching removed the material perpendicular to the substrate plane preferentially. Two different gases were used in etching the residual layer of the nanopores. Highly chemically reactive oxygen plasma was used to etch down to the substrate, thereby making what is called here nanoholes. When non-reactive argon plasma was fed into the RIE, a series of positive structures were observed, called here nanocaps. The understanding of the formation of the nanoholes is straight forward, however for the nanocaps, a bit of conjecture is required. It is hypothesized that the imprinting process locally compresses the film, thereby making certain sections more impervious to mechanical etching. Finally organic components are removed from both the nanoholes and nanocaps when annealed at high heat for an extended period.

It must be said that this body of work was the product of a collaboration between the Institut Català de Nanotecnologia (ICN), the Institut de Ciència de Materials de Barcelona (ICMAB-CSIC), and the Centro Nacional de Micoelectronica (CNM). The majority of the lithography experiments were carried out in the cleanroom at the CNM with solution preparation performed at the ICMAB. This was due to the vast amounts of experience at the ICMAB in oxide film formation on insulating single crystal substrates by chemical means and the superior technical knowledge at the CNM in nanofabrication tools. The work was under the framework of the Consolider project Nanoselect (CSD2007-00041). The core of this project is the study of self-organization at the nanoscale, generation of novel functional oxides, and new lithographic routes.

The goal of this work was to determine the correct technique, using electron beam and nanoimprint lithography along with chemical solution methods, to form arrays of LSMO nanocrystals on insulating single crystal substrates. This was partially accomplished with EBL and fully accomplished with NIL. The side phenomenon of nanowire growth gives insight into the surprising nature at the nanoscale and speaks to the intrinsic difficulties of nanocrystal synthesis. Future work in this area would consist of exploring other oxide combinations. Initial work imprinting and irradiating a precursor consisting of strontium and titanium isopropoxide, forming $SrTiO_3$ when annealed as a film, was performed. The results showed the formation of nanodots similarly to the EBL experiments with the LSMO precursor as well as the ability to create a nanoperforated film from a stamp. Thusly, it is thought that other oxide combinations and stoichiometries could also be successfully nanostructurated with the techniques described herein.

This work is organized as follows: Chapter 1 discusses the techniques involved in the precursor solution preparation and analysis, thin film preparation and analysis, general overview regarding electron beam and nanoimprint lithograph, and explanation of instruments used. Chapter 2 delves into the results of electron

beam lithography with regards to nanodot fabrication and its intermediate species along with analysis of their crystalline nature. Chapter 3 describes two methods involved with the generation of nanowires from electron beam lithography efforts. Chapter 4 centers around the positive and negative nanostructures made by nanoimprint lithography of the LSMO precursor.

References

1. Tao, J., et al., *Room temperature nanoimprint lithography using a bilayer of HSQ/PMMA resist stack.* Microelectronic Engineering, 2005. **78–79**(0): p. 665-669.
2. Martin, C., L. Ressier, and J.P. Peyrade, *Study of PMMA recoveries on micrometric patterns replicated by nano-imprint lithography.* Physica E: Low-dimensional Systems and Nanostructures, 2003. **17**(0): p. 523-525.
3. Mohamed, K., M.M. Alkaisi, and J. Smaill, *Resist deformation at low temperature in nanoimprint lithography.* Current Applied Physics, 2006. **6**(3): p. 486-490.
4. Carlberg, P., et al., *Lift-off process for nanoimprint lithography.* Microelectronic Engineering, 2003. **67–68**(0): p. 203-207.
5. Senn, T., et al., *Fabrication of photonic crystals for applications in the visible range by Nanoimprint Lithography.* Photonics and Nanostructures - Fundamentals and Applications, 2011. **9**(3): p. 248-254.
6. Brivio, S., et al., *Decrease of the Curie temperature in La0.67Sr0.33MnO3 thin films induced by Au capping.* Materials Science and Engineering: B, 2007. **144**(1–3): p. 93-96.
7. Majumdar, S., H.S. Majumdar, and R. Österbacka, *1.05 - Organic Spintronics*, in *Comprehensive Nanoscience and Technology*, L.A. Editors-in-Chief: David, D.S. Gregory, and P.W. Gary, Editors. 2011, Academic Press: Amsterdam. p. 109-142.
8. Obradors, X., et al., *3.10 - Nanostructured Superconductors with Efficient Vortex Pinning*, in *Comprehensive Nanoscience and Technology*, L.A. Editors-in-Chief: David, D.S. Gregory, and P.W. Gary, Editors. 2011, Academic Press: Amsterdam. p. 303-349.
9. Banach, G., R. Tyer, and W.M. Temmerman, *Study of half-metallicity in LSMO.* Journal of Magnetism and Magnetic Materials, 2004. **272–276, Part 3**(0): p. 1963-1964.
10. Kim, H.-J. and S.-I. Yoo, *Enhanced low field magnetoresistance in La0.7Sr0.3MnO3–La2O3 composites.* Journal of Alloys and Compounds, 2012. **521**(0): p. 30-34.
11. Kumar, J., et al., *Enhanced magnetoresistance in La0.82Sr0.18MnO3-π-conjugated semiconducting polymer heterostructure.* Solid State Communications, 2006. **138**(8): p. 422-425.
12. Liu, D. and W. Liu, *Growth and characterization of epitaxial (La2/3Sr1/3)MnO3 films by pulsed laser deposition.* Ceramics International, 2011. **37**(8): p. 3531-3534.
13. Liu, D. and W. Liu, *Room temperature ultrahigh magnetoresistance nanostructure (La2/3Sr1/3)MnO3 films growth on SrTiO3 substrate.* Ceramics International, 2012. **38**(3): p. 2579-2581.
14. Sahu, D.R., et al., *Annealing effect on the properties of La0.7Sr0.3MnO3 thin film grown on Si substrates by DC sputtering.* Physica B: Condensed Matter, 2007. **396**(1–2): p. 75-80.
15. Lussier, A., et al., *Stress relaxation of La1/2Sr1/2MnO3 and La2/3Ca1/3MnO3 at solid oxide fuel cell interfaces.* Thin Solid Films, 2008. **516**(6): p. 880-884.
16. Jin, C., et al., *La0.6Sr1.4MnO4 layered perovskite anode material for intermediate temperature solid oxide fuel cells.* Electrochemistry Communications, 2012. **14**(1): p. 75-77.
17. Li, J.Q. and P. Xiao, *Fabrication and characterisation of La0.8Sr0.2MnO3/metal interfaces for application in SOFCs.* Journal of the European Ceramic Society, 2001. **21**(5): p. 659-668.

18. Fiebig, M., *Multiferroic Manganites: Correlation between Magnetic and Electric Ordering*, in *Encyclopedia of Materials: Science and Technology (Second Edition)*, K.H.J.B. Editors-in-Chief: , et al., Editors. 2007, Elsevier: Oxford. p. 1-6.
19. Palstra, T.T.M. and G.R. Blake, *Multiferroic Materials: Physics and Properties*, in *Encyclopedia of Materials: Science and Technology (Second Edition)*, K.H.J.B. Editors-in-Chief: , et al., Editors. 2006, Elsevier: Oxford. p. 1-7.
20. Wördenweber, R., *4.06 - Ferroelectric Thin Layers*, in *Comprehensive Semiconductor Science and Technology*, B. Editors-in-Chief: Pallab, F. Roberto, and K. Hiroshi, Editors. 2011, Elsevier: Amsterdam. p. 177-205.
21. Chuang, C.M., et al., *Nanolithography made from water-based spin-coatable LSMO resist.* Nanotechnology, 2006. **17**(17): p. 4399-4404.
22. Wu, M.C., et al., *Surface potential and magnetic properties of La0.7Sr 0.3MnO3 periodic arrays fabricated by direct electron beam writing.* Journal of Applied Physics, 2008. **104**(2).
23. Wu, M.C., et al., *Fabrication and optical properties of periodical structures based on a water-developable and tunable La0.7Sr0.3MnO3 resist.* Journal of Materials Chemistry, 2008. **18**(7): p. 780-785.

Summary & Motivation

Nanotechnology has been hailed as integral to solving the problems of future generations. By its very nature, it belongs not only to the unseeably small, but also the techniques relevant to its masterful manipulation. It is this manipulation that so much of current scientific research is centered and also the work herein. These studies of nano-techniques are as important to new devices as the instruments used to drive their existence into being. Much as tools such as hammer and nails can build a house, the correct technique, not the tool, is the defining ingredient in its construction.

The overarching technique in this work was lithography. The name lithography gets its name from rather ancient origins, being an amalgamation of the Greek words for stone and writing. The technique was to take a flat stone with very few defects and paint a design on it with hydrophobic oil. The stone was then dipped in a nitric acid solution to cause the non-painted areas to become hydrophilic. At the end, the stone possessed a design which was hydrophobic on a surface which was hydrophilic, thus allowing hydrophobic ink to be selectively placed with high precision and regularity onto paper. This two hundred years old technique lends little to the lithography of modern science except for the concept of fine pattern transfer.

To that end, two main instruments were used in the lithography process, several instruments were then employed to analyze those results, and a multitude of techniques were attempted during the optimization. Specifically, an electron beam and a nanoimprinter were the two instruments driving the lithography. Electron beam lithography (EBL) works by directing electrons to certain locations for certain periods of time on to an electron sensitive film which is then developed to reveal the design, essentially writing with electrons. Nanoimprint lithography (NIL) is the process of pressing a film with a stamp replete with nanoscale features and then removing excess material to reveal the design. Both forms of lithography have advantages and disadvantages with regards to their implementation in next generation devices. EBL takes days to finish writing an intricate circuit design onto a six inch wafer, however its ability to make inexpensive one-off devices is considerable compared to expensive large-scale photolithography masking techniques. NIL is seen as favorable to large-scale production due to its quick turn-around time of minutes, although the ability to control finer design elements is difficult.

The film used in the lithography process was that of mixture of metal salts, polymer, and water, called a precursor. The metal salts were initially lanthanum, strontium, and manganese nitrates then later lanthanum, strontium, and manganese acetates. The specific amount of metal salts introduced into the mixture yielded a film of $La_{0.7}Sr_{0.3}MnO_3$ (LSMO) when annealed in an oven. The conditions of the annealing were such that the organic species present in the film were released and the inorganic metals had sufficient thermal energy to form a LSMO crystal. The polymer used was polyvinyl alcohol (PVOH) due to its ability to harden under low heat, becoming water insoluble. This low heat came in the form of focused electrons and hot silicon molds. The mechanism responsible for the hardening of the PVOH is the due to physical cross-linking of the polymer chains. The reason why a polymer which can be hardened locally is important to the EBL procedure is that the water solubility of the film. With this ability, arrays can be made water insoluble and thus will remain after developing the film in water. The importance to the NIL procedure of having a polymer in the precursor is critical insomuch that without it, no pattern transfer can occur. A novelty of this work is the nanoimprinting of a PVOH based precursor film, which stands in contrast to the vast majority of NIL done on and PMMA [1-5].

LSMO was the oxide crystal used in this work due to its interesting physical properties. This perovskite mixed valence crystal has a Curie temperature of 370 K, the ability to change electrical resistance dramatically under applied magnetic field, high electrical conductivity at high temperatures, half metallicity for spin conduction, a highly anisotropic magnetic nature, and the ability to alter its physical properties when strained [6-14]. Current applications of LSMO are centered on solid oxide fuel cells, however many future applications have been imagined [15-17]. These include magnetic memory sites and components in spin transistors. This coupled with the explosion in new research regarding oxides and in particular multiferroics, drove the motivation to fabricate LSMO nanocrystals in a controlled and economic way [18-20].

The method in which the thin film was formed comes from taking a drop of precursor and placing it on top of a spinning substrate. This process is called spin coating and is an inexpensive method of forming thin films as opposed to other high cost vacuum methods. The substrates used in this work were single crystal substrates (SCS) by and large and silicon occasionally for optimization purposes. Specifically the SCS used were lanthanum aluminate (LAO), strontium titanate (STO), and yttrium stabilized zirconia (YSZ). These SCS allow for the growth of single crystalline epitaxial LSMO when its thin film precursor is annealed on top, this umbrella procedure being called chemical solution deposition (CSD). It must be stressed that this work was inspired by the electron beam experiments on silicon, but it was thought to create interesting functional nanostructures, oxide single crystal substrates would need to be used [21-23]. The unit cell of STO and LAO is very similar to that of LSMO, thus a contorted cube-on-cube growth occurs, however the unit cell of YSZ is very different to that of LSMO. These non-conventional substrates' negative attribute is their highly insulating nature which makes writing with electrons more difficult.

The instruments employed in the analysis of the results by lithography were principally the scanning electron microscope (SEM), the atomic force microscope (AFM), and the transmission electron microscope (TEM). The SEM was used first to detect that the lithography was successful and that nanostructures were made. The surface was then probed with an AFM to determine the morphology with nanometer precision. Finally, to observe the crystalline nature of the nanostructures, a thinned slice was analyzed with a TEM. Other instruments were also employed to confirm the metal stoichiometry being inductively coupled plasma (ICP), x-ray diffraction (XRD), x-ray photoelectric spectrometry (XPS), and electron energy loss spectrometry (EELS).

Specifically regarding the structures formed in the electron beam lithography process, a morphological relationship was observed with dosage, distance between nearest neighbor (pitch), and the substrate used. Dosage here refers to amount of time in which a singular location was exposed with electrons, due to the current remaining constant; the larger the dosage, the wider the diameter of spot affected by electrons. When electrons initially were focused onto a single point on the precursor film, a nanosized depression was observed with AFM, called here a nanocavity. The film was then developed in water, the film was largely removed except for singular sites on the film which were irradiated with focused electrons, called here nanoislands. When the substrate with nanoislands was annealed at high heat for many hours, crystals were formed where the nanoislands were, called here nanodots.

If the dosage was low enough, only a small area would become a nanoisland and thus a small nanodot would form. Typically, the morphology of this nanoisland was round, however when purposefully made highly elliptical and sufficiently isolated, nanowires were seen to grow instead of nanodots when annealed. On the other end of the spectrum, when the dosage was sufficiently high, and surrounded by neighbors of appropriate distance, nanowires formed. These nanowires formed at the edge of the area that was irradiated and are orientated on the surface of the substrate. Both the nanodots and nanowires were made into cross-sectional lamellas so as to observe with TEM and EELS. It was noted that the nanostructures grew epitaxially on the surface of the single crystal substrate. However elemental analysis showed the oxide crystals to be devoid of manganese. The origin of this phenomenon is not entire understood, but was thought to lie with the electron radiation itself.

The reason for this hypothesis is that structures formed from nanoimprint lithography were observed to have epitaxial grown LSMO crystals with the correct amount of manganese. The nanostructures formed from NIL were as varied as those of EBL. The stamp used in this work was covered with nanoscale pillars, such that when pressed into the precursor film tiny depressions were formed. These depressions are called here

nanopores. These nanopores had depths less than that of the film, thus to remove the remaining film between the bottom of the nanopore and the top of the SCS, an etching step was performed. This etching was highly directional due to the applied field inside the reactive ion etcher (RIE). The anisotropic etching removed the material perpendicular to the substrate plane preferentially. Two different gases were used in etching the residual layer of the nanopores. Highly chemically reactive oxygen plasma was used to etch down to the substrate, thereby making what is called here nanoholes. When non-reactive argon plasma was fed into the RIE, a series of positive structures were observed, called here nanocaps. The understanding of the formation of the nanoholes is straight forward, however for the nanocaps, a bit of conjecture is required. It is hypothesized that the imprinting process locally compresses the film, thereby making certain sections more impervious to mechanical etching. Finally organic components are removed from both the nanoholes and nanocaps when annealed at high heat for an extended period.

It must be said that this body of work was the product of a collaboration between the Institut Català de Nanotecnologia (ICN), the Institut de Ciència de Materials de Barcelona (ICMAB-CSIC), and the Centro Nacional de Micoelectronica (CNM). The majority of the lithography experiments were carried out in the cleanroom at the CNM with solution preparation performed at the ICMAB. This was due to the vast amounts of experience at the ICMAB in oxide film formation on insulating single crystal substrates by chemical means and the superior technical knowledge at the CNM in nanofabrication tools. The work was under the framework of the Consolider project Nanoselect (CSD2007-00041). The core of this project is the study of self-organization at the nanoscale, generation of novel functional oxides, and new lithographic routes.

The goal of this work was to determine the correct technique, using electron beam and nanoimprint lithography along with chemical solution methods, to form arrays of LSMO nanocrystals on insulating single crystal substrates. This was partially accomplished with EBL and fully accomplished with NIL. The side phenomenon of nanowire growth gives insight into the surprising nature at the nanoscale and speaks to the intrinsic difficulties of nanocrystal synthesis. Future work in this area would consist of exploring other oxide combinations. Initial work imprinting and irradiating a precursor consisting of strontium and titanium isopropoxide, forming $SrTiO_3$ when annealed as a film, was performed. The results showed the formation of nanodots similarly to the EBL experiments with the LSMO precursor as well as the ability to create a nanoperforated film from a stamp. Thusly, it is thought that other oxide combinations and stoichiometries could also be successfully nanostructurated with the techniques described herein.

This work is organized as follows: Chapter 1 discusses the techniques involved in the precursor solution preparation and analysis, thin film preparation and analysis, general overview regarding electron beam and nanoimprint lithograph, and explanation of instruments used. Chapter 2 delves into the results of electron

beam lithography with regards to nanodot fabrication and its intermediate species along with analysis of their crystalline nature. Chapter 3 describes two methods involved with the generation of nanowires from electron beam lithography efforts. Chapter 4 centers around the positive and negative nanostructures made by nanoimprint lithography of the LSMO precursor.

References

1. Tao, J., et al., *Room temperature nanoimprint lithography using a bilayer of HSQ/PMMA resist stack.* Microelectronic Engineering, 2005. **78–79**(0): p. 665-669.
2. Martin, C., L. Ressier, and J.P. Peyrade, *Study of PMMA recoveries on micrometric patterns replicated by nano-imprint lithography.* Physica E: Low-dimensional Systems and Nanostructures, 2003. **17**(0): p. 523-525.
3. Mohamed, K., M.M. Alkaisi, and J. Smaill, *Resist deformation at low temperature in nanoimprint lithography.* Current Applied Physics, 2006. **6**(3): p. 486-490.
4. Carlberg, P., et al., *Lift-off process for nanoimprint lithography.* Microelectronic Engineering, 2003. **67–68**(0): p. 203-207.
5. Senn, T., et al., *Fabrication of photonic crystals for applications in the visible range by Nanoimprint Lithography.* Photonics and Nanostructures - Fundamentals and Applications, 2011. **9**(3): p. 248-254.
6. Brivio, S., et al., *Decrease of the Curie temperature in La0.67Sr0.33MnO3 thin films induced by Au capping.* Materials Science and Engineering: B, 2007. **144**(1–3): p. 93-96.
7. Majumdar, S., H.S. Majumdar, and R. Österbacka, *1.05 - Organic Spintronics*, in *Comprehensive Nanoscience and Technology*, L.A. Editors-in-Chief: David, D.S. Gregory, and P.W. Gary, Editors. 2011, Academic Press: Amsterdam. p. 109-142.
8. Obradors, X., et al., *3.10 - Nanostructured Superconductors with Efficient Vortex Pinning*, in *Comprehensive Nanoscience and Technology*, L.A. Editors-in-Chief: David, D.S. Gregory, and P.W. Gary, Editors. 2011, Academic Press: Amsterdam. p. 303-349.
9. Banach, G., R. Tyer, and W.M. Temmerman, *Study of half-metallicity in LSMO.* Journal of Magnetism and Magnetic Materials, 2004. **272–276, Part 3**(0): p. 1963-1964.
10. Kim, H.-J. and S.-I. Yoo, *Enhanced low field magnetoresistance in La0.7Sr0.3MnO3–La2O3 composites.* Journal of Alloys and Compounds, 2012. **521**(0): p. 30-34.
11. Kumar, J., et al., *Enhanced magnetoresistance in La0.82Sr0.18MnO3-π-conjugated semiconducting polymer heterostructure.* Solid State Communications, 2006. **138**(8): p. 422-425.
12. Liu, D. and W. Liu, *Growth and characterization of epitaxial (La2/3Sr1/3)MnO3 films by pulsed laser deposition.* Ceramics International, 2011. **37**(8): p. 3531-3534.
13. Liu, D. and W. Liu, *Room temperature ultrahigh magnetoresistance nanostructure (La2/3Sr1/3)MnO3 films growth on SrTiO3 substrate.* Ceramics International, 2012. **38**(3): p. 2579-2581.
14. Sahu, D.R., et al., *Annealing effect on the properties of La0.7Sr0.3MnO3 thin film grown on Si substrates by DC sputtering.* Physica B: Condensed Matter, 2007. **396**(1–2): p. 75-80.
15. Lussier, A., et al., *Stress relaxation of La1/2Sr1/2MnO3 and La2/3Ca1/3MnO3 at solid oxide fuel cell interfaces.* Thin Solid Films, 2008. **516**(6): p. 880-884.
16. Jin, C., et al., *La0.6Sr1.4MnO4 layered perovskite anode material for intermediate temperature solid oxide fuel cells.* Electrochemistry Communications, 2012. **14**(1): p. 75-77.
17. Li, J.Q. and P. Xiao, *Fabrication and characterisation of La0.8Sr0.2MnO3/metal interfaces for application in SOFCs.* Journal of the European Ceramic Society, 2001. **21**(5): p. 659-668.
18. Fiebig, M., *Multiferroic Manganites: Correlation between Magnetic and Electric Ordering*, in *Encyclopedia of Materials: Science and Technology (Second Edition)*, K.H.J.B. Editors-in-Chief: , et al., Editors. 2007, Elsevier: Oxford. p. 1-6.
19. Palstra, T.T.M. and G.R. Blake, *Multiferroic Materials: Physics and Properties*, in *Encyclopedia of Materials: Science and Technology (Second Edition)*, K.H.J.B. Editors-in-Chief: , et al., Editors. 2006, Elsevier: Oxford. p. 1-7.

20. Wördenweber, R., *4.06 - Ferroelectric Thin Layers*, in *Comprehensive Semiconductor Science and Technology*, B. Editors-in-Chief: Pallab, F. Roberto, and K. Hiroshi, Editors. 2011, Elsevier: Amsterdam. p. 177-205.
21. Chuang, C.M., et al., *Nanolithography made from water-based spin-coatable LSMO resist.* Nanotechnology, 2006. **17**(17): p. 4399-4404.
22. Wu, M.C., et al., *Surface potential and magnetic properties of La0.7Sr 0.3MnO3 periodic arrays fabricated by direct electron beam writing.* Journal of Applied Physics, 2008. **104**(2).
23. Wu, M.C., et al., *Fabrication and optical properties of periodical structures based on a water-developable and tunable La0.7Sr0.3MnO3 resist.* Journal of Materials Chemistry, 2008. **18**(7): p. 780-785.

Summary & Motivation 13
1. Techniques 22
1.1 Chemical Solution Deposition 26
1.1.1 PVOH Solution 27
1.1.2 LSMO Solution 27
1.1.3 STO Solution 28
1.1.4 Filtering 29
1.1.5 Spin Coating 30
1.1.6 Stability 32
1.1.7 Annealing 33
1.2 Oxide Thin Film Analysis 34
1.2.1 Film Thickness 34
1.2.2 Film Quality 37
1.2.3 Structural Characterization 38
1.2.4 Magnetic Nature 42
1.2.5 Elemental Analysis 43
1.2.6 Gravimetric Analysis 46
1.3 Electron Beam Lithography 47
1.3.1 EBL on Insulating Substrates 50
1.3.2 Nanostructures from LSMO Precursor 53
1.4 Nanoimprint Lithography 58
1.4.1 Reactive Ion Etching 64
1.5 Focused Ion Beam 65
1.6 Transmission Electron Microscope 71
1.6.1 Electron Energy Loss Spectroscopy 72
1.7 Specific Conclusions 73
1.8 Thin Film References 74
2. Oxide Nanodots 78
2.0.1 Motivation 79
2.0.2 Current State of Research 80
2.1 Nanocavities – After Electron Beam 81
2.1.1 Low Dosage Morphology 83
2.1.2 High Dosage Morphology 87
2.2 Nanoislands – After Water Development 90

2.2.1 Low Dosage Morphology 90
2.2.2 High Dosage Morphology 93
2.3 Nanodots – After Oven Treatment 97
2.3.1 Low Dosage Morphology 99
2.3.2 High Dosage Morphology 104
2.3.3 TEM Results for Structures Grown on LAO 107
2.3.4 TEM Results on YSZ 111
2.4 Applicability to Other Oxides 114
2.5 Fabrication Difficulties 117
2.6 Specific Conclusions 122
2.7 Nanodot References 125
3. Oxide Nanowires by Electron Beam Lithography 127
3.0.1 Nanowire Growth 128
3.1 ILD Nanowire Growth 131
3.1.1 Defocused ILD Nanowire Growth on YSZ 132
3.1.2 Astigmatic ILD Nanowire Growth on YSZ 135
3.2 Nanowires Grown from AHD Nanodots 140
3.2.1 AFM on Corner of AHD Nanodots on STO 142
3.2.2 Pitch Dependence for AHD Nanowires on STO 145
3.2.3 TEM Lamella of AHD Nanowires on STO 147
3.2.4 TEM Results of AHD Nanowires on STO 149
3.2.5 Orientational Relationship of AHD Nanowires 152
3.2.6 Number of Neighbors Dependence for AHD Nanowires on STO 154
3.2.7 Dosage Dependence for AHD Nanowires on STO 155
3.2.8 Neighboring Effect on AHD Nanowires on STO 156
3.2.9 AHD Nanowire Growth as a Function of Temperature 158
3.2.10 Unconstrained Growth as a Function of Annealing Time 160
3.2.11 Constrained Growth as a Function of Annealing Time 162
3.2.12 Long Distance Nanowire Growth due to Markers 164
3.2.13 Nanowires Grown at Overlaps between Arrays 166
3.2.14 AHD Nanowires Grown on Silicon 167
3.2.15 Analysis of TEM Lamellas of Nanowires on Silicon 168
3.3 Conclusions about Nanowire Growth 172
3.4 Nanowire References 173
4. Oxide Nanoimprinting 175

4.0.1 Current NIL Research 176
4.0.2 NIL Objectives 180
4.1 Silicon Mold 182
4.2 Imprinting 183
4.2.1 Dwell Temperature 188
4.2.2 Applied Pressure 190
4.2.3 Dwell Time 191
4.2.4 Demolding Temperature 192
4.3 Etching Residual Layer 194
4.3.1 Oxygen Plasma 197
4.3.2 Argon Plasma 199
4.4 Annealed Structures 201
4.4.1 TEM of NIL Structure 208
4.5 Specific Conclusions 213
4.6 Nanoimprinting References 215
General Conclusions & Future Work 218

1. Techniques

In order to obtain ordered arrays of oxide nanostructures on insulating substrates by nanoimprint and electron beam lithography, many steps must first be completed. These steps include the preparation of the precursor solution, the homogeneous spreading of this precursor on to the substrate, the application of electrons or mold, the removal of unwanted precursor, and finally the high temperature treatment inside a furnace. Each of these steps are multifaceted and contain several subtle procedures which will be revealed in this chapter. This includes the description how both the LSMO and STO solutions were derived, the filtering used to rid the solutions of larger particulates, and the ideal conditions for spin coating. Furthermore, the cleaning steps will be relayed here due to their importance in performing repeatable experiments.

In this chapter, the techniques used to analyze thin films will also be discussed. The analysis of thin films derived from the precursor solutions is paramount. This is due to the necessary verification that a given precursor can grow an epitaxial thin film with the same stoichiometry as was originally prescribed. This analysis comes in many forms including AFM to detect roughness and thickness, x-ray diffraction to determine crystalline nature, checking the magnetic nature via SQUID, and observing the ratio of metal constituents present in the solution by XPS and ICP. These analytical techniques will be touched upon due to the proceeding three chapters calling upon concepts assumed known to the reader.

The intricacies of the two forms of lithography used in this work will also be elaborated upon. This will come in the form of describing the nuanced approach used in focusing electrons on the thin film, the techniques used to mitigate charging effects, and the subtleties undertaken to remove a matrix of soluble material surrounding weakly adhered insoluble material. With relation to nanoimprint lithography, the general procedure will be explained along with details surrounding the process. Finally, three techniques used to peer at the very atomic structure of nanodots and nanowires will be described. Specifically, the focused ion beam (FIB) which is used to cut a thin electron transparent lamella, the transmission electron microscope (TEM) which analyzes the fine structure of the lamella, and the electron energy loss spectrometer (EELS) which can detect the presence of specific elements. These techniques constitute an avenue in which the epitaxy of the nanostructure can be verified to have grown on the single crystal substrate and that the structures have the correct ratio of metal constituents.

A schematic of the procedures taken to form oxide thin films by chemical solution deposition can be found in figure 1-1. More specifically, this calls for a precursor solution to be made, spin coated onto the substrate, and annealed in an oven to finally form the oxide thin film. Thin oxide films may be formed from other techniques which use ultra high vacuums and ablating oxide targets, however these techniques are relatively slow and require expensive apparatuses [1-6]. The employment of chemical solutions and not physical methods, lowers the cost significantly. However, this is a somewhat moot point here due to the inability to include polymers in the film with vacuum deposition techniques. Without a polymer additive, both the ability to write with electrons and imprintability from hard molds would be lost.

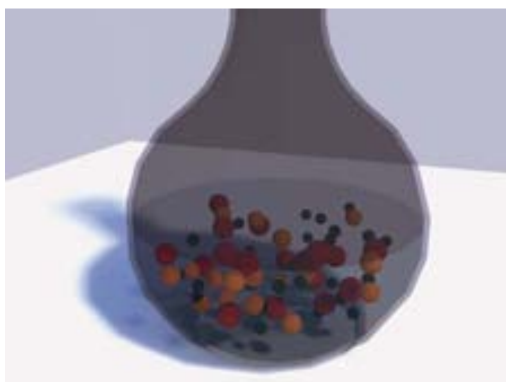

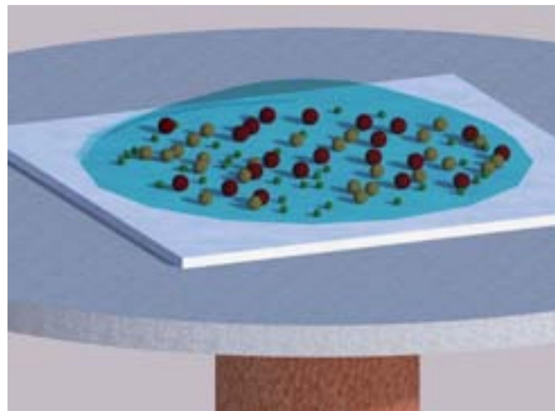

Figure 1-1 *General procedures undertaken to form oxide thin films by chemical solution deposition.*

The general procedure to form nanostructures by focused electron beam from a PVOH based oxide precursor which was spin coated on to a single crystal substrate is found in figure 1-2. Specifically it highlights the five steps undertaken to reveal nanodots: spin coating, drying, radiating with electrons in a controlled fashion, washing away the non-radiated film, and finally annealing in an oven at elevated temperatures. This procedure was outlined in by Wu et al., however the substrate used in that work was silicon [7-9]. The purpose of using a single crystal substrate instead of silicon stems from the desire to grow epitaxial single crystal LSMO nanodots. This growth mode is possible on the insulating single crystal substrates of strontium titanate (STO), lanthanum aluminate (LAO), or yttrium stabilized zirconium (YSZ). This is due to the the lattice mismatch between perovskite LSMO and the crystals STO, LAO, and YSZ are 0.82%, 2.3%, and 5.9% percent respectively [10-12]. The nature of LSMO is one of pseudo-cubic rhombohedral whereas STO and LAO are cubic and YSZ is fluorite in structure. When LSMO is grown on STO, a tensile strain occurs, whereas when LSMO grows on LAO, a compressive strain occurs.

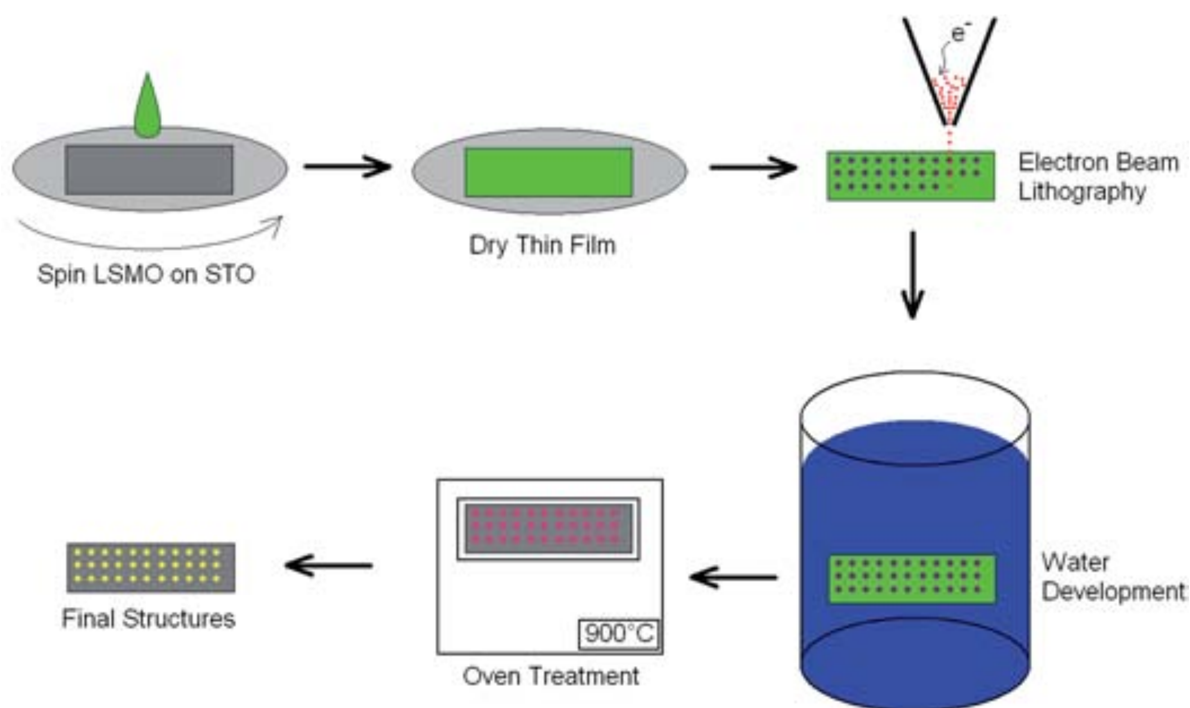

Figure 1-2 *General procedure to generate nanostructures from LSMO film by electron beam lithography.*

The intricate interaction between the LSMO precursor and the focused electrons is described visually in figure 1-3. There, one sees a schematic on how the precursor is affected differently as the dosage is increased left to right. The lowest dosage of electrons cross-links the precursor which when developed forms a cone that retains its shape when annealed. The highest dosage case shows how a non-linear shape is cross-linked and that at the very center a crystal is formed [7, 8]. This highest dosage nanosite can lead to the formation of nanowires when in an array or small groupings

of nanodots if isolated. Of course there are many gradations to these two cases which is represented here as the medium dosage case.

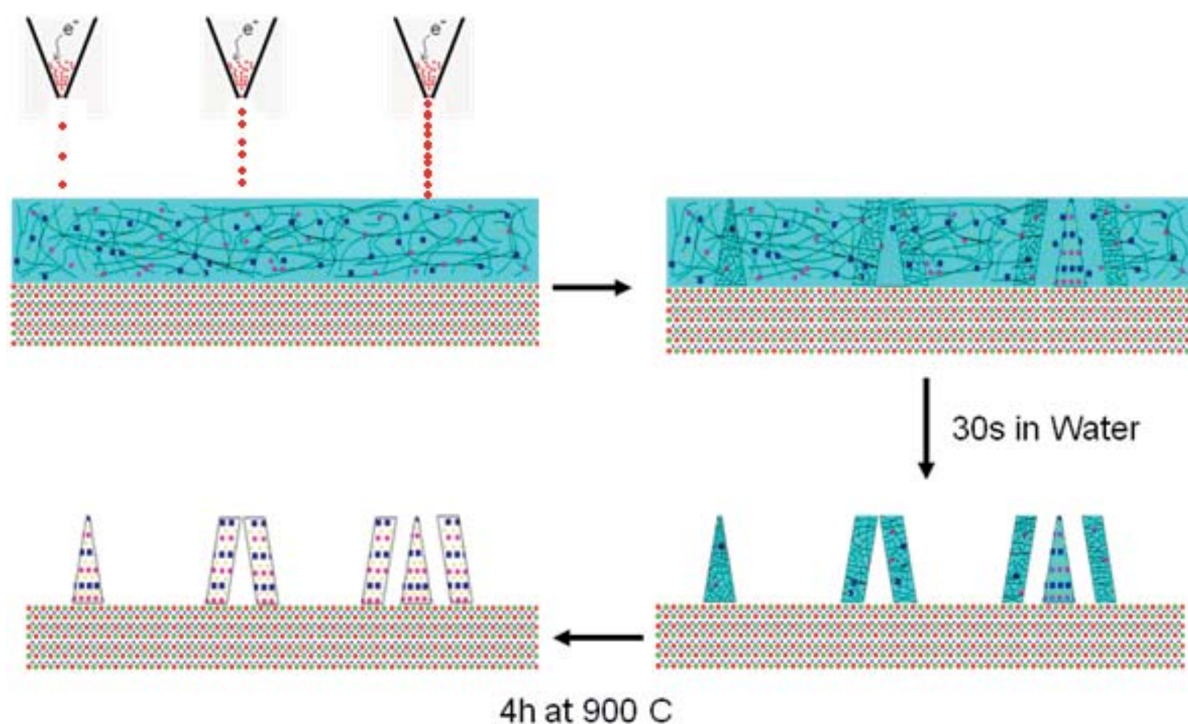

Figure 1-3 *Schematic indicating the effect having low to high dosages at the various stages in the lithography process.*

The other form of lithography explored in this work is that of nanoimprint lithography. The schematic for this process can be seen in figure 1-4. There one sees how the silicon mold presses into the heated precursor. This pushes the precursor away such that when cooled, forms a series of nanocavities. These nanocavities are then etched by directional plasma which reduces the overall height of the film while retaining their aspect ratio. Finally, the sample is annealed so as to remove the organic components and form a series of isolated LSMO nanostructures on a single crystal substrate.

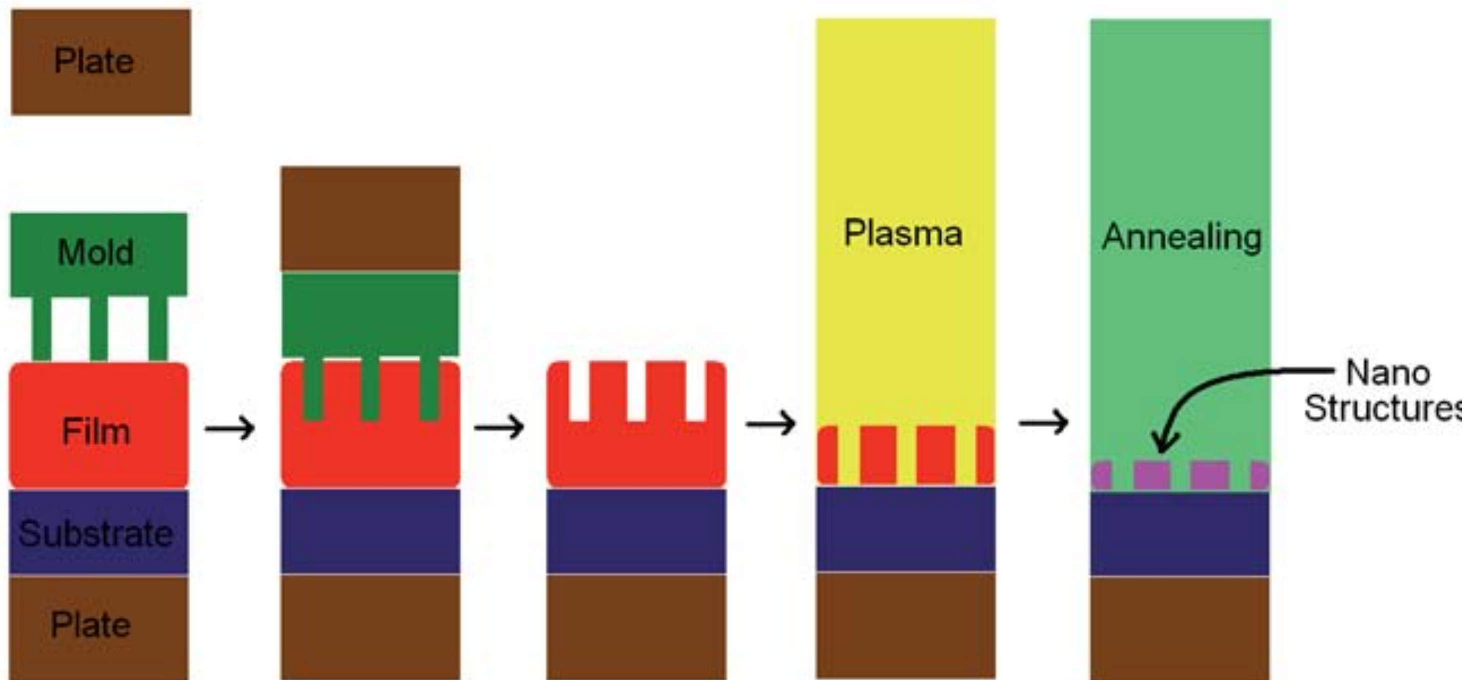

Figure 1.4 *Schematic for nanoimprint lithography of oxide precursors on single crystal substrates from a male mold with a reactive ion etching step followed by oxygen annealing.*

1.1 Chemical Solution Deposition

Of the many methods which produce thin films, chemical solution deposition was utilized in this investigation. The underlying reason was to broaden the base of knowledge for this highly scalable method for future industrial applications. Although the cost to spin coat a film is relatively low, other beneficial characteristics made it the ideal choice for this study such as precise control of constituent stoichiometries, an aqueous based solution, and homogenous distribution over the substrate. The procedure calls for combining metal nitrate salts together with a polymer [7-9]. In the work here nitrates as well as acetates metals were combined in the stoichiometric amount to form $La_{0.7}Sr_{0.3}MnO_3$ once annealed. The polymer here was polyvinyl alcohol and was introduced into the aqueous solution as a function of weight, namely two percent for EBL experiments and fifteen percent for NIL experiments. In order to prove the broad applicability of this procedure to the field of oxides, a precursor containing Sr and Ti were combined with PVOH so as form $SrTiO_3$ when annealed.

1.1.1 PVOH Solution

At the heart of this technique in which oxide nanostructures are formed from both electron and imprint lithography, is polyvinyl alcohol. PVOH can come in many forms from high molecular weight to low molecular weight, highly crystalline to highly plasticized. Its physical properties such as strength, gas permeability, and thermal characteristics will vary with the degree of crystallinity, the molecular weight of the chain, and the pH of the solution[13]. Thus it is difficult to ascertain from literature what the cross-linking temperature is for the precursor films used here. Although it has been reported that very thermally stabile PVOH will cross-links at temperatures around 260 °C, typical cross-linking temperatures are between 130 °C and 230 °C [13, 14]. The melting temperature of PVOH has been reported to be much lower than the decomposition temperature if a plasticizer is present [15]. Water works as a plasticizer here due to PVOH being hydrophilic and subsequently separates the long chains, bringing the glass transition temperature lower. Heat can come from a concentrated beam of charged particles or a hot silicon mold. In order for the PVOH to work properly, it needs to be homogeneously distributed throughout the solution.

Practically speaking, PVOH needs to be at a high enough concentration such that the film can wet the substrate completely. This amount of polymer in the precursor is the lower limit, however it also has a higher limit. This higher limit stems from the inability to spin coat ultra non-viscous liquids. It was found that the weight percentage of PVOH in the solution was able to be spin coated from two to fifteen percent. For the thin films used in electron beam lithography they consisted of two percent by weight PVOH and nanoimprinted samples had fifteen percent by weight. PVOH is soluble in water, albeit the process is slow at room temperature, thus to dissolve the granules of PVOH in water, the solutions was stirred for two days. The molecular weight of the PVOH was on average 18 kilograms per mole. The aqueous PVOH solution was then filtered to remove any large undissolved colloids. To determine how much polymer was present in the filtered solution, twenty grams of the solution was poured into a pre-weighed vial. The vial was then heated at fifty degrees for two days, insuring that the water was removed. The vial was then weighed again, thus confirming how much of the original twenty grams of solution was PVOH. The appropriate amount of PVOH was later added to the metal organic solution so as to assure a given weight percent of polymer in the final solution.

1.1.2 LSMO Solution

The first and most analyzed of our oxide systems was $La_{0.7}Sr_{0.3}MnO_3$. LSMO is extensively studied due to the high Curie temperature, colossal magnetoresistance, and potential to be an integral component in next generation magnetic memory devices [16-21]. The ratio of metals in $La_{0.7}Sr_{0.3}MnO_3$ is a necessary characteristic for it to be ferromagnetic at room temperature. Conversely, when one of the components in $La_{0.7}Sr_{0.3}MnO_3$ is removed or altered drastically, the

material ceases to be ferromagnetic at room temperature. In order to produce the nitrate based LSMO, 3.03 grams of lanthanum (III) nitrate hexahydrate along with 0.64 grams of anhydrous strontium nitrate followed by 2.51 grams of manganese (II) nitrate hydrate were mixed with 100 mL of pure deionized water. The weight of the individual chemicals was chosen to give a molarity of 0.1M if those metals were constituted as a $La_{0.7}Sr_{0.3}MnO_3$ molecule. This solution was then combined with an exact amount of filtered PVOH solution, yielding the LSMO precursor solution.

To confirm the presence of the correct ratio of metals in the LSMO precursor solution, an inductive coupled plasma analysis was performed. The machine used was Perkin Elmer model 3200L. This technique takes a highly diluted portion of the solution without any polymer present, then uses a plasma to remove any water. This then allows the spectrometer to detect in parts per million how much of a specific metal is present. Thus for $La_{0.7}Sr_{0.3}MnO_3$ an ideal ratio would be 0.7 : 0.3 : 1.0 between the three metals, regardless of the actual amount of parts per million detected. It was found that the number of parts per million between La, Sr, and Mn metals was 9296, 2816, and 5767 respectively when diluted. Optimally, the amount in parts per million would be 9700, 2600, and 5400. Setting the manganese amount to one, the lanthanum and strontium give $La_{0.64}Sr_{0.31}Mn_{1.0}O_{3.0}$. This technique is useful in the initial optimization process, for it tells if a certain metal was absent or at an incorrect amount with respect to the other metals.

Later in the project another type of manganese, strontium, and lanthanum salt was desired for mixing water, in the form of acetate. Similarly, to produce the acetate based LSMO, 2.40 grams of lanthanum (III) acetate along with 0.62 grams of strontium acetate followed with 2.45 grams of manganese (II) acetate were mixed in 100 mL of pure deionized water. This came about due to a manganese deficiency in the final nanostructures when using a nitrate based solution. This effect was attributed to the explosive nature of nitrates [21-23]. The LSMO solution using acetates was initially observed to be insoluble in water. However, after the addition of a small amount of acetic acid, the LSMO acetate solution became optically clear with no signs of precipitation. The ratio of glacial acetic acid to LSMO acetate solution containing two percent polyvinyl alcohol was one to ten by volume. The rationale behind using acetic acid was the pH had to be sufficiently low so as deprotonate the colloid causing molecule and thereby producing a homogeneous solution.

1.1.3 STO Solution

In order to prove the general applicability of this procedure which generates nanocrystals from PVOH based precursors and lithography techniques, another solution which produces $SrTiO_3$ in thin film form was made. This solution was based on the work published by Truijen et al [24-27]. The procedure was to weigh 1.05 grams of anhydrous strontium

nitrate or 1.03 grams of strontium acetate and combine that with 1.42 grams of fresh titanium (IV) isopropoxide in 1.92 grams of citric acid along with 0.41 grams of hydrogen peroxide and dilute to 100 mL with water. As with the LSMO solution, the STO solution was combined with two percent by weight PVOH. The reason why $SrTiO_3$ was chosen is due to its high dielectric constant which could be useful for certain applications as an array of nanocrystals. The orange colored solution is unstable over a period of months, however sufficiently stable as to prove that the precursor was both electron beam writable and nanoimprintable. It is believed that a wide range of combinations and stoichiometries regarding nitrate or acetate metals could be formed from this method and $SrTiO_3$ is but one.

The strontium titanate solution proved more difficult to find a stable configuration with acetates however. After introducing strontium acetate followed by citric acid and hydrogen peroxide to water, titanium (IV) isoproproxide was added. This generated an orange cloudy solution after stirring for several days. Initially it was assumed that the difficulties which rose with the LSMO acetate solution would lend some insight into the possible courses of action combating the insolubility. However after adding acetic acid in copious amount as well as other acids, the solution remained turbid. It was also suggested that barium acetate might be less polar and hence less prone to forming a complex, but alas, this also failed to produce a uniform liquid. The strontium titanate solution using acetates was eventually abandoned.

1.1.4 Filtering

The filtering of the solution is an important step in the preparation of the precursor solutions. The main objective in filtering the PVOH solution was to get a uniform solution composition and to decrease the roughness of the spin coated and annealed film. The idea behind filtering the PVOH solution came from the initial AFM analysis of the LSMO thin films which showed an unacceptably high roughness. The stirring conditions were two days at room temperature. This left an assortment of small undissolved PVOH grains visibly suspended in the solution. This observation coupled with the high roughness motivated the filtering of the PVOH prior to inclusion with the metal organics. Increasing the temperature at which the solution is stirred from 25 to 50 degrees was noted to have dissolved the PVOH grains considerably. However, this solution too required a filtering step as the resultant roughness was still high.

The filter used was a porous glass puck with pore size of one micrometer. The solution was vacuum filtered through it, thus readying it for usage in the metal organic solution. The process of filtering the solution through the glass puck generated a copious amount of bubbles which were agitated by a magnetic stirring bar in a receptacle flask so as to reduce the longevity of the bubbles. Even through the use of a receptacle flask of two liters in volume, large enough to

accommodate lots of generated bubbles, the process of filtering two hundred milliliters of PVOH solution took more than a day to allow for the bubbles to settle. The roughness of a spin coated films without filtering can be seen in figure 1-5.

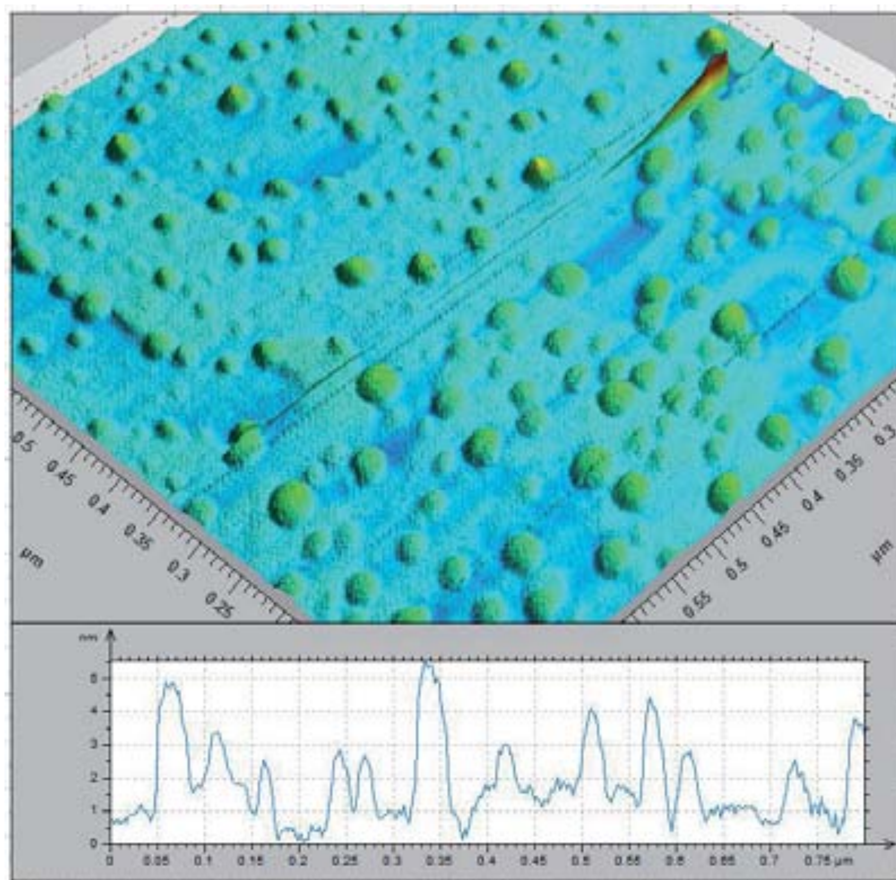

Figure 1-5 *Unfiltered solution after spin coating yields a rough surface, nitrate based 0.1M LSMO with 2 wt% PVOH after 6000 rpm 120 seconds spin coating on YSZ.*

1.1.5 Spin Coating

A key characteristic in chemical solution deposition which differs from other thin film fabrication techniques is the use of a spin coater. The thin films generated from spin coating are, on the whole, homogenous and uniform. However, perhaps the defining characteristic of spin coating a thin film over vacuum deposition methods is cost. This cost comes from the number of films spin coated in a given time, the expense of the raw materials, the maintenance required for the machine, and the quantity of raw materials not recovered in the process. For these reasons, it is felt that spin coating is a highly desirable technique and subsequently it was used exclusively in this study.

The spin coating conditions used to spread the precursor evenly across the single crystal substrate called for twelve thousand revolutions in a span of two minutes. This insured a very even distribution across the substrate with a relatively fast spin rate while allowing sufficient time so that the solvent could be ejected. The spin coating process was conducted under a nitrogen atmosphere to ensure a homogeneous film. The nitrogen gas was introduced into the dry box container, where the spin coater was, until the humidity was five percent. This lack of oxygen and water in the spin coater container prevented aggregation on the film, thus producing films with a relatively lower quantity of defects.

Another key aspect in the production of low defect thin LSMO precursor films was a rigorous cleaning protocol. The substrates were sonicated in a bath of acetone/ethanol/water for two minutes, then cleaned with nitrogen to remove any remaining solvent before being placed inside cleaned boxes. The substrate holder inside the dry box was cleaned with solvents after every use and once every two weeks the dry box was rigorously cleaned of any foreign particles. This removal of any potential contaminants, along with a low humidity atmosphere provide for a consistent platform in which to spin coat homogeneous films. It must also be mentioned that the vials used to clean the substrates were also new and cleaned with solvents in a sonicator prior to introducing the substrate. This was all in an effort to reduce the unwanted effect of thin film defects. They are unwanted due to the extremely small areas under which radiation was directed. These write areas are on the order of one hundred micrometers and thus are on same scale of a small dirt generated defect on the thin film. These two objects could possibly coincide and cause sections of nanodots to be written on an overly thick or overly thin film. This can, in turn, cause unintended variations in the ultimate size of the nanodots after development.

Once a suitable clean substrate has been obtained, one must prepare the spin coater and solution for the deposition step. In the experiments undertaken herein, all the solutions were agitated with a magnetic stirrer for ten minutes prior to drawing the liquid into the syringe. This also brought the temperature of the vial up to just under room temperature from five degrees which it is normally kept at. Once the humidity of dry box was sufficiently low, one milliliter of the precursor was drawn into a new syringe and the substrate was adhered to the aluminum holder. Around twenty drops were sacrificially excreted at this point so as to clean the needle of any contaminants that might reside inside it. Finally two drops of the precursor was placed carefully in the center of the substrate and was immediately spun at six thousands revolutions per minute for two minutes. The sample would then be removed placed on a hot plate at 75C for 20 minutes so as to expel any remaining water that might remain on the surface of the film.

1.1.6 Stability

Both the LSMO and STO solutions and their subsequent thin films showed instability in ambient conditions over time. The most pronounced instability came from the STO solution in the form of white particulates appearing several weeks after making it. Thus, the STO solution had a shelf life of a few weeks before a new batch would need to be produced. This precipitation was controlled by initially starting with newly opened titanium (IV) isopropoxide, i.e. not an already heavily oxidized specimen. Another attempt at controlling the amount of titanium oxide precipitate was to mix the components of the strontium titanate solution in a nitrogen atmosphere. This increased the time scale in which the solution could be worked and still maintaining a one to one stoichiometry between strontium and titanium.

The LSMO solution did not show any precipitation over time, however a new batch was made every three months or so. The films made from the LSMO solution however did show some form of instability after several days in ambient conditions in the form of small outcroppings. This effect was emphatically seen to be lessened if the just spun film was placed on to a hot plate for twenty minutes at 75 °C in a nitrogen atmosphere. This allowed for the polymer molecules to relax and time to dispel any trapped water at the thin film surface. The films were then directly inserted into the SEM or nanoimprinter. Samples left over night seemed to formed small out-croppings as in figure 1-6 and thus was subsequently avoided. When the samples were taken out of the SEM they were immediately developed and annealed to as to avoid unforeseen deterioration in the film quality.

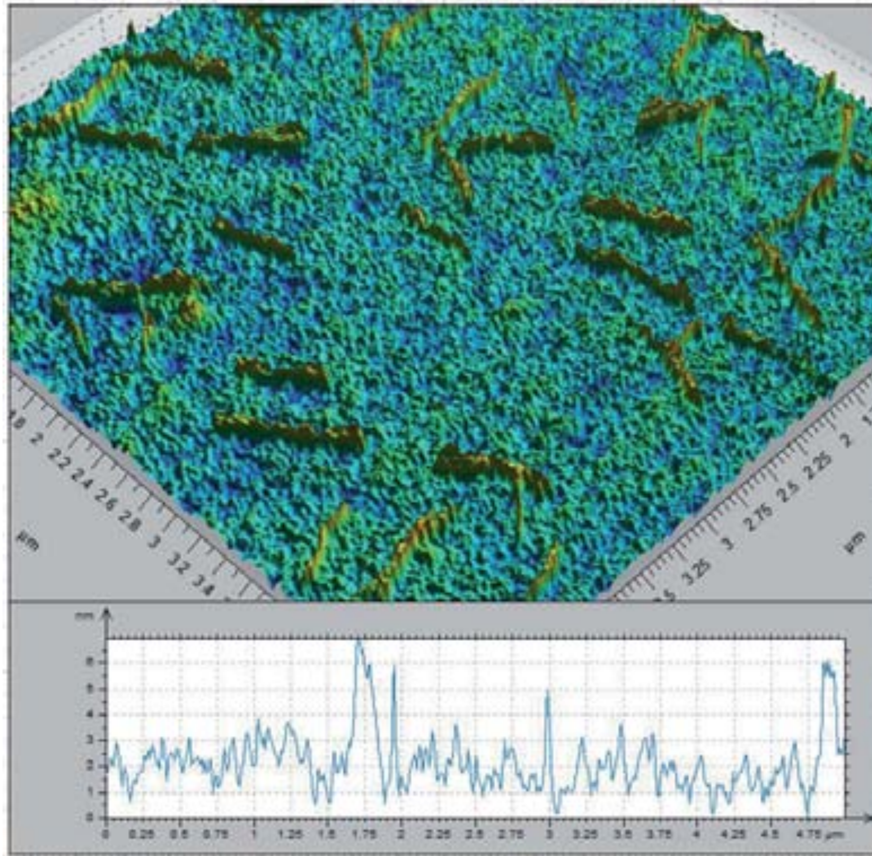

Figure 1-6 *Outcroppings seen in thin films of 0.1M nitrate based LSMO with 2 wt% PVOH after several days in ambient conditions on silicon.*

1.1.7 Annealing

The final step in the chemical solution deposition method is of course the annealing. This is where the organic components are removed from the thin film at temperature below 500 °C and above 700 °C the phase formation along with crystallization takes place. The method calls for introducing the substrate into the very center of a cleaned quartz tube and placing the tube centered in the furnace. The reason for centering is that the temperature difference even a few centimeters away from the center can be up to ten degrees warmer or colder. This then ensures more consistent results over many samples. The tube is then capped with rubber stoppers which allow oxygen to be pumped into the chamber. The volume of oxygen gas placed into the tube every minute was three hundred milliliters. This gas ensured that the LSMO precursor would get sufficient oxygen so to maintain oxygen stoichiometry in the LSMO phase while removing any out gassing from the organic components in the film.

The annealing profile for oxide films calls for a slow ramp followed by a dwell period at a temperature high enough to form the crystalline phase, and finally the slow ramp back down to room temperature. The ramp rate should be slow enough so as to allow the organics to be expelled from the film while leaving the film pore free. The ramp rate used in this work was three degrees every minute for both ascending and descending temperatures. The length of time in which the dwell temperature is seen by the sample must be sufficiently long so as to ensure homogeneity of the crystallization process. The length of time at the dwell temperature in this work was four hours. The dwell temperature for the annealing step was originally 1000 °C and later was lowered to 900 °C. The reason why the annealing temperature was original set at 1000 °C was to ensure that ample mobility of the inorganic species. However, after initial experiments regarding nanodots devoid of manganese fabricated by EBL, it was hypothesized that the high temperature was exacerbating the situation. Thus, the dwell temperature was lowered to 900 °C, which was seen as a compromise between ensuring even crystallization and reduced elemental mobility.

1.2 Oxide Thin Film Analysis

Once the LSMO or STO precursor was spin coated onto the single crystal or silicon substrate, analysis regarding thickness and roughness of the non-annealed film occurred. The results lent insight during the optimization process with regards to precursor film thickness and quality. The film was then placed in an oven at high temperatures for an extended period of time and again analyzed. This then gives knowledge regarding the annealed crystal with regards to its magnetic nature, growth direction, and elemental composition. The analytical tools used when determining the nature of the thin film were ellipsometry, profilometry, AFM, X-ray diffraction, SQUID, EDX, and XPS. In this next section, the data collected with these instruments will be presented with an eye to how these films would behave after undergoing lithography.

1.2.1 Film Thickness

In order to determine the thickness of a given thin film, two methods were employed. Ellipsometry is a technique where a thin film is radiated with optical light which is polarized at small angles. This reflected light is then passed through another polarizer and onto a detector. If one has the index of refraction of the film, then the thickness of the thin film can be known with nanometer resolution. The reason that the resolution of the ellipsometry can be less than the wavelength of the incident light is due to measurement in the change in polarization in the reflected light. For the case of LSMO and STO thin films the knowledge of thickness at various stages was necessary. One may place the unknown film in the ellipsometry, but the parameter of index of refraction is unknown. To obtain the index of

refraction of a material which is unknown, one must first know the thickness of that thin film. With this knowledge, one may work backwards with the ellipsometry in order to calibrate the machine to the new film.

The other way to gauge the thickness of thin film is make a scratch across the surface and then probe with an AFM. The scratch must be sufficiently deep so as to displace the film down to the substrate while giving a sharp edge in which to take measurements. Another requirement is that making the scratch must not carve anything out from the substrate. This would alter the topography of the substrate and thus not reveal the true thickness of the film. To this end, a sharp plastic knife was utilized to make the scratch. One problem which was often seen from this method was that the displaced film would be piled up along the edge, creating an effect similar to clearing a road of snow. The only solution that was found was to selectively probe with the AFM at certain locations which had less material accumulated.

The results of making scratches into the non-annealed precursor can be seen in figure 1-7. Here on the left one sees a very thick film partially removed to reveal the substrate floor and thus one is able to infer that the film height is roughly 500 nm. On the right hand side of figure 1-7, a smaller scratch is seen on a thinner film thus indicating a thickness of 125 nm. This method enables the user to quickly ascertain the thickness of a film without knowing the index of refraction of the precursor. One can also use this information to calibrate the ellipsometry and find the index of diffraction for the precursor. This enabled the use of the ellipsometry to determine thickness thereafter for further samples with similar parameters. The index of diffraction was measured to be 2.2 for a film with 2 wt% PVOH content with 0.1M LSMO concentration. This is slightly less than a reported index of diffraction of a similar solution [8].

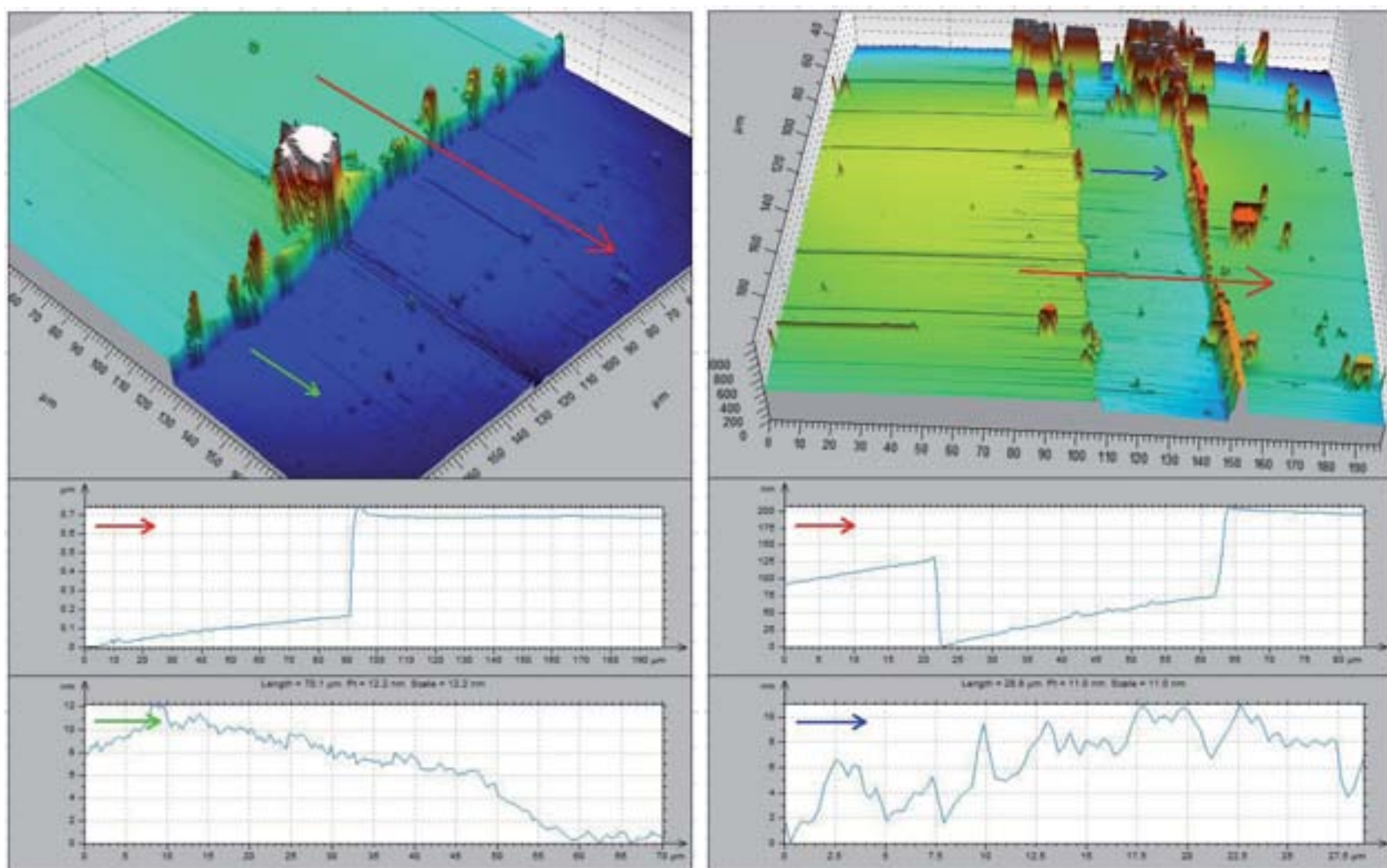

Figure 1-7 *Non-annealed thin film scratched to reveal thickness. Left: a 500 nm thick film from 0.1M nitrate based LSMO with 4 wt% PVOH spun at 2000 rpm for 15 seconds. Right: a 125 nm thick film from 0.1M nitrate based LSMO with 0.5 wt% PVOH spun at 6000 rpm for 120 seconds on silicon.*

Another technique that was initially used but later abandoned was the use of acids and masks to remove a clean portion of material from half of the substrate for later AFM analysis. This technique works by taking an already annealed film and placing a coating on half of the film with a durable polymer. The whole sample is then placed in a caustic acid bath for a few seconds so as to remove any unprotected areas of the annealed thin film. This technique does exactly that, however it was found that the acid also ate away portions of the protected thin film, thereby not truly creating a clean wall between protected and unprotected regions. Another disadvantage to this technique was its inability to be used in conjunction with non-annealed films. If any of this durable polymer protection touched the precursor, there would be a mixing of the two liquids and thereby altering the thin films inherent thickness.

1.2.2 Film Quality

A tremendous amount of film quality information can be made with atomic force microscopes (AFM). This microscope allows for the determination of morphology at the surface with nanometeric resolution. The technology stems from a laser being reflected off a scanning tip, where the exact location of this reflection is measured by photo detectors. When this tip moves over a rough surface, the tip moves up then down and thereby the reflection moves accordingly. The primary purpose of scanning with the AFM on non-annealed films is to characterize the surface roughness. If the surface roughness is too high, then it is a good indication that the structures derived from lithography will not be optimal. The relationship between the non-annealed and annealed roughness of 0.1M nitrate based LSMO on LAO can be seen in figure 1-8 on the left and right respectively. *In figure 1-9 one observes a very high roughness. The high roughness comes from the extremely high concentration of La, Sr, and Mn nitrates. Namely, the concentration of the left of figure 1-9 was 1.6M and on the right 0.4M was used. Thus one can see that the concentration of metals does alter the roughness of the resultant film tremendously.*

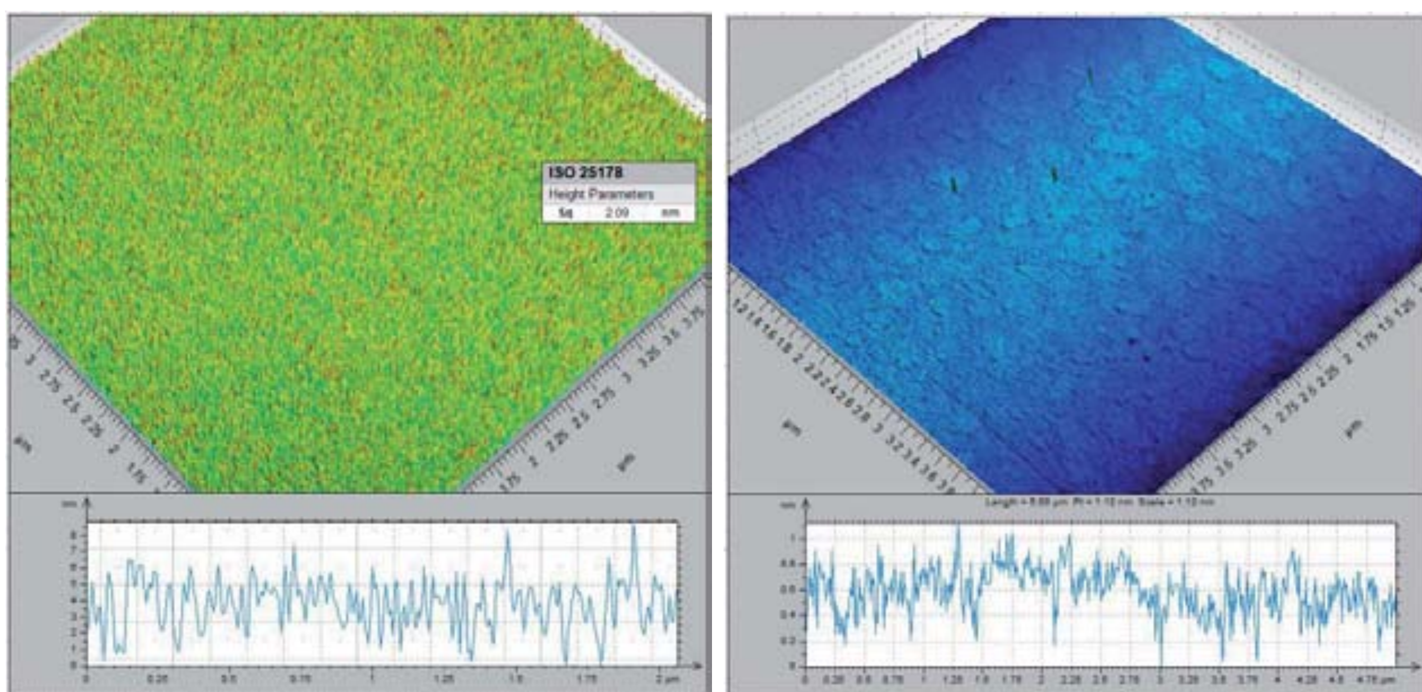

Figure 1-8 *Left: thin film topography of non-annealed 0.1M nitrate based LSMO with 2 wt% PVOH on LAO. Right: thin film topography of annealed film with 0.1M nitrate based LSMO with 2 wt% PVOH on LAO, annealed at 1000 °C for 4h.*

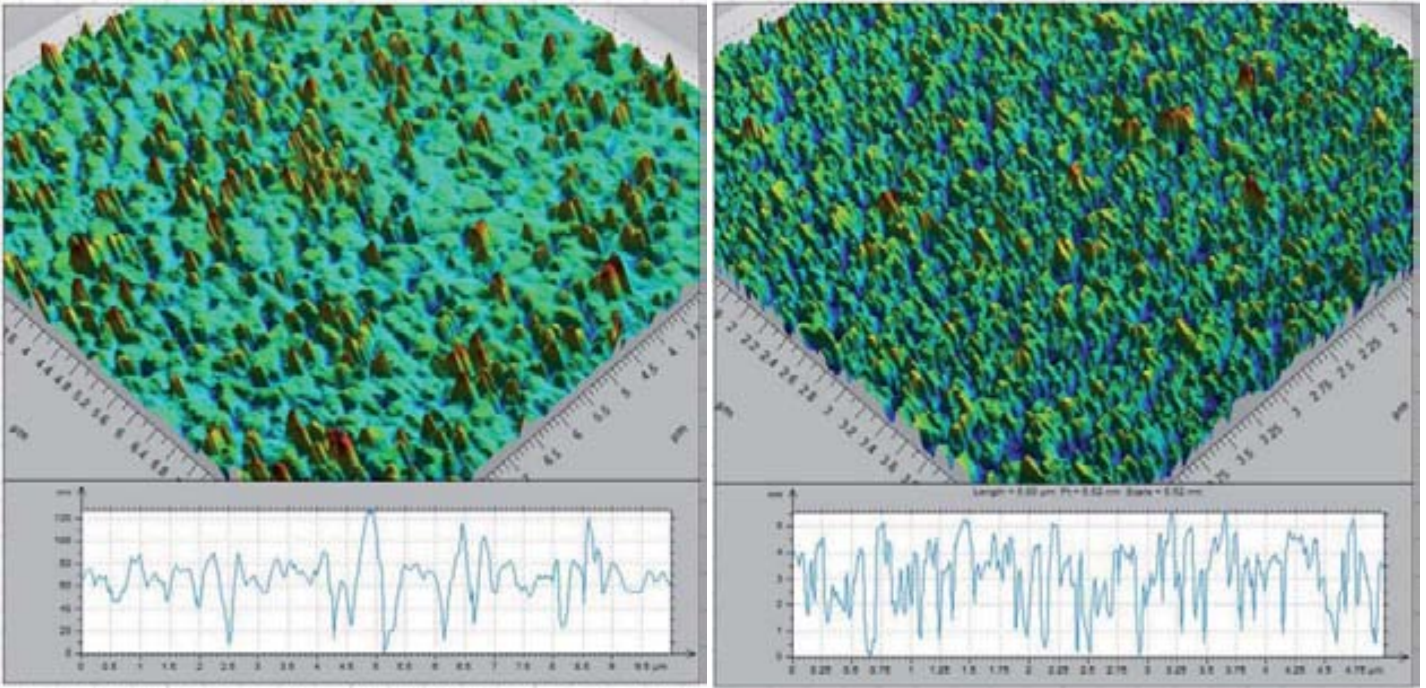

Figure 1-9 *Left: surface roughness of annealed 1.6M nitrate based LSMO film with 2 wt% PVOH on LAO. Right: surface roughness of annealed film 0.4M nitrate based LSMO with 2 wt% PVOH on LAO, annealed at 1000 °C for 4h.*

1.2.3 Structural Characterization

The crystalline, magnetic, and topographically characteristics of annealed thin films are critical to understanding the nanostructures subsequently generated by lithography. Therein, the characteristics of the thin films relay that a solution/substrate combination would give us single-phase magnetic epitaxial nanodots after lithography. There exists many and varied techniques in which thin films may be probed. These include x-ray diffraction, SQUID measurements, and checking film roughness with AFM. Each of these techniques gives a slightly different insight into the true nature of these films. When one of the annealed films was analyzed to give proper epitaxial growth upon a single crystal insulating substrate and showed a magnetic signature in-of LSMO, a new film was spin coated and subjected to one of the lithographic procedures.

The most common analysis performed on annealed films was that of x-ray diffraction. X-ray diffraction is a technique in where a beam of x-rays are radiated at various angles on to a crystalline film where they are subsequently scattered and then detected. The scattering occur at certain angles and not at others, this relays that there was a crystalline structure to the film. The basic principal is this, when x-rays are emitted onto a crystal, a diffraction pattern is generated. This is due to the crystalline nature of the film, i.e. if the film was completely amorphous, no diffraction pattern would be generated. This is due to the general destructive interference from the reradiated photons and thereby resulting in no

peaks. However, if the allotment of atoms has a repeating pattern, then the reradiated photons will produce constructive interference in certain places. This constructive interference can be seen as peaks with described angles relative to the central beam. These peaks are unique to the crystal being analyzed and serve as a finger print to indentify the crystal.

An example of the reflection pattern generated from LSMO thin films can be seen in figure 1-10 as function of molarity and annealing time. There on sees four large peaks in the image which is characteristic of the substrate in which the film was grown. Also one sees smaller peaks just to the left of each of the four main peaks, these come from the epitaxial reflections of LSMO. The reason why the epitaxial peaks from LSMO are so close to that of the single crystal substrate is due to the similarity between the two unit cells. The exact angle in which the peak occurs can be compared to other known diffraction patterns and theoretical calculations. The intensity of the peak belonging to the substrate is much larger than that of the thin film due to the much larger number of atomic planes the x-rays reflect off of.

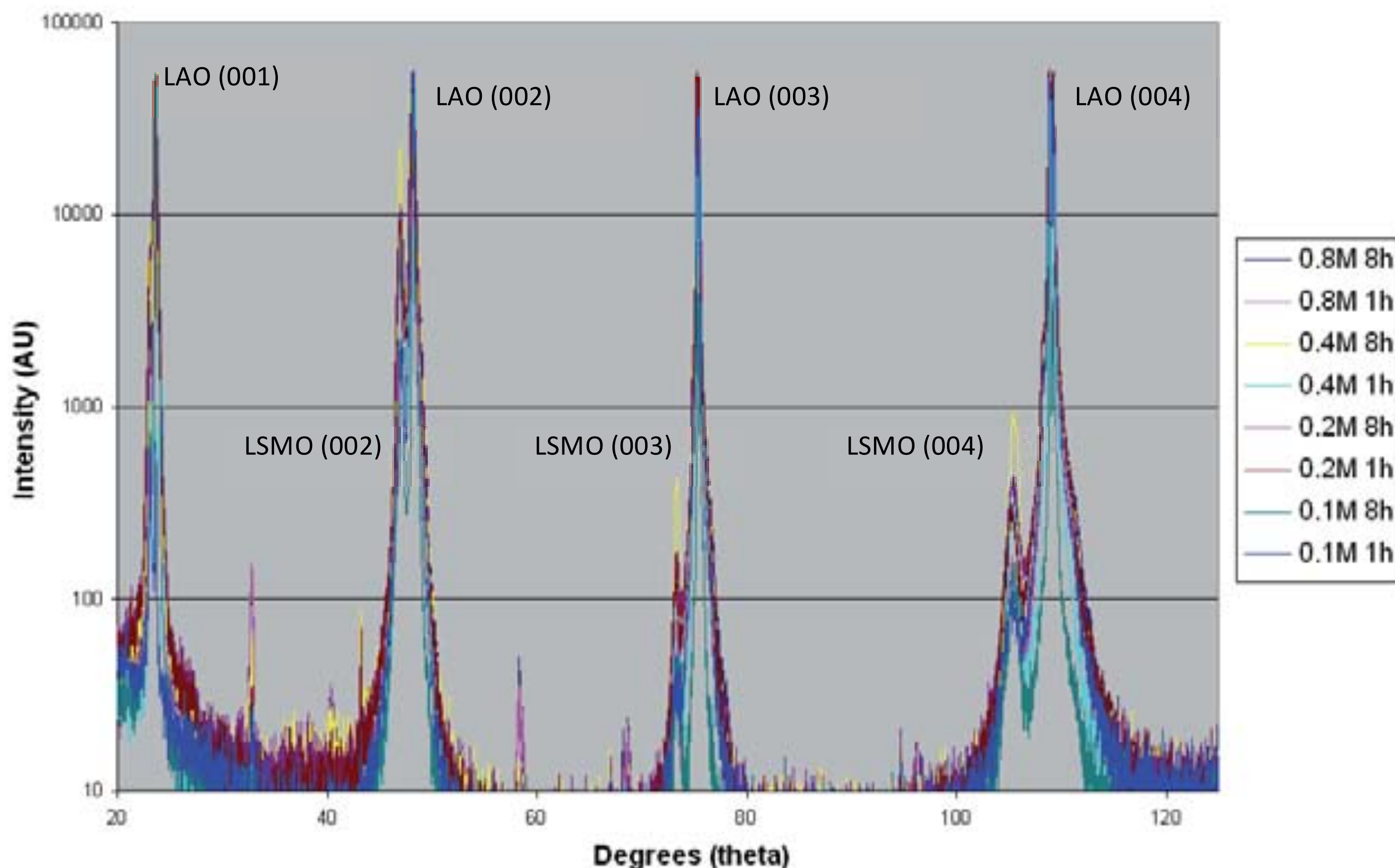

Figure 1-10 *X-ray diffraction peaks of the grown LSMO film on top of the substrate LAO showing a range of concentrations from 0.1 to 0.8 M nitrate based 2 wt% solutions and two different annealing times of one and eight hours at 1000 °C.*

One can also see more closely the sum total of scattered x-rays for a single peak in figure 1-11. There the peak from the substrate is seen on the right and the peak from LSMO is seen on the left. The reason why the epitaxial peaks from LSMO are so close to that of the single crystal substrate is due to the similarity between the two unit cells. The exact angle in which the peak occurs can be compared to other known diffraction patterns and theoretical calculations. The intensity of the peak belonging to the substrate is much larger than that of the thin film due to the much larger number of atomic planes the x-rays reflect off of. Regarding the response to altering the molarity of the precursors from 0.8M to 0.1M one can see no change except in intensity. The same could be said when altering these molarities from an annealing time of one hour to eight hours at 1000C. Thus one could conclude that annealing for one hour at 1000C using a molarity of one tenth would yield suitable single phase epitaxial LSMO films. These conditions were then used in the making of LSMO nanostructures by lithographic means.

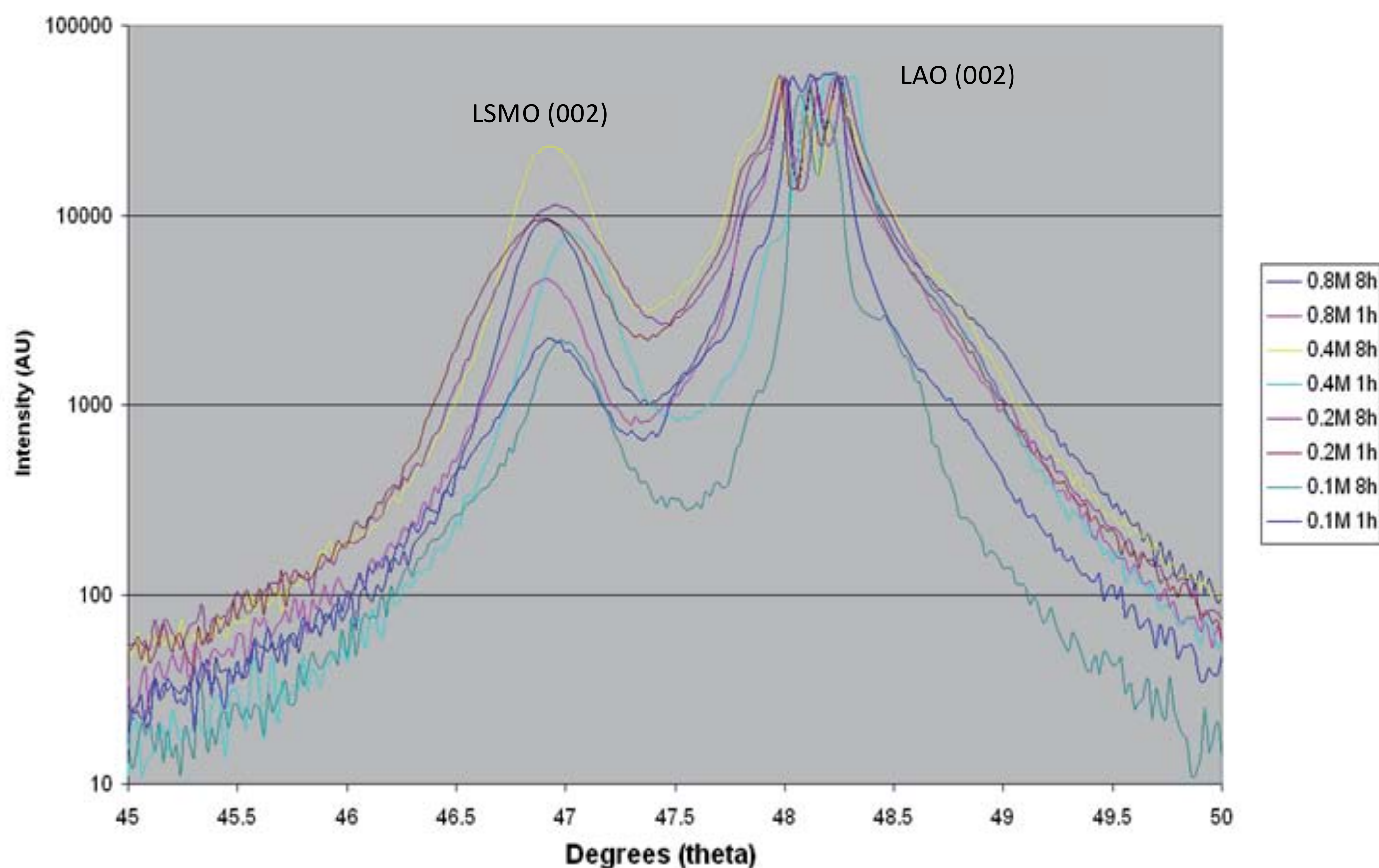

Figure 1-11 *Close-up of a single peak of film grown from 0.1M nitrate based LSMO with 2 wt% PVOH solution on LAO by being annealed at 1000 °C for 4h.*

Furthermore, with two-dimensional x-ray diffraction, one can see the strain induced in the thin crystal film as a result of growing cube-on-cube on a substrate with a slightly different unit cell. This measurement of angular lattice strain distribution can be obtained by determining the how the unit cell is modified at different orientations. This can be seen in figure 1-12 where the (002) reflection for LSMO is very close to the (002) reflection for LAO, specifically 47.8° for the (002)LAO peak and 46.5° for the (002)LSMO peak. The (002)LSMO peak is very similar, but different than reported reflections from powder LSMO, namely being a peak of 46.9° [28]. This discrepancy is the result of the LSMO growing epitaxially on the LAO substrate in a compressed manner. This pole figure displays information about the crystallinity of the film, for if the peak were ring instead of a singular peak than the film would be polycrystalline as well as indicating its lack of uniformity.

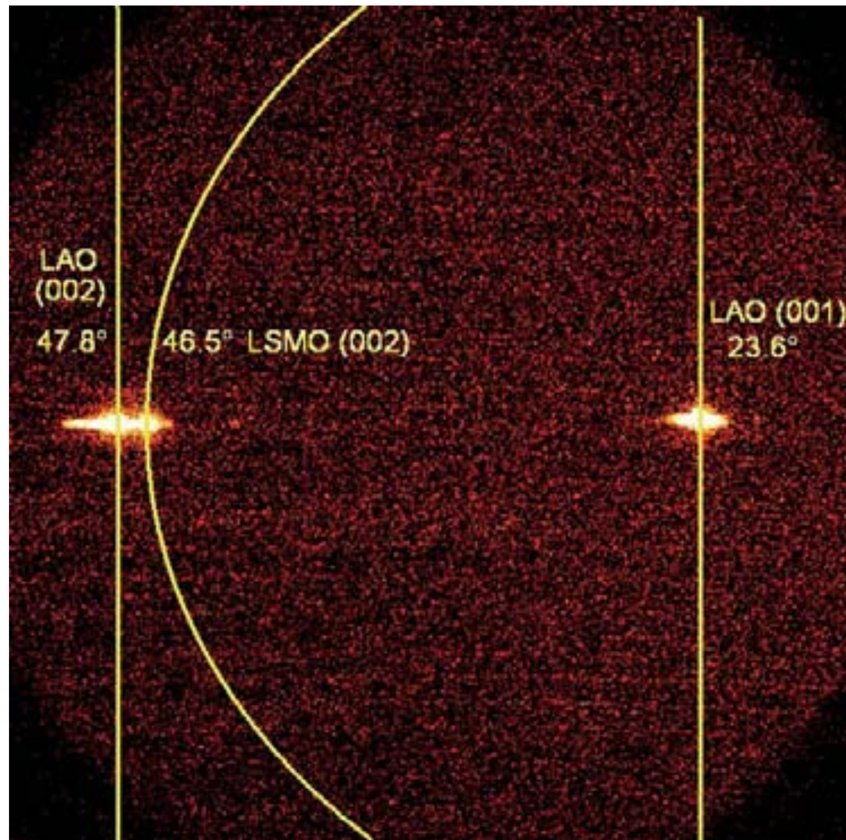

Figure 1-12 *Two dimensional representation of two peaks on the LAO substrate and one for the LSMO film which was grown from the 0.1M nitrate based LSMO solution with 2 wt% PVOH, annealed 1000 °C for 4h.*

1.2.4 Magnetic Nature

In order to further confirm that the grown film is LSMO, samples would be given for magnetic analysis in the SQUID. Simply put, the SQUID is a way to measure small magnetic moments from thin films at temperatures ranging from near absolute zero to higher than room temperature. It can also measure the resultant magnetization when varying the induced magnetic field in-plane and out. In figure 1-13, one can see the response of a LSMO thin film in terms of magnetization under applied field and temperature. On the left hand side a thin film was subjected to an applied magnetic field, ranging twelve teslas, at ten degrees above absolute zero. On the right, one notes how the film's ferromagnetic nature decreases as the temperature is increased in a half telsa field. The point at which the sample ceases to be ferromagnetic at a given temperature is called the Currie temperature. This temperature along with the emu per cubic centimeter is on par with reported results for LSMO [16, 17, 29].

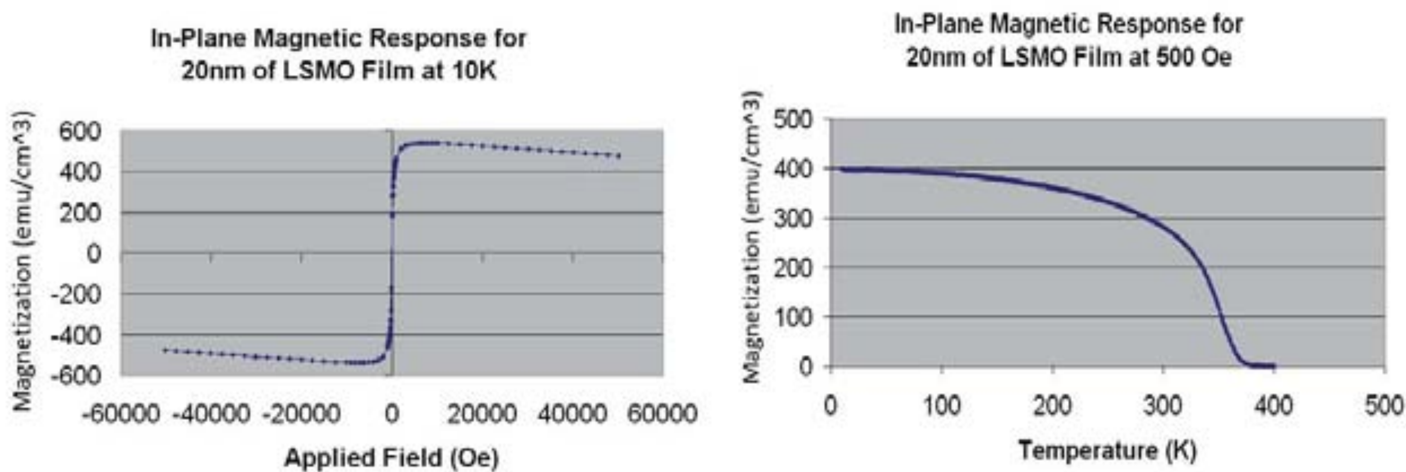

Figure 1-13 *SQUID results of 0.05M nitrate based LSMO with 1 wt% PVOH thin film grown on LAO after 1000 °C for 4h. Left: magnetization to an applied field. Right: magnetic response to a change in temperature*

1.2.5 Elemental Analysis

Another technique that was used to clarify the presence of specific elements was energy dispersive x-ray spectroscopy (EDX). The technique was used initially in this work due to an existing module on the SEM chamber making it readily available. However, it was soon ascertained that this form of spectroscopy penetrated into the thin film too much and only registered elements in the substrate. It works by radiating electrons at the surface on the film and then registering what the energies of the emitted x-rays are. This technique allows control over the voltage potential of the electron emitter, hence can be scaled to probe different depths of the sample. Unfortunately, at the lowest energies the instrument could emit, the penetration depth was still too much and all but the thickest samples were not analyzed with EDX as seen in figure 1-14.

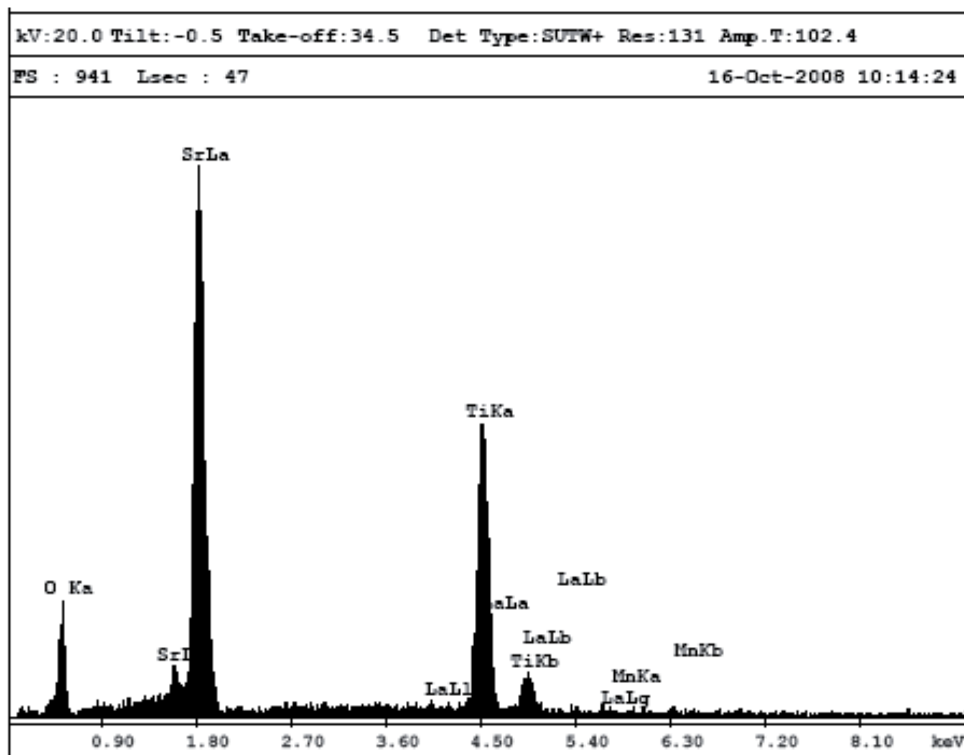

Figure 1-14 *Results from a EDX instrument showing elemental presence of Sr, Ti, and O from the substrate but failing to detect La, and Mn in the thin annealed film which stemmed from 0.1M nitrate based LSMO with 2 wt% PVOH after 1000 °C for 4h on STO.*

X-ray photoelectron spectroscopy (XPS) was used later due to the limitations of using EDX. The goal of exploring the presence of individual elements was to determine if any of the elements were lost at any stage in the lithography process. This form of spectroscopy allows one to not only see peaks corresponding to particular elements of a very thin film, but also to see the shift in peaks due to functional groups those elements are a part of. The basic principal which underlies XPS is the following: the sample is pumped down to an ultra high vacuum where x-rays are able to be directed on to it at a particular angle. The detector placed near the sample then measures the quantity and energy of emitted electrons. This technique allows only the very surface of a sample to be analyzed and therefore can be a limiting factor. To remove excess organic material on the very surface of the annealed film, the sample is irradiated with high energy x-rays prior to analysis. The results of a XPS analysis on a series of LSMO non-annealed and irradiated films can be seen in figure 1-15.

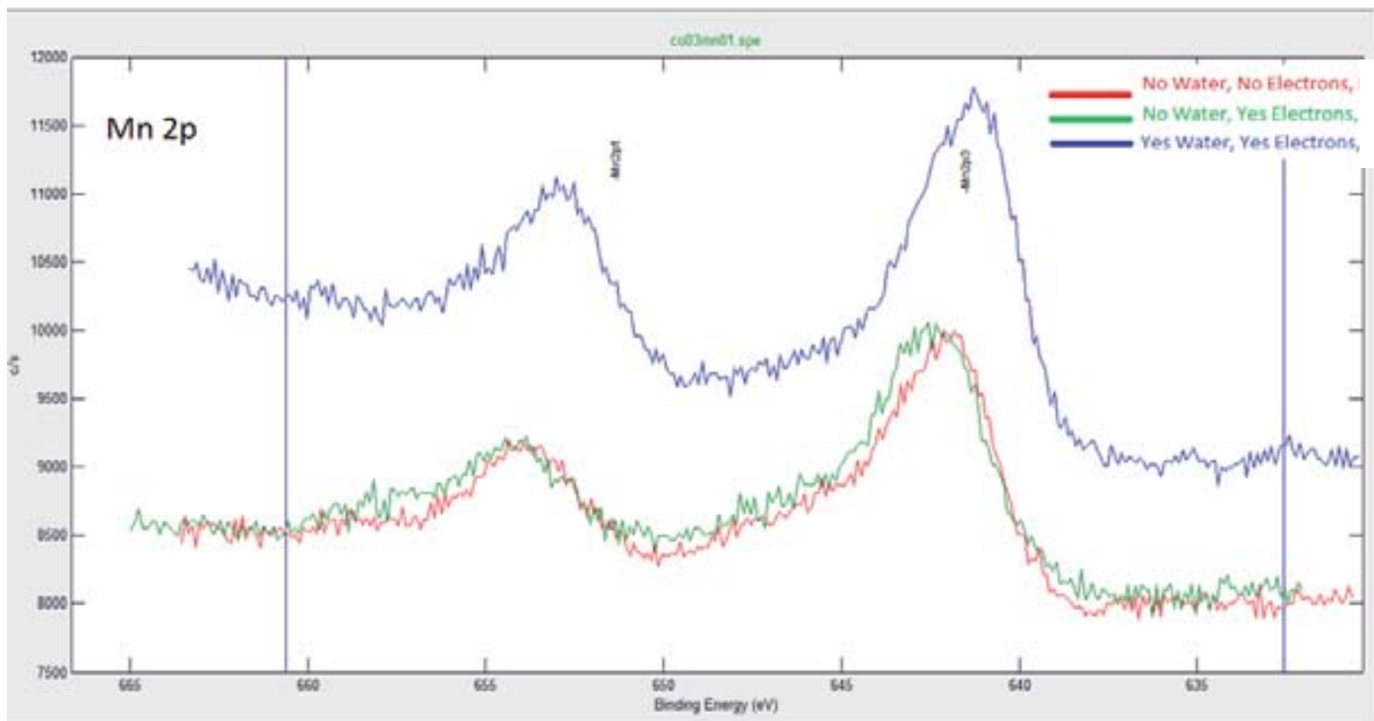

Figure 1-15 *XPS analysis of three non-annealed 0.1M nitrate based LSMO films with 2 wt% PVOH, all showing elemental presence of manganese. Red line shows film immediately after spin coating, green line shows film after spin coating & irradiation, and the blue line shows film after spin coating & irradiation & water development.*

Analyzing figure 1-15, one notes that there are two peaks present at 654 and 641 electron volts which correspond to 2p1 and 2p3 orbitals for manganese. Manganese was an element of interest due to its absence from nanostructures from LSMO precursors made by EBL. These peaks correspond to elements detected in the first few nanometers of the film. The red line represents a film freshly spun onto a substrate without any alteration. The green line signifies a film spun onto a substrate after being irradiated with one square millimeter of electrons. The blue line also was irradiated with one square millimeter of electrons but afterwards was washed with water to reveal non-annealed nanostructures. The purpose of analyzing these three substrates was to determine if the element manganese was being eliminated in the electron beam process, and if it was, was it immediately eliminated after irradiation or after the water development step. The results show that manganese is present in all three films. One can conclude several things from this experiment; namely that the process of radiating a sample with focused electrons does not detect a loss in manganese, and when removing the soluble precursor from the insoluble nanoislands, the manganese is also not detected to have been removed. Thus one infers that the difference between the unmolested film, the irradiated but undeveloped film, and the irradiated/developed film is minimal in relation to elemental loss.

In figure 1-16 one see the effect of annealing nanodots by EBL on YSZ and STO substrates at various temperatures with regards to elemental presence. That is, the presence of manganese was detected for films grown on STO and YSZ when the annealing took place at only 500 °C for four hours. This contrasts with the film grown on YSZ annealed at 900 °C for four hours where the presence of manganese was not detected. Analyzing the results of figure 1-16 one concludes that the manganese is being removed when annealing at higher temperatures than 500 °C.

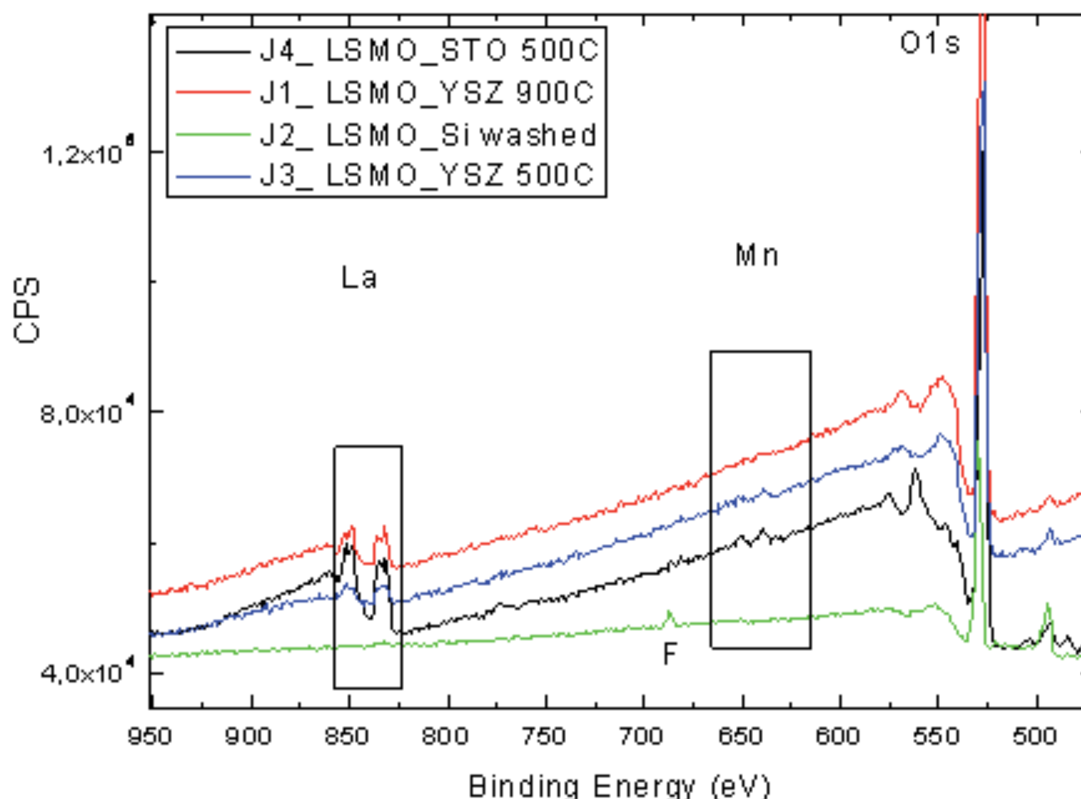

Figure 1-16 *Three annealed films derived from 0.1M nitrate based LSMO solution with 2 wt% PVOH, analyzed by XPS on STO, YSZ, and silicon substrates in order to detect lanthanum and manganese. Green line is film on silicon after being water developed, black line is film on STO after annealing at 500 °C 4h, blue line is film on YSZ after annealing at 500 °C 4h, and red line is film on YSZ after annealing at 900 °C 4h.*

1.2.6 Gravimetric Analysis

In order to determine at what temperature the organic components of the thin LSMO film decompose, a gravimetric analysis was performed. This type of analysis measures the minuet mass loss of the sample as the temperature is slowly raised. One can see the subsequent mass loss as a function of temperature along with the differential thermal analysis (DTA) on the left hand side figure 1-17 for LSMO and on the right hand side for a STO solution. DTA is a process in which the exothermic or endothermic response to temperature is measured versus a standard, thus giving information about phase changes.

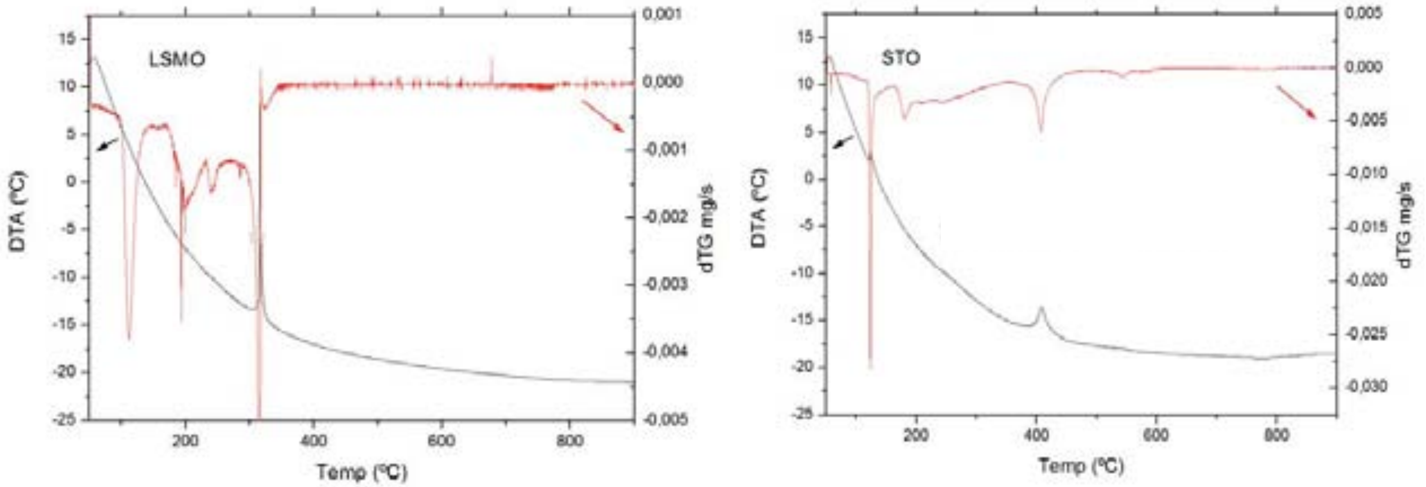

Figure 1-17 *Left: the amount of weight loss as temperature increases for a 0.1M nitrate based LSMO film with 2 wt% PVOH. Right: weight loss as a function of temperature for a 0.1M nitrate based STO film with 2 wt% PVOH.*

Analyzing the results of figure 1-17 with regards to the amount of mass lost per second, one can see that after 350 °C for the LSMO film and 500 °C for the STO the films do not lose any more mass. One can thus conclude that the organic components have been removed from the film at temperatures higher than that. At temperatures less than 375C, several peaks are seen 110 °C, 195 °C, and again at 325 °C in the LSMO film are recorded while the STO film 125 °C, 175 °C and 400 °C. These constitute points in the annealing process where a species was removed. It is assumed that the 110 °C peak is from the removal of water due to its breadth and proximity to the boiling point of water. Whereas the 195 °C & 175 °C peaks and the 325 °C & 400 °C peaks are harder to identify, they are assumed to come from the decomposition of PVOH and the nitrates respectively [30-33]. The DTA shows that below 150 °C, the thermal reaction is exothermic while above that temperature it is endothermic. At 325 °C & 400 °C there are also sharp peaks in the DTA curve, suggesting that a major exothermic phase change has occurred. This is consistent with the idea that nitrate/PVOH based films are highly exothermic in decomposition, called an auto-combustion reaction, and that the LSMO film had a larger amount of nitrates than the STO film by weight [9, 34].

1.3 Electron Beam Lithography

The advent of the scanning electron microscope (SEM) in 1935 eventually allowed for electron beam lithography [35]. This was realized with recent add-on control units which moved an electron beam on a pre-arranged route. This

coupled with a pre-arranged series of commands to blank the electron beam at certain locations over a developable film led to what is now called electron beam lithography. This breathed new life into the expensive SEM, thereby allowing one to irradiate with focused electrons for various durations as low as microseconds at locations which could be mapped out beforehand. When coupled with an electron active thin film such as a positive type PMMA resist, could easily produce holes which would be developed in two types of solvents. This gave nanofabrication a new and very controlled tool in which to construct nanoscale features.

The main technology behind electron beam lithography is of course a focused electron beam [36, 37]. This focused column of fast moving electrons causes the thin film to either become locally soluble for positive resists or locally insoluble for negative resists. A schematic on how electrons are focused can be seen in figure 1-18. This focused beam of electrons is then allowed to interact with resist until the desired area is affected. The electron beam is then stopped from impinging onto the thin film by an ultra fast electrostatic shutter. If the next area to irradiate is sufficiently close, the electron beam with simply be reshaped by the objective lens until it falls onto the new area and then the blanker would open allowing irradiation. If the next area is far away, then the stage must be moved by either mechanical or interferometer based servos. In any case, once the totality of the irradiated areas has been written, the sample is removed and emerged in a developer liquid or liquids. This developing step removes soluble remnants of the thin film, leaving only those areas which were desired to remain. The sample is then placed into the tube furnace for annealing or coated with a capping layer for further lithography steps.

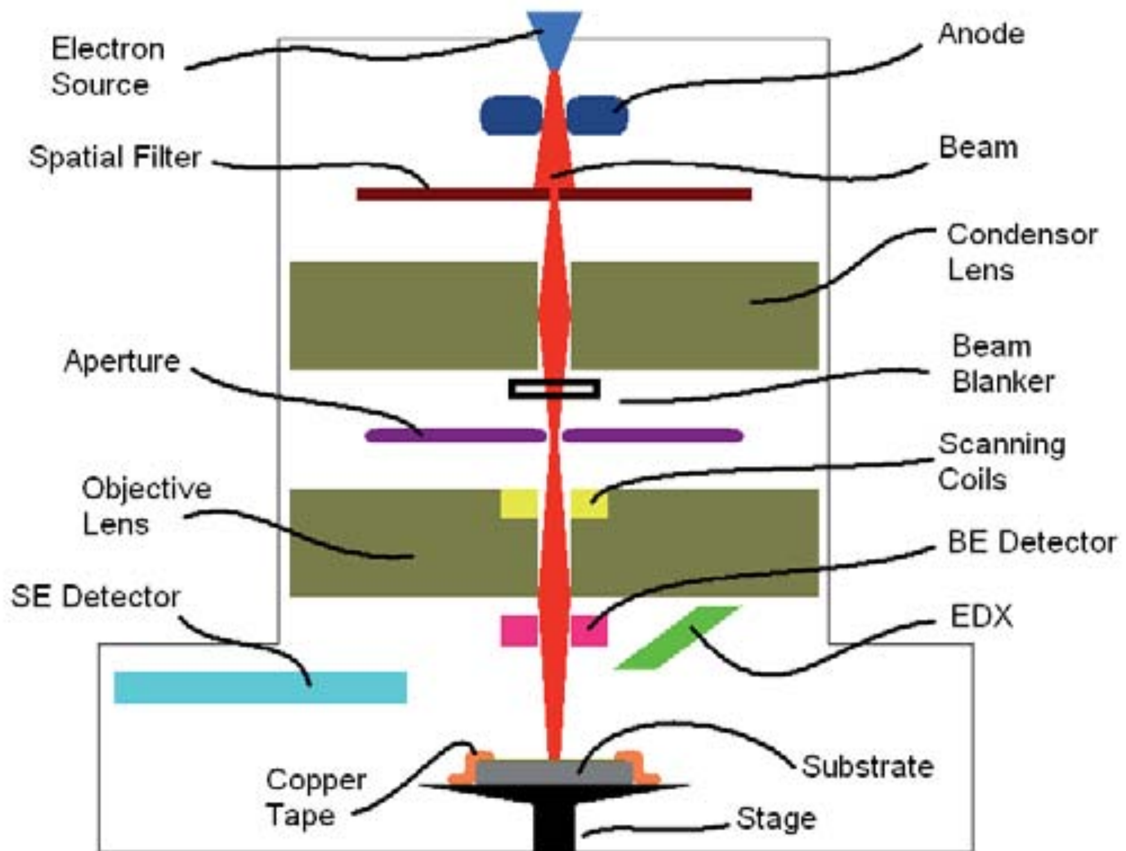

Figure 1-18 *Schematic of SEM column used in electron beam lithography.*

Certain parameters must be optimized to bring the electron beam onto the surface at a single point. Correcting for astigmatism is where the beam is not perfectly round, but rather is elliptical. This comes from the electromagnetic condenser lenses, not being properly adjusted. Aperture alignment refers to moving a disk with a small hole in it which primary purpose is to control the amount of electrons focused onto the film. This aperture can also be moved perpendicular to the beam and also serves to align the focused electrons. One can see if the aperture is not aligned and the strength of one of the electromagnetic lenses is weakened, the beam moves preferentially in direction instead of simply growing larger. The larger the aperture, the more electrons and thus higher contrast, however the less collimated the beam is and visa versa for a lower aperture. The working distance refers to the distance from the objective lens to the surface being focused upon. When the working distance is extremely small, the beam will not be able to focus and when it is extremely far, the electrons will be overly dispersed. At normal small working distances, the depth of field will be small but the beam collimated, while at normal large working distances, the depth of field will be large but the beam less collimated.

1.3.1 EBL on Insulating Substrates

The exposure in which the film interacts with is typically thought of as coming from the primary electron beam, however secondary electrons coming from the non-focused primary beam as well as backscattered electrons coming from random directions inside the film, may affect the final quality if not enough consideration is paid to focusing, localized charging, or exposure times are too long. On the subject of localized charging, it must be stated that this subtle but influential effect must be taken into account for substrates such as YSZ, STO, and LAO. The conductivity of these single crystals range from slight charging for STO and LAO, to heavy charging for YSZ. This is markedly different than for silicon oxide substrates which distribute the newly deposited electrons rather quickly away from the area of impingement. This problem of localized charging allows only a limited range of voltage energies and aperture openings when working with single crystal substrates, thus one has balance between local surface charge and surface conductivity. Remedies to this surface charging on the oxide single crystal substrates led to attaching copper tape as close to the irradiated area as possible so as to draw off any persistent charge.

The consequence of non-perfect surface conduction is two-fold. First, is that the initial attempt to focus onto the thin film surface proves to be very difficult. Second, once the electron beam radiation process has commenced, the beam is forced off its intended spot due to charging in the vicinity. A more in depth analysis of the effects of substrate charging on the initial attempt to focus onto the thin film surface are as follows. When one adjusts the three focusing mechanisms so as perfectly resolve as piece of dirt at the edge of the thin film, for example, one is met with a dynamically altering image. In other words, the longer one looks at an area and the better one is able to normally focus. However, in this case the more charge is also deposited, making it harder to see. This effect is seen most dramatically on YSZ with waves of relative charge moving quite quickly across the surface. This continually changing image makes it difficult to see any dust particles on thin film or annealed nanostructures. Thusly, one is never entirely confident of the level to which the beam has been focused on to the resist.

The second unintended consequence of local charge build-up is with regard to beam drift. The electron beam may, over time, start to move off highly charged portions of the thin film. This can be seen more readily when using relatively large time scales for individual radiated points which lie relatively close together. For arrays of dots in symmetric arrangement, this can mean the last of these dots maybe written far away from its intended target. For an array of dots, structures are written from one corner in series of descending rows, much like how one reads a book. However due to local charging, each row of dots can be perturbed slightly more on every consecutive row, finally giving a non-uniform distribution of written dots as can be seen in figure 1-19.

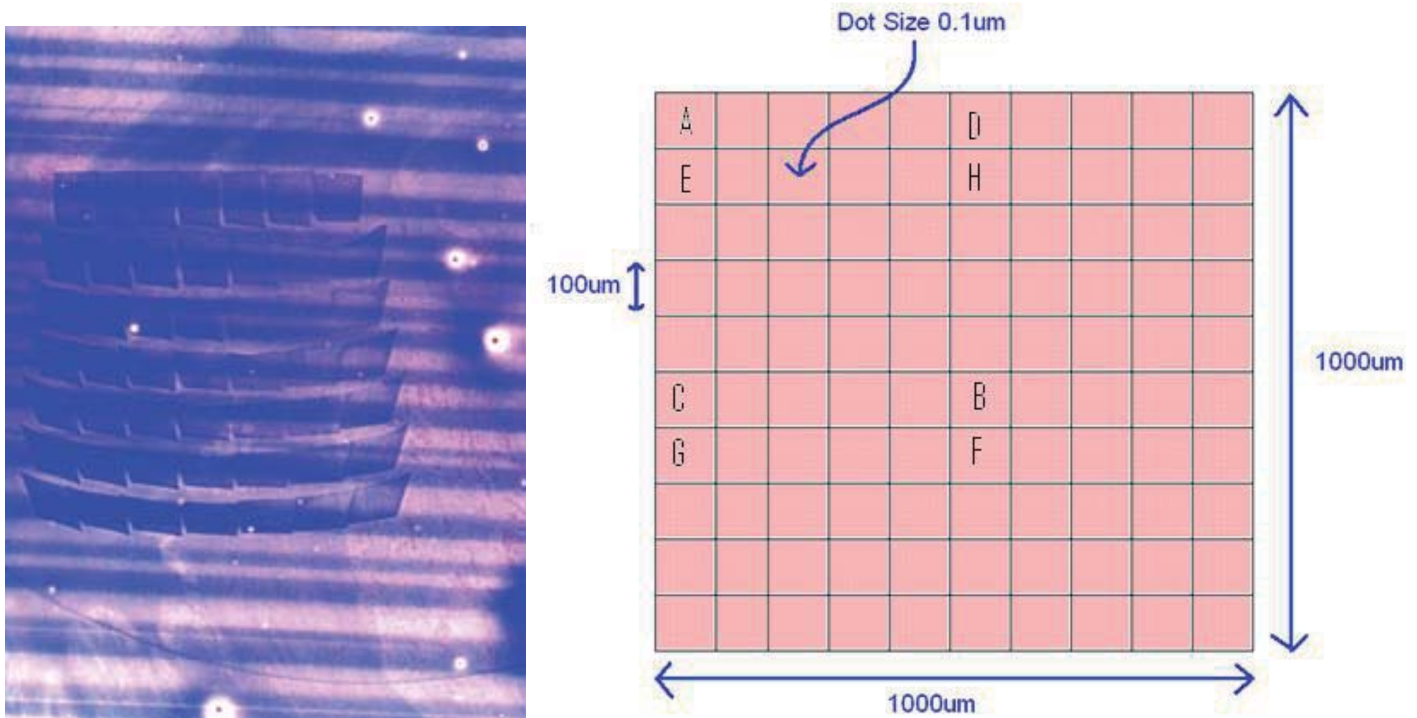

Figure 1- 19 *Left: an array 700 µm x 700 µm in size showing long ranging surface charging problems from writing on YSZ substrate with LSMO precursor. Right: a schematic showing a four quadrant scheduling to reduce charge build up.*

Other considerations that will influence the final output of the written structures include: distance between write fields, time delay between writing fields, order in which fields are written, and the order in which structures in a write field are told to be irradiated. The distance between write fields alters the dosage radiated on a larger area, thus increasing charge build up on the films surface. There are two ways in which this local charge build up can be remedied, but not completely eliminated. One tactic is simply to wait extra time between writing the next area. Thus, the charge would dissipate naturally due to atmospheric gases and charge diffusion. However the time between written areas is in reality prohibitively long thus making it impractical. The other tactic is to write the proceeding area as far away from the last written area. This can be seen visually on figure 1-19 where the letters A, B, C, D, E, F, G, H et cetera are the order in which the 100 micrometer squares are written to make a one square millimeter array. This strategy works well, because the time it takes to go between the four different quadrants is typically long enough for some reduction in charge build up.

Another important point which should be made is with regard to maintaining a consistent focus across the entire sample. When writing an area of one millimeter square, variations in where the electrons converge can cause unintended discrepancies in the nanostructures as a final product. A remedy to this is firstly to focus in the middle of the intended write area instead of in a corner when writing large arrays. This will reduce the small shift in the focusing plane which exists as a function of distance. Of course, this adversely alters your final design directly in the middle,

however this sacrificial area is small relative to the larger whole. Another remedy is to have the working distance slightly further from the aperture opening than would otherwise be recommended. Typically the working distance is roughly thought to be one millimeter for every kilovolt of voltage applied. All of the experiments undertaken in this work were performed at five kilovolts, however a working distance roughly twice this distance was used to prevent significant discrepancies between corners of a largely written area. Hence, the greater the distance away from the aperture a focused object is, the smaller the variation in spacial dosage will be. Another consideration related to electron beam lithography is the beam stabilization. One should wait for at least ten minutes if previously turned off so as to allow the output from the filament to produce little variation in dosage.

Another procedural hurdle is to mount the sample flat on the stage. This detail is important in getting uniform irradiated dots for a large write area. When mounting a sample, one has two options as far as what they are placing the sample on to, aluminum or a flexible carbon sticker. With aluminum, one achieves a much more planer surface on which you place the sample, hence more uniformity as a function of distance, although little in the way of charge reduction. With the carbon sticker, one gets a stronger contact underneath the sample to something which is highly conductive, hence slightly less charging. However with the carbon sticker, great care must be taken when placing the substrate onto it, for if one side of the sample is slightly higher than the rest of the sample, then a non-uniformity in focusing will occur. Initially, the samples irradiated in this work were fitted atop carbon stickers, however, after it became clear that uniformity was of higher concern than charging, the substrates were simply placed on the aluminum stage and adhered in the corners with copper tape.

Defining a write field is also an important step in the e-beam lithography process. This entails telling the instrument where electrons fall exactly onto the stage for a given magnification for a write field size. To accomplish this, one must focus on a part of conducting substrate which has some small recognizable feature; typically this is a piece of dirt. Then the user tells the computer where three points around the recognizable feature are, the stage is then moved three times and the user then adjusts this alignment. The reason for the write-field alignment is the signal to deflect the beam has to pass through several electromagnetic stages which can cause long term drift.

There also exists various strategies in which the patterns can be written. The strategy lies, from a practical point of view, on the ultimate goal of the sample. An example of this would be if the sample is intended to simply check the feasibility of writing nanodots onto a highly conducting substrate, then a small write area directly in the center without markers would be advisable. This small area could contain various dosages and densities in a single area. This is because the sample will be checked with a SEM to see if the nanodots are there due to its high conductance, hence an AFM analysis is unnecessary. However, if that same sample needed to be analyzed by AFM, then many markers would

need to be made surrounding the centrally written area. Another example is that of an array of dots all with a particular pitch or dosage written next to an array of dots with a different pitch or dosage. These large arrays of nanodots can yield information about the likelihood of obtaining a particular height for a nanodot at a particular dosage. However, making a series of these arrays would in themselves be difficult to analyze with the AFM. This is because the AFM can roughly scan up to ten square micrometers at a time when the structures are small, and roughly thirty square micrometers for larger structures. Small structures typically consist of annealed low dosage nanodots whereas large structures are those of nanowires and markers. This problem forces the heavy use of markers which not only indicate where the main section of low dosage nanodots is written, but also what dosage the nanodots you are observing received. The markers that were used for later indication of where the main section was written were simply several arrows each made up of high dosage dots written to insure that they could be read easily read. Obtaining both SEM and AFM images to support the idea that a particular combination of dose, pitch, and substrate produces is of the highest importance.

1.3.2 Nanostructures from LSMO Precursor

Briefly the procedure for generating nanostructures by EBL will be touched upon in this section so as to put the rest of this work in perspective. The process is such that first a single crystal substrate which has a spin coated LSMO precursor is placed onto the stage inside the SEM chamber and attached with copper tape. The vacuum is then pumped to below a millipascal along with the applied voltage and aperture diameter. The surface of the holder is then focused on and jogged to the location of the substrate. Next the surface of one of the corners of the thin film is focused on and the working distance adjusted. The astigmatism is then corrected so that the image appears sharp followed by an aperture alignment. The system needs to have new relative coordinates entered in, so the very corner is defined as the origin and two points are taken along one edge so as to define the x and y axis. The write field is then defined at a given magnification around a recognizable piece of debris. Next the write head is blanked and told to jog to the very center of the substrate. The beam is then unblanked and a single spot is made and noted for its shape. Depending on whether the spot is elliptical or diffused, the focus and astigmatism is corrected. This process of making single dots and observing them may occur four or five times until the spot is sufficiently small and round. The computer is then told to move and expose in a controlled predetermined manner such that the desired locations are cross-linked. When all the appropriate locations have been correctly exposed, the sample is removed from the SEM chamber.

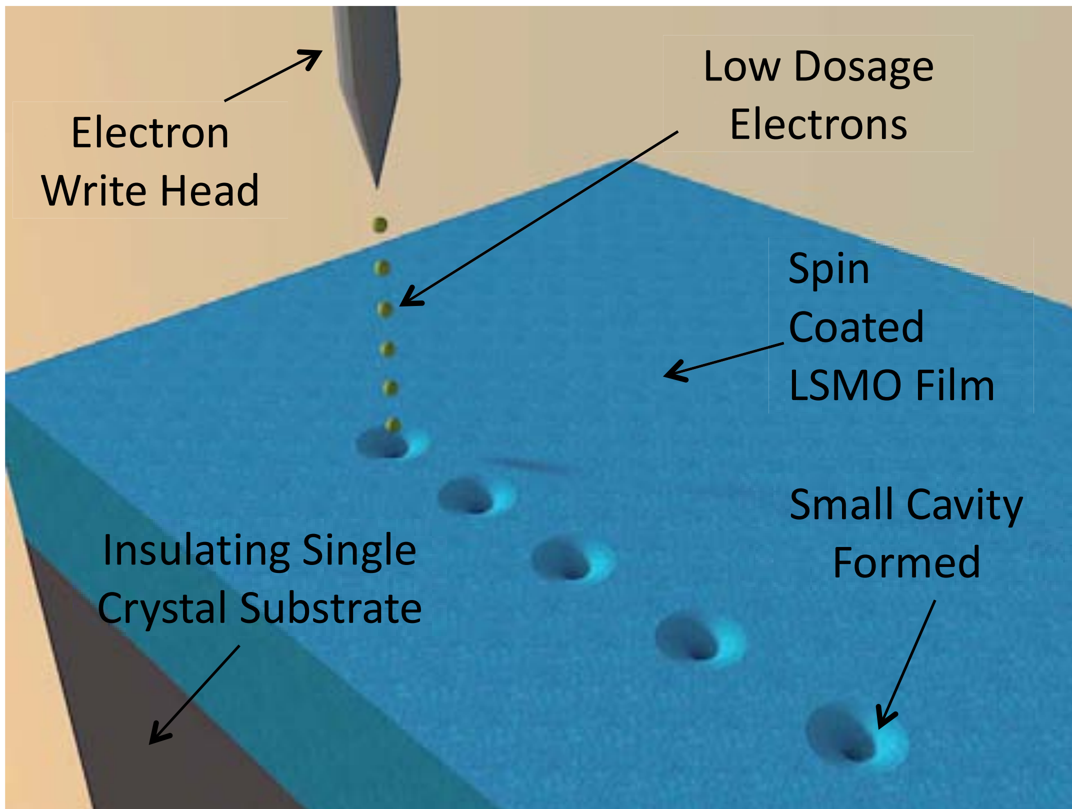

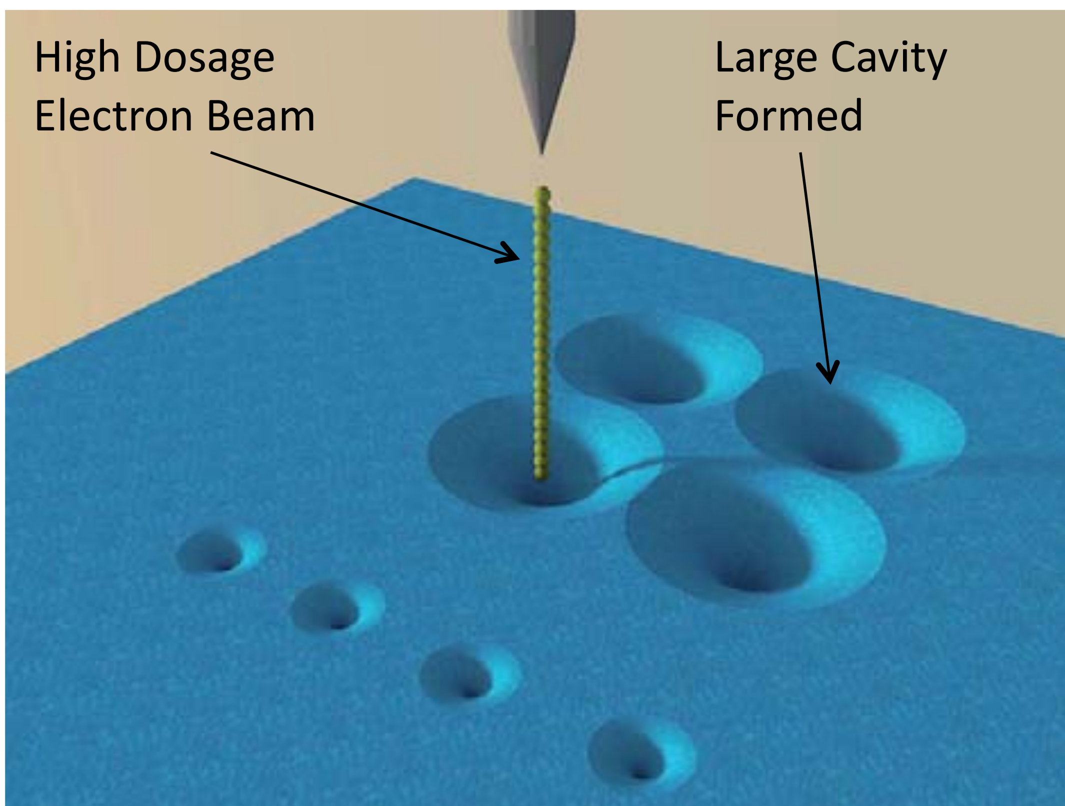

Figure 1-20 *Left: Schematic showing how low dosage nanocavities are formed. Right: Schematic showing when dosage is increased, large cavities are formed.*

The process of making nanostructures can be seen schematically in figures 1-20 and 1-21. On the left of figure 1-20 one sees the small nanocavities formed by low dosages on spin coated LSMO precursor. On the right of figure 1-20 ones the effects of increasing the dosage, namely the nanocavities become wider. Also the schematic serves to illustrate that the low dosage nanocavities are spaced far apart while the high dosage ones are close to each other. On the left of figure 1-21, one notes how the same positions of the nanocavities reveal cross-linked nanoislands once the film is developed in water. Here the size difference between the low and high dosage nanoisland is meant to illustrate that high dosage nanoislands are wider than the those of lower dosages. Finally on the right of figure 1-21, the same nanoislands have crystallized into nanostructures when placed in high heat oven for a period of time. Specifically nanodots are seen stemming from the low dosage, well spaced, radiated sites and nanowires stemming from the high dosage, closely spaced, radiated sites. Of course, this is simply a cartoon schematic, however it serves to illustrate the complex interplay at the various stages in the lithography process.

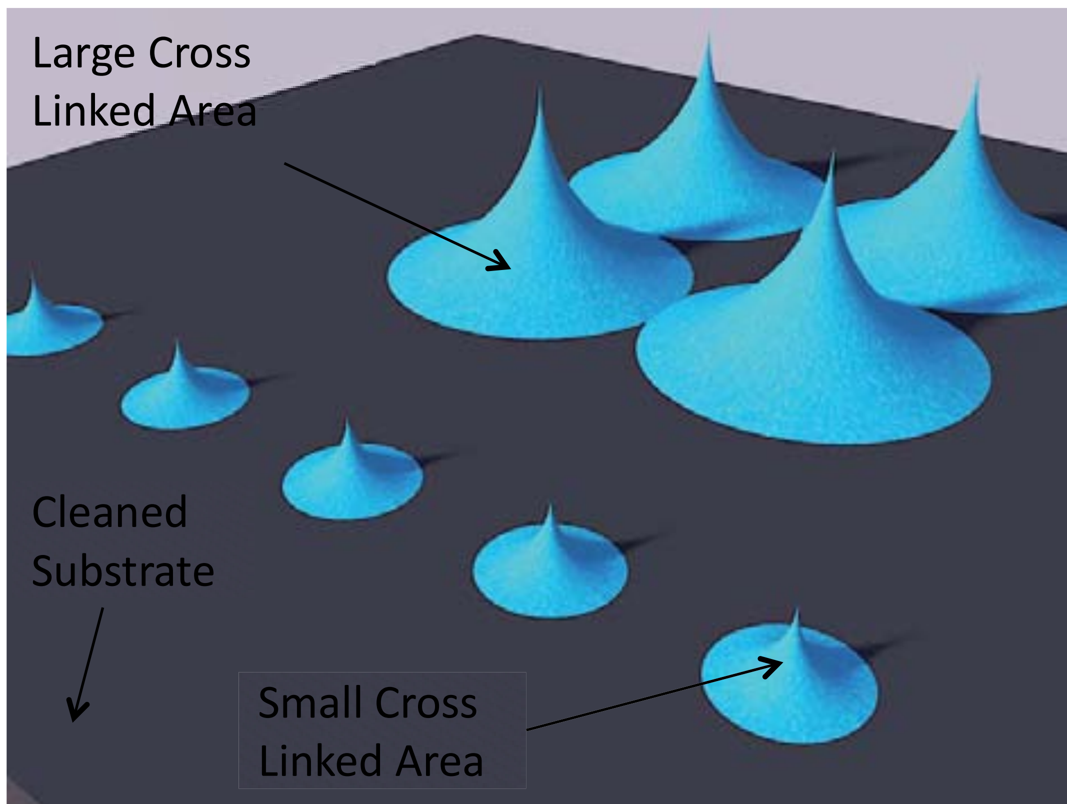

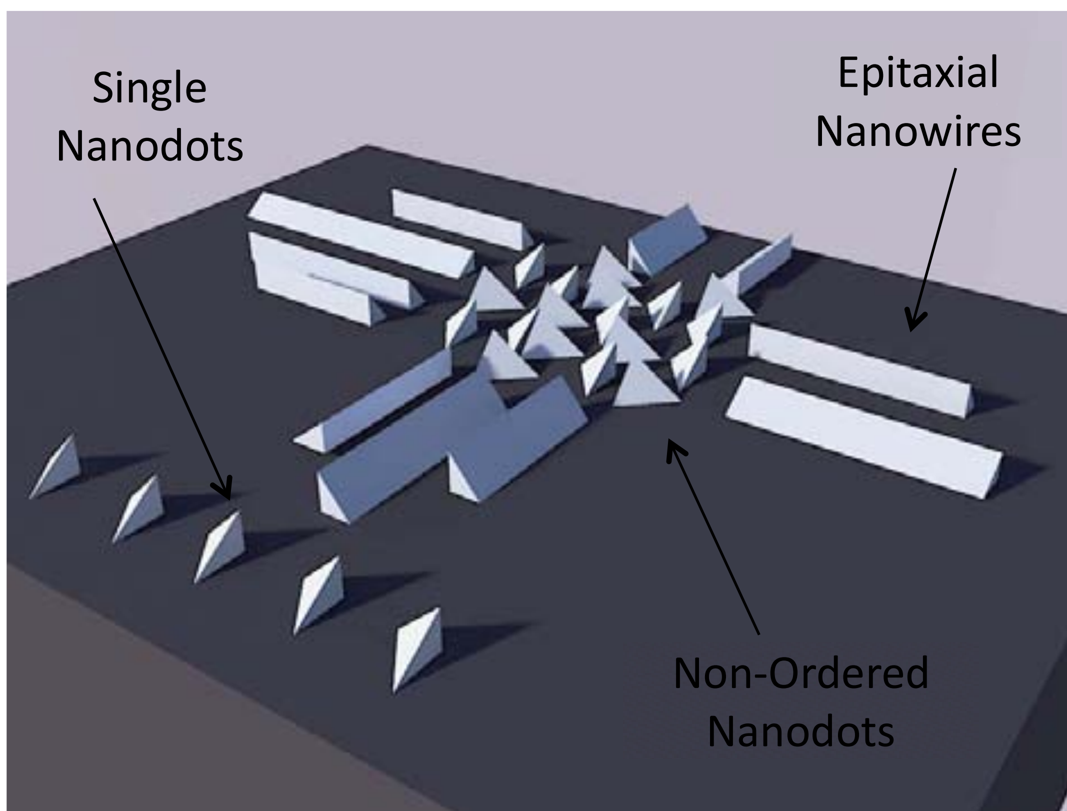

Figure 1-21 *Left: nanoislands remain after the film has been washed with water. Right: nanodots and nanowires are the result of annealing at high temperature for many hours.*

One may then look with AFM to observe nanocavities have formed where the electron beam had been focused as on the left of figure 1-22. The chip is then developed in water such that the non-radiated parts of the film are washed away. One can see an AFM scan showing the resultant nanoislands located where the electron beam had been focused on the right of figure 1-22. The cause for this interaction with the LSMO precursor, mainly the ablation at the surface and cross-linking directly beneath it, is due to the PVOH. The PVOH has the quality that it cross-links under focused electrons, in the process decreasing in volume, and then becomes water insoluble while attaching to the substrate. Thus, one can tell the write head to place a small amount of electrons at a certain place, remove the rest of the film, and what remains is an organic nanostructure on a single crystal substrate.

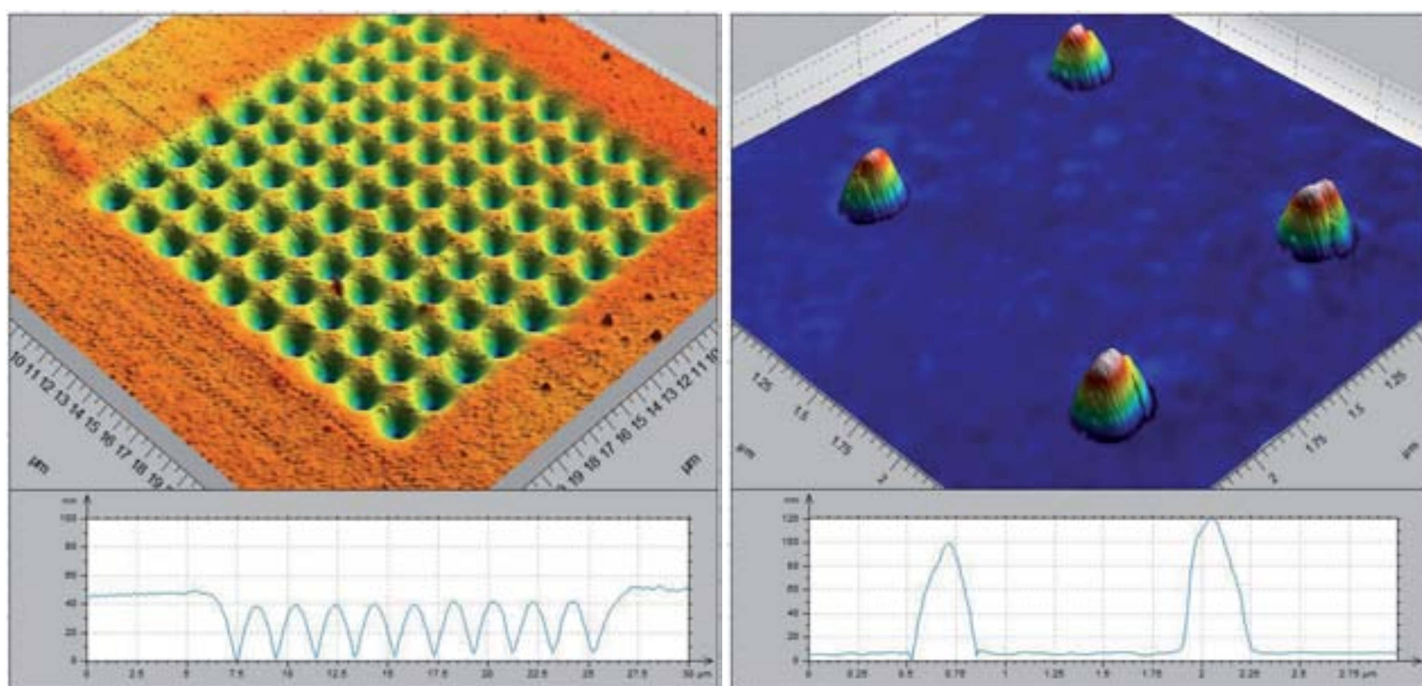

Figure 1-22 *Left: 0.1M nitrate based LSMO film with 2 wt% PVOH on STO which has been irradiated by a dosage of 1.5 pC with pitch 2.5 μm and subsequently show a series of nanocavities. Right: nanoislands revealed from developing that same film in water.*

When these organic nanostructures are annealed at high heat for an extended period of time, the nanoisland crystallizes into a nanodot. This entails the organic species being removed due to their volatility and the inorganic species recombining into an oxide nanocrystal. An AFM image of an array of low dosage annealed nanodots on the single crystal substrate STO is seen on the left of figure 1-23. When high dosage annealed nanodots are placed in close quarters, nanowires spontaneously grow in the fashion seen on the right of figure 1-23. The reason why high dosage nanodots in tight arrays grow these nanowires is not entirely understood, however it is thought that the initial large

amount of spatially confined electrons is enough to crystallize the precursor locally, thus acting as seeds for nanowire growth.

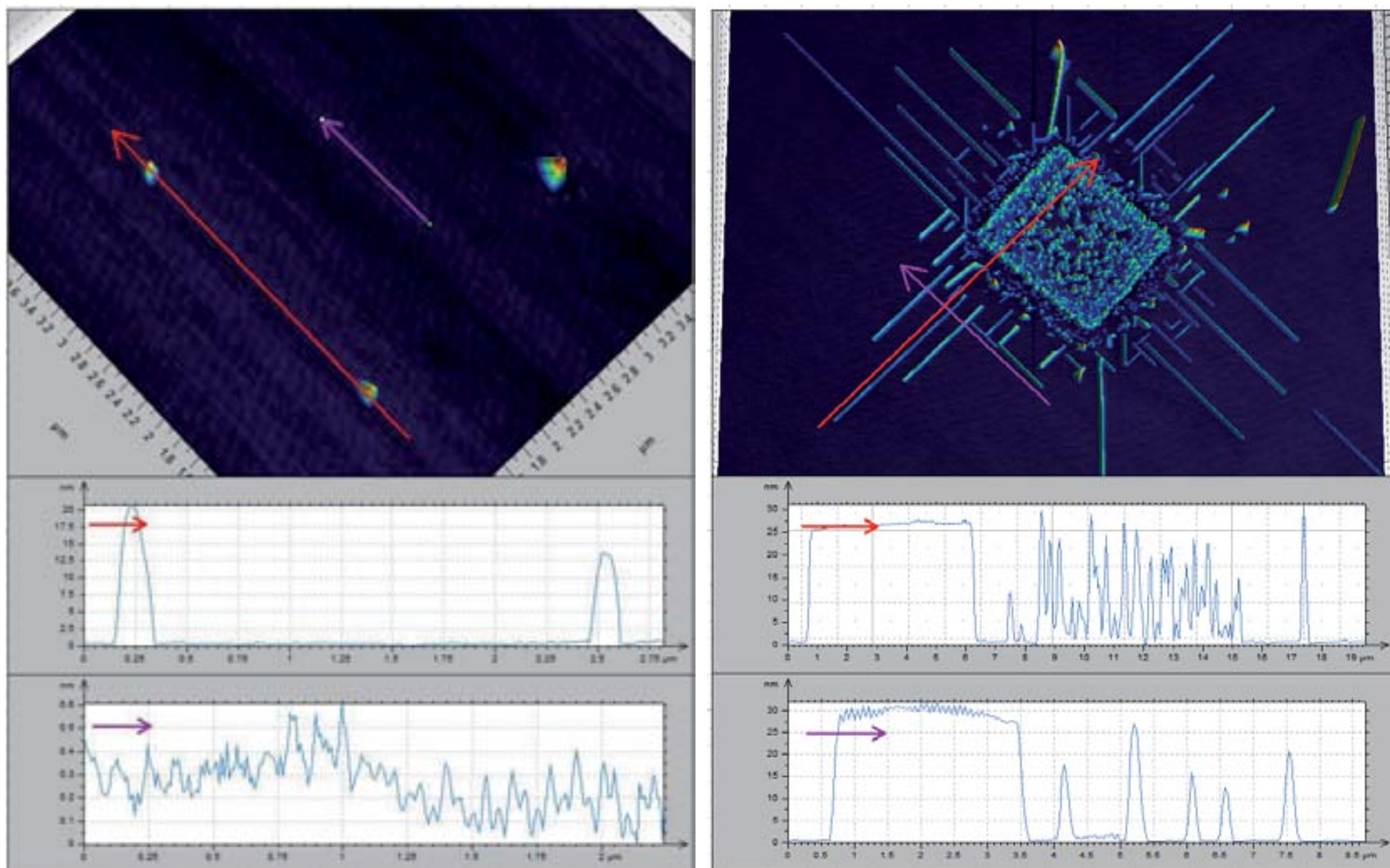

Figure 1-23 *Left: a series of low dosage 900 °C 4h annealed nanodots formed from 1.5 pC irradiation with pitch of 2.5 µm and water developed 0.1M nitrate based LSMO film with 2 wt% PVOH on STO. Right: nanowires grown from a grouping of annealing for 4h at 900 °C of high dosage nanodots of 1500 pC with pitch of 750 µm.*

1.4 Nanoimprint Lithography

Of the two methods in which nanostructures were produced in this study, nano imprint lithography is the most applicable to industry. The reason for this mainly comes from the time necessary to perform lithography on a six inch wafer is significantly reduced relative to electron beam efforts. The general procedure of nanoimprinting is a simple one, however many contributing factors must be taken into account to achieve high final nanocrystal quality and uniformity. The basics are one takes a hard mold with nano-sized features and hot presses into a malleable film which has been thinly applied to a substrate; finally there is a demolding step which subsequently reveals the reversed nano-

sized features in the film. One may then remove material in a preferential way and then anneal it or one may apply a metallic top layer via sputtering for further lithography [38-40].

The more specific procedure related to nanostructuring with a LSMO precursor and male mold can be seen schematically in figures 1-24 and 1-25. First a LSMO film is spin coated on a single crystal substrate. The film is then heated well above its glass transition temperature while in contact with the male silicon mold. The mold is then pressed into the film and left there for a time scale of minutes. The mold is disengaged from the film once the temperature of the film is then lowered well below the glass transition temperature. This leaves a series of nanopores as seen on the right of figure 1-24. The nanopores however do not reach to the substrate surface, thus a reactive ion etching step is performed. This removes the excess material leaving smaller features than previous and critically exposing the substrate as seen on the left of figure 1-25. The sample is then annealed further reducing the size of the perforated film but causing the film to crystallize as seen on the right of figure 1-25.

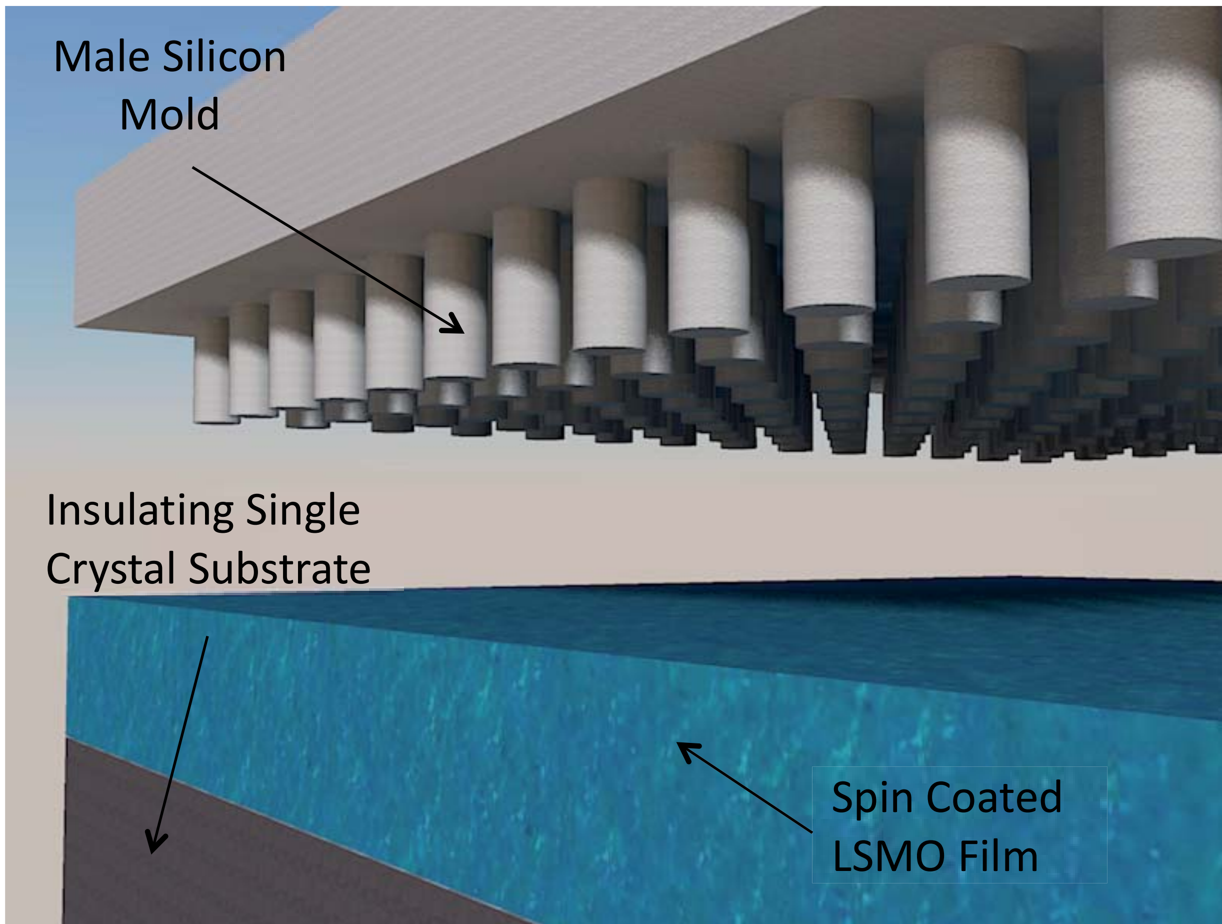
Male Silicon
Mold
Insulating Single
Crystal Substrate
Spin Coated
LSMO Film

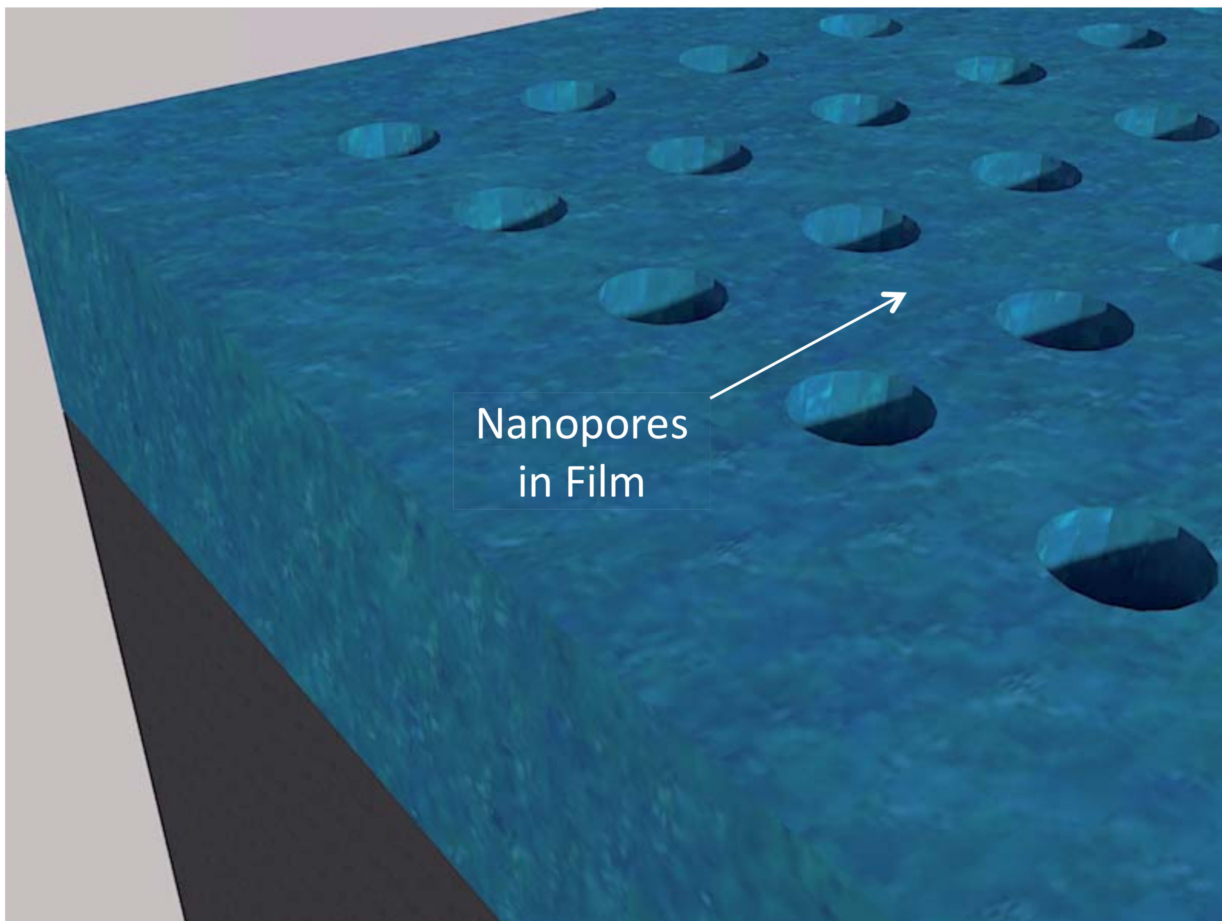
Nanopores
in Film

Figure 1-24 *Left: schematic of male silicon mold before being pressed into a spin coated LSMO film. Right: a series of nanopores are the result of nanoimprinting with mold.*

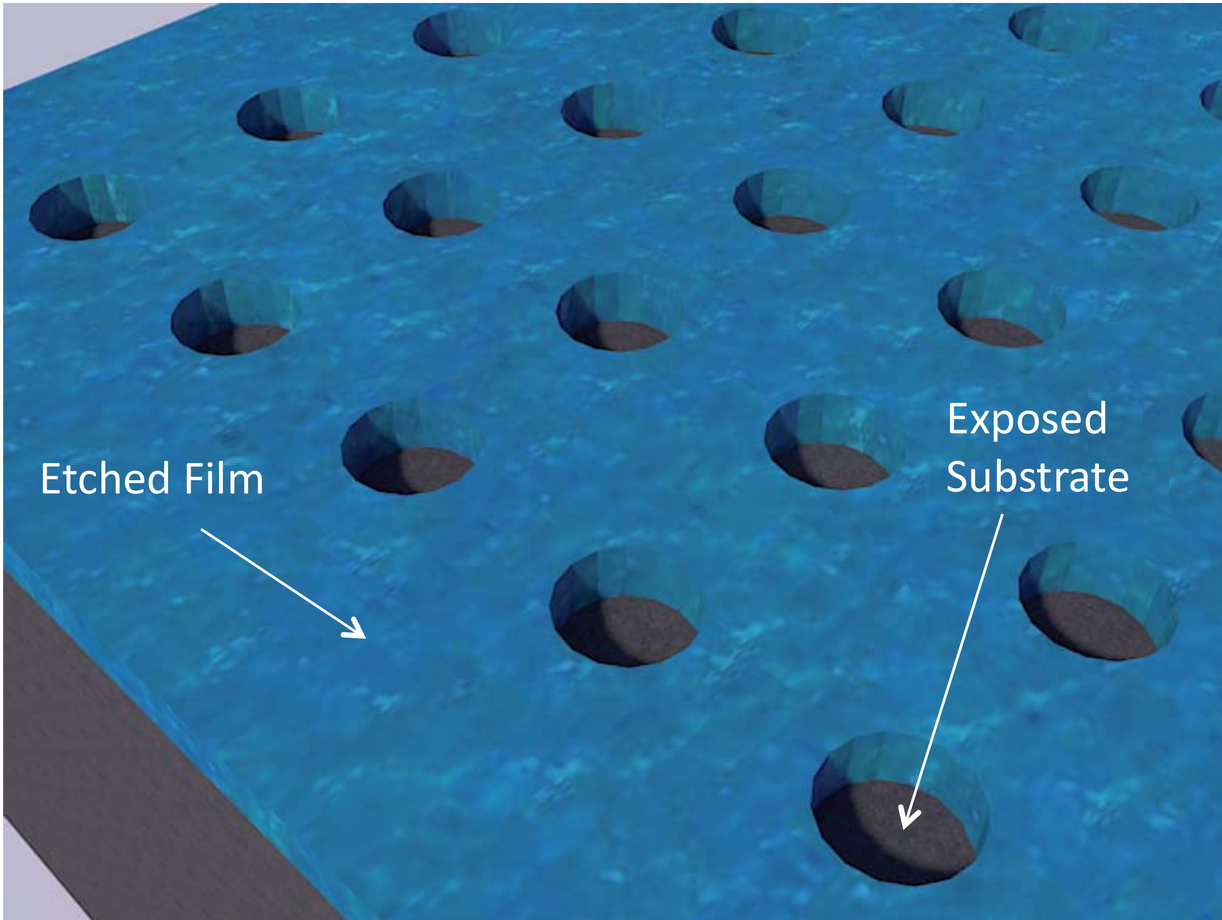
Etched Film
Exposed
Substrate

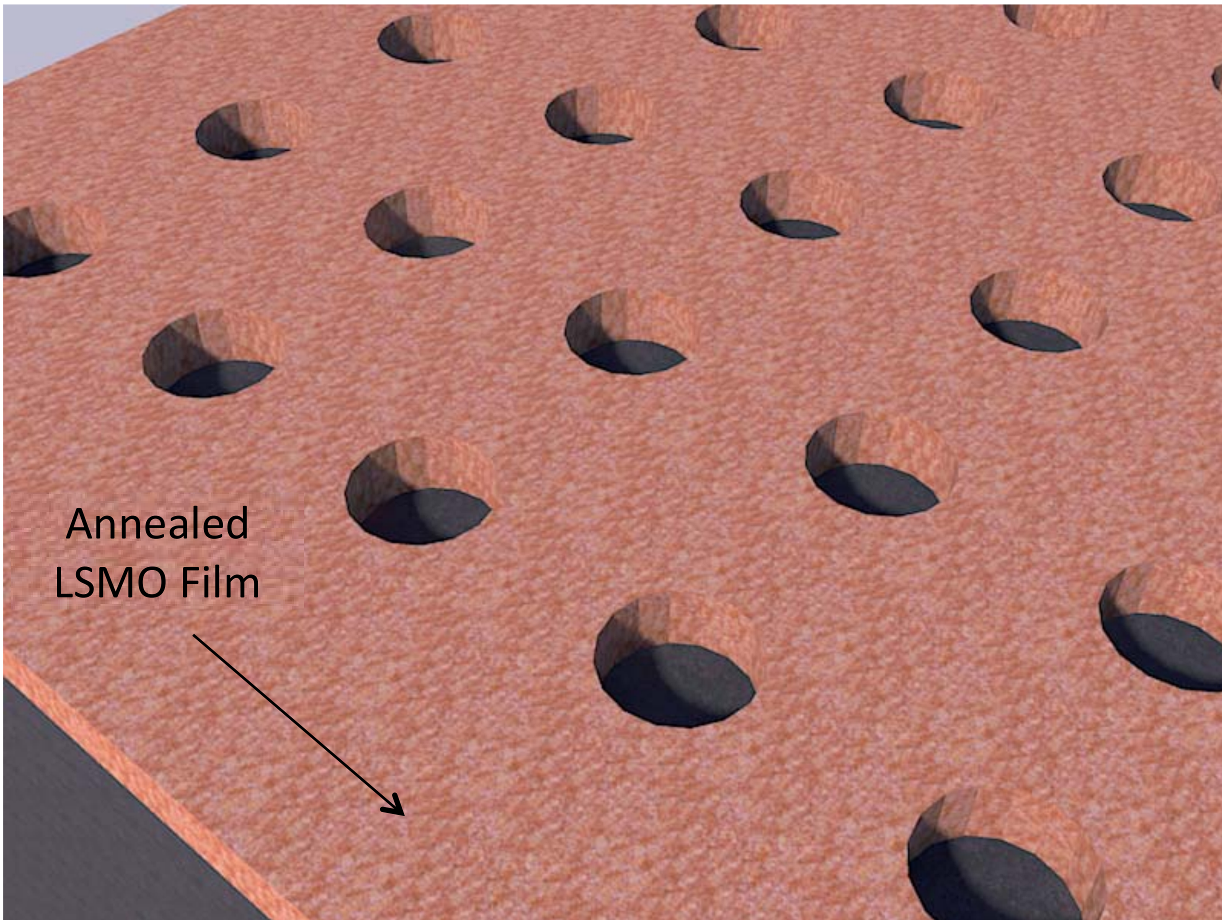
Annealed
LSMO Film

Figure 1-25 *Left: film after being anisotropically etched with plasma. Right: film after annealing retains nanostructures.*

Of course, nanoimprint lithography in reality is much more complex and depends on many factors to successfully stamp an oxide film. Various parameters must be accounted for such as the ramp rate, dwell temperature, applied pressure, dwell time, and demolding temperature. The ramp rate must be slow enough to allow for viscous flow of the polymer into or away from the nanosized features but also fast enough so to be efficient. The dwell temperature must be higher than the glass transition temperature but cool enough not to have any organic combust. The applied pressure must be enough to force the mold into the film but not enough to deform the nanofeatures. The dwell time must be long enough to allow for polymer relaxation while being efficient. While the demolding temperature must be below the glass transition temperature but hot enough to prevent mold sticking. An AFM image of an imprinted but unetched 0.1M nitrate based LSMO film with 2 percent by weight PVOH is seen on the left of figure 1-26 while an oxygen etched example is seen on the right of figure 1-26. They show that the structure of the male mold has been transferred to the film and that the substrate can be etched to by 150 watts of oxygen plasma for five minutes.

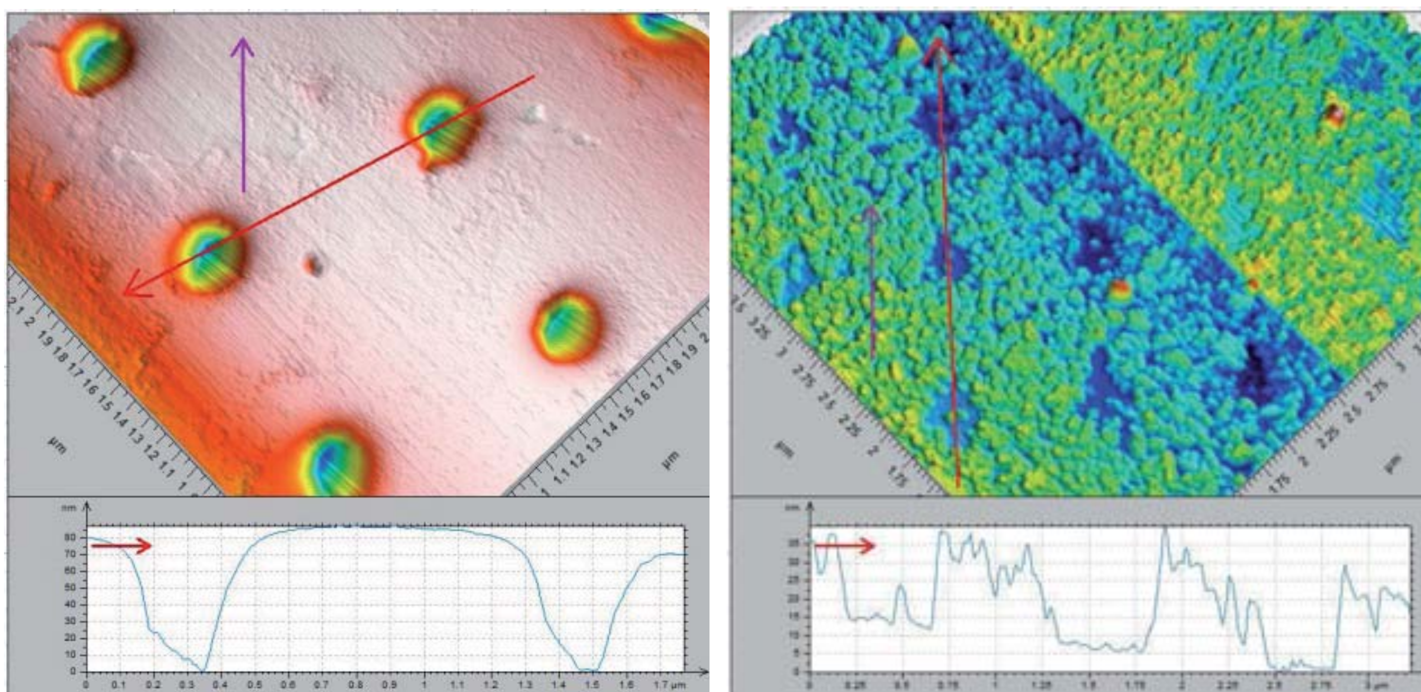

Figure 1-26 *Left: nanopores are formed after hot pressing with a male stamp. Right: a series of nanoholes etched with oxygen plasma. Conditions used were dwell temperature 160 °C, applied pressure 40 MPa, dwell time 5 min, demolding temperature 80 °C, etching of 150 watts for 5 minutes at 200 sccm, from 0.1M nitrate based LSMO precursor with 2 wt% PVOH, 900 °C annealing temperature for 240 minutes.*

In order for the film to imprinted, several layers of aluminum and plastic must be placed with the sample. This consists of the following: bottom most layer is a cut strip of aluminum, then the substrate, then the upside-down mold, then a full piece of plastic, then finally two layers of aluminum. Each of these layers has a purpose with regards to protecting the two halves of the press from damaging the mold and substrate. The reason why the substrate is placed below the mold is due to the mold being smaller than the substrate. This ensures that neither the substrate nor the mold will be broken after applying pressure. The sample must be centered with respect to the mold so as to insure a homogeneous pressure is applied.

1.4.1 Reactive Ion Etching

In order to remove excess material after nanoimprinting, the film must be subjected to an anisotropic plasma treatment. The instrument which does this is called a reactive ion etcher (RIE) [41]. The reason why the excess material must be removed is two-fold. The primary purpose is that the floor of the nanopore is not that of the single crystal substrate. An anisotropic etching step will allow the floor to be said substrate and thereby increase the likelihood of forming single crystal LSMO nanodots when using a female mold. The secondary purpose is to reduce the height of the nanopores. This drive stems from the high mobility that the precursor has when annealed. Reducing the size of the nanoscale features allows the small nanopores from not closing on themselves, thus allowing for nanoholes to form.

The procedure for the RIE begins by having nothing first inside its stainless steel chamber. The chamber is then vacuum pumped so as to remove any atmospheric gases. Then desired flow rate of either argon or oxygen or any number of other gases and mixtures is introduced into the chamber. When the chamber pressure is sufficiently high, the gas is turned into a plasma by applying megahertz radio frequency field. The plasma is highly directional due the parallel nature of the negative and grounded plates inside the chamber as can be seen in figure 1-27. The voltage is applied for a sufficiently long period of time so as to tune the reflected voltage. This procedure of tuning the reflected voltage for a given power and atmosphere allows for the sample to be uniformly etched in one direction. Once this has been accomplished, the voltage is turned off and the chamber vented. The imprinted substrate is then placed in the chamber and the procedures above are repeated but with a set time period in which the plasma will interact with the film. After the etching process has occurred, the sample is removed and inspected. The etching process works by having the ions chemically interact with the nanoimprinted film. Thus, oxygen ions are good at removing organic species while argon ions do not preferentially attach any material.

The parameters in which one must select when etching a film with directional plasma are the power, the gas flow, the duration, and the type of gas. There being four variables in which to choose from, the optimization process becomes daunting. However, certain the duration of ten minutes should be chosen as a starting point with power being in the middle range, the gas at full flow for a given gas. The sample is then inspected and if found to still have film, the time is doubled until no film remains. If none remains, then the duration is incrementally decreased while recording the resulting film's thickness, which is typically a linear function [42, 43]. This then gives the film thickness reduction as a function of time at a given power for a given gas and flow as can be seen on the right of figure 1-27. The results of which show that the argon gas is less efficient at removing the 0.1M nitrate based 2 wt% PVOH LSMO film compared to oxygen. Also the removal of the film is more efficient for oxygen initial while become more inefficient as the organic components are removed.

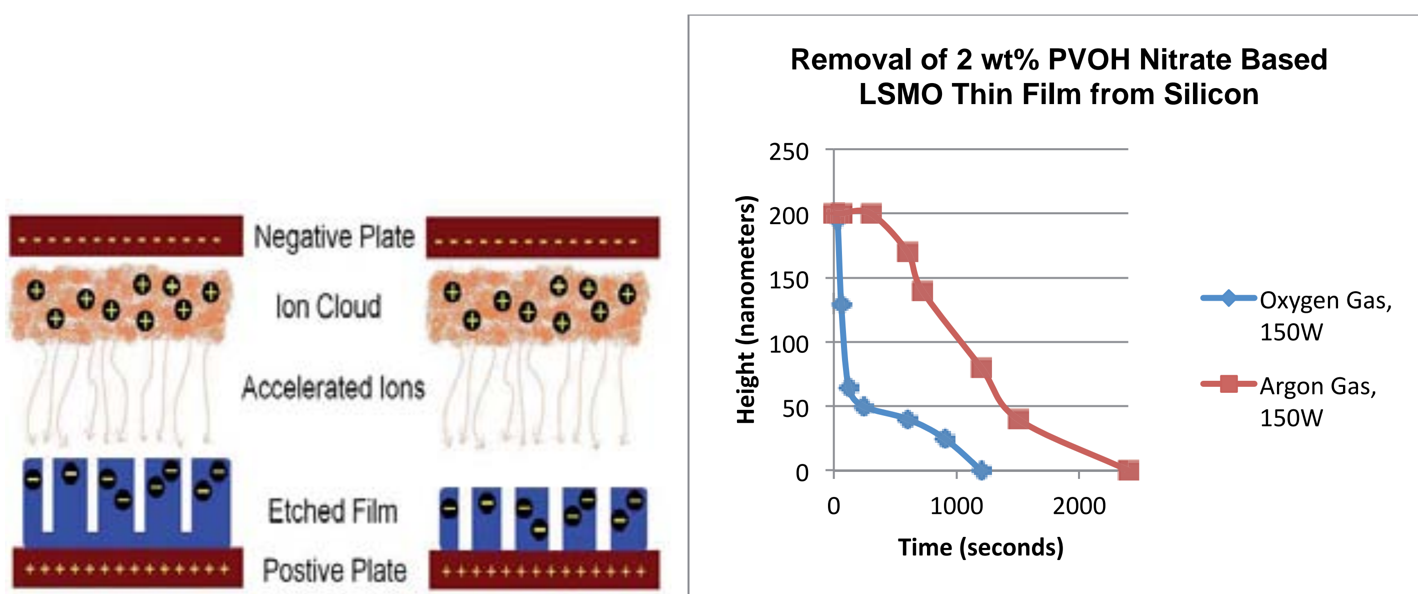

Figure 1-27 *Left: schematic of charge movement for a RIE before etching and after etching. Right: graph of amount of thin film removed during a reactive ion etching for oxygen and argon gases as a function of time for 0.1M nitrate based LSMO film with 2 wt% PVOH on silicon.*

1.5 Focused Ion Beam

Once a substrate has been obtained which had objects of interest upon it, and all morphological analysis has been exhausted, a focused ion beam is used to cut an electron transparent lamella. This lamella was then peered through with a transmission electron microscope. This gave vital information concerning the atomic structure of the objects of interest as well as the elements present via an electron energy loss microscope. However, making a lamella thin enough for TEM by cutting an insulating substrate all the while trying not to destroy the nanostructures, is in itself a refined

technique. So critical is the FIB lamella cutting step, that without it, information ranging from the epitaxial growth of nanodots on single crystal substrates to the interdiffusion of particular elements through the interface would be impossible to determine. The basic premise is that the nanostructures are coated first with a global gold protective layer then a local platinum layer, afterwards a wedge is cut out of the substrate by ions leaving a thin bridge, the bridge is then attached to a robotic arm, the bridge is severed from the substrate, the lamella is then attached to a holder, and the lamella is finally thinned [44].

The name itself lends the best description for the instrument. That is, the FIB uses a beam of focused ions to cut away defined parts of objects. In order not to damage the nanostructures with a high energy beam of gallium ion, a gold protective layer is first administered by deposition outside the chamber and then a layer of aluminum is put down inside the chamber. With this, the nanostructures are protected from contamination and the surface is much more conductive. This is extremely important for insulating substrates due to two malevolent consequences for charge build-up. They are the inability to cut with the ion beam in a straight manner over time and the other being that the robot arm cannot approach and attach to the bridge easily. Specifically the robotic arm has a long thin aluminum tip at the end of it, which is tends to accumulate the opposite charge to that of the insulating surface. This then puts the aluminum tip into a vibrational oscillation, making it extremely difficult to accurate marry the two objects.

After the protective layers are applied, two wedges are cut very close to each other. The resultant form made to the sample is a 10 μm long by 1 μm wide bridge. This bridge contains a row of closely spaced nanostructures in the very middle. Thus, when the bridge is polished of material on both sides, the five micrometer will be a hundred nanometers thick and will thus expose the nanostructures to TEM inspection. The energy used to cut the bridge is very low at 5 kV when used on insulating substrates versus conductive substrates at 30 kV. The bridge is then brought into contact with the robotic arm tip. The tip is then locally coated with aluminum, so as to bond the tip to the bridge. The bridge is then cut away from the substrate, allowing the robotic arm to move the lamella to a holder as can be seen in figure 1-28. The lamella is subsequently polished in two sections until the contrast of the nanostructures is seen, noted in the two SEM images in figure 1-29. This tells the operator that the lamella is sufficiently thinned so that electrons can travel freely through it.

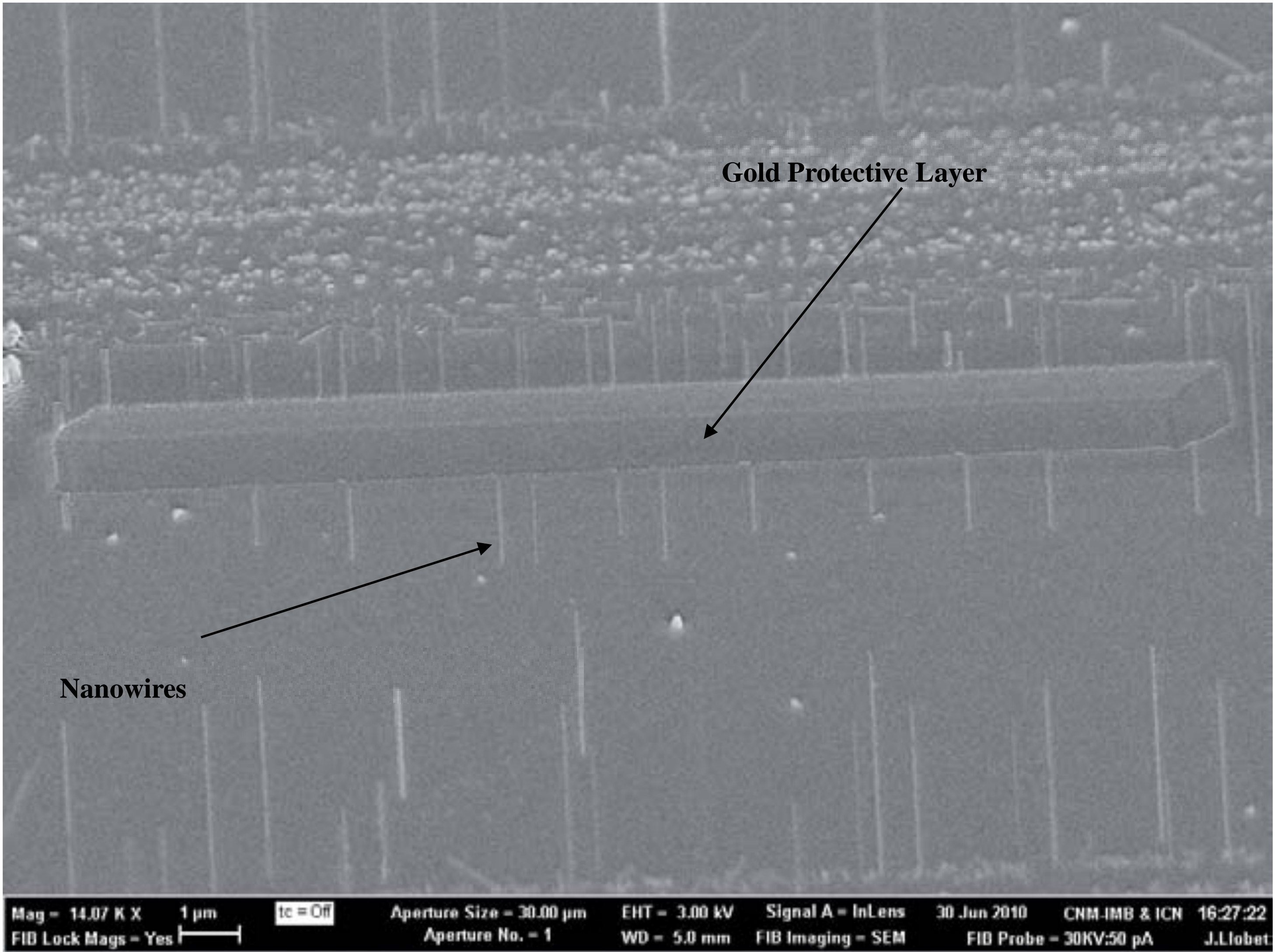
Gold Protective Layer
Nanowires
Mag = 14.07 K X
1 μm
FIB Lock Mags = Yes
tc = Off
Aperture Size = 30.00 μm
Aperture No. = 1
EHT = 3.00 kV
WD = 5.0 mm
Signal A = InLens
FIB Imaging = SEM
30 Jun 2010
FIB Probe = 30KV:50 pA
CNM-IMB & ICN
16:27:22

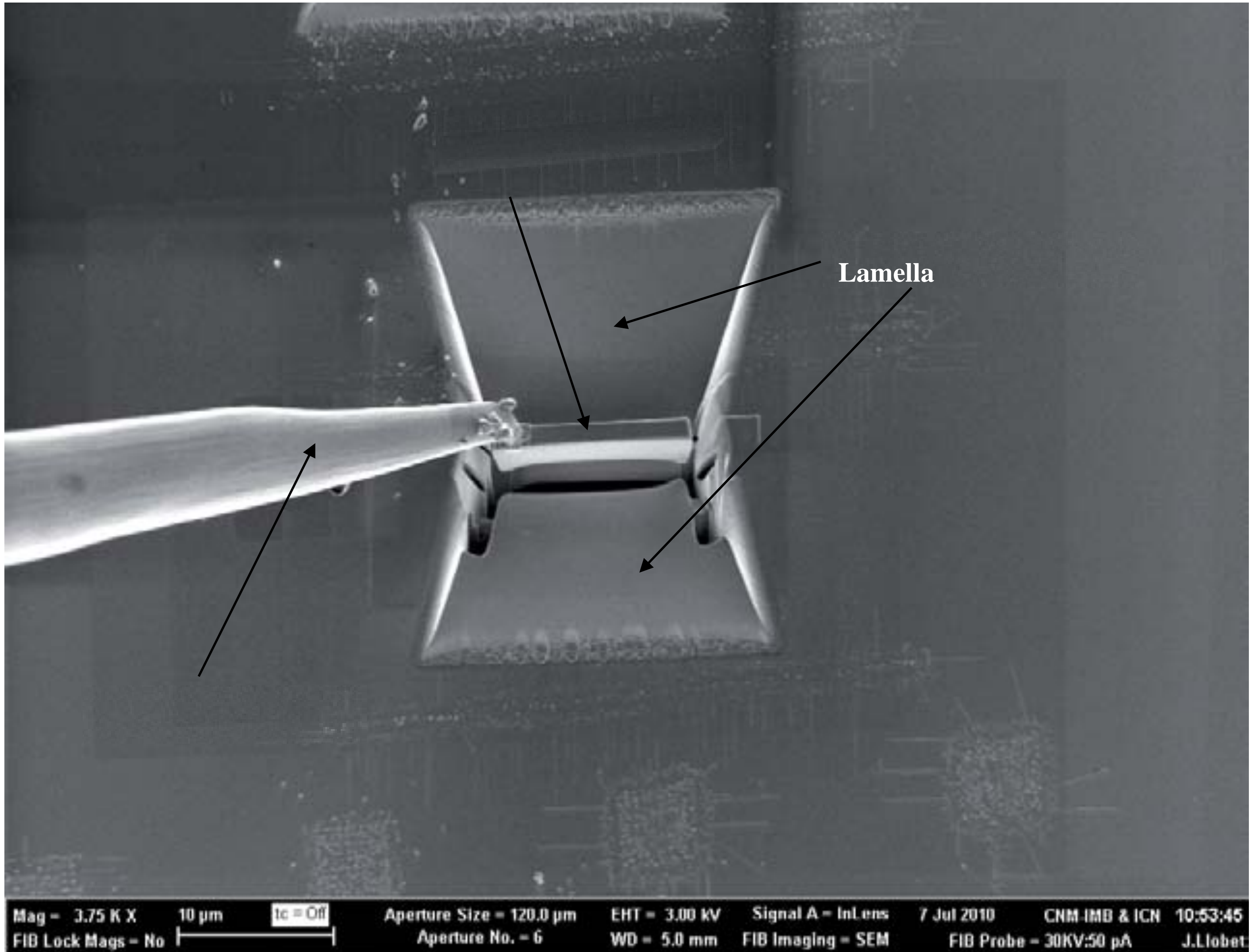

Figure 1-28 *Left: nanowires on STO after having protective platinum deposited for lamella prepartation. Right: probe arm removing same lamella from the STO substrate.*

A key stipulation before any cutting with the FIB can occur, is first having a good sample. This entails having structures which have seen high enough temperatures for a long enough time such that they are truly crystalline. Also the structures are easier to identify if they are much taller than the gold/aluminum protective layers. In the case of YSZ, which is highly insulating, the protective layers are more than thirty nanometers in height, thus structures fifty or sixty nanometers in height become buried and difficult to identify when polishing. Another difficulty when attempting to analysis nanodots with the TEM by this method is that large amount of gold in front of the object of interest. This effectively blocks partially the nanostructures which are of interest. However, perhaps the greatest difficult lies in samples which are thinned too much or too little. These structures are unable to give valuable insight to how the nanostructure grew on the substrate from either simply not being there or from being electron opaque. Lastly, one

incidental but important step in the procedure is grounding the tweezers against static electricity. This static electricity can force the holder to jump from the box to the floor the second contact is made if not grounded.

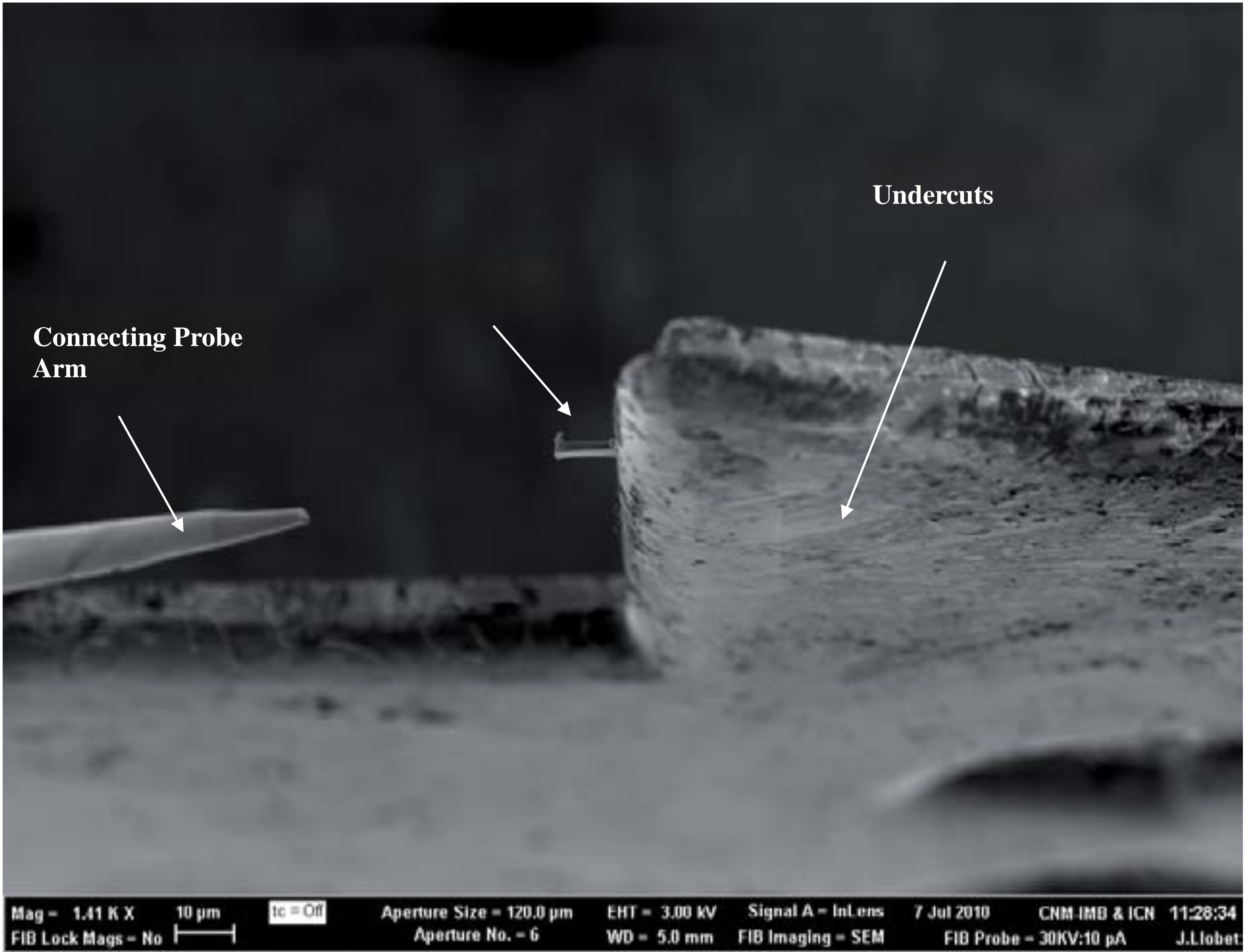
Undercuts
Connecting Probe
Arm
Mag = 1.41 K X
FIB Lock Mags = No
10 µm
Aperture Size = 120.0 µm
Aperture No. = 6
EHT = 3.00 kV
WD = 5.0 mm
Signal A = InLens
FIB Imaging = SEM
7 Jul 2010
FIB Probe = 30KV:10 pA
CNM-IMB & ICN
11:28:34

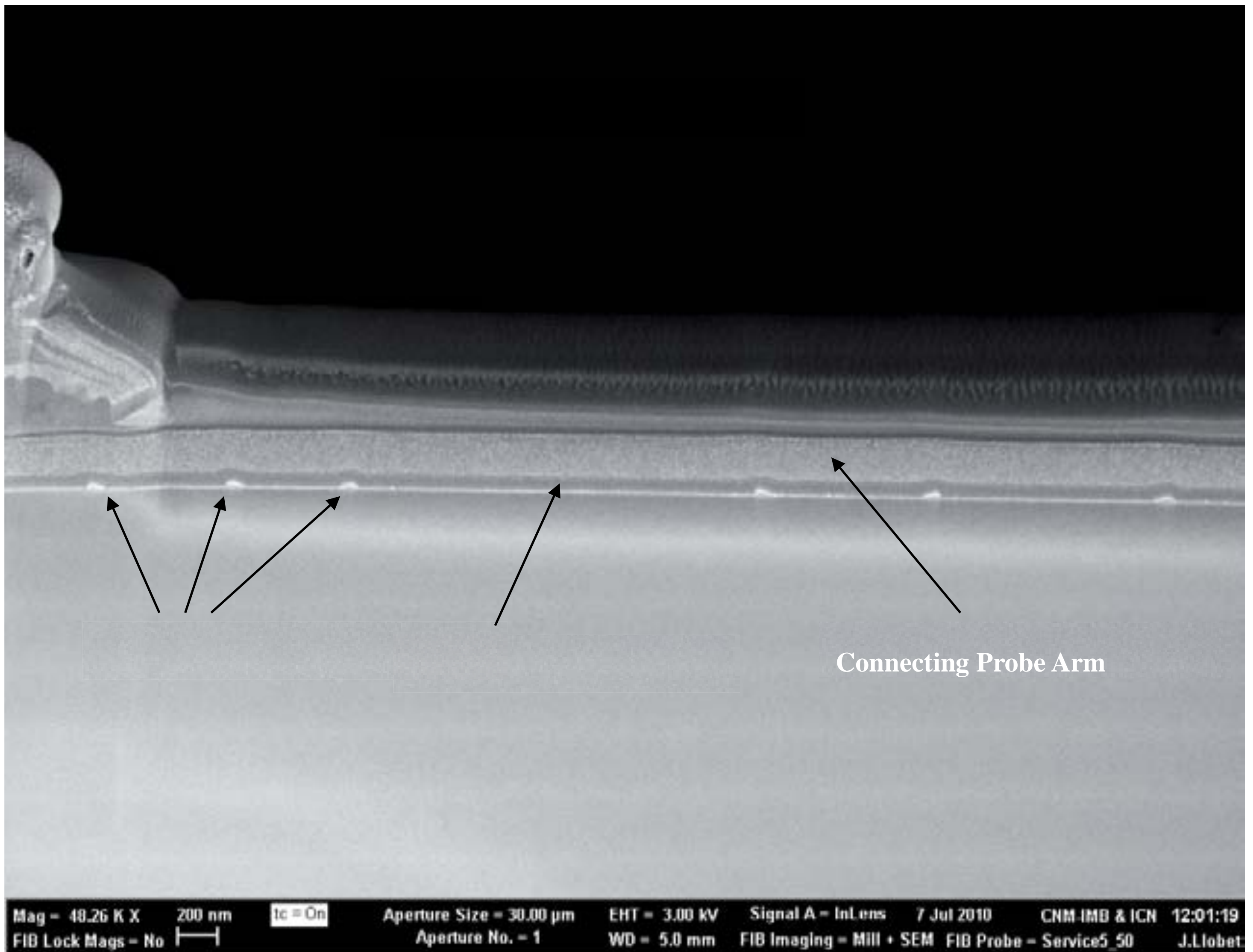

Figure 1-29 *Left: lamella being attached to the TEM holder. Right: exposed nanowires after being polished thin on top of an STO substrate and thus exposing the metallic protective layers.*

1.6 Transmission Electron Microscope

Once the lamella has been made and attached to the holder, it may analyzed with a transmission electron microscope. There exist many gradations of TEM's, some which are able to peer at the very atoms in from which the crystal is made, others which can only give the slightest hint to the structures morphology. Mainly, this has to do with the energies used to propel the electron in the column and with the ability to correct for aberration. However, all TEM's work on the principle that a focused beam of high energy electrons is propelled onto a thinned lamella at which point some of them do not pass through to the detector [45, 46]. The reason some of the electrons do not transmit through to the detector is that they are either absorbed at the lamella level or reflected away. The resultant images will either be black were there was no transmission or white where there was total transmission as can be seen on the left of figure 1-30 of an

oxide nanowire on STO. This typically will yield images with a unit cell resolution of the nanostructure which will give insight into the spacing of the atomic planes. This occurs by processing the images through a fast Fourier transform, resulting in a two dimensional representation of the atomic planes. These planes may be numerically compared against other known crystalline structures so as to ascertain a commonality an example of which is seen on the right of figure 1-30. Here the atomic planes do not correspond to a known crystal, thus the oxide nanowire's unit cell remains unknown. Two different TEM's were used in this work with the following model names: JEOL 2010F Field Emission Gun 200 kV and FEI Tecnai F30 Field Emission Gun at 300 kV

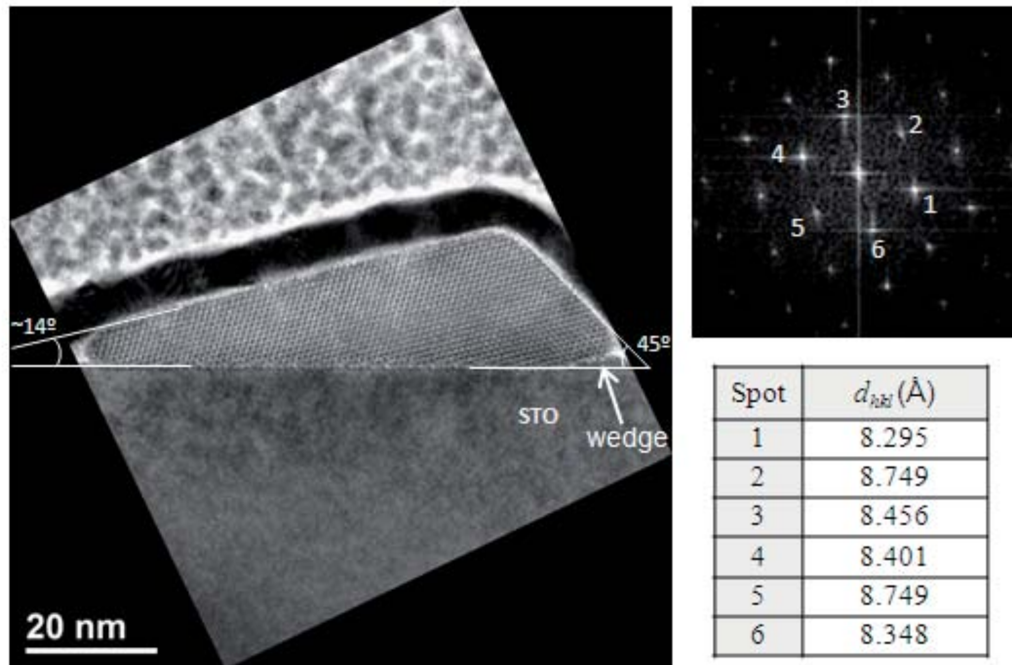

Spot	d_{hkl} (Å)
1	8.295
2	8.749
3	8.456
4	8.401
5	8.749
6	8.348

Figure 1-30 *Left: TEM image of oxide nanowire from polished lamella showing manner in which it grew on the STO substrate. Right: a fast Fourier transform of the nanowire showing six atomic planes and their spacings in angstroms which do not correspond to any known crystal.*

1.6.1 Electron Energy Loss Spectroscopy

An attachment module on the TEM is a instrument called an electron energy loss spectrometer (EELS). This spectrometer is able to detect the presence of individual elements as it scans a lamella. EELS works by the principal that when electrons are radiated onto a sample at a given energy, there exists certain elements which interact with those particular electrons [47, 48]. Thus by emitting electrons at a wide range of energies, then certain elements in the lamella will be detected or failed to be detected. EELS is typically performed as line scanned from substrate to nanostructure. This does two things, namely as a control against faults in the instrument in that two different

materials, one known and one unknown, will show this transition clearly. The other being that the mobility of individual elements across a boundary can occur, which will come across in the line scan as seen in figure 1-31.

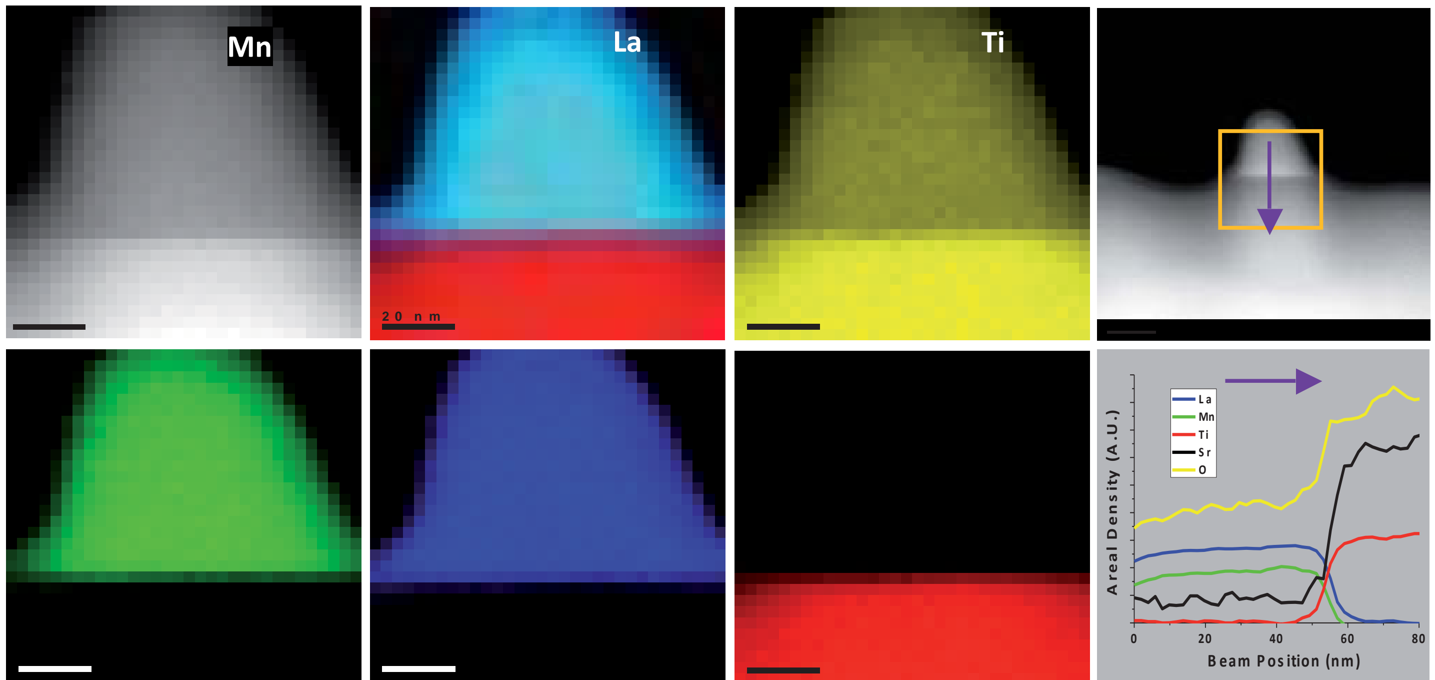

Figure 1-31 *EELS linescan showing the spacial elemental presence of Sr, O, Mn, La, and Ti on a nanodot on STO made by imprinting 0.1M acetate based LSMO & 15 wt% PVOH with a male mold and etching with oxygen in a RIE for 120 seconds at 1200 watts.*

Naturally, the energies necessary to detect some elements are unavailable when scanning with low energy columns. The element strontium is one those that is unable to be detected on all but the most energetic columns. This is unfortunately due to the STO lamellas having strontium as well as LSMO being strontium rich. Thus the complete picture of what elements were present and at what ratios was absent for the some EELS analysis. This became contentious when the element manganese was not detected in EBL lamellas and thus a verification of the presence of strontium was desired.

1.7 Specific Conclusions

The objective of this work was the creation of oxide nanostructure arrays by lithographic means, however in order to better ascertain their nature, thin films made from precursors were thoroughly analyzed. These thin films consisted of the polymer PVOH along with either nitrate or acetate metals in water. Specifically, the PVOH was two and fifteen percent by weight after being filtered and the amount of organic metals was 0.7 : 0.3 : 1.0 for La, Mn, Sr yielding $La_{0.7}Sr_{0.3}MnO_3$ when annealed. The LSMO precursor solution was then applied to a substrate via spin coating in a low humidity atmosphere. The spin coating conditions were 6000 rpm for 120 seconds in 5% humidity followed by being left on a hot plate for 20 minutes at 75C. The substrates used were STO, YSZ, LAO, and silicon. Except for silicon, these substrates allow for epitaxial growth of LSMO. This then allows for single crystal LSMO nanostructures to be fabricated by lithographic means.

To confirm that LSMO could be grown as a film, several analytical techniques were performed. This included checking the thickness and roughness with AFM, confirming the epitaxial growth of LSMO by x-ray diffraction on single crystal substrates, making sure that the film was ferromagnetic, observing the elemental presence inside the film by XPS, and noting the change in mass as the film was annealed. These analytical techniques to study the thin precursor films made by spin coating on single crystal substrates, was necessary to confirm that the chemical solution deposition method would produce LSMO. After this was confirmed, then further experiments regarding the optimization of lithographic methods could commence. However, it was found that a direct connect between what annealed film produced by only spin coating was similar to that by nanoimprint lithography, those structures produced by electron beam lithography more complex.

The electron beam lithographic means taken up in this work consisted of focusing a beam of electrons at a film inside a vacuum chamber, irradiating a given location for a given amount of time, and then washing the film of any non-exposed areas. The cleaning regime under taken was to insure as high a level of constancy across samples as well as reducing any unwanted local film thickness aberrations. Nanoimprint lithography consisted of taking a male silicon mold and hot pressing it into the spin coated precursor film. This created a nanoperforated film that was etched with a directional plasma which reduced the overall thickness while retaining the aspect ratio of the features. Both the electron beam and nanoimprint samples were then lastly annealed at high temperatures and durations. The resulting nanostructures were then cut with a focused ion beam so as to lift out an electron transparent lamella. This lamella was then observed with a transmission electron microscope to reveal the unit cell of the crystal and its growth mode. The lamella was also used to inspect the local elemental presence by using an electron energy loss spectrometer.

1.8 Thin Film References

1. Hausmann, D.M. and R.G. Gordon, *Surface morphology and crystallinity control in the atomic layer deposition (ALD) of hafnium and zirconium oxide thin films.* Journal of Crystal Growth, 2003. **249**(1–2): p. 251-261.
2. Kukli, K., et al., *Influence of thickness and growth temperature on the properties of zirconium oxide films grown by atomic layer deposition on silicon.* Thin Solid Films, 2002. **410**(1–2): p. 53-60.
3. Dolbec, R., et al., *Influence of the nanostructural characteristics on the gas sensing properties of pulsed laser deposited tin oxide thin films.* Sensors and Actuators B: Chemical, 2003. **93**(1–3): p. 566-571.
4. Rajendra Kumar, R.T., et al., *Pulsed laser deposited vanadium oxide thin films for uncooled infrared detectors.* Sensors and Actuators A: Physical, 2003. **107**(1): p. 62-67.
5. Chen, X.L., et al., *Temperature-dependent growth of zinc oxide thin films grown by metal organic chemical vapor deposition.* Journal of Crystal Growth, 2006. **296**(1): p. 43-50.
6. Matsui, Y., M. Mitsuhashi, and Y. Goto, *Early stage of tin oxide film growth in chemical vapor deposition.* Surface and Coatings Technology, 2003. **169–170**(0): p. 549-552.
7. Wu, M.C., et al., *Surface potential and magnetic properties of La0.7Sr 0.3MnO3 periodic arrays fabricated by direct electron beam writing.* Journal of Applied Physics, 2008. **104**(2).
8. Wu, M.C., et al., *Fabrication and optical properties of periodical structures based on a water-developable and tunable La0.7Sr0.3MnO3 resist.* Journal of Materials Chemistry, 2008. **18**(7): p. 780-785.
9. Chuang, C.M., et al., *Nanolithography made from water-based spin-coatable LSMO resist.* Nanotechnology, 2006. **17**(17): p. 4399-4404.
10. Pailloux, F., et al., *Twinning and lattice distortions in the epitaxy of La0.67Sr0.33MnO3 thin films on (0 0 1) SrTiO3.* Applied Surface Science, 2001. **177**(4): p. 263-267.
11. Kim, D.-W., *Interfacial spin interactions of ferromagnetic and antiferromagnetic manganite bilayers.* Solid State Communications, 2006. **137**(10): p. 545-548.
12. Zabaleta, J., *Nanoscale magnetic structure and properties of solution-derived self-assembled La0.7Sr0.3MnO3 islands.* Journal of Applied Physics, 2012. **111**(2): p. 024307.
13. Alexy, P., et al., *Poly(vinyl alcohol) stabilisation in thermoplastic processing.* Polymer Degradation and Stability, 2002. **78**(3): p. 413-421.
14. Hodgkinson, N., *Thermoplastic Poly (Vinyl Alcohol) (PVOH).* Materials World, 2000. **8**(April): p. 24-25.
15. Zhen, W., et al., *Structure and properties of thermoplastic saponite/poly(vinyl alcohol) nanocomposites.* Applied Clay Science, 2012. **57**(0): p. 64-70.
16. Covaliu, C.I., et al., *Synthesis and studies on the structural and Electrical properties of Sr doped lanthanum manganites.* Digest Journal of Nanomaterials and Biostructures, 2011. **6**(4): p. 1491-1505.
17. Gu, J.Y., et al., *In-plane grain boundary effects on the magnetotransport properties of La0.7Sr0.3MnO3-δ.* Applied Physics Letters, 1998. **72**(9): p. 1113-1115.
18. Haghiri-Gosnet, A.M., et al., *Spintronics: Perspectives for the half-metallic oxides.* Physica Status Solidi (A) Applied Research, 2004. **201**(7): p. 1392-1397.
19. Hoffman, J., X. Hong, and C.H. Ahn, *Device performance of ferroelectric/correlated oxide heterostructures for non-volatile memory applications.* Nanotechnology, 2011. **22**(25).
20. Huang, L., et al., *Study on the resistive switching properties of epitaxial La0.67Sr0.33MnO3 films.* Solid State Communications, 2007. **143**(8-9): p. 382-385.
21. Keshavarz, M.H., *A simple way to predict heats of detonation of energetic compounds only from their molecular structures.* Propellants, Explosives, Pyrotechnics, 2012. **37**(1): p. 93-99.
22. Wu, X., L. Xu, and D. Weng, *The NO selective reduction on the La1-xSrxMnO 3 catalysts.* Catalysis Today, 2004. **90**(3-4): p. 199-206.
23. Yan, Z. and J. Yu, *Preparation of nanocrystalline magnesium aluminate spinel powder by thermal explosion mode of LCS*. 2012: Shenyang, Liaoning. p. 1248-1252.

24. Truijen, I., et al., *Influence of synthesis parameters on morphology and phase composition of porous titania layers prepared via water based chemical solution deposition.* Journal of the European Ceramic Society, 2007. **27**(16): p. 4537-4546.
25. Truijen, I., et al., *Study of the decomposition of aqueous citratoperoxo-Ti(IV)-gel precursors for titania by means of TGA-MS and FTIR.* Thermochimica Acta, 2007. **456**(1): p. 38-47.
26. Truijen, I., et al., *Synthesis of thin dense titania films via an aqueous solution-gel method.* Journal of Sol-Gel Science and Technology, 2007. **41**(1): p. 43-48.
27. Truijen, I., et al., *Preparation of nanocrystalline titania films with different porosity by water-based chemical solution deposition.* Journal of Sol-Gel Science and Technology, 2007. **43**(3): p. 291-297.
28. Petrov, N., *Crystal Structure of the Mixed Oxides* Journal of Solid State Chemistry, 1999. **143**(1): p. 52-57.
29. Li, T., et al., *Annealing effect on the structural and magnetic properties of La 0.7 Sr 0.3 Mn O 3 films.* Journal of Applied Physics, 2005. **98**(12).
30. Paralikar, S.A., J. Simonsen, and J. Lombardi, *Poly(vinyl alcohol)/cellulose nanocrystal barrier membranes.* Journal of Membrane Science, 2008. **320**(1-2): p. 248-258.
31. Willcox, P.J., et al., *Microstructure of poly(vinyl alcohol) hydrogels produced by freeze/thaw cycling.* Journal of Polymer Science, Part B: Polymer Physics, 1999. **37**(24): p. 3438-3454.
32. Gilman, J., *Thermal Decomposition Chemistry of Poly(vinyl alcohol).* Fire and Polymers II:American Chemical Society, 1994. **Symposium 599**(11): p. 25.
33. Yuvaraj, S., *Thermal Decomposition of Metal Nitrates in Air and Hydrogen Environments.* J. Phys. Chem. B, 2003. **107**(4): p. 4.
34. Kim, M.-G., et al., *Low-temperature fabrication of high-performance metal oxide thin-film electronics via combustion processing.* Nat Mater, 2011. **10**(5): p. 382-388.
35. Knoll, M., *Aufladepotentiel und Sekundaeremssion elektronenbestrahlter Koeper.* Zeitschrift fuer Technische Physik, 1935. **16**: p. 467-475.
36. Vieu, C., et al., *Electron beam lithography: resolution limits and applications.* Applied Surface Science, 2000. **164**(1–4): p. 111-117.
37. Broers, A.N., A.C.F. Hoole, and J.M. Ryan, *Electron beam lithography—Resolution limits.* Microelectronic Engineering, 1996. **32**(1–4): p. 131-142.
38. Sotomayor Torres, C.M., et al., *Nanoimprint lithography: an alternative nanofabrication approach.* Materials Science and Engineering: C, 2003. **23**(1–2): p. 23-31.
39. Shields, P.A. and D.W.E. Allsopp, *Nanoimprint lithography resist profile inversion for lift-off applications.* Microelectronic Engineering, 2011. **88**(9): p. 3011-3014.
40. Lan, H., et al., *Review of the wafer stage for nanoimprint lithography.* Microelectronic Engineering, 2007. **84**(4): p. 684-688.
41. Coburn, J.W., *Plasma and Reactive Ion Etching*, in *Encyclopedia of Materials: Science and Technology (Second Edition)*, K.H.J.B. Editors-in-Chief: , et al., Editors. 2001, Elsevier: Oxford. p. 7015-7022.
42. Rangelow, I.W., *Reactive ion etching for high aspect ratio silicon micromachining.* Surface and Coatings Technology, 1997. **97**(1–3): p. 140-150.
43. Buder, U., J.P. von Klitzing, and E. Obermeier, *Reactive ion etching for bulk structuring of polyimide.* Sensors and Actuators A: Physical, 2006. **132**(1): p. 393-399.
44. Langford, R.M., *Focused Ion Beam Systems: Application to Micro- and Nanofabrication*, in *Encyclopedia of Materials: Science and Technology (Second Edition)*, K.H.J.B. Editors-in-Chief: , et al., Editors. 2010, Elsevier: Oxford. p. 1-13.
45. van Benthem, K. and S.J. Pennycook, *4.09 - Atomic Resolution Characterization of Semiconductor Materials by Aberration-Corrected Transmission Electron Microscopy*, in *Comprehensive Semiconductor Science and Technology*, B. Editors-in-Chief: Pallab, F. Roberto, and K. Hiroshi, Editors. 2011, Elsevier: Amsterdam. p. 287-307.

46. Marassi, R. and F. Nobili, *MEASUREMENT METHODS | Structural and Chemical Properties: Transmission Electron Microscopy*, in *Encyclopedia of Electrochemical Power Sources*, G. Editor-in-Chief: Jürgen, Editor. 2009, Elsevier: Amsterdam. p. 769-789.
47. Verbeeck, J., et al., *ELECTRON ENERGY LOSS SPECTROMETRY*, in *Encyclopedia of Analytical Science (Second Edition)*, W. Editors-in-Chief: Paul, T. Alan, and P. Colin, Editors. 2005, Elsevier: Oxford. p. 324-331.
48. Browning, N.D., et al., *Atomic Resolution Electron Energy Loss Spectroscopy*, in *Encyclopedia of Materials: Science and Technology (Second Edition)*, K.H.J.B. Editors-in-Chief: , et al., Editors. 2004, Elsevier: Oxford. p. 1-9.

2. Oxide Nanodots

The road to the generation of oxide nanodots has come from two main avenues, the top-down approach where expensive instruments make arrays, and the bottom-up approach which is largely uncontrolled but inexpensive. The expense of the instruments aside, a major disadvantage to the top-down to this technique is the speed in which structures are written and the number of steps required in the lithography process. The advantage of using a top-down approach is that intricate designs of nanodots may be written in a controlled way. The bottom-up approach comes mainly by way of the use of solutions and spin coating. It produces nanostructures very quickly and with little up front cost, however the placement and nature of the nanostructures is left to chance. The tactic used in this work is to use the best of both worlds and thus be inexpensive while highly controllable. This control can be used to make a litany of nanoscale devices in ways a bottom-up approach could never emulate. The method used in this work to that end is focusing electrons to write arrays of oxide nanodots on single crystal substrates.

The systems of oxides that were studied here was largely $La_{0.7}Sr_{0.3}MnO_3$ and later partly $SrTiO_3$ as a proof-of-concept for general applicability. The LSMO was derived from acetate and nitrate based precursors; this was due to project beginning by using nitrate as the counter ion and then later shifting to the use of acetates. Regardless of the counter ion used, the immediate result of radiating with electrons on to the precursor film was the production of nanocavities due to the presence of PVOH. These small nano-sized craters directly beneath where the electrons were focused are studied in-depth due to their interesting morphology. Underneath the nanocavities, hardened areas were formed which were revealed when cleaned with water. This water developed sample left a series of, what is referred to here as, nanoislands. This sample was then annealed in an oven at high temperature for local phase formation and crystallization, which are called here nanodots. Nanocavities, nanoislands, and nanodots are shown to be dosage dependent as well as

morphologically dependent on the neighboring sites. It must be noted that all the samples in this chapter contained two percent by weight PVOH in the precursor solution as well as being spin coated to yield a film thickness of around two hundred nanometers.

2.0.1 Motivation

Arrays of functional oxide nanodots generated from electron beam lithography have been thought to be a key component for next generation integrated circuit design. One particular characteristic of LSMO which has excited researchers is that of colossal magnetoresistance (CMR). Magnetoresistance is the observation that through a change in magnetic field, the resistance of a material switches between insulating and conductive states. The much smaller but similar effect of giant magnetoresistance (GMR) is behind all the magnetic spinning hard disks which are now so prevalent. CMR hints at the possibility of ultra small, low power magnetic memory. The most promising emerging technology which uses CMR is that of magnetic tunnel junctions (MTJ).

A device which employs a MTJ has two layers of a CMR material separated by an insulator such that when a local magnetic field is felt by one of the layers, its resistance changes and thus allows or forbids an electron from tunneling through that insulator. The ability to change only a single layer's resistance comes from the idea that the layers have different magnetic coercivity and thus one is more susceptible to a small magnetic field. This spin valve is based on the principal that electrons with a particular spin, regardless if they are under the presence of a strong potential, do not want to travel to another material with opposite spin state predominance. Possibly MTJ devices in the future will employ two layers of LSMO which will have been written in very precise locations with controlled morphology.

The technique described in this chapter is a combination of recent effort made by scientists in the fields of electron beam lithography and oxide nanostructuration. This growing community of researchers has origins in the sudden availability of relatively inexpensive methods to control where and how electrons were written onto a film. This came in the form of add-on modules which could be purchased relatively cheaply and fitted to the already existing infrastructure of SEM's. This allowed groups who normally would not have had access to the ability to write with electrons, an opportunity to fabricate nanostructures by lithography. This in turn facilitated a myriad of devices with feature sizes unimaginable to researchers a generation ago.

As far as oxide nanostructures go, the main driving inspiration for their research was from the amazing bulk properties they had. Typically these inorganic ceramics were made from powder and then sintered. These bulk materials gave way to thin films made by various forms of deposition. Eventually it was possible to create nanowires and nanodots through a self-assembly process. Unfortunately, while these methods were inexpensive, the control of exactly where a oxide nanostructure would grow was impossible. Of late, the possibility to generate oxide nanostructures at a desired location from top-down methods became a reality. At the fore front of this push is the electron beam lithographic method.

2.0.2 Current State of Research

As was just illustrated, the lure of colossal magnetoresistance has allowed researchers to conjure up potential devices which use LSMO. However, there are several other controllable properties which are of interest concerning oxides. For instance, researchers have recently begun to become interested in controlling domain walls in LSMO. The creation of domain walls in LSMO by electron beam was investigated for the first time in 2001 at IBM. They found that the resistance increased dramatically when a domain wall was created or annihilated [1]. It has been noted that domain wall scattering can cause systematic resistance alterations in manganite nanostructures at half tesla magnetic fields [2]. This is highly important for the fabrication of future magnetic track memory devices.

Another important property in memory devices is the Curie temperature, where a material goes through a phase change from ferromagnetic to paramagnetic. It was observed that as the annealing temperature for sol-gel derived polycrystalline nanoparticles of LSMO is increased, the Curie temperature also increases [3]. Understanding better the nature of resistive switching of LSMO is also important for future devices. A group in Germany under Kalkert el al has shown bipolar resistive switching between LSMO nanopillars and has revealed tunnel magnetoresistance with four distinct resistive states [4]. Lee et al from Korea have confirmed that modulating the oxygen vacancies at the manganese oxide layer induces resistive switching on aluminum substrates [5]. Perhaps the most difficult to fabricate but which yield the most control are superlattices. These superlattices have been shown to have a magnetic field-induced metal to insulator transition which is induced when LSMO nanodots are separated by monolayers of LSMO [6]. This type of configuration might be possible with the procedures outlined in the work. Researchers in the Ukraine under Ulyanov et al also found ferromagnetic phases differences between the inside and outside of LSMO nanoparticles. They showed that below a characteristic dimension, this phase stratification became energetically unfavorable and thus destroying the double exchange between layers [7]. Another interesting piece of research points to a tunable metal/insulator transition in LSMO films by altering the density of LSMO nanodots on the surface of a film [8].

An avenue in which researchers have recently explored was that of variations in physical properties stemming from the reduction in size from bulk down to nano. Similarly, a wide variety of properties are possible in LSMO which are determined by strain, local composition, types of defects, size of the nanoparticles, and orientation on the crystal [9]. For confined geometries of LSMO, interesting physical properties can develop. When comparing LSMO made from sol-gel versus ceramic powder fabrication, the former was shown to have a slightly lower metal/insulator transition temperature and is thought to be due to its relatively smaller grain size [10]. A group led by Guo has made a half micrometer wide bridge of LSMO by EBL efforts and has observed that the metal-insulator transition temperature decreased as the width of the bridge was lessened [11]. LSMO nanoparticles of various dimensions were fabricated to test for any variation in magnetization and resistivity. It was found that resistivity, Curie temperature, and ferromagnetic ordering increased when the size decreased [12].

Clearly the generation of LSMO nanodots is paramount to their continued study. The method used in this work for their generation was based on the principal that PVOH would cross-link under the presence focused electrons. It was found in 1989 that when polyvinyl alcohol was acetalized, it was able to be easily cross link by electron beam and that depending on the structure of the acetal group, the easy of cross linking was altered [13]. Another group used nitrates instead of acetates and found that when LSMO was mixed with PVOH it was shown to be both a positive and negative resist depending on the dosage of the electron beam used [14]. However, the commonality between them was the PVOH and thus can be used in the absence of either nitrates or acetates. Abarques et al have done just that, such that a nanocomposite consisting of PVOH and silver nanoparticles was patterned by EBL for plasmonic devices. They note that to develop a device suitable for plasmonic circuitry, a material needs to have a high concentration of nanoparticles relative to the matrix [15].

2.1 Nanocavities – After Electron Beam

The immediate effect of radiating with an electron beam upon the LSMO precursor film was the formation of a nanocavity at the focal point. This local absence of film is observable with the AFM but not with the SEM due to the nature of the SEM emitting electrons which would in-affect alter the local environment. With the AFM, one can probe the film and observe morphologically features without altering the surface. The resulting nanocavities vary slightly when radiating on more insulating substrates at higher dosages. This is due to the normal surface charging that is present from applying such high amounts of electrons on a single spot.

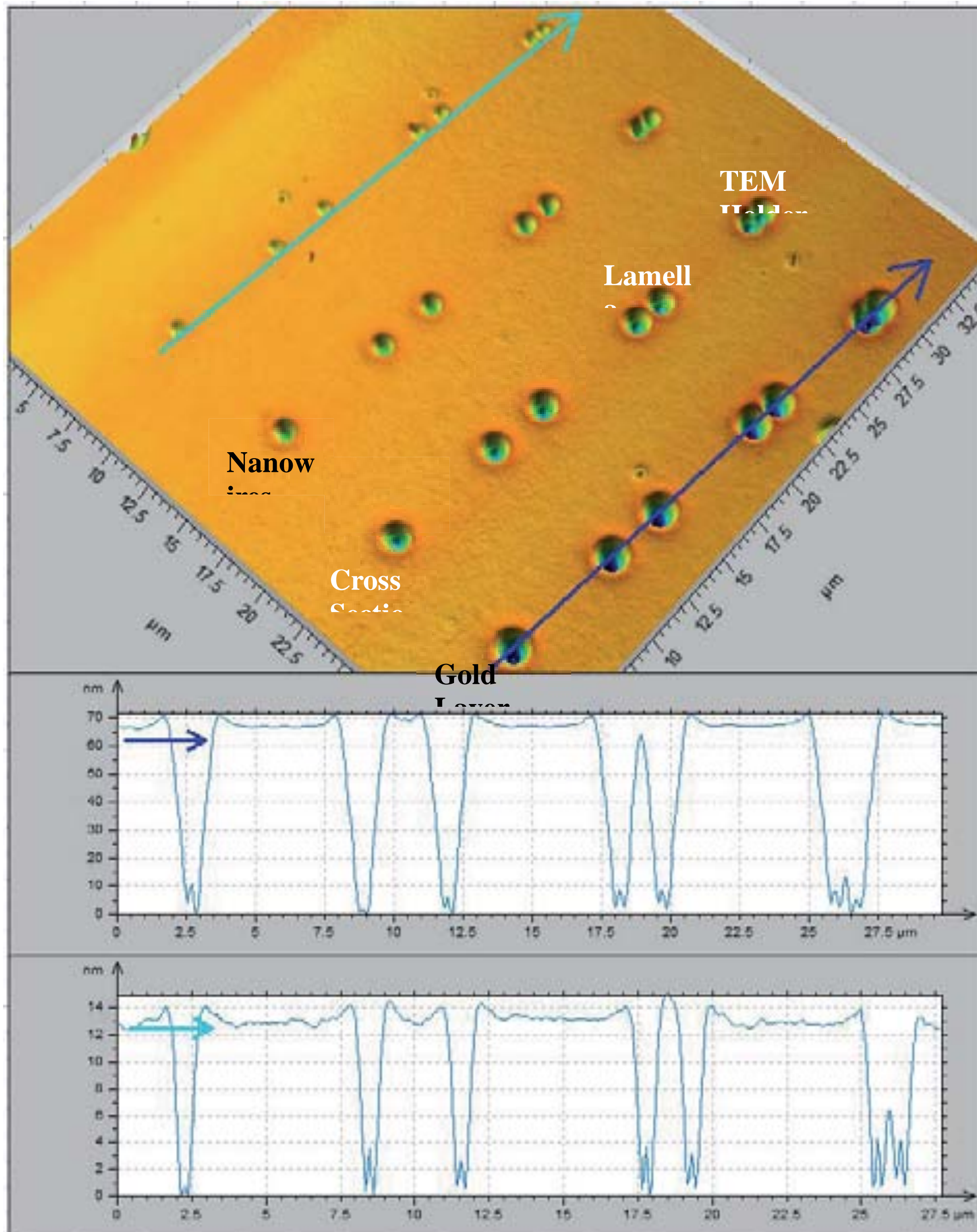

Figure 2-1 *Nanocavities generated by electron beam at four different dosages and at various pitches. The pitches were 6 µm, 3 µm, 1.5 µm, and 0.75 µm, while the dosage was 1.5, 15, 150, 1500 pC. The substrate was STO, the counter ion was acetate.*

Two different regimes were observed when focusing electrons on to the precursor and are thus described as low and high dosage regimes. The low dosage regime gave nanocavities in the sub 15 nm range, while the high regime was around 80 nm respectively, as in figure 2-1. While classifying the regimes stems more from if the annealed nanodots would generate nanowires as an array or not, one can observe different mechanisms at work immediately after radiation in both regimes. This is clearly seen in the low dosage regime when the dosage is increased, another angle in the slope is observed, and finally at max dosage a multitude of distinct

features are noted as seen in figures 2-3 and 2-5. In the high dosage regime two different resultant nanocavities were observed, a flat bottom one on STO, and a long elongated on YSZ.

The study of these nanocavities are of interest here due to it illuminating the complex mechanism of focused electrons interacting with PVOH and the counter ions. The idea that nitrates in conjunction with PVOH and LSMO cause an auto combustion reaction by focused electrons has been reported [14]. The chemical mechanism dictates that the high heat made by focusing an electron beam is enough to combust the film locally. Perhaps this concept in and of itself could be used to further a nanofabrication procedure by using the form of the nanocavities to make a soft mold.

2.1.1 Low Dosage Morphology

In figure 2-2 the local morphological changes are visible as the dosage is increased. The dosage dependence of the nanocavities suggests that the morphology is linearly dependent on the amount of electrons focused onto the film. This linear dependence in the low dosage regime is indicative of an electron activated combustion process, where the more electrons added, the more of the film combusts. Graphically this can be seen in figure 2-33. The consistence of the nanocavities at a specific dosages shows a variance of around two nanometers. This variation in morphology is thought to stem from the inherent auto-combustion process and not the amount of electrons being emitted onto the surface. One could imagine that a small explosion on the surface of the film would yield variations in surface depth and width. It was reported in 2008 that LSMO nanoparticles could be generated by applying microwave radiation to a solution of metal nitrites and that the microwaves made the nitrate solution combust [16].

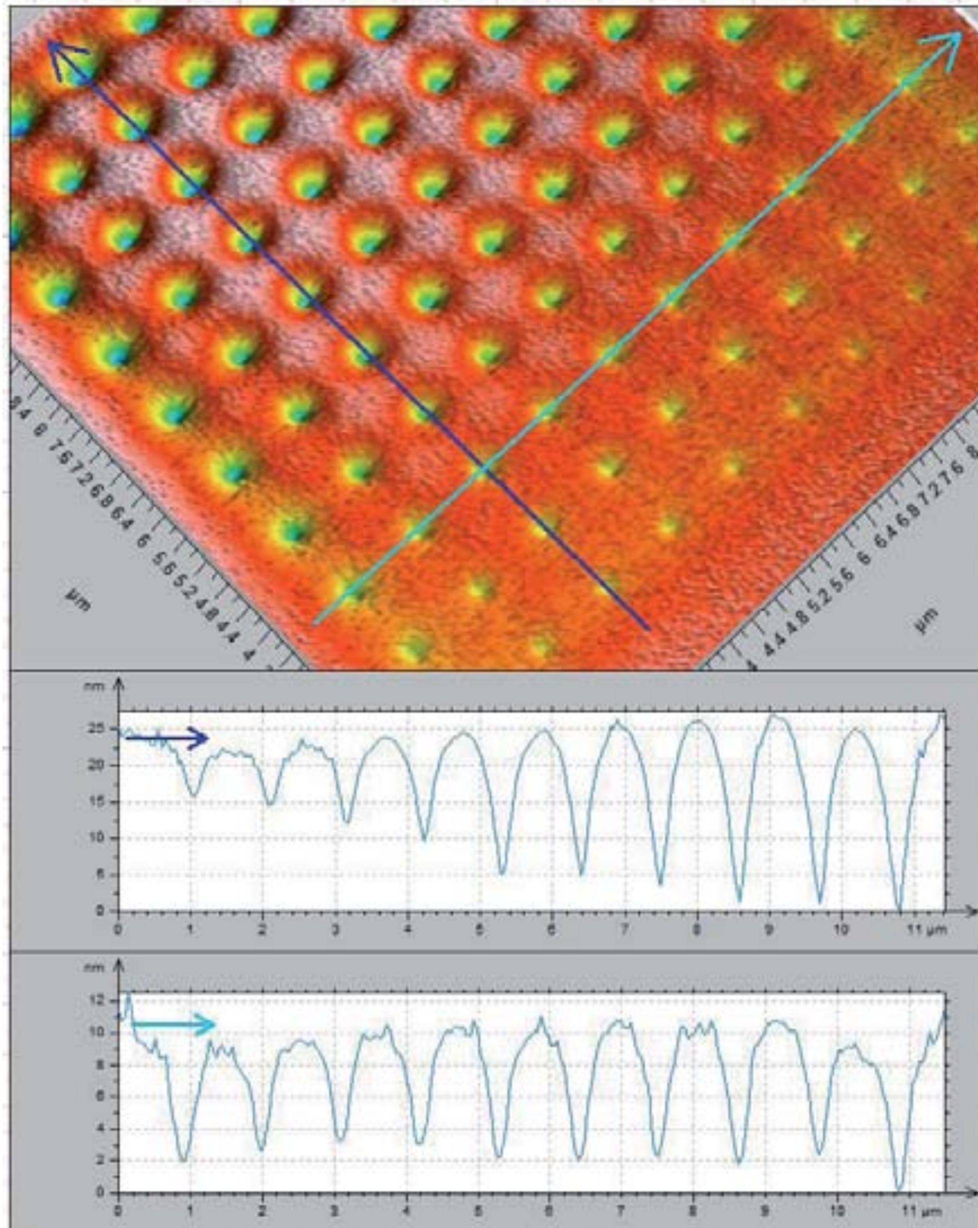

Figure 2-2 *Low dosage array of nanocavities showing dosage dependence and consistency. The pitches were 1.25 µm, while the dosage ranged from 0.05 to 0.14 pC in increments of 0.01 pC. The substrate was STO, the counter ion was nitrate.*

In the lowest energy regime, the morphology of the nanocavities is characterized by a small depression. The resultant form is dependent on the dosage, the distance between nanosites, and is influenced by the type of counter ion used. This can be seen clearly in figure 2-3 where one sees on the left an isolated nanocavity and on the right a pair of nanocavities. The distance to the next nanocavity is five micrometers on the left hand side of figure 2-3, thus the morphology seen here is truly the resultant deformation of only that stream of electrons. This is in contrast to the nanocavities observed when the nanocavities are spaced close together on the right hand side. This closeness causes an overlap in the effective radiation an individual nanosite

encounters. This overlap does effect the finally morphologically outcome of the annealed nanodot as will be demonstrated here.

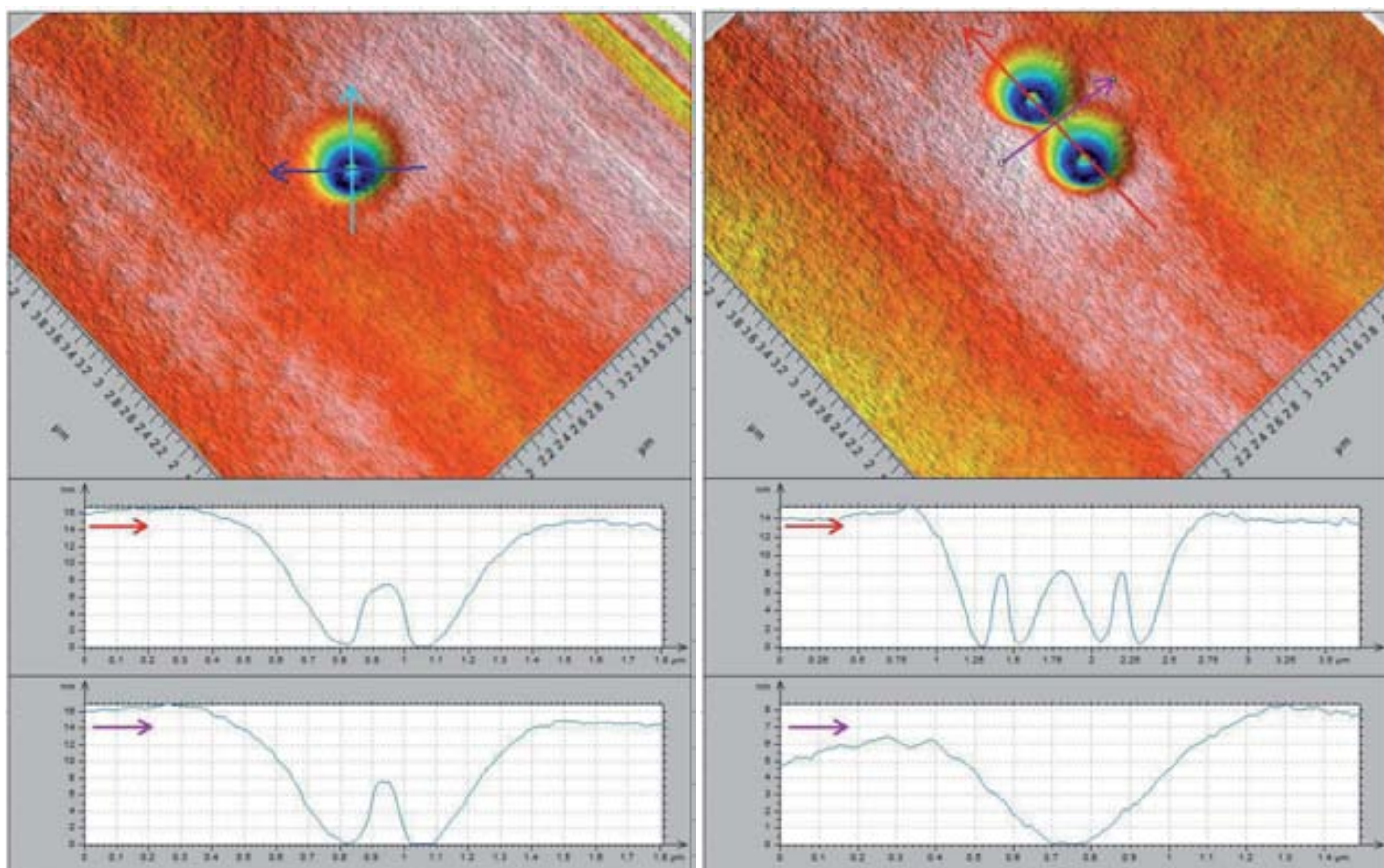

Figure 2-3 *Left: single isolated nanocavity. Right: two nanocavities with 750nm pitch. Nanocavities generated by the low dosage of 1.5 pC. The substrate was STO, the counter ion was acetate.*

In figure 2-3, one notes the form taken by the thin LSMO-Ac precursor film after radiating with electrons. On the left, one sees a completely isolated nanocavity which was formed by an single stream of electrons at 1.5 pC. On the right is the product of two streams of electrons separated by 750 nm at the dosage as the isolated site. One notes that a commonality between both images is the central column where the beam was focused. This central column, as it will be discussed in the next section, could be the top part of the hardened nanoisland or it could be simply a splash of precursor. The diameter of this central column is on the order of 100 nm and the height it reaches is roughly eight nanometers. The depth of the cavity caused by the electron impact in both cases was approximately fifteen nanometers. One also notices there exists an overlapping effect when the two beam sites are sufficiently close together. This overlap is observed by the reduction in the film between the two sites by around seven nanometers. The diameter of the affected area is on the order of one micrometer, so it stands to reason that when the two nanocavities are closer than that, a cumulative effect is seen. This cumulative effect is observed in the width of the affected area when the two nanosites are

separated by 750 nm. On the right of figure 2-3, one sees that the width of the affected zone is two micrometers, however this would be 1750 nm if there was no stacking effect from the two beams. This observation of a non-linear response to electron beams when the pitch is sufficiently small must be taken into account when writing large close-packed arrays.

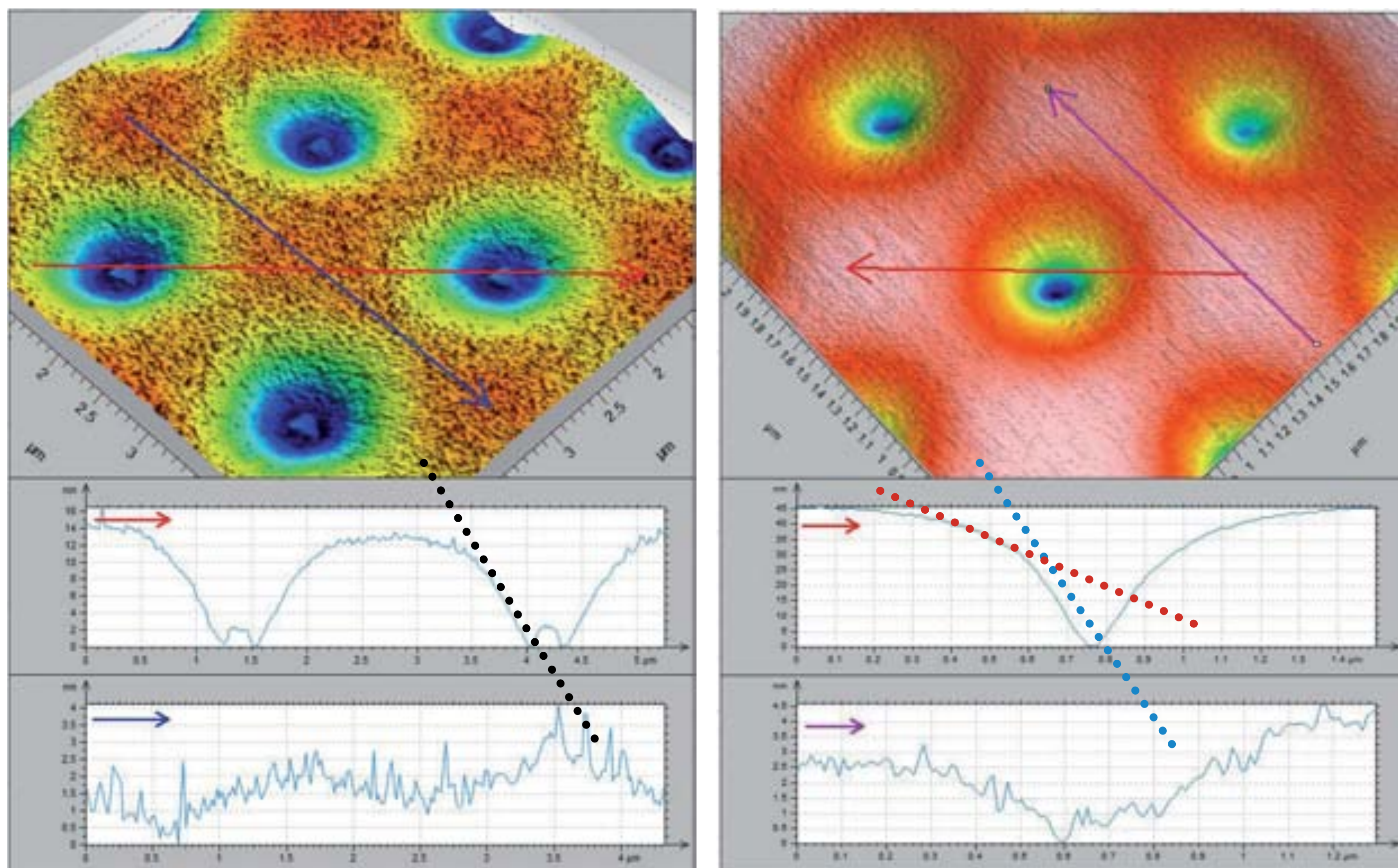

Figure 2-4 *Morphology of low dosage nanocavities on LSMO nitrate based film LSMO. Left: pitch of 3 µm at 0.05 pC. Right: pitch of 1 µm at 0.15 pC. Nanocavities generated by the low dosage of 1.5 pC. The substrate was STO, the counter ion was nitrate.*

When the same dosage was applied to a film whose counter ions were nitrates, this results are seen on the left of figure 2-4. One can see a central column similar to those found when radiating on to the LSMO-Ac film. The pitch here was two micrometers and it appears that the overlap at this pitch is not influencing neighboring nanocavities. Here also a linearity is seen in the slope of the nanocavity. When the dosage is increased to 1.5 pC, there exists a threshold at which above that point, a bifurcation in the slope is observed. This point can be seen on the right of figure 2-4, where two slopes exist. The slope at the bottom is more steep than the slope at the top. Their slopes are 1/30 at the top and 1/5 at the bottom. One theory is that the flash point of PVOH is lower than the nitrate and acetate components, thus when slightly heated by passing current, the polymer decomposes first. Another morphological difference between the acetate and nitrate precursors is the

disappearance of the central column at higher dosages. Where the central column is clearly visible on the left of figure 2-4, on the right hand side the feature is gone. The disappearance of the central column is consistent at all higher dosages for the nitrate based films.

2.1.2 High Dosage Morphology

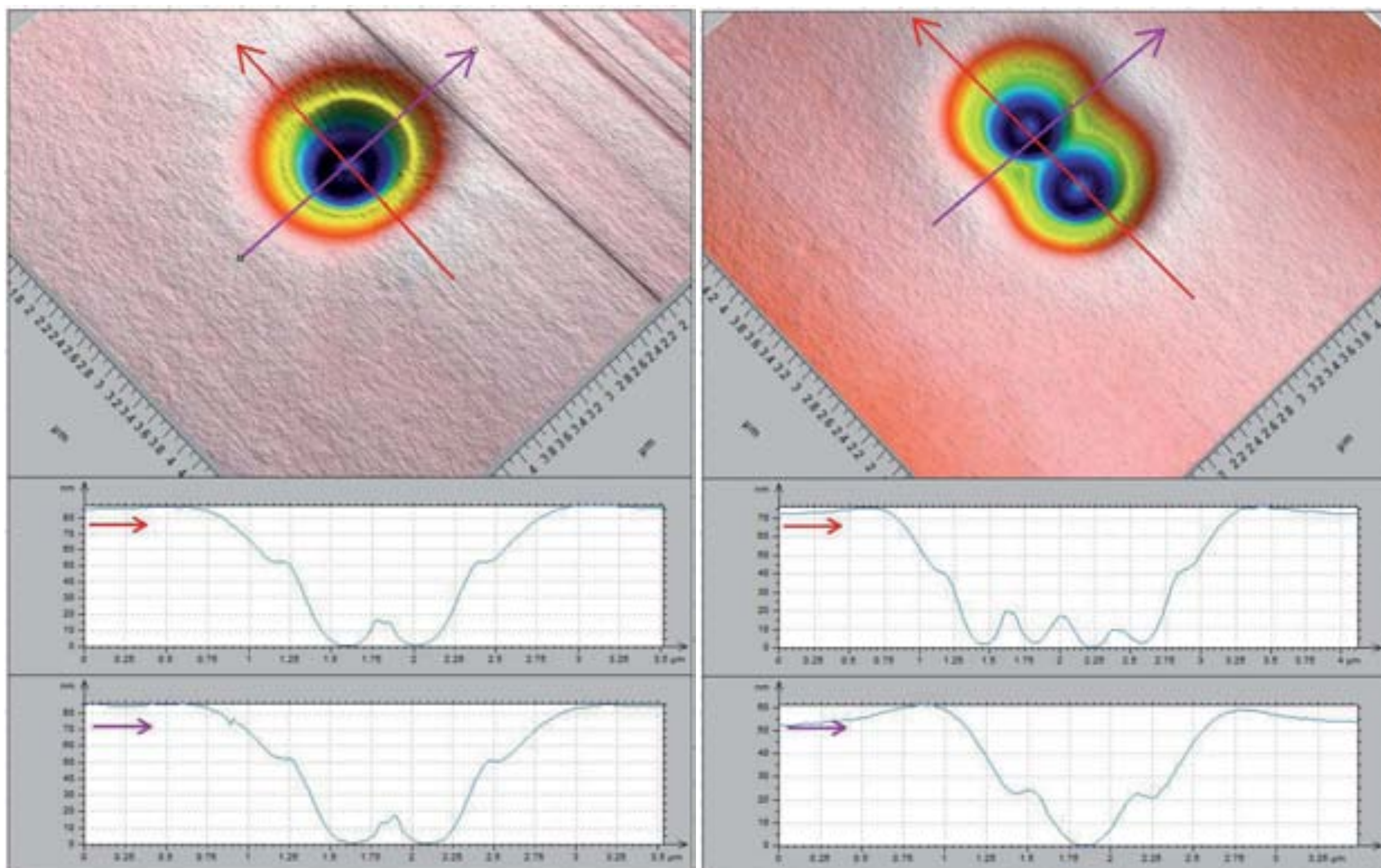

Figure 2-5 *Nanocavities formed by high dosage electron beams. Left: an isolated site. Right: two sites with 750nm pitch. Generated by the dosage of 1500 pC. The substrate was STO, the counter ion was acetate.*

When the dosage is increased significantly to 1500 pC, the resultant formed nanocavities differ significantly from those generated from less potent dosages as can be seen in figure 2-5. Namely, the high dosage nanocavities are deeper, wider, and they possess ridges where the lower dosage ones did not. The feature of a central column is still present however, their height has increased to twenty nanometers. The overall dimensions of the impact site have increased to roughly 70 nm high and 2250 nm wide. For the double nanocavity site separated by 750 nm, the width has enlarged to 2500 nm. The width should have been 3000 nm for the double site if the process was linear, however that was not the case. Interestingly, the width for

double low dosage nanocavity sites are larger than expected, while those in the high dosage regime lower than expected.

A possible explanation for this observation is that the film is not undergoing a similar decomposition than when exposed to low dosage beams. It is suspected that when the first nanocavity is formed, the electrons from another close-in high dosage beam could not further decompose the surrounding area with weak secondary electrons and could only drive a high aspect ratio cavity from the primary electrons. This non-linearity in decomposition can be observed morphologically from the AFM line scans. In figure 2-4 one notices a curious ridge approximately 50 nm from the bottom of the nanocavity. This ridge marks a bifurcation in the way the precursor is decomposed in the presence of focused electrons.

For the low dosage regime, the slope is 1/25. On the outer part of the high dosage nanocavity, the slope is 1/15, whereas this slope increases even further at the inner part with 1/8. Thus, the outer part of the high dosage nanocavity is more similar to the low dosage morphology than the inner part is. Therefore, both the outer part of the high dosage nanocavity and the low dosage nanocavity are probably formed from similar mechanisms. This leads to the conclusion that when the dosage is increased beyond a certain point, the LSMO-Ac film ablates in a dissimilar way to the low dosage manner.

Another interesting observation concerning the double nanocavity is that there appears to be a small lip of five to ten nanometers high which has raised the immediate film above that of the surrounding film. The lip is more pronounced in the bottom right line scan in figure 2-5. Here it appears that film has swollen due to the introduction of two close-in high dosage beams. The effect is seen more in the double than single high dosage nanocavity case. Naturally, this leads to the inquiry of where the film went after radiation. Perhaps this lip can explain where some of the film went. If the film directly beneath the beam were to change in density and if it were to be pushed away from the beam, then the walls of the nanocavity would be raised. However, this does not account for all the mass of film that disappeared. Some of the mass could have become ablated and decomposed as gas. It is also entirely possible that the some of the mass condensed and traveled further into the film, perhaps as the central column. The two mechanisms under which the LSMO-Ac film decomposes under focused electrons are not entirely clear. What is clear is that focused electrons act as a catalyst to the combustion reaction between the components of the film. This reaction causes the underlying film to become cross-linked, and thus able to withstand a solvent bath, however a consequence to this is the ablation of material.

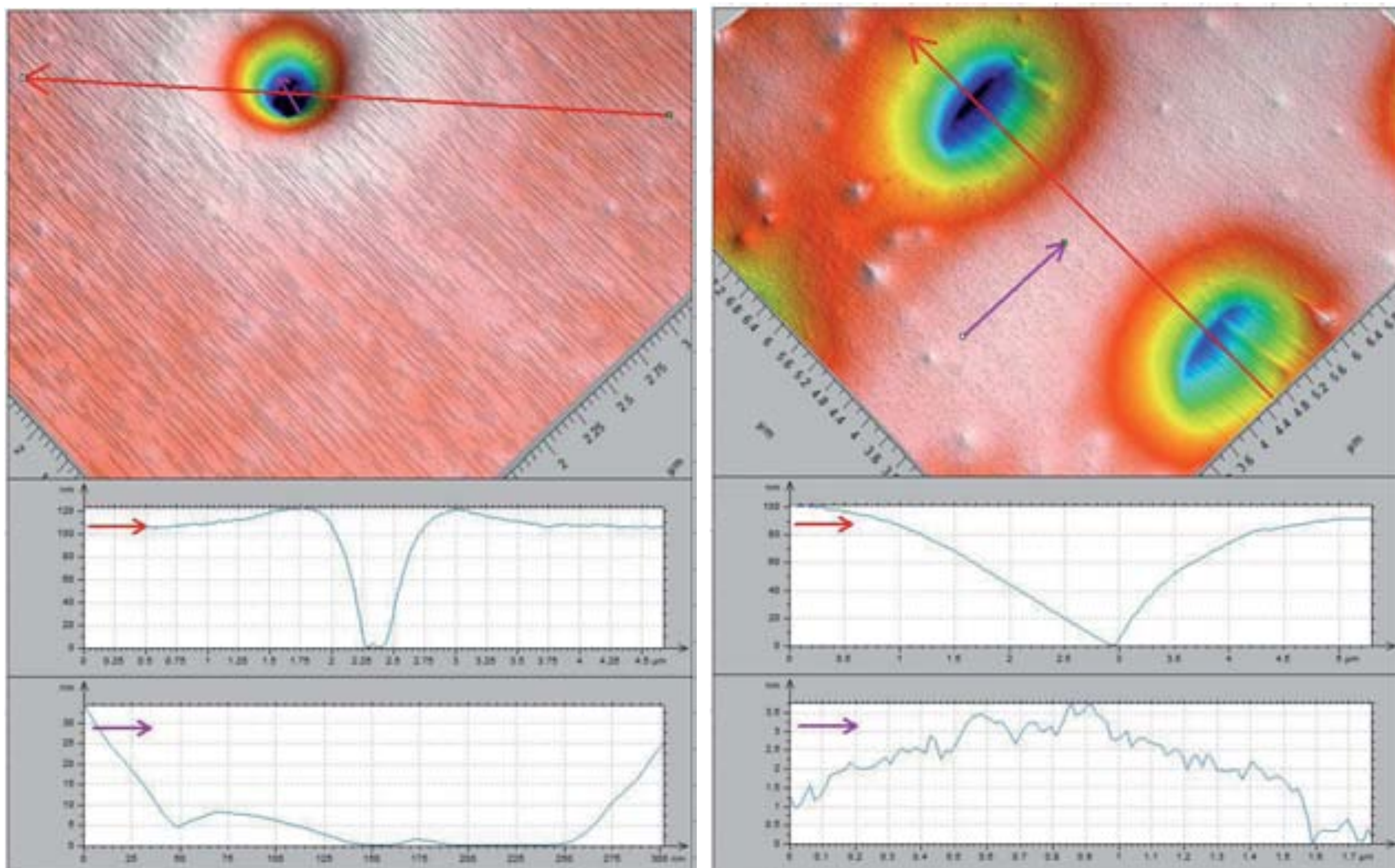

Figure 2-6 *High dosage nanocavities made on nitrate LSMO film. Left: STO substrate. Right: YSZ substrate with pitch of 5 µm. Generated by dosage of 1500 pC.*

The resultant nanocavities left on a LSMO-nitrate film from high dosage electron radiation can be seen in figure 2-6. Here the differences between radiating with high dosage on very insulating and slightly insulating substrates are seen. Mainly this morphological difference comes in the form of an elongated nanocavity. The cause of this anisotropic elongation is the charge build-up on the surface of the YSZ. This charge build-up forces the electron beam off of the initial starting point and on to an adjacent less charged area. The nanocavity found on the YSZ sample is more flat than that of the YSZ sample. This is thought to stem from the increased time in which the electron beam has in contact with the film in a concentrated form. The more conductive STO substrate allows for a larger amount of electrons to impinge on one point as compared to the YSZ substrate. When writing with low dosages on YSZ, morphologies similar to that of LAO and STO are seen due to a lack of extreme localized charge build-up.

These nanocavities also do not display the central column which was present in the acetate films at this high dosage. However, what now is present instead of the central column on the STO sample is a two hundred nanometer flat region. This is significant for the reason that it brings insight into the mechanisms at work in the

lithography process. The observation that the bottom of the nanocavity can be either a positive, flat, or negative feature speaks to the interplay between temperature and precursor composition. The cause of this discrepancy can be thought to stem from central column being nothing more than a splash of precursor and not the top of the nanoisland. The sharp nanocavity floor of the YSZ sample could be caused by insufficient temperature and spacial confinement to melt an isotropic section of the film, however energetic enough conditions to destroy the central column.

2.2 Nanoislands – After Water Development

After the LSMO precursor has been radiated with focused electrons at predetermined locations and durations, the non-radiated film must be removed. To do this, the sample is submerged in water which acts as a solvent. The water removes the vast majority of non-cross linked film while leaving the cross-linked film in place. The duration of rinsing the sample in water depends on the substrate in which the film was written. For the STO, LAO, and silicon substrates, the process lasts approximately thirty seconds while for the YSZ a short submersion of five seconds is performed. These temporal requirements to these procedures were determined from optical micrographs which showed that above these substrate dependent rinsing times, the nanoislands started to separate from the given substrate. Furthermore, the developed films were analyzed with AFM afterwards to determine the amount of remaining film which was still present. This was determined by the roughness of a given non-radiated section. If the substrate was very rough in these regions, the sample was cleaned for a longer time until a balance was achieved. The cause for this substrate dependent debonding is unclear, however what is clear is that one cannot leave the sample sonicating in water for an extended period of time or else all nanoislands will disappear.

In this section, the morphological effect on the sample will be remarked upon after water development. Here it will be shown that the general shape of the final nanodot is taken from the cone of radiation which is observable once the surrounding film has been removed. This cone shape is the product of the electron beam focusing very near to the film's surface and thus the reverse of this shape cross links the polymer. One can think of this process in similar terms to how light is focused from a lens and how the light leaves that focal plane.

2.2.1 Low Dosage Morphology

The morphology of the nanoislands alters drastically as dosage and pitch are varied. At the very lowest dosages, the height grows slightly with an increase in dosage. However, it soon reaches an asymptote and

thus a maximum height is reached at slightly higher dosages as can be seen on the left of figure 2-7. This observation is explained by the premise that the more electrons focused onto a site the more that site will cross-link and adhere to the substrate. This occurs until a certain dosage is reached and thereafter the height of the nanoisland reaches a maximum due to the geometrical considerations of the film. Graphically this can also be seen in figure 2-33.

The nanoislands belonging to the low dosage regime can be seen on the left hand side of figure 2-7. There at the lowest dosages one can see that the maximum height has not been reached and that there is still a proportionality to height from dosage. It can also be seen that when the maximum height is reached, the nanoislands still grow however in a fashion perpendicular to the beam direction. These particular nanoislands were close packed and made from a nitrate based LSMO precursor. What is clear is that the nanoislands formed directly underneath where the electrons were incident and formed a cone thusly. Also what is visible in the AFM image is that the tops of the nanoislands become more flattened as the dosage increases. This is a natural artifact stemming from the base growing wider while the height remaining constant. It is unknown the maximum height that nanoislands may reach, however one could postulate that with a much thicker film, the maximum height would scale proportionally.

On the right hand side of figure 2-7, one sees a series of nanoislands generated from a range of dosages at various pitches on acetate based LSMO. The dosages were 1.5, 15, 150, 1500 pC and resided at pitches 750, 1500, 3000, and 6000 nm. There exists an interesting interplay between dosage and pitch which this AFM image portrays. When analyzing the right hand side of figure 2-7, one notices that as the pitch decreases, the two nanoislands begin to merge. This is the result of the spray of electrons overlap per site. This overlap causes a lack of non-radiated precursor and thus disenabling the surrounding region to be cleared. The general consequence of this observation is that there exists a minimum distance for which isolated nanosites may be written at a given dosage, while the specific consequence is that combined system is too large for isolated nanostructures to form, such as 750 nm for 0.1 pC on LSMO-nitrate. Obviously, at a pitch of 6000 nm it is essentially an isolated nanosite and thus it can be certain that the morphology of said nanoisland is as it would be with no radiation overlap from neighbors. This gives an opportunity to analyze the morphology of the single and double nanoislands at low and high dosages.

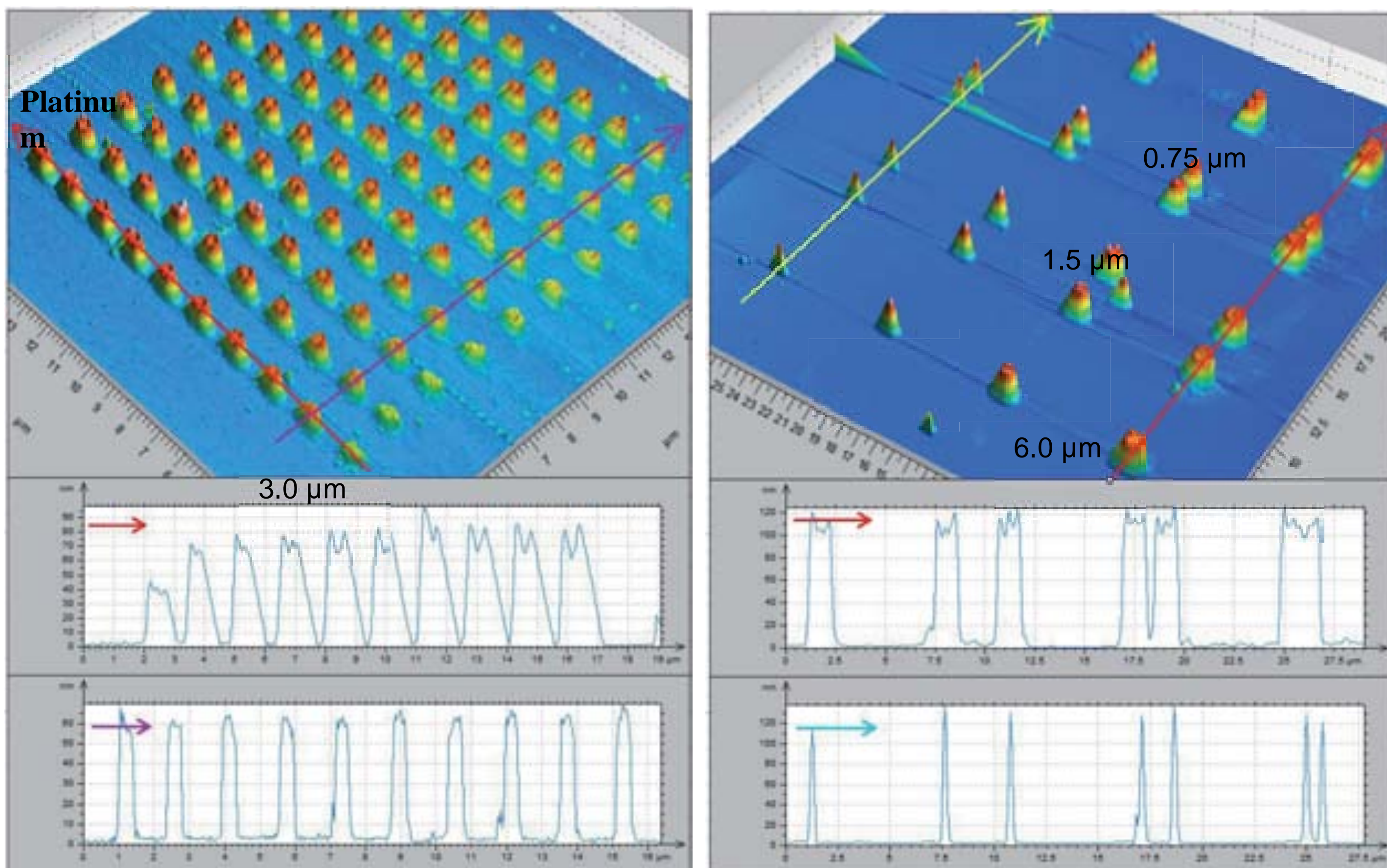

Figure 2-7 *Left: low dosage nanoislands on STO from LSMO-Nt. Dosage were 0.05 to 0.14 pC with a pitch of 1.25 µm. Right: nanoislands on STO from LSMO-Ac. Dosages were 1.5, 15, 150, 1500 pC , pitches were 6, 3, 1.5, 0.75 µm.*

In order to more closely examine the morphology of the nanoislands from the previous image written on acetate based LSMO, a series of more closely zoomed in AFM images were made. First the effect of low dosage electron beams will be analyzed when isolated and then as a close-in pair in figure 2-8. On the left hand side, one sees what is the resulting morphology after a water cleaning of a singular, essentially non-neighboring, electron beam onto a film of LSMO-Ac. Here one can see the nanoisland is almost 140 nm tall and 375 nm in width and has a generally cone-like shape. One can also see the lack of surrounding material next to the nanoisland by virtue of the the linescan along the bare substrate floor showing low roughness. It must also be pointed out that the form of this solitary nanoisland is very cone-like in nature. This contrasts with the pair of nanoislands seen on the right hand side of figure 2-8. There the form is more truncated, as if the top section of both nanoislands has decomposed. This may be a consequence of being roughly 50 nm smaller height than the isolated nanoisland. If the pair of nanoislands had their angled edges continue 50 nm higher, than the form would have been a non-truncated cone. The width of the individual dots in the pair remained the same as that of the isolated nanoisland. One can observe that the original intended pitch of 750 nm has been retained after electron beam radiation and cleaning. If the system was linear in scaling, then the closest pitch that could be obtained with this dosage would then be roughly 400 nm. However, the electrons

do not interact with the precursor in a linear fashion and thus at a pitch of 400 nm, the spacing between the nanostructures cannot be consistantly cleaned free. Another consideration is that with a close-in formation, charging effects of radiating a large field of nanosites, and secondary electron spill, a practical limit to how close-packed the nanosites can be at this dosage is on the order of 750 nm.

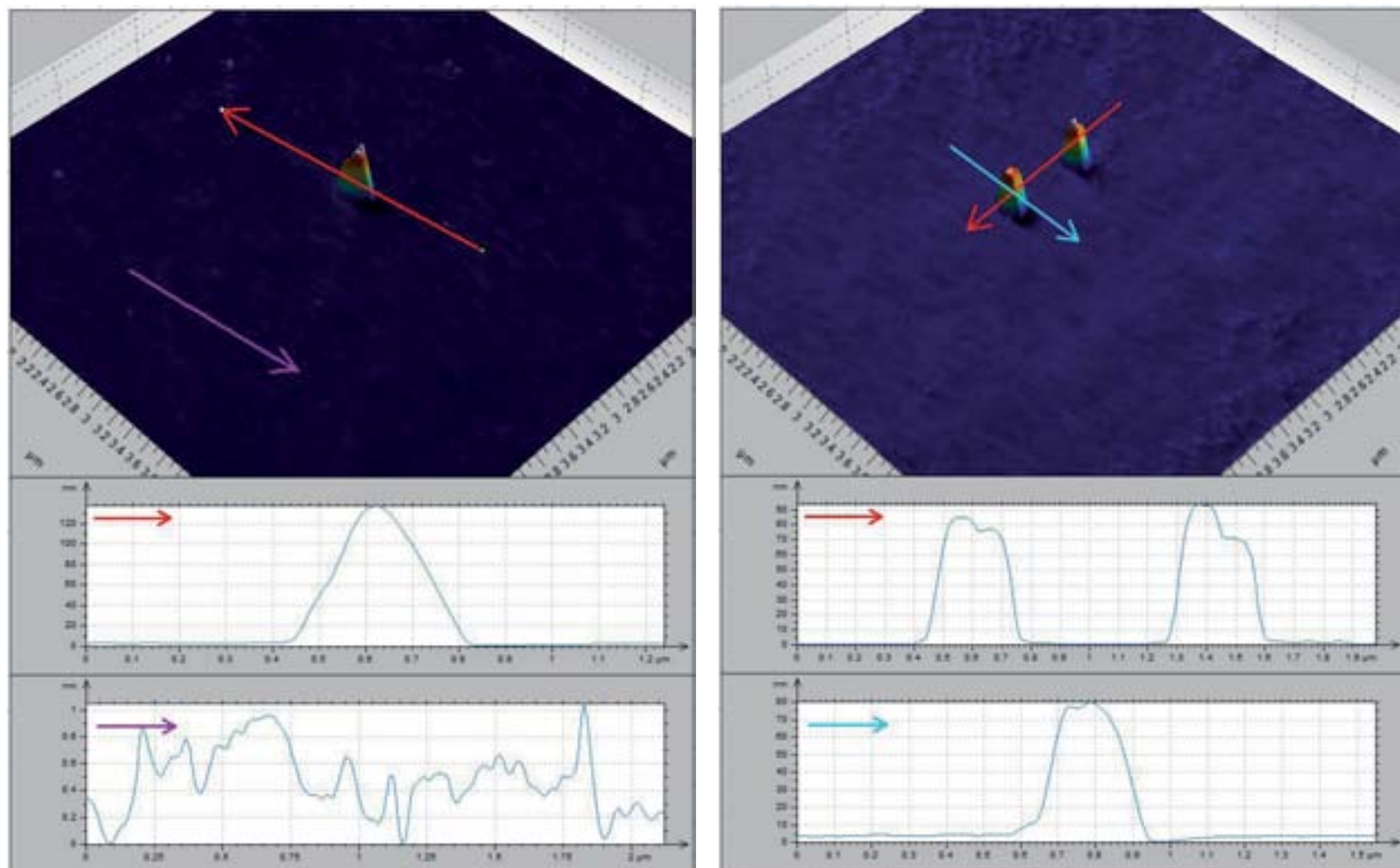

Figure 2-8 *Nanoislands formed by low dosage electron beams. Left: an isolated site. Right: two sites with 750nm pitch. Generated by the dosage of 1.5 pC. The substrate was STO, the counter ion was acetate.*

2.2.2 High Dosage Morphology

When the dosage is augmented to 1500 pC, the morphological ramifications to the film are significant. One can clearly see that both the individual and pair of nanoislands increase in width substantially in figure 2-9. It is true that there are intermediate structures between the low and high dosages explored here, however these structures do not produce isolated triangular nanodots nor oriented nanowires, so they were not studied in depth. This has occurred due to the increase in the amount of electrons which have traveled through the film as the exposure time was increased. These electrons may be thought of traveling in two possible different modes at high dosage, one where the beam remains perfectly still over the course of ten seconds and the

secondary electrons are the ones broadening the nanoisland, or one where the beam itself is moving in a transient way and therein the primary electrons are making the nanoisland wider. The base width recorded by the AFM for the isolated nanoisland was 1250 nm while its height was seen as just under 120 nm. This gives an aspect ratio of one tenth whereas for the lower dosage nanoisland is was roughly one third, thus the structures have become more two dimensional as dosage in increased.

Comparing the single to double high dosage nanodots case in figure 2-9, one notices that at 750 nm pitch the cross-linking has clearly overlapped. There one sees two nanoislands sharing a common interior and thus this would be unsuitable for the purposes set out for this project. For the pitch to be as small as possible with the high dosage set about here, the nanosites would have to be around 1500 nm. Of course, as it will be seen in the next section, the nanodots made from high dosages are not optimal for the fabrication of controlled single crystal LSMO.

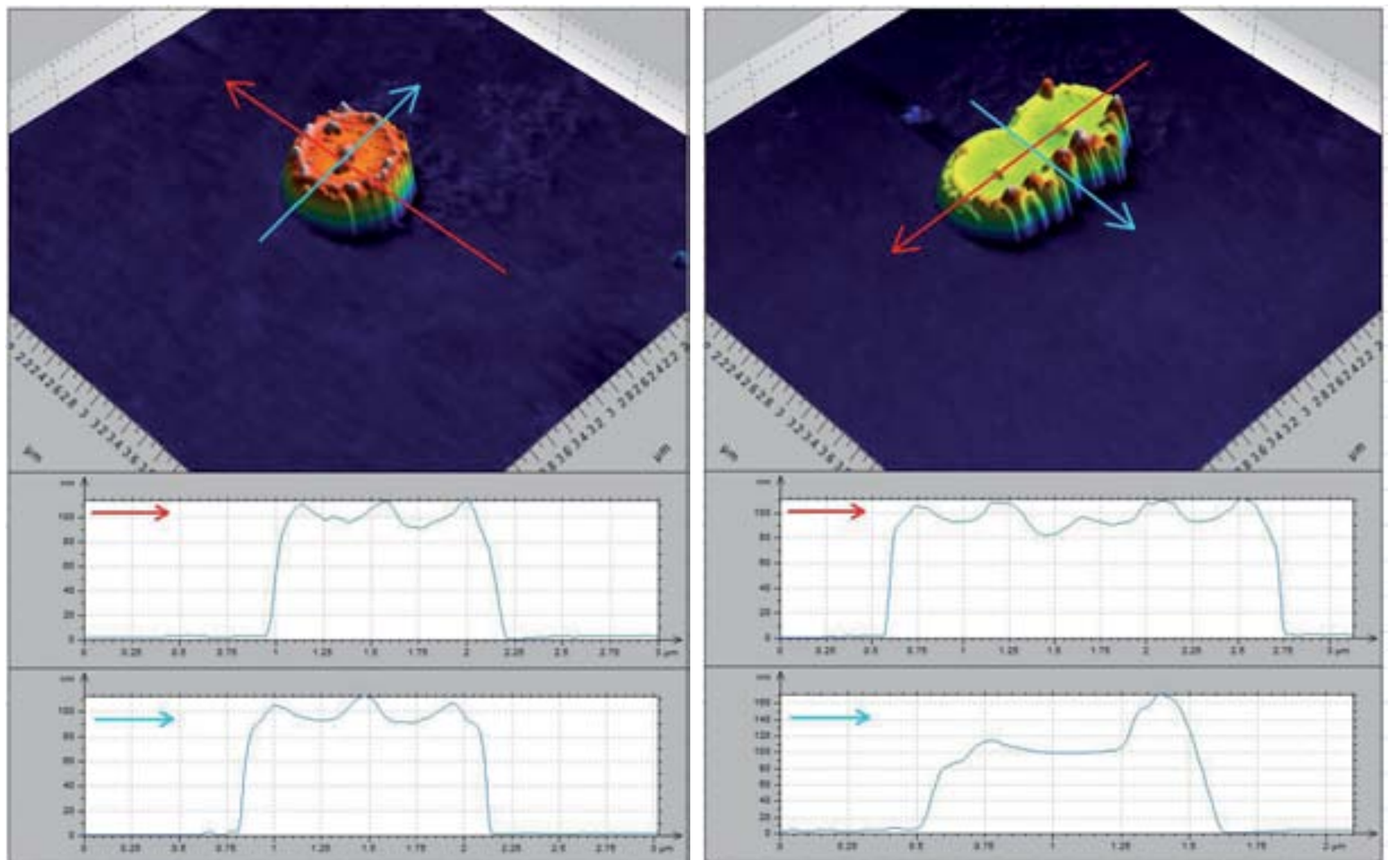

Figure 2-9 *Nanoislands formed by high dosage electron beams. Left: an isolated site. Right: two sites with 750nm pitch. Generated by dosage of 1500 pC. The substrate was STO, the counter ion was acetate.*

Another feature seen in the high dosage nanoislands is the central bump extending some twenty nanometers from the flat area on top. This feature constitutes the point at which the primary radiation entered into the film and thus the surrounding film was cross-linked by secondary electrons. The reason why this central bump is higher than that of surrounding film is perhaps due to the secondary electrons being much more diffuse in their approach to the film. Another theory is that the central column in the non-developed film is the same as that of the central bump.

Another interesting feature of these high dosage nanoislands is the existence of a raised ridge along the edge of the structure. Also twenty nanometers in height, this ridge could be the result of a more complex mechanism. *If the precursor cross-linked in a more conventional manner, then the top part of the nanoisland would be flat or gaussian.* An explanation for this non-conventional morphology is that the film undergoes a non-conventional *decomposition where the film initially is cross-linked from a small amount of radiation but with continued radiation, either compresses or becomes more slightly more soluble. This model holds that as the shutter is allowed to be open and radiation pours down on the site, the sharp point of the insoluble cone becomes more volcano-like. The volcano-like structure then widens as the radiation continues, driving the mouth of the volcano ever wider until a point is reached where the ridge diminishes in height. At this point the central part of the nanovolcano hardens even more whereas the rest of the cross-links in the structure start to weaken. This can be seen on the left hand side of figure 2-10 in the case of radiation on LSMO-Nt.*

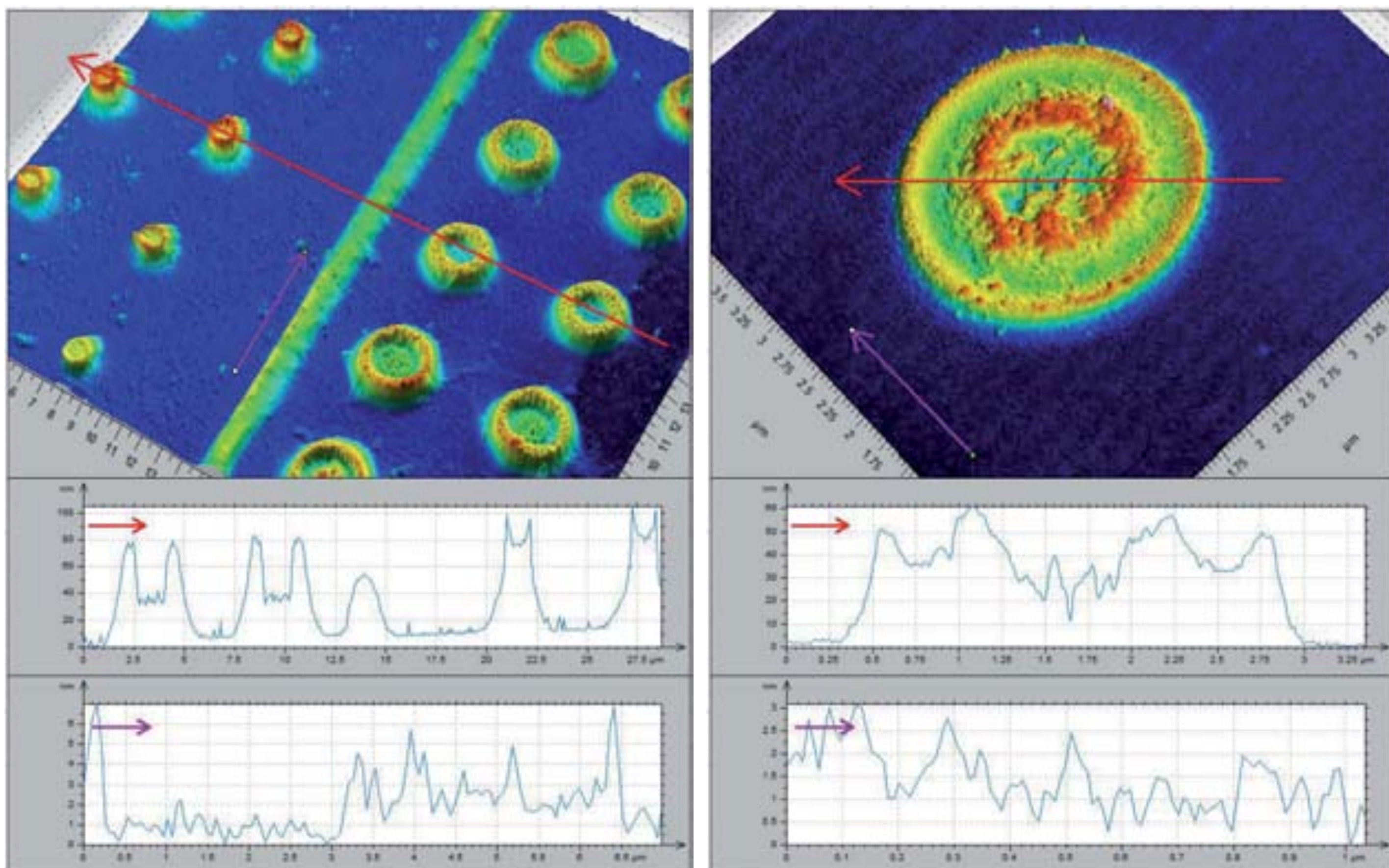

Figure 2-10 *A series of volcano-like nanoislands from LSMO-Nt on STO. Left: pitch of 5 µm and dosages of 150 and 1500 pC. Right: isolated nanoisland with dosage of 2500 pC.*

On the left of figure 2-10 one is able to note how the height of the nanoislands decreases as dosage increases for nanoislands made from LSMO-Nt. The suspected mechanism is the non-linear decomposition of the precursor under the presence of concentrated electrons. This effect is highlighted in the figure on the right hand side of figure 2-10. The AFM linescan shows a similar structure to that of the lower dosage volcano-like nanoisland in the sense that the ridges of the mouth are higher than the center. However, one key difference between the two morphologies is the inclusion of a central raised caldera ring. This ring appears to stem from an excessive amount of electrons being focused in the center of the nanosite. This radial symmetry of the raised ridge, the lower plateau, and the central caldera ring are symptomatic of a non-linear reaction to electron radiation. Mainly, the raised ridge forms from the lowest dosage secondary radiation, while the higher dosage secondary radiation forms the plateau by compressing the precursor locally, the central caldera forms from lower dosage primary radiation turning the precursor into a crystal, and finally the very center of the nanoisland is destroyed from the highest dosage of primary radiation.

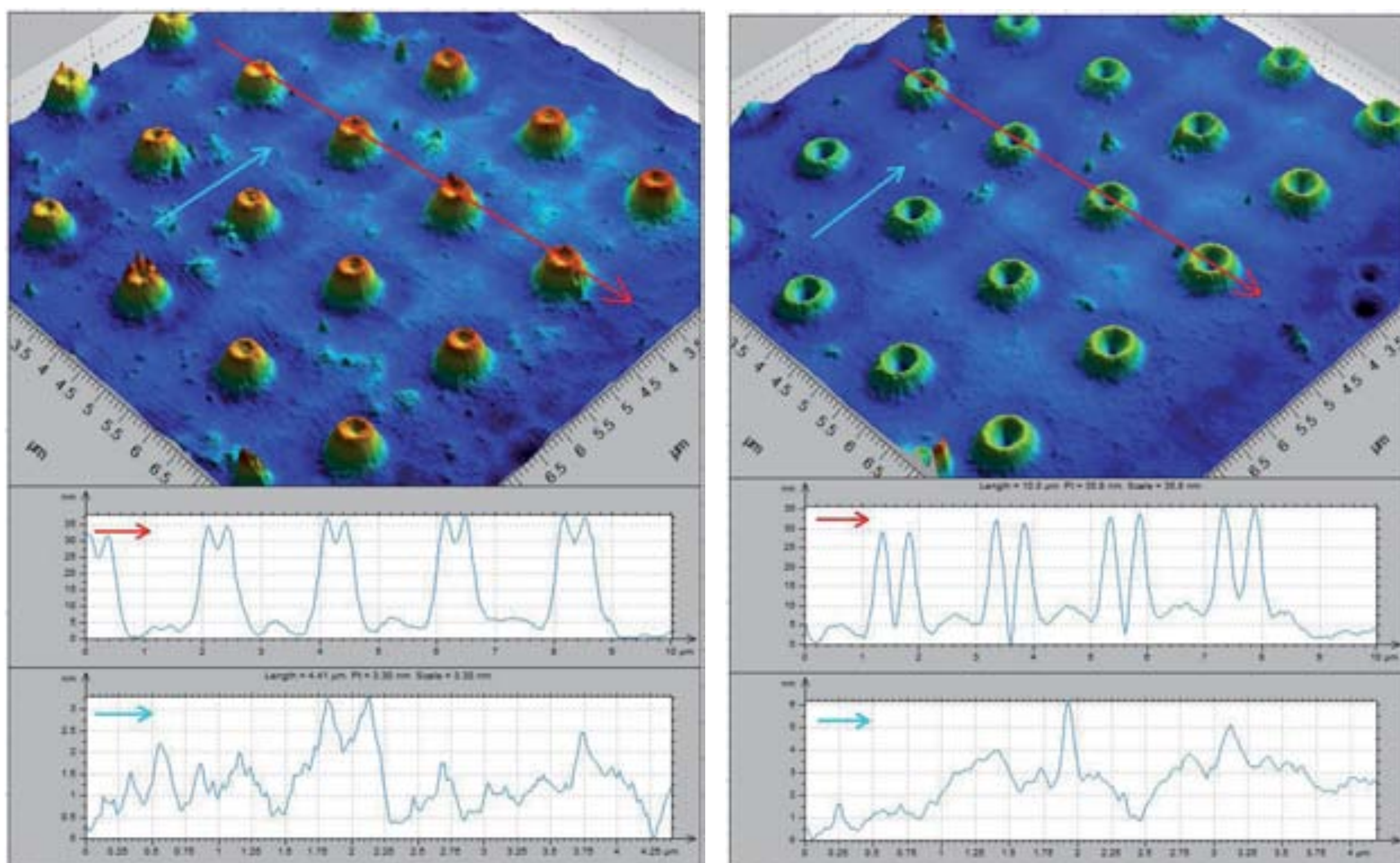

Figure 2-11 *Volcano-like forms of nanoislands from LSMO-Nt on STO. Left: pitch of 2 µm at dosage of 1.0 pC. Right: pitch of 2 µm at dosage of 1.5 pC.*

This complex interplay is also highlighted by small changes to the dosage. This comes in the form seen in figure 2-11, where the volcano-like nanoisland morphology is drastically altered by the edition of only a slight increase in dosage. One observes by AFM how the mouth of the volcano-like nanoisland deepens considerable and the overall width increases negligibly. This illustrates the non-typical response the nitrate-based precursor has to focused electrons.

2.3 Nanodots – After Oven Treatment

In spite of the interesting yet complex mechanics which yield nanoislands, they are but an intermediate state in the final goal of achieving arrays of single crystalline LSMO nanodots. In order to do this one must anneal the sample at high temperature at an extended period of time. Essentially what this oven treatment does is increase the molecular mobility significantly while removing organic components from the nanoislands. The removal of all organic components, thus leaves only the inorganic species of La, Mn, Sr, and oxygen to form nanocrystals. It has been observed by Zou et al that the line width of sol-gel derived LSMO micropatterns was

reduced by thirty percent when annealed [17]. It was thought that this removal of organic components is relatively destructive for the nitrate based LSMO and less so for the acetate based one [18]. The mechanism of organic removal is an important one due to the single crystal's final morphology being so critical. To that end, the ramp rate of the annealing process must be a slow, non-dramatic one, to insure the morphological preservation of the nanoisland.

In figure 2-12 one notices that after annealing the height of the nanodots has been reduced. One can see the close-up images of the single and double low dosage nanodot in figure 2-13 as well as the high dosage ones in figure 2-14. What is clear is that distance between neighboring nanodots is an influencing factor on the final morphology in that when they are too close, they form a continuum. Also, as it was noted with the nanocavities and nanoislands, the dosage has directly influenced the dimensions of the final nanodots. Thus, if a specific desired height for a nanodot were desired, then the dosage could be tuned to bring about that dimension as seen in figure 2-33. These final nanodots do not possess any organic components and are solely composed of inorganic species. Consequently, when observing the morphology of these nanodots, one must bear in mind that these are poly or single crystalline species. However, this cannot truly be ascertained until observed with a high resolution TEM, however many inferences solely from morphology can be put forth. For instance, if the nanodot is highly triangular in form, this is typically perceived as more likely single crystalline than not. Conversely, if there are several undefined angles on a nanodot, this is seen as more probably a polycrystalline structure. This rough guide can serve in the choosing of candidate nanodots in which to inspect with the TEM.

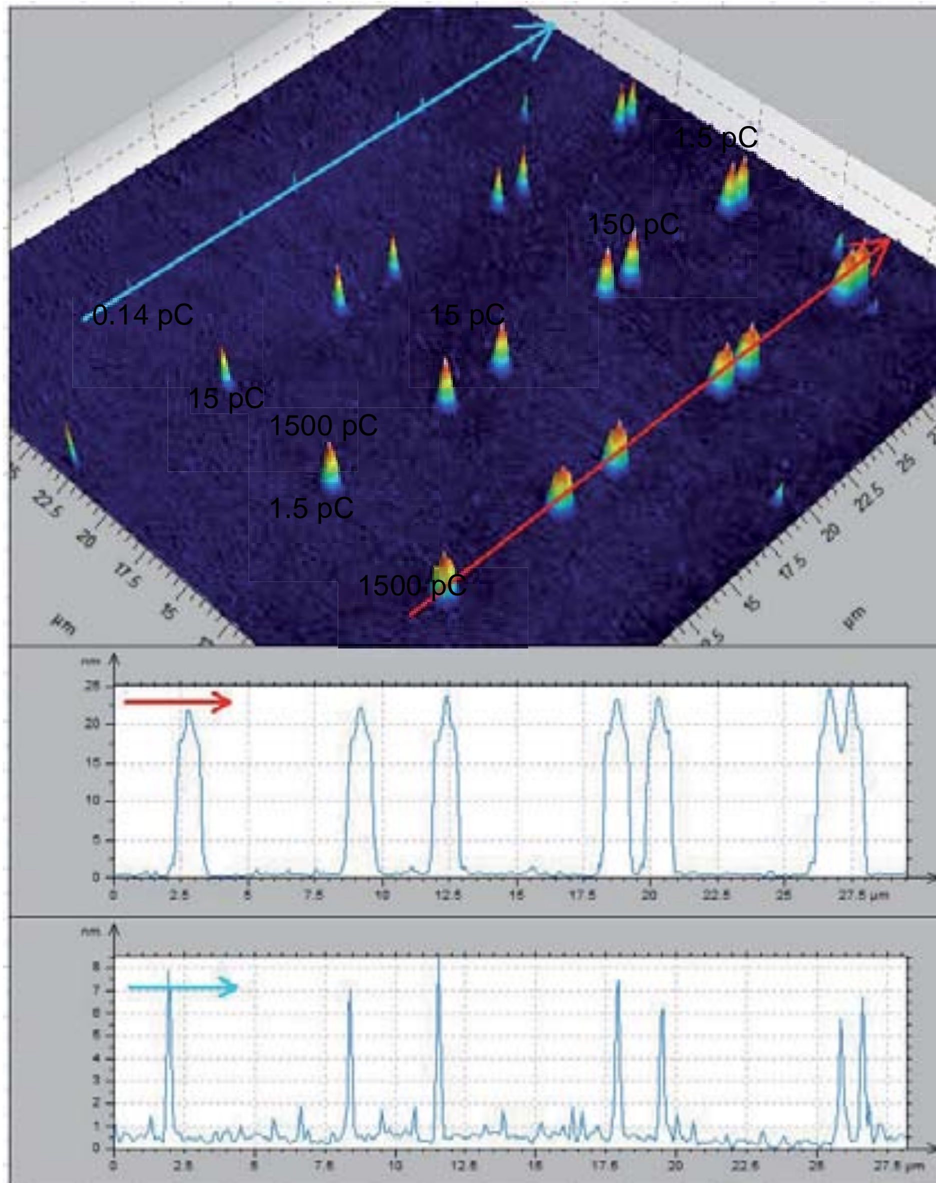

Figure 2-12 *Array of nanodots from LSMO-Ac on STO annealed at 1000C 4h at dosages of 1.5, 15, 150, and 1500 pC. The pitch was 6, 3, 1.5, and 0.75 µm.*

2.3.1 Low Dosage Morphology

When more closely analyzing the low dosage nanodots present in figure 2-13, one notices the decrease in height from 120 nm as a non-annealed nanodot to roughly 10 nm when annealed at 1000C for four hours from the figure 2-13. Another reduced dimension is that of the width from 375 nm to 175 nm after the high temperature treatment. With this one can clearly see that the resultant morphology is one of a smaller structure than that after water cleaning. This is directly due to the loss of organic mass in the form of the PVOH and the acetate counter ion as well as the formation of the denser crystal. One is also confronted by

the decrease in height relative to the decrease in width. This is similar to what happens for film growth, the majority of the contraction is in the vertical direction.

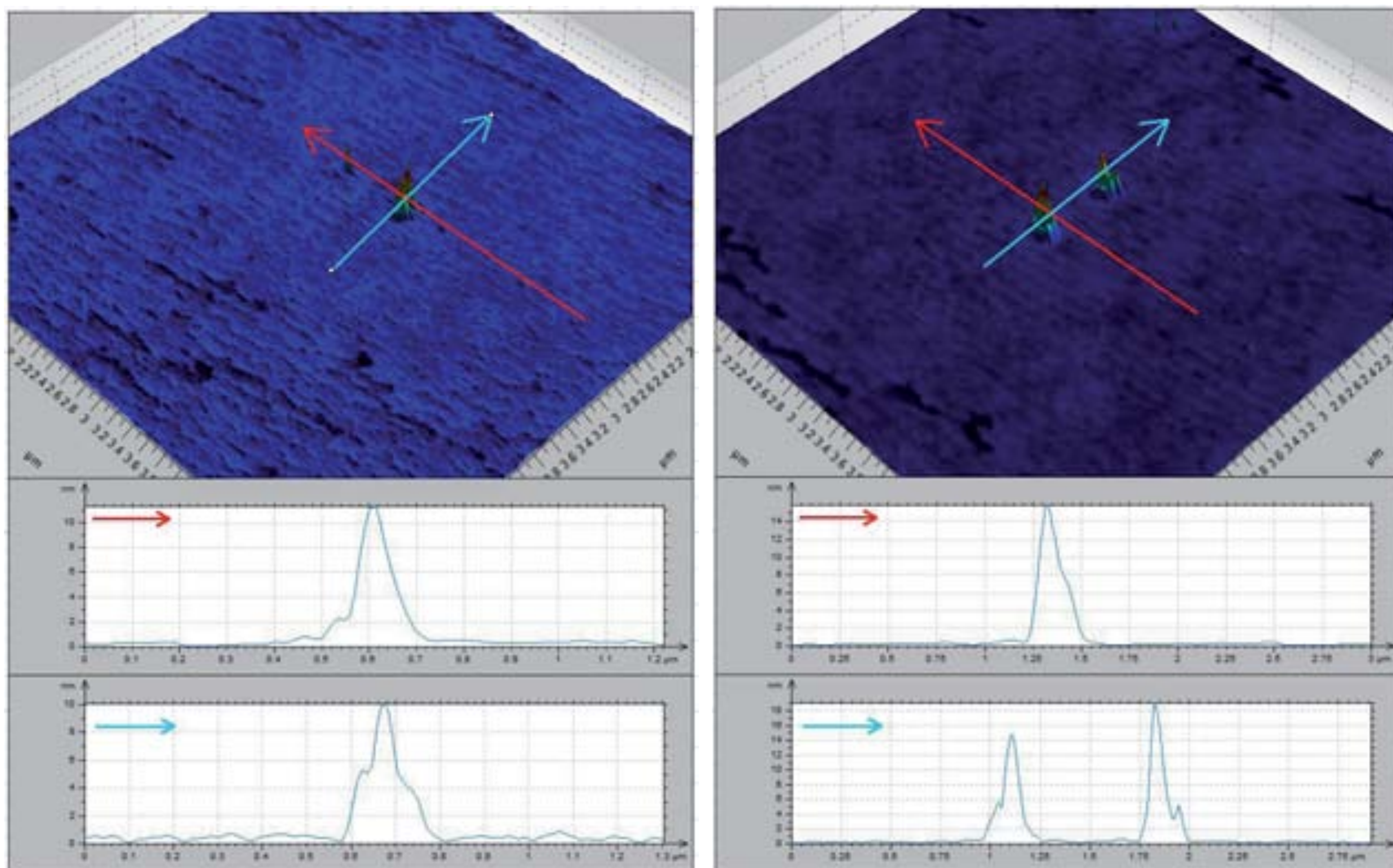

Figure 2-13 *Nanodots formed by low dosage electron beams and annealed at 1000C for 4h. Left: an isolated site. Right: two sites with 750nm pitch. Dosage was 1.5 pC. The substrate was STO, the counter ion was acetate.*

In the double nanodot case, the pair appears to be well isolated despite the small spacing of 750 nm between them. As was mentioned previously, the spacing for a pair of nanodots may be lessened considerably from the 750 nm seen in figure 2-13, however when making a large array of these nanodots, charging will affect the manner in which electrons are projected on to the substrate and thus would make a pitch smaller than this unsuitable for single crystal fabrication. When noting the morphological differences between the singular and double nanodot sections, there exists more similarities between the two configurations than was the case for the nanocavities and nanoislands. Also the height and width of all three nanodots appears very similar, thus highlighting that the minimum pitch at this dosage may be lowered to 750 nm with no discernible alteration of the nanocrystal versus the ideal isolated case for a small size array.

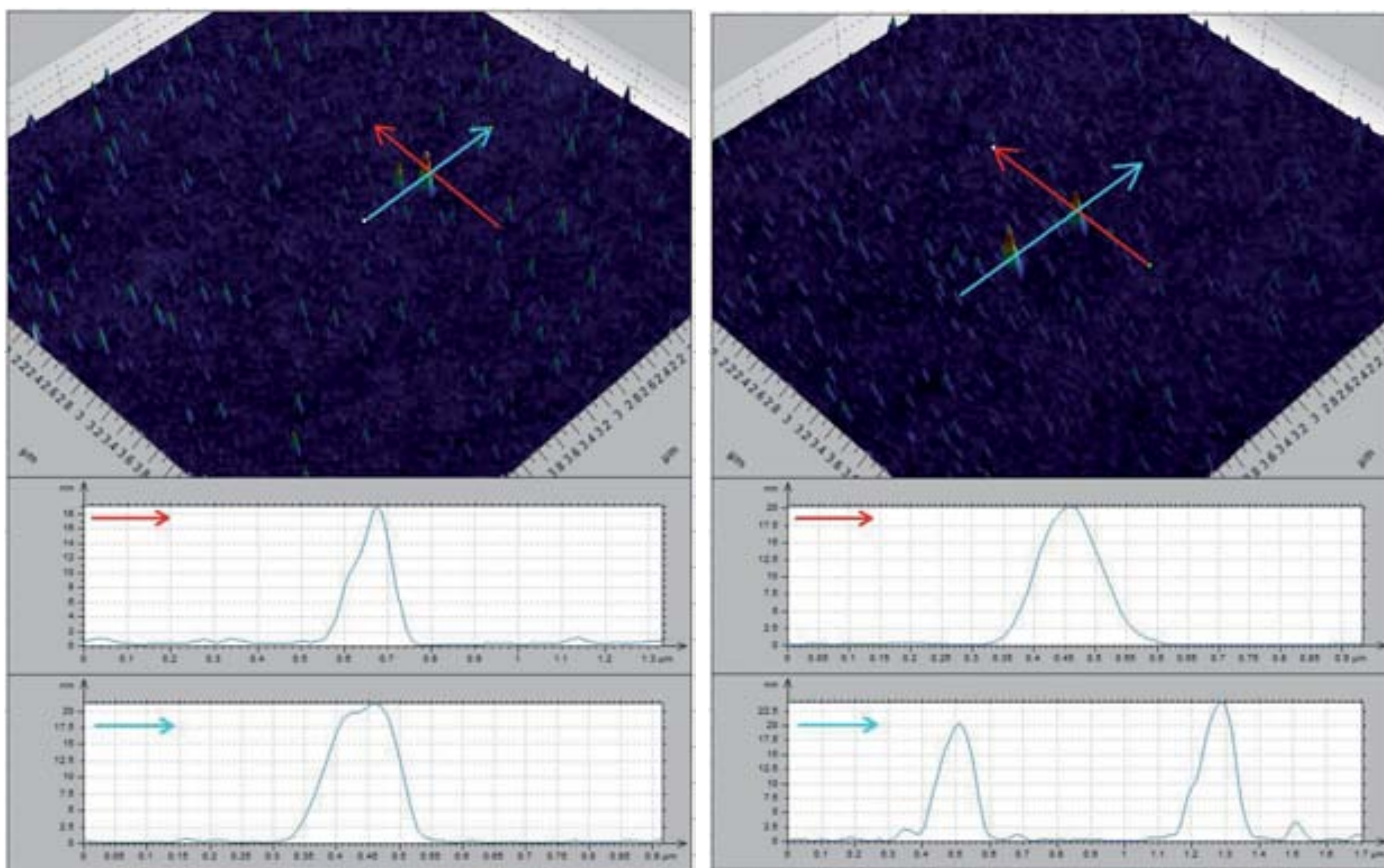

Figure 2-14 *Nanodots formed by high dosage electron beams and annealed for 500C for 4h. Left: an isolated site. Right: two sites with 750nm pitch and dosage of 1.5 pC. The substrate was STO, the counter ion was acetate.*

The manner in which a non-annealed nanoisland becomes an annealed nanodot is a complex one. For that reason, an AFM image was taken after four hours at the intermediate temperature of 500 C. This was to analyze the intermediate morphology of the nanodots after the organic components were liberated. Although at 500 C for four hours the metal constituents have not yet formed a crystal and thus the nanodot has not fully compressed, insight can be gained. The length of time at this intermediate temperature allows the PVOH, acetates, and water to move to the surface of the nanodot and into the oxygen atmosphere. Shinde et al has investigated the temperature when the LSMO phase formation starts to be 575C for a nitrate based LSMO precursor in the presence of PVOH [19]. This AFM also lends insight into the retention of the cone-like form and that all further reduction in mass comes at the expense of height lost and not width. As one can see in figure 2-14, the height of the nanodots at this stage are twenty nanometers in height and roughly 200 nm in width. Thus the decompression of the nanodot due to crystalline formation is roughly ten nanometers or half its volume. Also this leads to the conclusion that the organic components in the nanoisland were approximately 75% of the volume.

The morphology of the individual low dosage nanodots have been observed to be triangular in nature when performing e-beam lithography with the nitrate based LSMO precursor on single crystal substrates. A close-up of this formation can be seen in the AFM on the left of figure 2-15. Here the growth of the nanodot clearly has a high degree to which it has conformed to the crystal substrate. Observing the morphology of the triangular nature of the low dosage isolated nanodot signifies a higher likelihood of being single crystalline and epitaxial than an amorphous nanodot does. The angle in which the base of the triangular are oriented is parallel with the cut of the STO substrate in which they have grown. The angle of the side facets of the nanodot also hints at a non-isotropic structure, with one being steeper than the other. A metrological difficulty of obtaining the true facet angle is also seen here when using a relatively blunt AFM tip combined with the noise in the system.

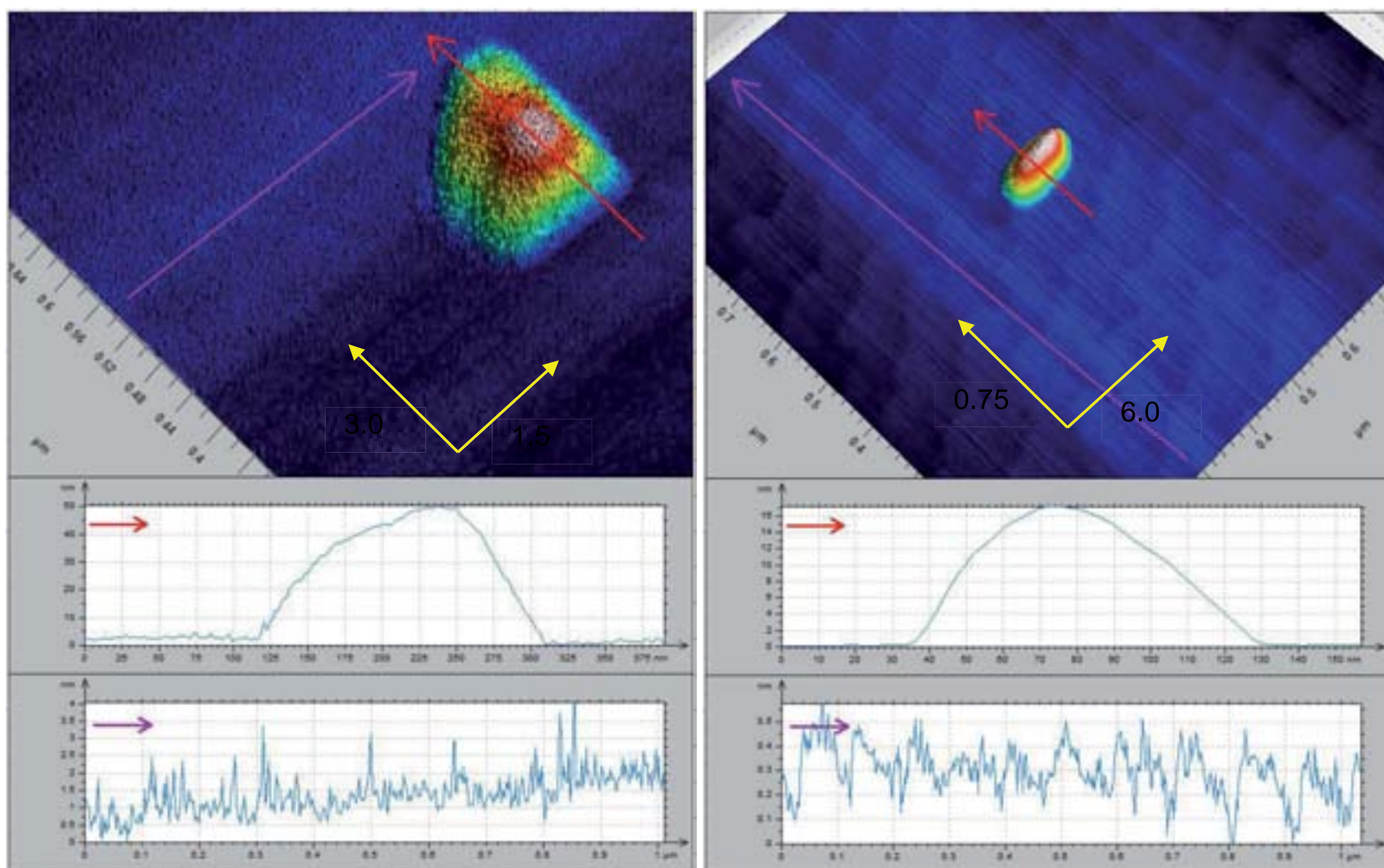

Figure 2 – 15 *Nanodots on YSZ made from a nitrate based LSMO and annealed at 900C for 4h. Left: triangular nanodot from dosage of 0.15 pC. Right: non-triangular nanodot on YSZ and substrate terraces from dosage 0.05 pC.*

On the right hand side of figure 2-15, one also observes the atomic planes of the single crystal substrate beneath the grown nanodot. The surface roughness being so low as to see the atomic planes was brought about by vigorous water cleaning. This particular nanodot was one of the smaller ones that was observed, at

90 nm in width and 16 nm in height. The triangular nature of the nanodot is not observed here and it is unclear if this is a consequence of the diminished size, however triangular nanodots were observed on YSZ.

An array of nanodots written on nitrate based LSMO with a pitch of 750 can produce a high concentration of structures on a substrate. This was demonstrated on the left of figure 2-16. Here the pitch is just below the limit of what would be considered a continuous corrugated surface or an ultra high density of isolated nanodots. On the right hand side of figure 2 -16, one sees the height dependence on dosage from a LSMO-Nt sample. The heights encountered range from 15 to 45 nm with a pitch of 1250 nm so as to insure little influence from a neighboring site but close enough to compare the full range on one AFM image. The individual dosages of the nanodots are relatively similar, only varying by a few nanocoulombs. This strong morphological susceptibility to dosage has the advantage that a specific height can be written but it has the disadvantage that any slight fluctuation to the dosage will give a wide spread to heights at a given value.

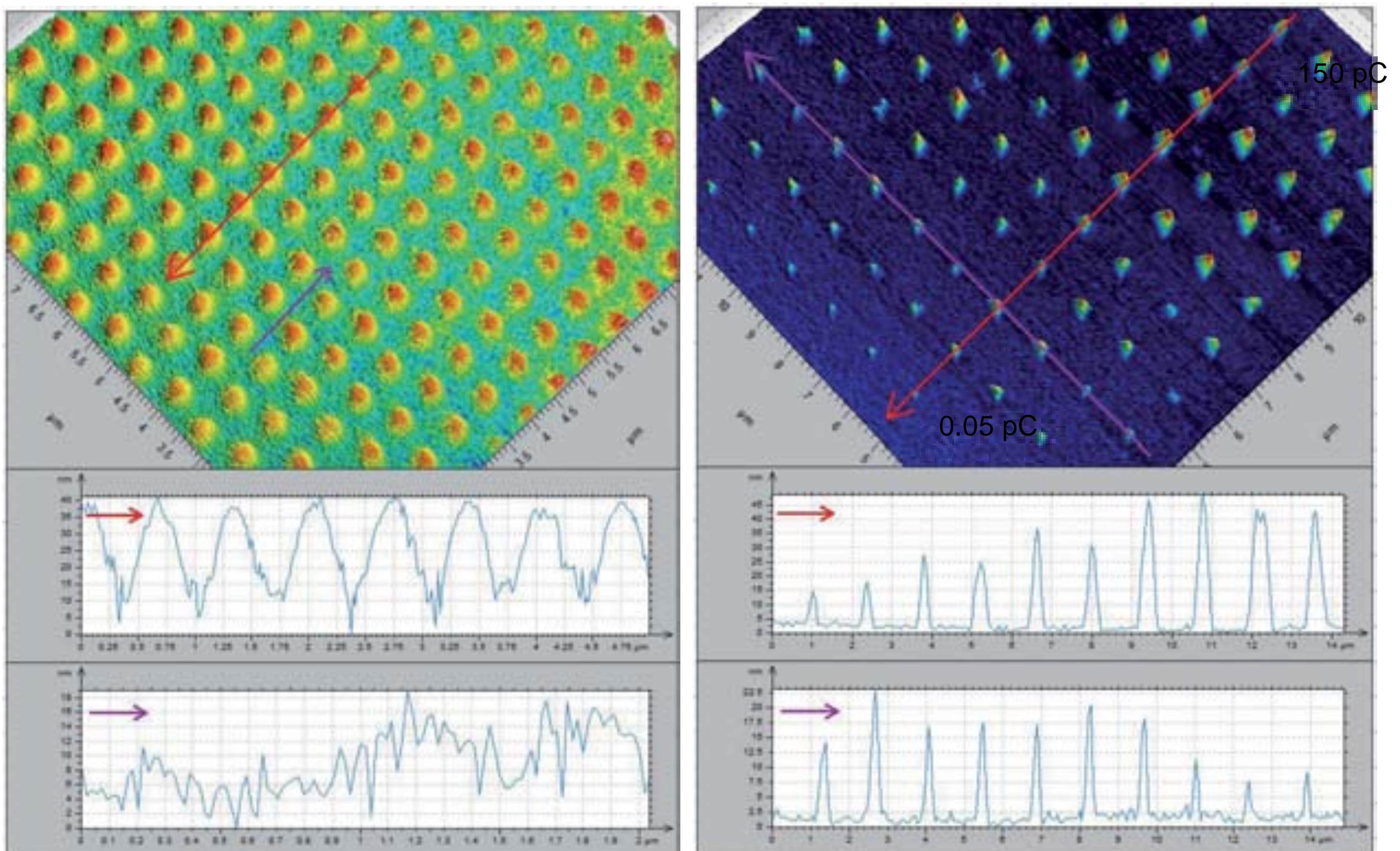

Figure 2 - 16 *Series of nanodots on STO after annealing for 900C for 4h made from 2 wt% PVOH LSMO-Nt with film thickness of 175 nm. Left: pitch of 750 nm and dosage 0.15 pC. Right: pitch of 1250 nm and dosage of 0.05 to 0.14 pC at steps of 0.01 pC.*

2.3.2 High Dosage Morphology

When the dosage increased significantly such that the aperture is open so as to give 1500 pC, the cone-like morphology changes into a far different shape. This can be seen in figure 2-17 where the sample was annealed for 4h at 500C on the left hand side and 1000C for 4h on the right hand side. Thus one can see the dimensional changes the isolated high dosage nanoisland evolves to take on. Compared to the low dosage nanodots, these high dosage ones obviously processes a greater amount of cross-linked precursor material to begin with as was noted in the images taken after washing with water. This starting configuration alters the way in which the organic components are released. Another consideration is that the composition of the nanoisland is not uniform in its density. The clearest consequence of this can be seen in the central bump which was relatively small as a nanoisland, but increased in relative size after the intermediate annealing. This central bump is observed to be one third of the total height of the isolated high dosage nanodot, whereas previous to being placed in the oven it was one sixth the total height.

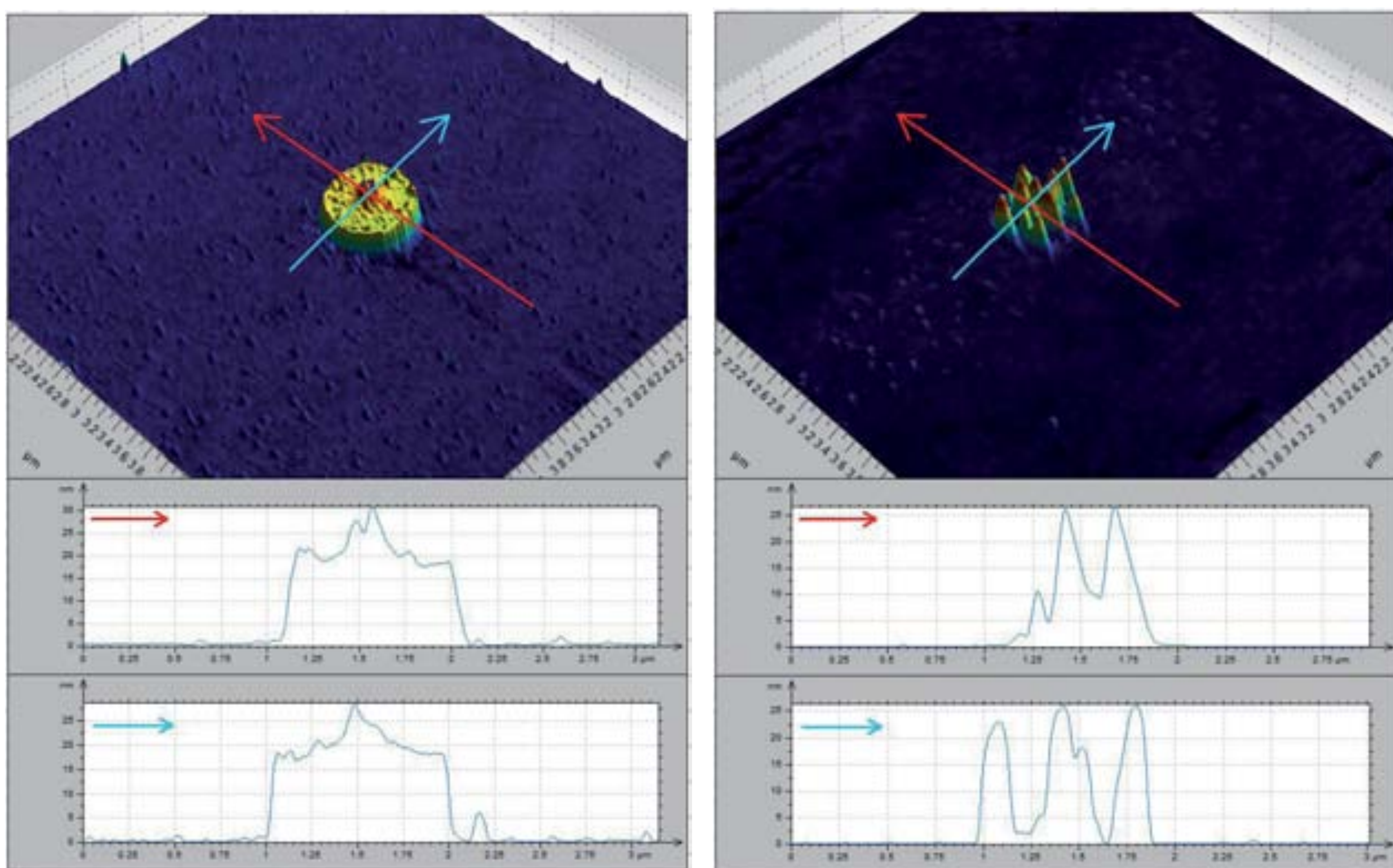

Figure 2-17 *Left: a high dosage nanodot after annealing at 500C for 4h. Right: same nanodot after 1000C for 4h. Generated by dosage of 1500 pC. The substrate was STO, the counter ion was acetate.*

The original height was 120 nm and this was reduced to 30 nm after partial annealing and to 20 nm after a complete annealing step. This result shows a similar mass loss after heating at 500C as the low dosage case, however the height here is composed largely by the central bump, and thus does not fully explain the complex dynamics at work. The plateau of the high dosage nanodot previously was 100 nm while after partial annealing falls to less than 20 nm. Concerning the width of the partial nanodot, a reduction of 250 nm was observed to reach one micrometer in width.

On left hand figure of 2-18 one sees the effect of annealing two nanodots with spacing of 750 nm at 500C for 4h. Namely the feature of the central bump for each nanodot in the case of the intermediate annealing is seen along with the same plateau as the single nanodot. Thus the fact that the two nanodots shared a common border did not alter the form found in the isolated case in a significant way. The height of the major features, as well as the width, are in line with the single intermediate nanodot. The footprint of both nanodots together is equal to slightly more than the width of two halves of an individual nanodot plus the pitch, and thus it is concluded that there was a small but noticeable overlapping effect of having written the two nanodots so close together. Another feature previously not seen in the intermediate isolated nanodot case was that of a decreased height on the plateau between the two nanodots. This is symptomatic of another local density inhomogeneity due to a reduced local dosage or it could be a consequence of the fact that the two nanodots are being reduced in width relative to their centers.

On the right hand side of figure 2-18, it is noted that intermediate nanodot has now lost all its form except for the outline of precursor material that it previously had. Here one notices that that the material that previously was continuous prior to high temperature annealing has devolved into several of smaller nanodots. The main reason why the continuous proto-nanodot cannot form a fully crystalline large nanostructure is due to energy considerations. Therein the energy to form an epitaxial nanodot with such a footprint would be highly energetically unfavorable while a system of several smaller nanodots is favorable. One can garner that the method in which to grow controlled isolated nanodots using a series of high dosage dots is not advisable.

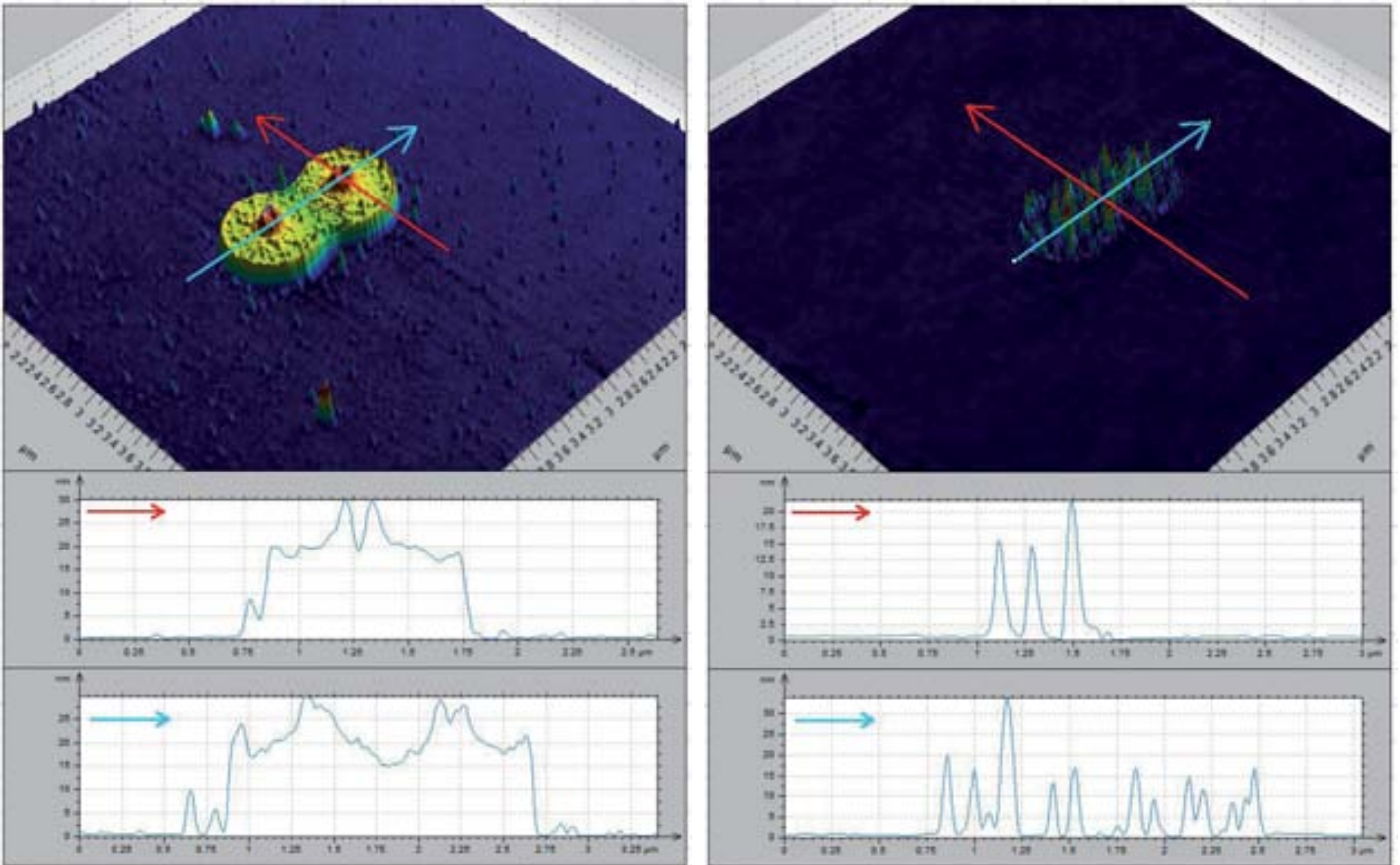

Figure 2-18 *Left: two high dosage nanodots with pitch 750 nm after annealing at 500C for 4h. Right: same nanodot after 1000C for 4h. Generated by dosage of 1500 pC. The substrate was STO, the counter ion was acetate.*

Of course, the interesting byproduct of writing these high dosage nanodots in close formation is spontaneous formation of nanowires. This can be clearly seen to be the case in figure 2-19 where nanodots are written in a three by three configuration and small nanowires have grown to the side. More on the growth of nanowires is discussed in the next chapter, however suffice to say that the mechanism for their growth is also quite complex. One hypothesis is that the high dosage nanodots possess already formed nanocrystals prior to annealing, therein this would allow them to act as seeds for the nanowire growth in the surrounding unassembled material.

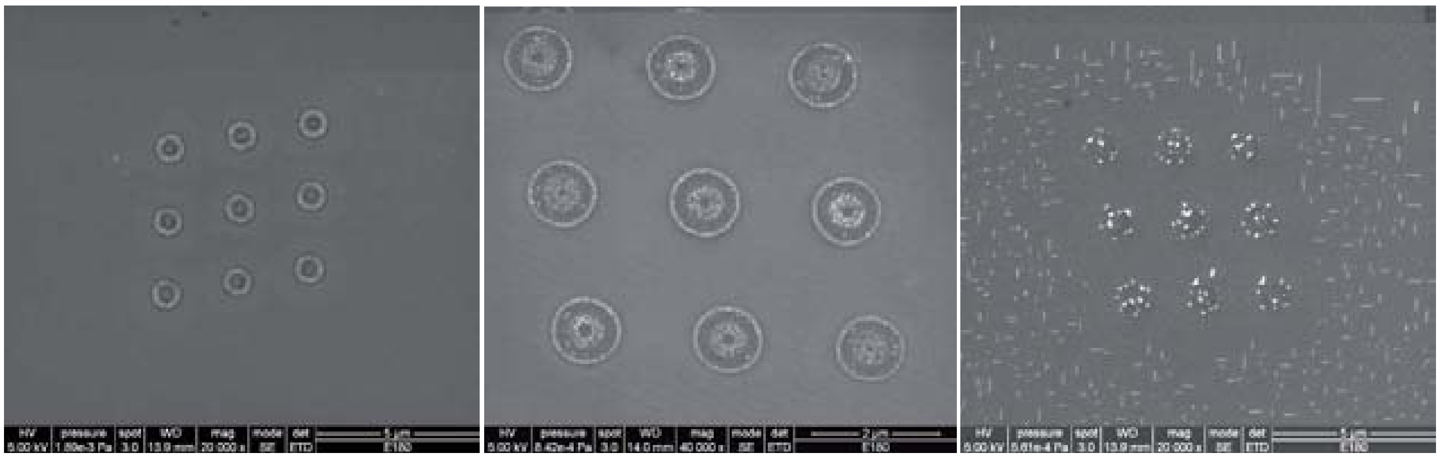

Figure 2- 19 *Nanodot array with pitch of 2000 nm and dosage 20 pC on nitrate based LSMO after four hours annealing at various temperatures. Left: nanodots after 600C. Center: nanodots after 800C. Right: nanodots after 1000C.*

2.3.3 TEM Results for Structures Grown on LAO

In order to understand the elemental composition and crystalline structure of the annealed nanodots, one must go beyond simple morphological measurements. To gain a deeper understanding of the nanodots, one needs to observe it with a TEM and EELS. This allows for the precise confirmation of the elemental composition inside the nanodot as well as determining the degree of epitaxy on the substrate. In figure 2-20 one can see the AFM image of a single nanodot which belonged to an array. This nanodot is clearly triangular in nature and is around 35 nm in height and 100 nm in length along the short side. Its sharply angled morphology was thought to be indicative of epitaxial growth on the substrate, thus it was an ideal candidate for inspection with high resolution TEM. The sample itself was cut with a low energy FIB and then polished until electron transparent.

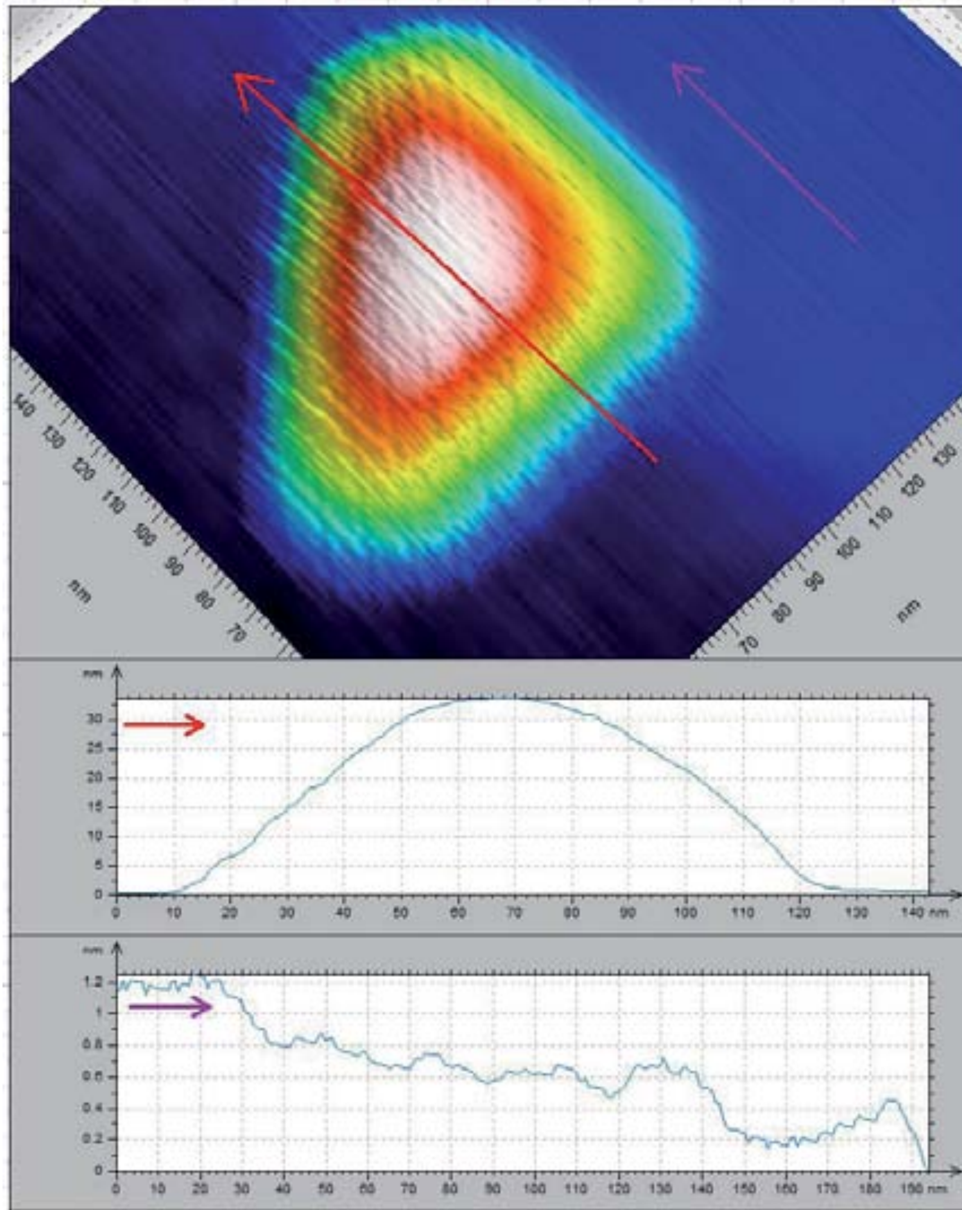

Figure 2-20 *Annealed nanodot on LAO showing anisotropic triangular nature suitable for FIB lamella fabrication. Triangular nanodots made from a nitrate based LSMO and annealed at 1000C for 4h. Triangular nanodot from dosage of 0.15 pC.*

This crystalline nature of the nanodot was successfully observed with the TEM even though the majority of the nanodot was made amorphous probably due to the cutting process. The part which was spared this amorphization was the very edge of the nanodot as can be seen in figure 2- 21. From this perfectly intact sliver of nanodot, it was confirmed that the nanodot was single-crystalline. On this spot an EELS linescan was performed to confirm the presence of Mn and La. Strontium was not one of the elements which was possible to observe due to the low voltage used to eject the electrons.

The result of the electron energy loss spectroscopy was that lanthanum was present however manganese was not. This was not a wholly unexpected result due to other reported work showing a migration of manganese on single crystal substrates [20]. Although the reports had shown that manganese was present however below the nanodot as either a film or as an inclusion. It was reported La/Sr oxide nanodots formed spontaneously on a LSMO thin film which was prepared by a chemical route on STO. These oxide nanodots were thought to form due to the cooperative effect involving the minimization of the elastic strain energy and a thermodynamic instability of the LSMO phase [21]. LSMO films thickness has also been reported to be a dependent variable as to whether La/Sr oxide nanodots form at the film substrate interface or as outcroppings [22]. The presence of any manganese at any location on the lamella was not detected. This indicated that either there was no manganese in the precursor when spin coated or that at some point in the lithography process, the manganese had disappeared. The likelihood that no manganese was present in the spin coated film is remote due to thin films using the same precursor being made and LSMO being detected by x-ray analysis.

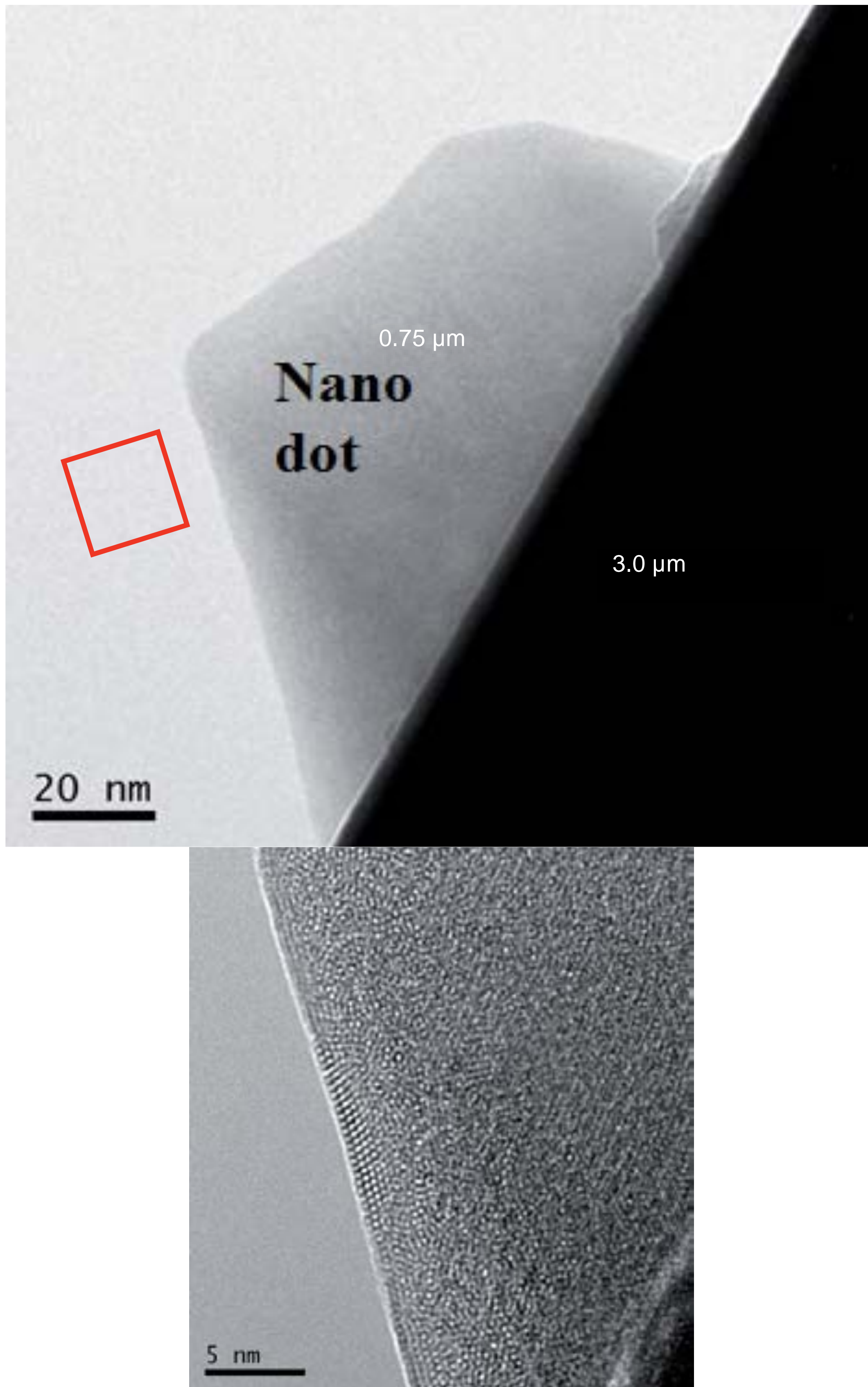

Figure 2- 21 *Left: Overview of nanodot on substrate. Right: Zoom of edge of nanodots showing amorphous and crystalline parts. Triangular nanodots made from LSMO-Nt on LAO and annealed at 1000C for 4h. Dosage was 0.15 pC.*

2.3.4 TEM Results on YSZ

The first TEM lamella that was made for the project was on LAO. One of possible explanations as to where the manganese disappeared to was into the LAO substrate. This was thought to have occurred due to the low degree of lattice mismatch between the LAO substrate and the LSMO crystal [23]. This interface would allow for an easy migration of metal constituents in a high mobility environment such as the conditions used for annealing. Thus, the manganese could have migrated into the LAO substrate, remaining undetected due to their small absolute amount, thereby leaving the oxide nanodot depleted. Hence, the solution to this envisioned migration was to grow the nanodot on a substrate with a high lattice mismatch. This would not permit the migration of manganese away from the nanodot and therefore leave the nanodot with the original ratio of metals, forming LSMO instead of LSO.

In figure 2-22 one can observe a series of nanodots on the left which were cut out of the YSZ substrate to form the lamella seen on the right. One notices on the left hand side the elongation of the nanodots which stems from the substrate not being perfectly orthogonal to the beam coupled with astigmatism. One can see two nanodots visible in the cross sectional view of the lamella. It was hoped that the this lamella would have several thinned LSMO nanodots which would be visible to a TEM. As a side note, making a TEM lamella on YSZ substrates is a difficult task due to surface charging and that it requires a much larger amount of gold to be deposited onto the sample than a LAO or STO substrate. This large amount of gold can be seen in figure 2-22.

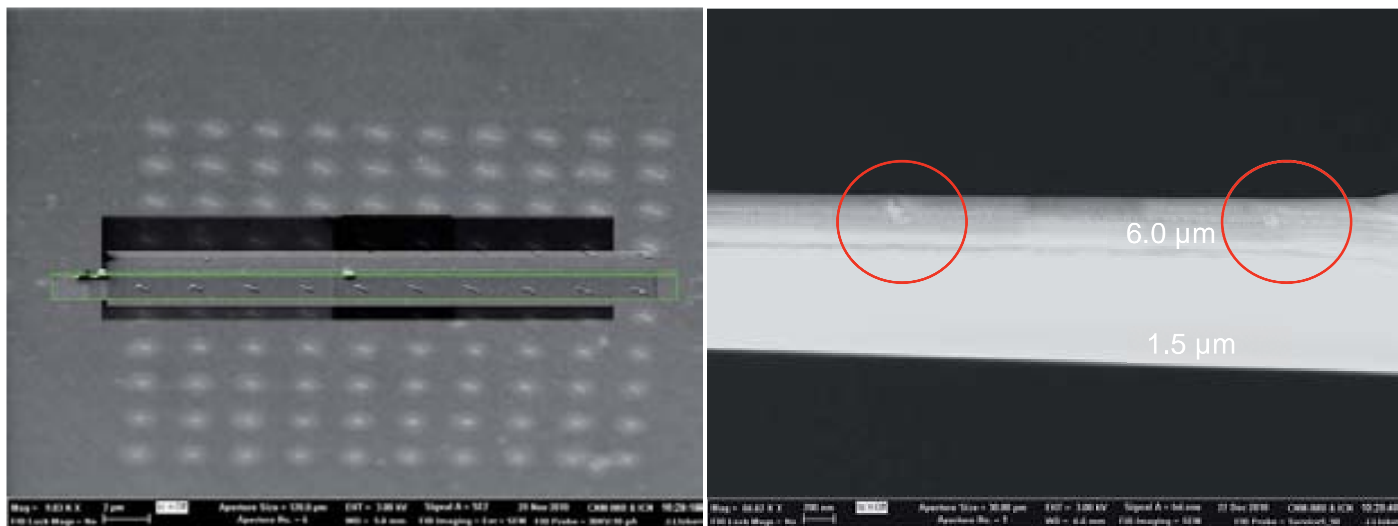

Figure 2 - 22 *Left: a series of nanodots written onto YSZ. Right: a thinned lamella for TEM inspection showing two nanodots. Elliptical nanodots made from a nitrate based LSMO and annealed at 1000C for 4h. Dosage of 0.15 pC.*

In figure 2 - 23, images generated with the TEM of a nanodot written on YSZ are visible. On the left, one can observe the gold surrounding the epitaxially grown nanodot and the facet angles of the direction it grew. On the right, a close-up of the interface between substrate and nanodot is displayed showing epitaxy. On the left hand side of figure 2-24, the left hand Fourier transform of the crystal on YSZ is seen along with the numerical values of the atomic planes. On the right of figure 2-24, the Fourier transform of the nanodot grown on LAO is also seen and its atomic planes can be compared to that grown on YSZ. One can see that it appears that the crystals are different due to their non-similar atomic plane spacings. The reason a ring is visible in the Fourier transform on the nanodot grown on LAO is due to a high amount of amorphization.

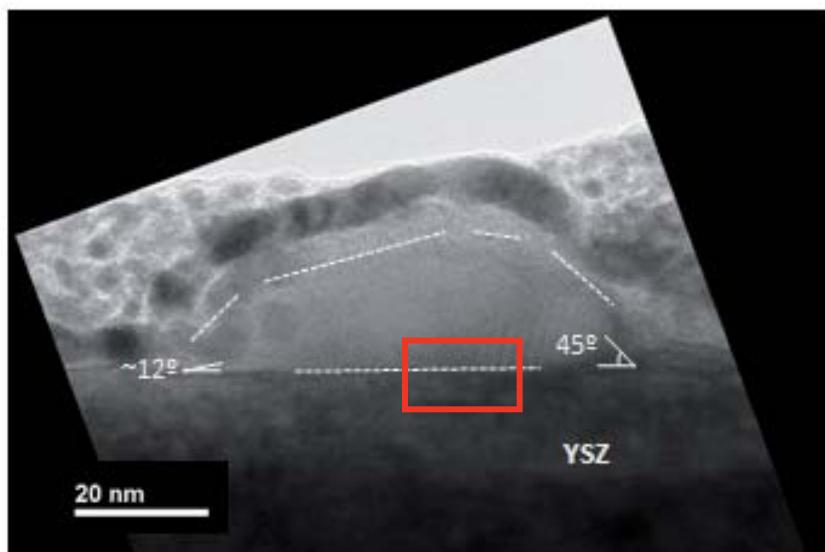

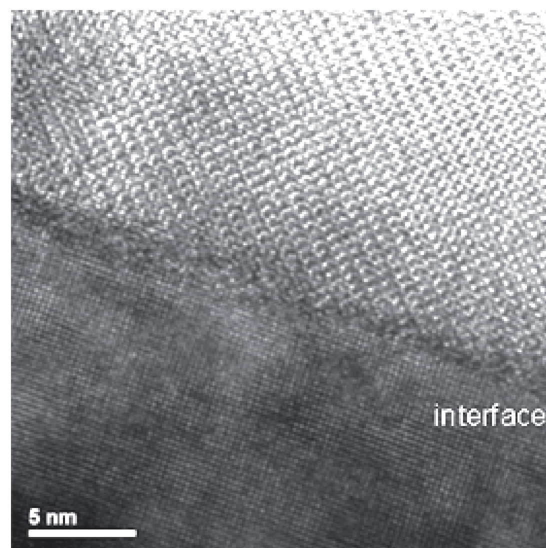

Figure 2-23 *Left: low resolution TEM image of same nanodot in figure 2-22. Right: high resolution zoom of interface.*

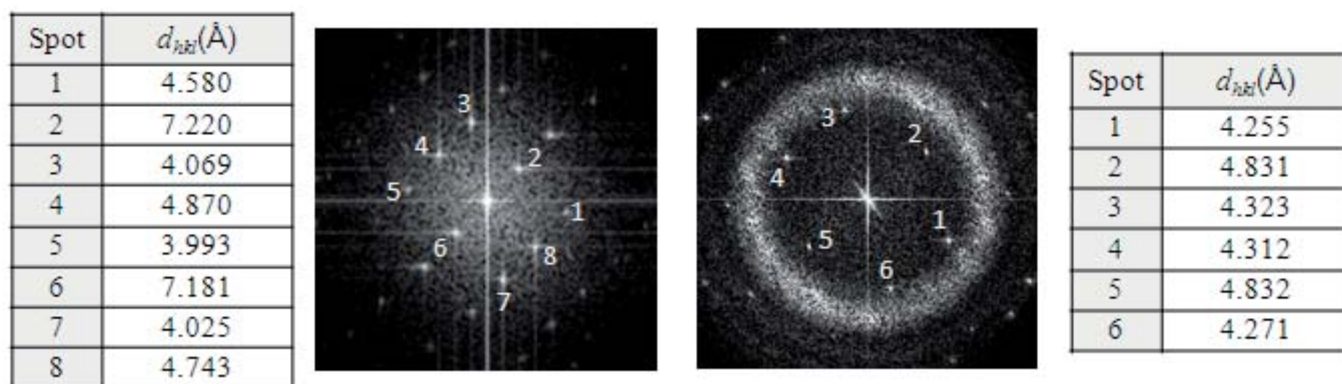

Spot	d_{hkl}(Å)
1	4.580
2	7.220
3	4.069
4	4.870
5	3.993
6	7.181
7	4.025
8	4.743

Spot	d_{hkl}(Å)
1	4.255
2	4.831
3	4.323
4	4.312
5	4.832
6	4.271

Figure 2–24 *Left: Fourier transform of crystal showing atomic planes for the nanodot on YSZ seen in figure 2-22. Right: Fourier transform of crystal showing atomic planes for the nanodot on LAO seen in figure 2-21.*

An EELS linescan of the interface between the YSZ and the nanodot grown on it was performed as see in figure 2-25. It shows the elemental presence at two different locations, namely on the nanodot at low and high energies, and the interface of the YSZ substrate. It shows characteristic peaks for oxygen and lanthanum but not manganese in the nanodot and a weak signal from strontium. This elemental detection from EELS on the nanodot grown on LAO was similar to that grown on YSZ. The absence of manganese from the both nanodots grown on LAO and YSZ indicate that the generated nanostructures were not LSMO, rather a lanthanum strontium oxide with an unknown unit cell.

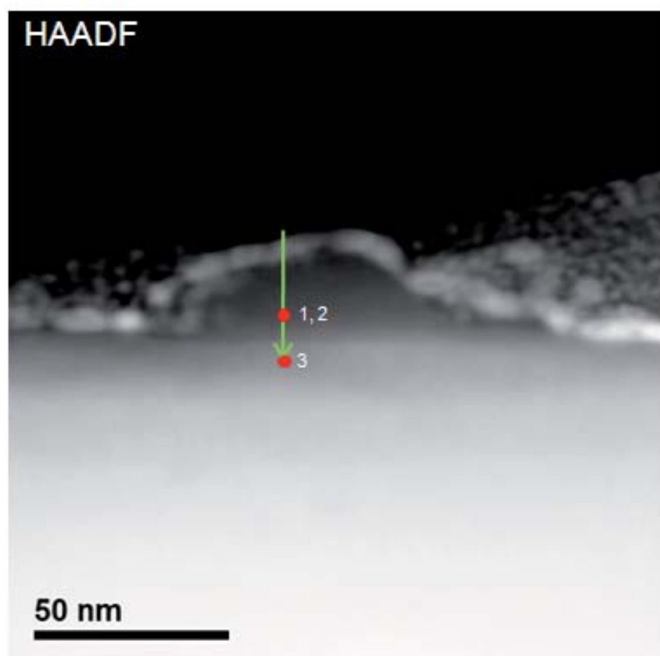

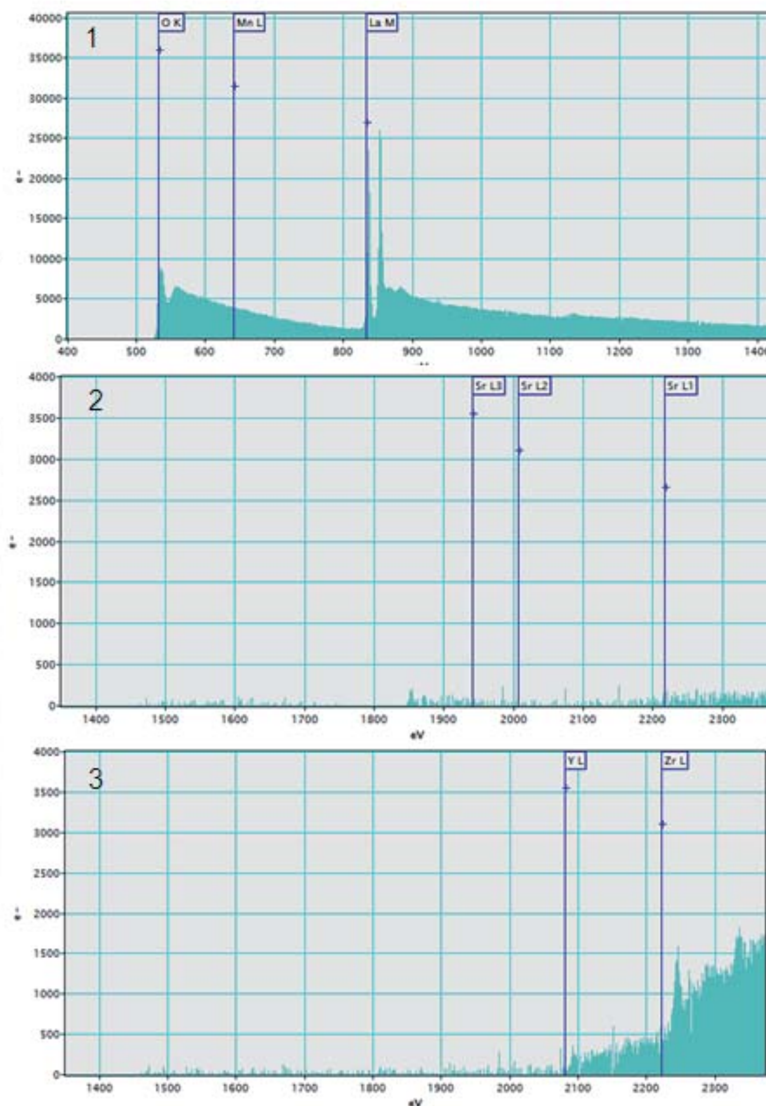

Figure 2-25 *Left: Annular dark field image of nanodot seen in figure 2-22 showing direction of EELS linescan. Right: EELS linescan results showing the elements present at various position.*

2.4 Applicability to Other Oxides

The results of performing electron beam lithography on LSMO based films has been described herein. However, this does not disclude the usage of other metal organics or other stoichiometries. The underlying mechanism for this procedure is the presence of PVOH in an aqueous solution with metal salts. Thus the film is polymerizable locally by electron beam and water developable regardless of the specifics of the metal used in the precursor. This allows for the metal to act as a spectator in the electron beam lithography process until the annealing step when the nanostructure crystallizes. Theoretically, one should be able to include any number or nitrate or acetate metal salts into the aqueous PVOH solution, radiate, develop, anneal, and obtain nanostructure arrays of the original stoichiometry. However, as has been noted here, the process is more

complex than that simple interpretation. As with the disappearance of manganese, perhaps other species could be volatile and thus susceptible to stoichiometric changes.

The robustness of this procedure was demonstrated when making nanoislands from a nitrate based strontium titanate precursor via electron beam and then annealing them. The rational in making strontium titanate arrays of nanodots was due to the high centrosymmetric paraelectric nature at room temperature. Besides strontium titanate, there exists a multitude of functional oxides which are of interest to researchers. Typically to obtain nanostructures for these oxides, one must execute a series of complicated lithography steps to achieve final structures. The advantage of starting with an inexpensive chemical solution method of deposition and then direct writing nanostructures is clear. With the continued pursuit of new multiferroics, a cheap platform in which nanostructures are fabricated could be of interest.

The morphology of nanoislands produced from electron dosages comparable to the LSMO precursor are shown in figure 2-26. They show a morphological dependence to dosage similar to the nanodots produced from the LSMO precursor. Also the consistency in height and width is on par with the aforementioned manganite system. This is an important demonstration of the concept with regards to locally polymerizing any combination of constituents and then removing the remaining film. The strontium titanate system required two orders of magnitude more electron dosage than the LSMO case. This is thought to stem from the reduction in the weight percent of nitrates in the precursor as compared to LSMO. This in turn reduces the sensitivity of the precursor film to being locally polymerized by electrons due to a simple lack of available nitrates.

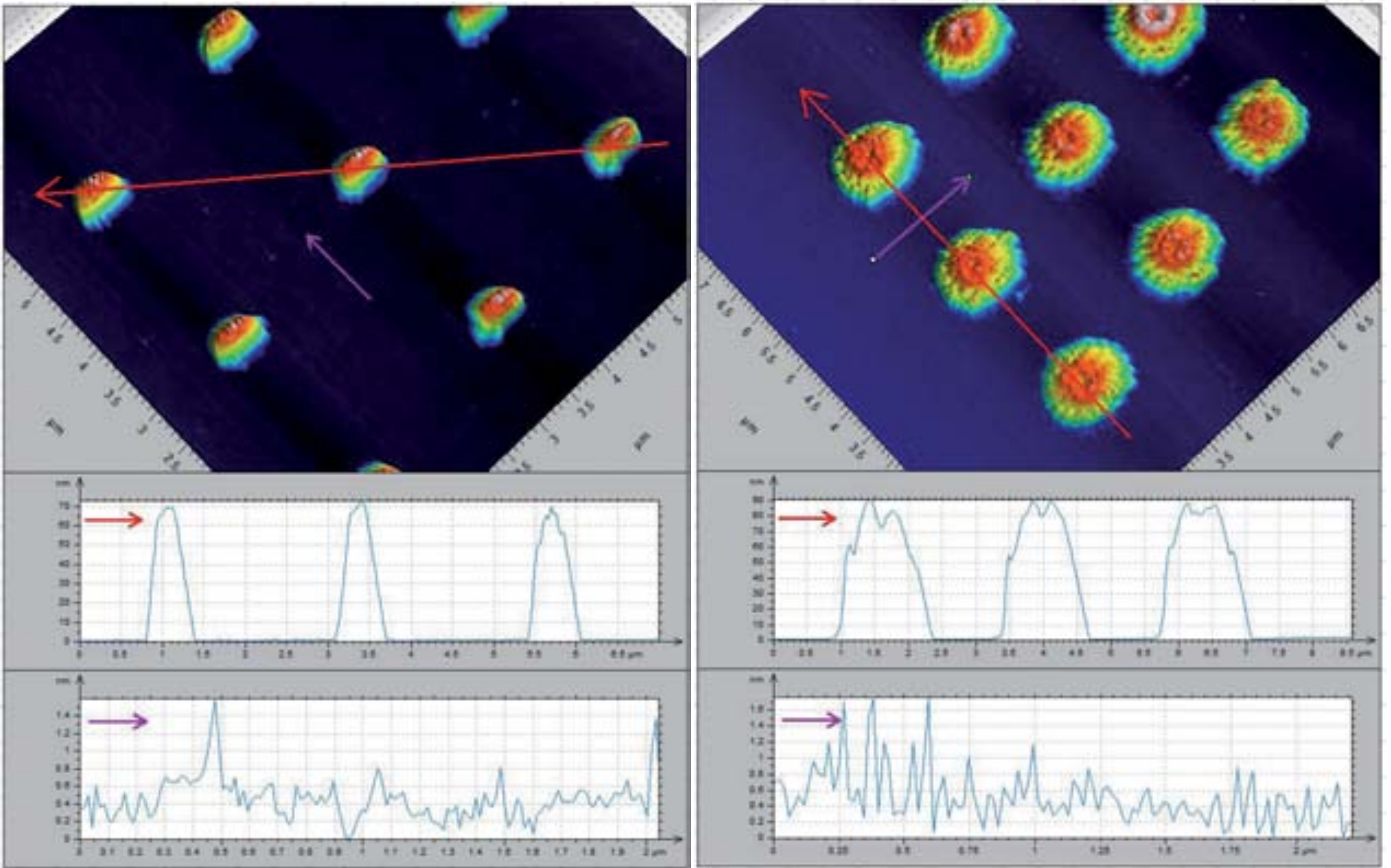

Figure 2- 26 *Strontium titanate array of nanoislands on LAO substrate after water cleaning. Left: dosage of 150 pC. Right: dosage of 750 pC.*

The strontium titanate nanodots were also observed to form crystals after annealing. This can be seen in figure 2- 27 where they were noted to have reduced in size considerable from the left hand image in figure 2-26. A closer inspection of one of the strontium titanate nanodots on the right hand side in figure 2-27 shows non-triangular final morphology. Most likely this nanodot is polycrystalline due to an excess amount of starting material. If the dosage was optimized to reduce the nanoisland down to its smallest size, there stands a high likelihood that single crystal nanodots could be produced. However, that effort was beyond the scope of this study and was simply fabricated as a proof-of-concept.

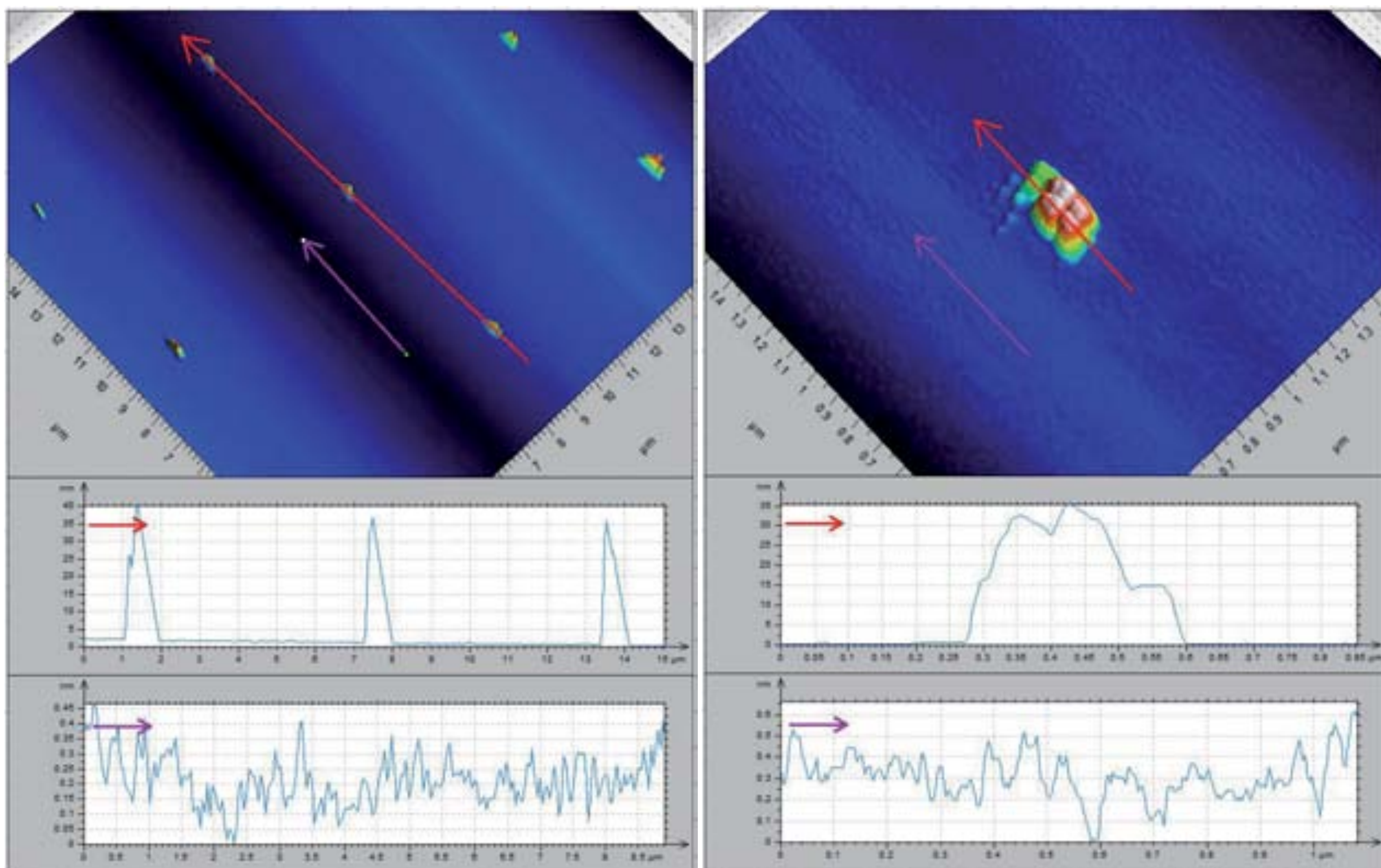

Figure 2- 27 *Left: same strontium titanate nanodots on the left hand side of figure 2-26 after annealing for 4h at 1000C. Right: zoom of area.*

2.5 Fabrication Difficulties

There are several difficulties in the fabrication of nanodots on SCS using the LSMO precursor by EBL. One of the most poorly understood is the presence of outcroppings in the film if left in ambient conditions for days. The observance of these outcroppings motivated the timely manner in which radiation, cleaning, as well as annealing were performed. Typically this would consists of reducing the time the recently spin coated was in ambient conditions by keeping the film under nitrogen gas and then in vacuum once in the SEM. Then immediately after confirming that film was correctly written with an optical microscope, the film would be developed in water. It was then confirmed immediately with the optical microscope that the development of the nanodots was successful. Then the sample was rushed to the tube furnace and annealed. When this process was interrupted for many days, inhomogeneities would be observed as in figure 2- 28.

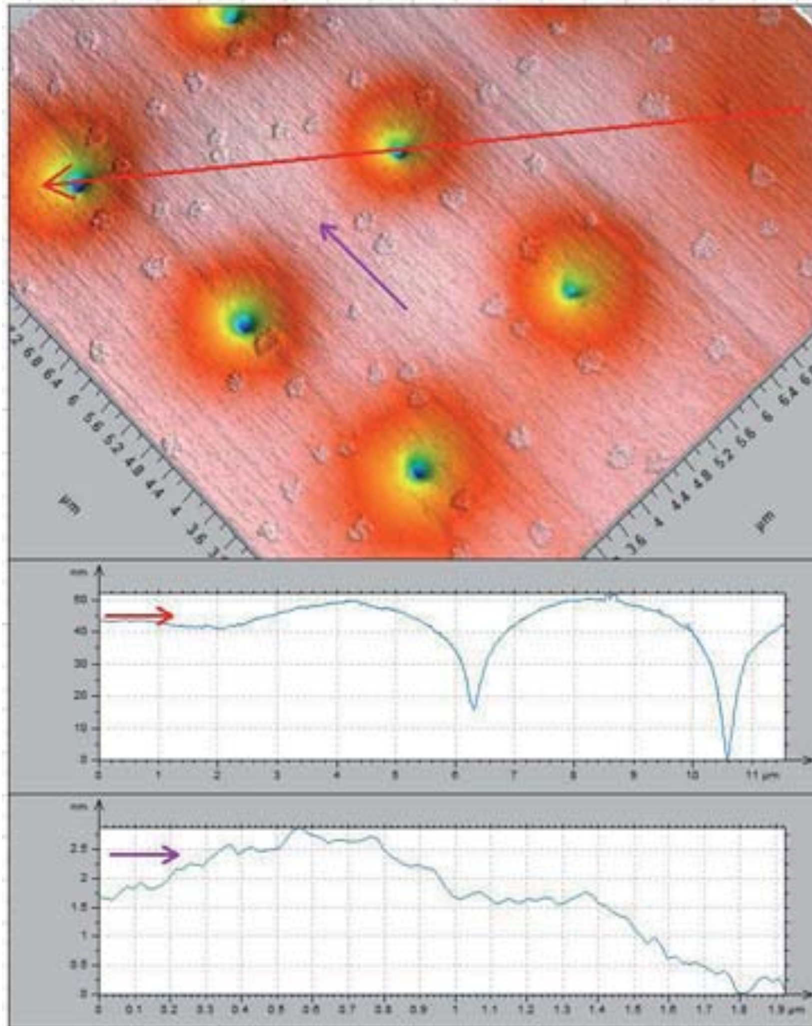

Figure 2 -28 *Spontaneous outcroppings form on nitrate based LSMO film after radiation and several days in ambient conditions.*

Another hurdle when fabricating nanodot arrays is the loose attachment of the nanoislands to the substrate. This loose attachment can be observed when cleaning vigorously in the development stage. What is observed is the spontaneous absence of nanoislands on a highly cleaned substrate. The relative attachment of the nanodots to the substrate is also dependent on the substrate used in the lithography process. All substrates barring YSZ can withstand thirty seconds of gentle agitation in water and even sonication for a short period of time, whereas nanodots written on YSZ may only be agitated for less than ten seconds. This dislodging of nanodots from the surface can be seen clearly in figure 2-29 where a section of an array is no longer attached. This variability in how much water agitation can be applied to the samples does not have a clear explanation. However, a balance between the amount of dislodging of nanoislands and the cleanliness of the substrate must be struck.

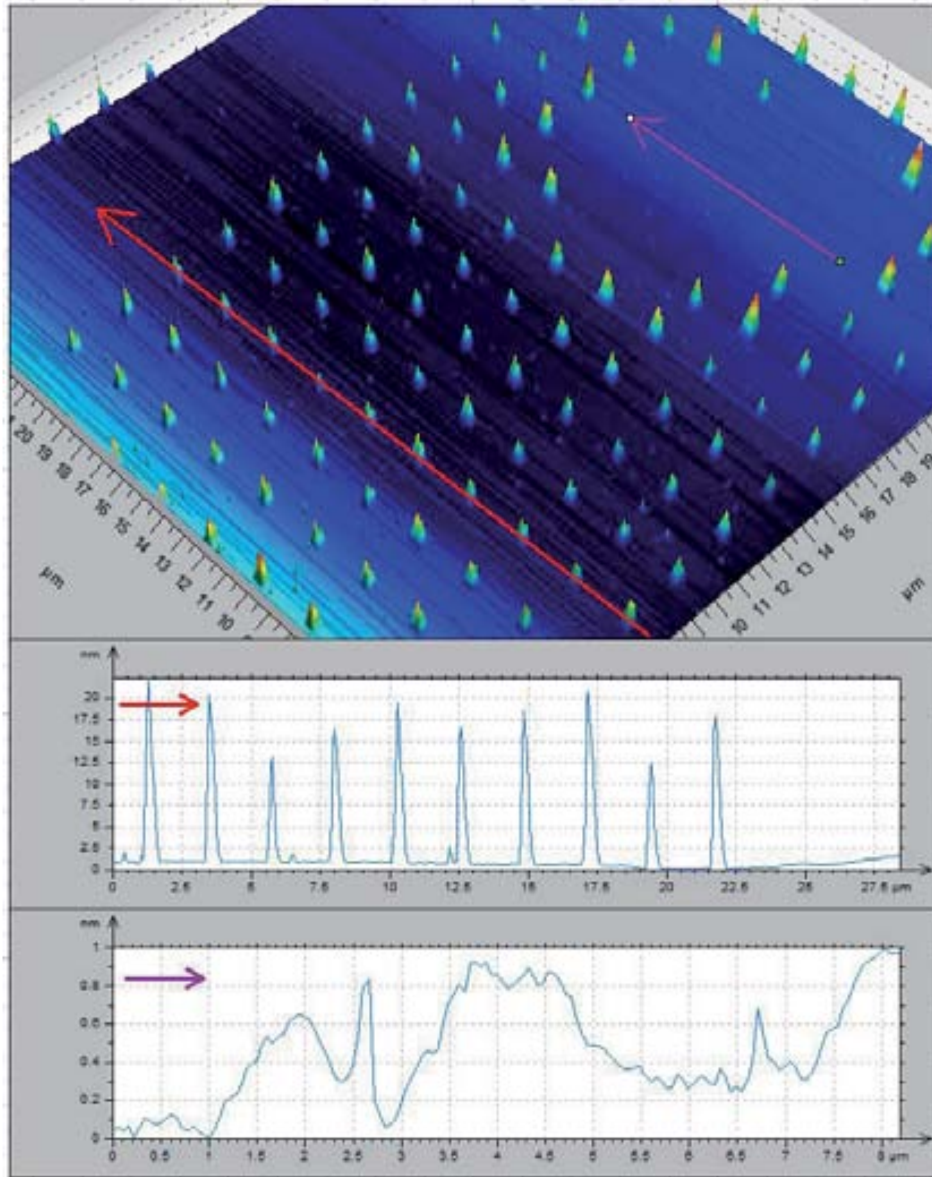

Figure 2-29 *Dislodged nanodots were observed due to a vigorous water development stage of LSMO-Nt on STO.*

Insufficient cleaning of the substrate can also have grave ramifications on the final goal of isolated single crystalline nanodots. This can lead to a sample being surrounded by unintended polycrystalline material, thus negating the nanodot's isolation. This excess material remains on the substrate directly as a result of an insufficient developing step. The deficiency primary lies with a short contact time with water or a stationary submersion into the developer. The detrimental affect of this short coming is seen in figure 2-30. Here one sees a relatively thick layer of non-purposeful poly-crystalline material encompassing the nanodot.

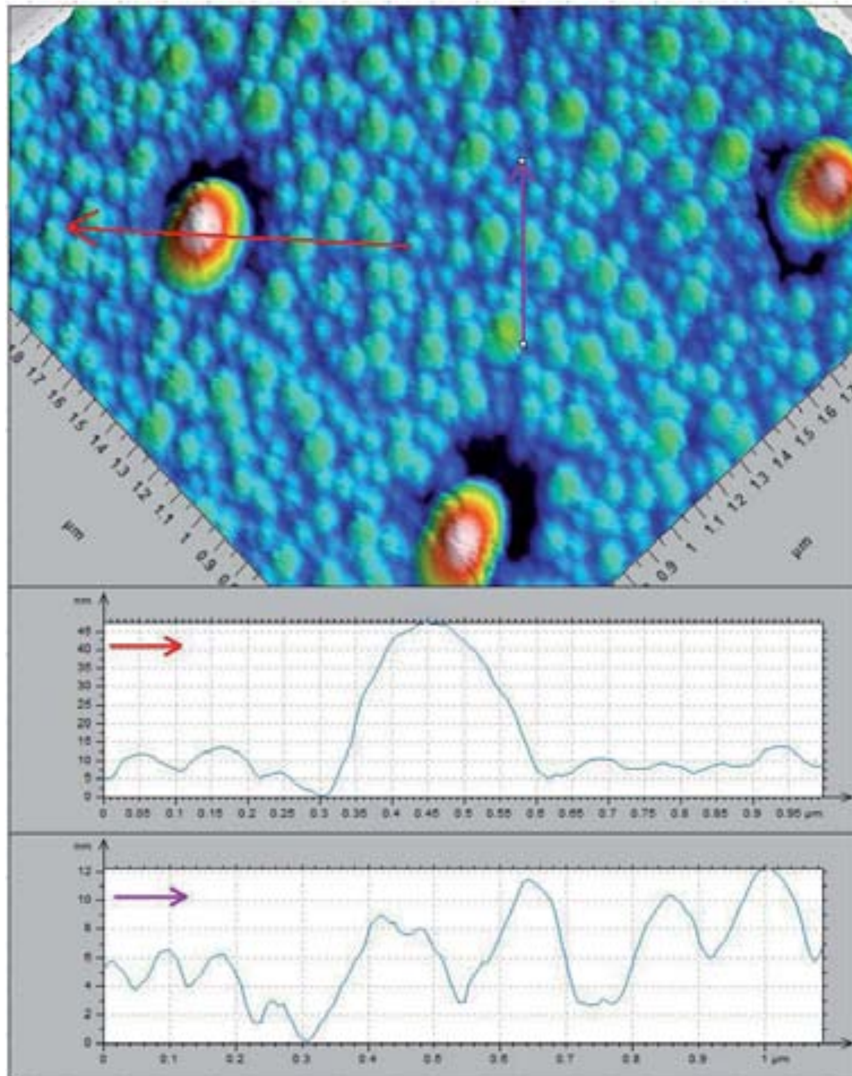

Figure 2-30 *Example of insufficient cleaning produces aberrant nanocrystal growth along the substrate.*

Another difficulty when writing on highly insulating substrates with electrons is the local charging. The effects of surface charging can be quite wide ranging, however one that was highly prevalent on YSZ substrates can be seen in figure 2-31. There one can see that the time scale for individual nanodots was such that after an initial polymerization at the intended site, the beam drifted away from center. The drifted beam polymerized to a lesser extent the surrounding film in a linear fashion, thus producing the anisotropic nanodots seen here. This beam drift has a tendency to move in the direction away from the other recently written parts of the sample. Thus, if the beam is writing a one millimeter sized array in hundred micrometer increments, and doing this in a top-to-down, left-to-right way, then the bottom right array will have see the greatest surrounding surface charging and will push the electron beam away from the center. This fabrication difficulty can be overcome by writing the hundred micrometer sections in a random-walk fashion, thus eliminating charge build-up in any particular direction. Another solution is to wait an extra allotted time between writing sections so as to allow for excess charge to be removed by atmospheric gases.

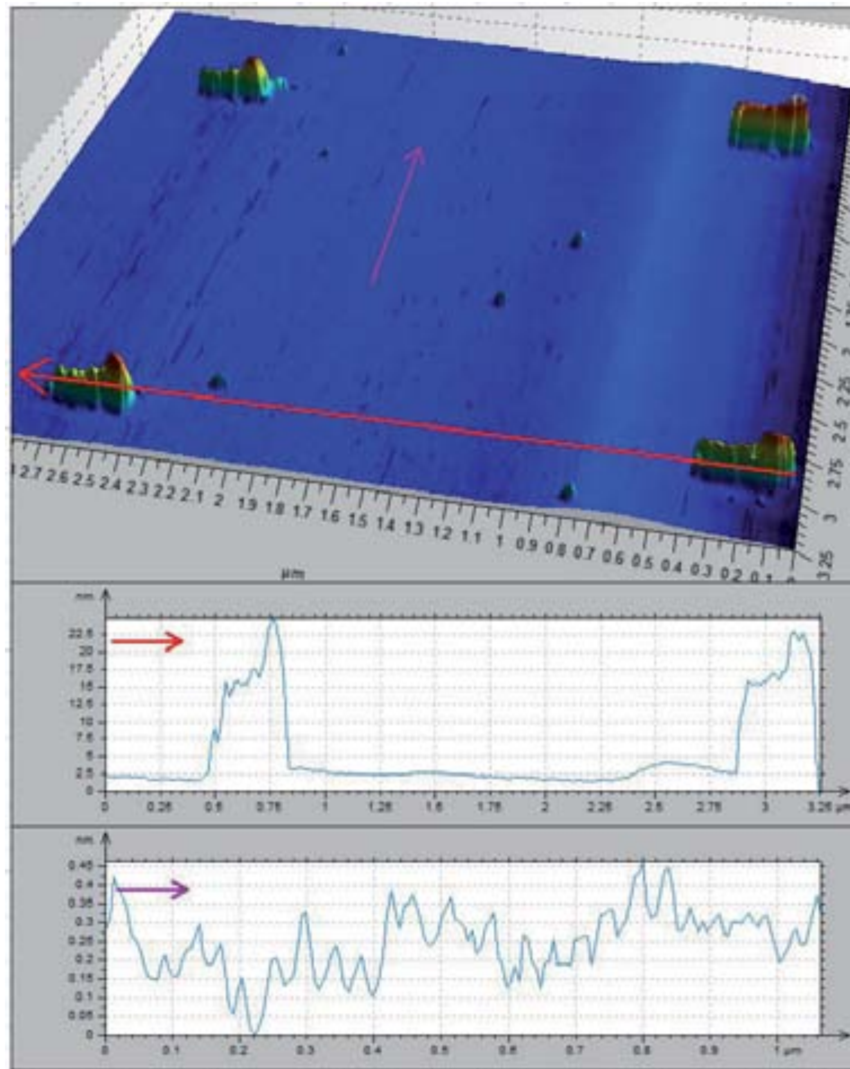

Figure 2-31 *The effect of charge build up alters the final morphology of nanodots on YSZ.*

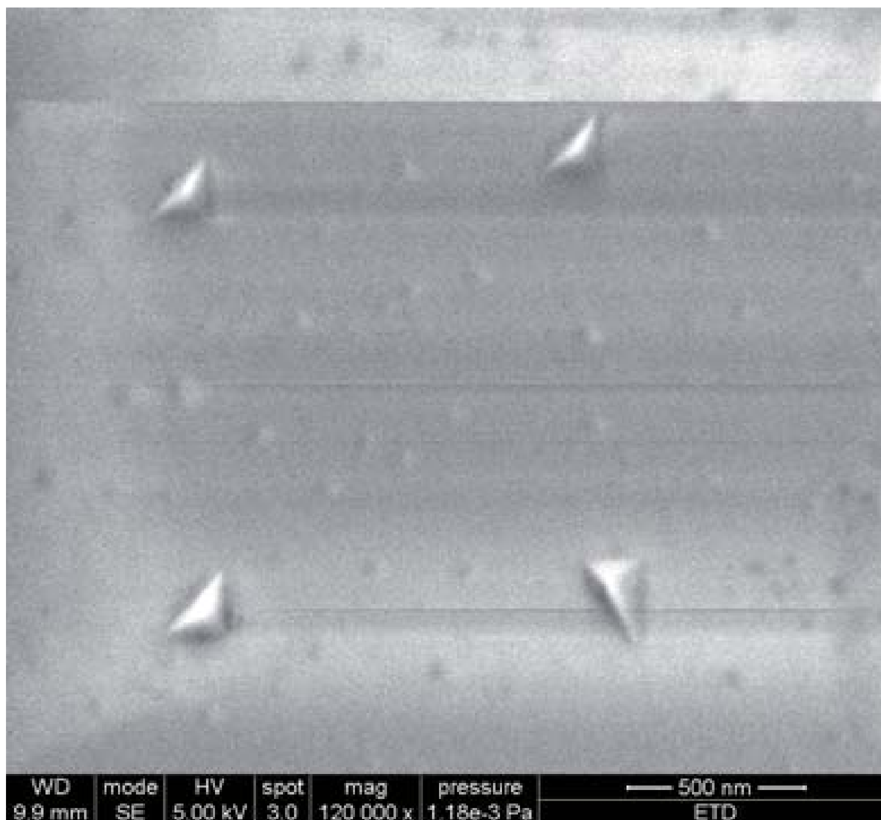

Figure 2-32 *Four nanodots with differing triangular orientations from nitrate based LSMO on STO after annealing for 4h at 1000C.*

Another difficulty in the fabrication of the arrays of nanodots is controlling their orientations. An example of this is seen in figure 2-32 where three of the triangular shaped nanodots are facing one direction, while the other is facing the opposite direction. All the short sides of the triangles share the same orientation, however the long hypotenuse sides are orthogonal to each other. The functional properties of these nanodots would be slightly altered due to this lack of orientational symmetry. This lack of control for the triangular orientation is due to the energy for being in one direction is the same as the other. Thus, half the triangles have one orientation, and half the other. It is unknown if a procedural modification exists which could align all the nanodots to the same direction, but it is thought that this would very challenging.

2.6 Specific Conclusions

As it has been shown, nano sized crystals can be grown in an ordered pattern on insulating single crystal substrates by way of electron beam radiation onto LSMO precursors. This method to generate nanocrystals leverages the economics of solution based deposition with the precision of writing with electrons. The applications for this technique are many fold due to the wide variety of functional properties oxides may have.

One of them is colossal magnetoresistance which could be used in next generation magnetic memory devices. The general procedure is that a spin coated thin film precursor is then locally radiated yielding nanocavities, the sample is then developed with water thus leaving only nanoislands where exposed, finally the sample is annealed at high temperature for many hours thus removing the organic components and thereby revealing nanodots by crystallization. In order to nucleate the oxide crystal, the sample is annealed in an oxygen furnace.

The immediate result of radiating with focused electrons onto the thin precursor film, is the generation of nanocavities. These nanocavities have depths which are dependent on dosage in the low dosage regime but reach a maximum depth at higher dosages. Another consequence of increasing the dosage is the walls of the nanocavity begin to become non-linear. It is also observed that there exists a small central feature which exists at all dosages for the acetate based precursor, while remaining only in the nitrate based precursor at low dosages. At high dosages, for the nitrate based precursor the bottom of the nanocavity would flatten out on conductive STO substrates while on YSZ substrates the structure would become highly elliptical. The effect of applying focused electrons to multiple sites which are very close together is that a superposition of dosage is observed.

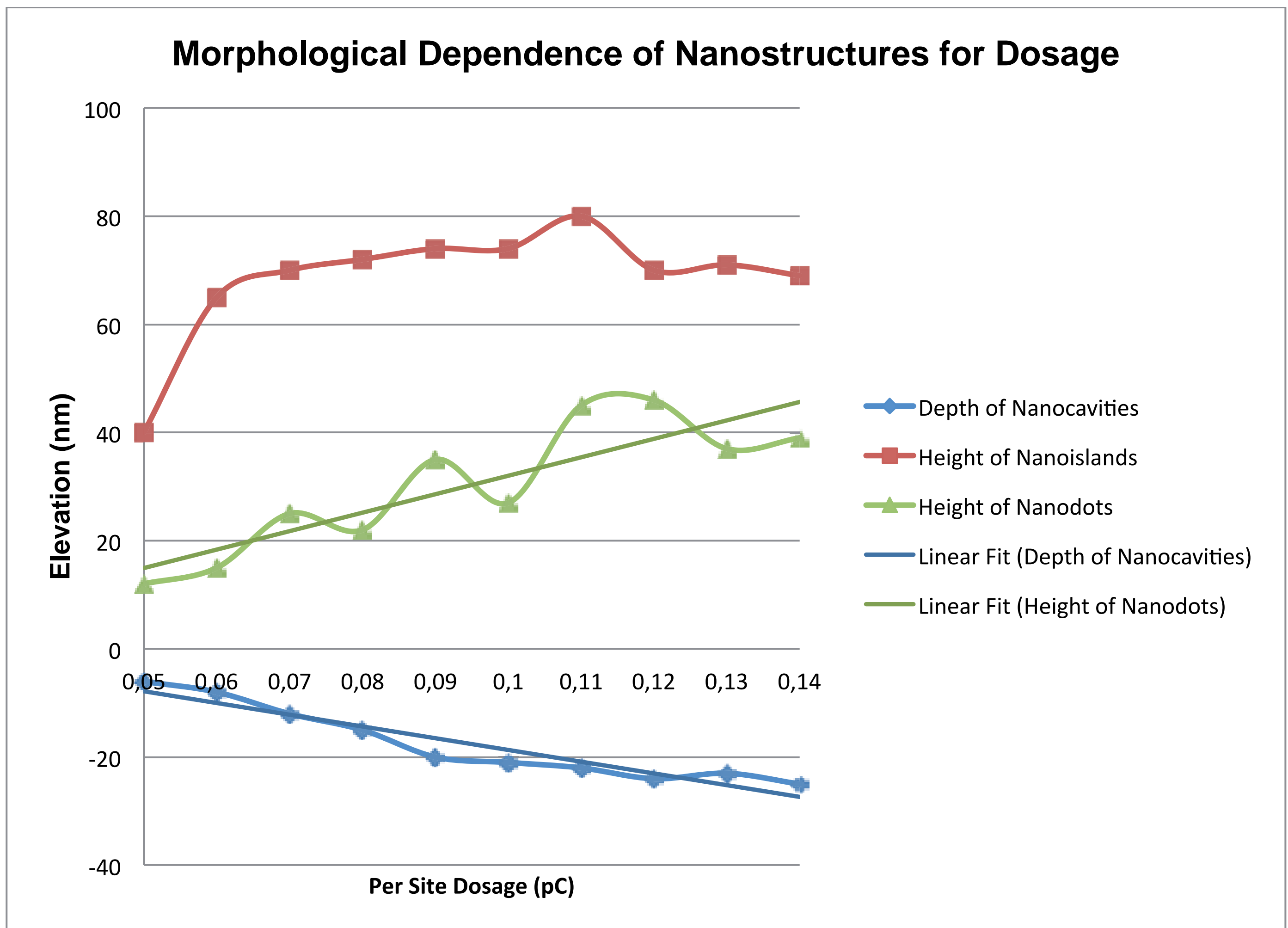

Figure 2-33 *Height and depth changes for individual nanosites as a function of dosage.*

After cleaning away the undeveloped precursor, what remains are nanoislands due to the cross-linking from the electron beam due to the electron sensitivity of LSMO [24]. The amount of cleaning by water is a compromise between low roughness of the area surrounding the nanoislands and the amount of nanoisland dislodged in the process. The height of these nanoislands are also linearly dependent to dosage at lower quantities of electrons as seen in figure 2-33. When the dosage increases, the height of the nanoislands levels off while the width continues to increase. The pattern which becomes insoluble in water as a function of dosage is quite complex. This pattern starts as a high aspect ratio cone and as dosage increases becomes more volcano-like. When the dosage becomes very high, the center of the nanoisland starts to harden again and as the electrons continue to rain down, the hardened center becomes a ring. The nanoislands must be written with a pitch large enough such that the final structures are isolated once annealed.

The nanoislands lose their organic components when annealed and subsequently the inorganic metals are able to form crystals. These nanodots have a height dependence which is proportional to the locally applied

dosage. At low dosages the final morphology of the nanodots are triangular and at high dosage the material breaks apart to form an unorganized grouping of polycrystalline nanodots. The nanodots were then analyzed with TEM and EELS to reveal that the element manganese was absent from the crystals. This could be a consequence of the volatile manganese oxide being vaporized during the electron beam writing process. As it will be seen in the chapter on nanoimprint lithography, the manganese was successfully retained in the nanostructures.

2.7 Nanodot References

1. Wolfman, J., et al., *Large domain wall magnetoresistance up to room temperature in La0.7Sr0.3MnO3 bridges with nanoconstrictions.* Journal of Applied Physics, 2001. **89**(11 II): p. 6955-6957.
2. Arnal, T., et al., *Low-field magnetoresistance in a nanopatterned manganite track.* Journal of Magnetism and Magnetic Materials, 2006. **300**(1): p. e274-e276.
3. Xi, L., et al., *Critical behavior near ferromagnetic-paramagnetic phase transition in nano-polycrystalline La0.7Sr0.3MnO3.* Cailiao Gongcheng/Journal of Materials Engineering, 2008(10): p. 72-75.
4. Kalkert, C., et al., *Resistive switching at manganite/manganite interfaces.* Applied Physics Letters, 2011. **99**(13).
5. Lee, J., et al., *The impact of Al interfacial layer on resistive switching of La0.7Sr0.3MnO3 for reliable ReRAM applications.* Microelectronic Engineering, 2009. **86**(7-9): p. 1933-1935.
6. Nakagawa, N., et al., *Magnetic and transport properties of Mn-based fractional-layer oxide superlattices.* Japanese Journal of Applied Physics, Part 2: Letters, 2002. **41**(3 B): p. L302-L304.
7. Ulyanov, A.N., et al., *Local structure and magnetic inhomogeneity of nano-sized La 0.7Sr0.3MnO3 manganites.* Journal of Applied Physics, 2011. **109**(12).
8. Ward, T.Z., et al., *Tuning the metal-insulator transition in manganite films through surface exchange coupling with magnetic nanodots.* Physical Review Letters, 2011. **106**(15).
9. Vrejoiu, I., et al., *Functional perovskites - From epitaxial films to nanostructured arrays.* Advanced Functional Materials, 2008. **18**(24): p. 3892-3906.
10. Karmakar, S., S. Taran, and B.K. Chaudhuri, *Magnetoresistance of sol-gel derived manganite nanoparticles.* Physica Status Solidi (B) Basic Research, 2004. **241**(15): p. 3563-3571.
11. Guo, X., et al., *Anomalous positive magnetoresistance effect in La0.67Ca0.33MnO3 microbridges.* Journal of Alloys and Compounds, 2009. **485**(1-2): p. 802-806.
12. Dyakonov, V., et al., *Magnetic, resonance and transport properties of nanopowder of La 0.7Sr0.3MnO3 manganites.* Journal of Magnetism and Magnetic Materials, 2010. **322**(20): p. 3072-3079.
13. Oguchi, K., et al., *Relationship between electron sensitivity and chemical structures of polymers as electron beam resists. VI: Electron sensitivity of various acetalized poly(vinyl alcohol)s.* Polymer Engineering and Science, 1989. **29**(6): p. 353-358.
14. Chuang, C.M., et al., *Nanolithography made from water-based spin-coatable LSMO resist.* Nanotechnology, 2006. **17**(17): p. 4399-4404.
15. Abargues, R., et al., *High-resolution electron-beam patternable nanocomposite containing metal nanoparticles for plasmonics.* Nanotechnology, 2008. **19**(35).
16. Shi, J., et al., *Study on microwave-assisted hydrothermal synthesis of La0.7Sr0.3MnO3 nano-powder and its magnetism.* Yadian Yu Shengguang/Piezoelectrics and Acoustooptics, 2008. **30**(SUPPL. 2): p. 177-178+180.
17. Zou, G., X. You, and P. He, *Patterning of nanocrystalline La0.7Sr0.3MnO3 thin films prepared by sol-gel process combined with soft lithography.* Materials Letters, 2008. **62**(12-13): p. 1785-1788.
18. Keshavarz, M.H., *A simple way to predict heats of detonation of energetic compounds only from their molecular structures.* Propellants, Explosives, Pyrotechnics, 2012. **37**(1): p. 93-99.
19. Shinde, K.P., et al., *Solution-combustion synthesis of La0.65Sr0.35MnO3 and the magnetocaloric properties.* Materials Science and Engineering B: Solid-State Materials for Advanced Technology, 2010. **167**(3): p. 202-205.

20. Faaland, S., M.A. Einarsrud, and R. Høier, *Reactions between La1-xCaxMnO3 (x = 0.3 and 0.6) and CaO-stabilized ZrO2 powder mixtures studied on a nano-meter scale.* Journal of Materials Science Letters, 2000. **19**(15): p. 1379-1381.
21. Moreno, C., et al., *Spontaneous outcropping of self-assembled insulating nanodots in solution-derived metallic ferromagnetic la0.7sr0.3mno 3 Films.* Advanced Functional Materials, 2009. **19**(13): p. 2139-2146.
22. Abellán, P., et al., *Misfit relaxation of La0.7Sr0.3MnO3 thin films by a nanodot segregation mechanism.* Applied Physics Letters, 2011. **98**(4).
23. Carretero-Genevrier, A., *Vertical (La,Sr)MnO3 Nanorods from Track-Etched Polymers Directly Buffering Substrates.* Advanced Functional Materials, 2010. **20**(6): p. 892-897.
24. Bray, J., *Poly(vinyl alcohol) hydrogels. Formation by electron beam irradiation of aqueous solutions and subsequent crystallization.* Journal of Applied Polymer Science, 1973. **17**(12): p. 3779-3794.

3. Oxide Nanowires by Electron Beam Lithography

The work of this chapter centers on forming nanowires from a LSMO spin coated precursor by electron beam lithography on insulating single crystal substrates and silicon. The precursor had two percent by weight PVOH and used nitrates as the counter ion. The nanowires were formed from two different methods, namely by writing low dosage isolated sites and high dosage arrays. The subsequent nanowires have very unique growth characteristics which will be illuminated. Nanowires grown on STO and silicon were analyzed with TEM and were found to have unique morphologies. Analysis with EELS showed the nanowires to be lanthanum strontium oxide crystals, devoid of manganese. This is an unfortunate consequence of growing nanowires with this method due to the desire for the nanowires to single crystal ferromagnetic LSMO.

Nanowires are defined as quasi one-dimensional nanostructures with a non-hollow interior and lengths multiple times greater than their diameters. Nanowires can be grown vertical or horizontal, isolated or in bundles, in ordered arrays or randomly across a surface, on conducting metal substrates or insulating glass [1-5]. These narrow nanostructures have been also made out of a multitude of different materials ranging from organic to inorganic. Nanowires are seen as potential integral components for next generation devices. One-dimensional nanostructures are seen being included in the fields of energy harvesting, photonics and also biosensors [6]. An example of sensor applications for nanowires can be found in the work of Comini et al, where various oxide quasi one-dimensional Sn, In, Zn nanowires were optimized for their diameters to sharpen their electrical response to specific gases [7].

Researchers have been exploring techniques in which to make LSMO nanowires by electron beam lithography. Typically, a thin LSMO film is grown on top of substrate and then subsequently topped with a layer of an electron writable negative resist. This resist is then developed revealing nanometer wide lines, then a metal layer is deposited, a lift off is performed, and finally an etching gives a thin LSMO strip. The most popular resists uses polymethyl-methacrylate (PMMA) or hydrogen silsesquioxane (HSQ). It was reported that LSMO nanowires have been made by patterning HSQ resist and then etching with argon by Gaucher et al. They found that the electrical transport properties of the LSMO nanowires were on par with that of LSMO thin films [8]. It was also found that when thin films of LSMO are made by pulsed laser deposition and then patterned to form long mesoscopic structures, their coercive field is larger than that for bulk films [9]. A group headed by Yang et al used PMMA with HSQ to make a bilayer resist which was able to make deep well defined masks for potential nanowire fabrication [10]. This masking method of nanowire fabrication can be seen in the work of Pedersen et al where a polymerizable hexane resist is irradiated with focused electrons to create 150 nm wide tracks which are then used to make silicon nanowires [11]. Another usage of electron writable HSQ being employed to make LSMO nanowires was reported by Arnal et al. and showed bridge of nanowires could be successfully fabricated [12].

Aside from masking methods, oxide nanowires can be grown from a multitude of other techniques. For instance, STO nanowires have been grown by placing $Sr(OH)_2$ on top of titanate nanowires, MnOx nanowires by anodic deposition of manganese acetate on to conducting substrates, and lanthanum borate nanowires were grown by confining LaOx with boron on a carbon nanotube template [13-15]. Another popular method to generate oxide nanowires is by using the hexagonal form of porus anodized alumina. This has produced nanowires consisting of $LaNiO_3$, CoO_3, and $LaMnO_3$ [16-18]. Few reports exist of using electron beam lithography to directly write nanowires where the work of Kazuyuki et al is an example. They have reported the direct formation of graphite nanowires by electron beam irradiation [19].

3.0.1 Nanowire Growth

Of all the features seen in the LSMO nitrate-based precursor, perhaps the most surprising is the spontaneous growth of nanowires after electron beam lithography. In chapter two the morphology of nanoislands and nanodots was explored along with high resolution TEM analysis. These structures are quasi zero-dimensional and are generated from standard usage of an electron beam. However, through more exotic electron beam shaping as well as high energy configuration, quasi one-dimensional nanostructures may also be generated. A partial goal of this project was the generation of LSMO nanowires via electron beam lithography on insulating single crystal substrates. As it will be elucidated in this chapter, a straight foreword path to this goal

was impossible. Nonetheless, two more circuitous paths were discovered and many surprising features therein are explored. As was discussed in chapter one, the main driving motivation for generating LSMO nanowires share many of the same technological potential benefits as with LSMO nanodots. While this work on nanowires does not has a direct application to industry, a deeper understanding of the curious nature of generating oxide nanowires on insulating single crystal substrates by electron beam lithography may be of use.

Two main types of nanowires were observed to have grown. One type stemmed from Isolated Low-Dosage (ILD) nanoislands producing isolated nanowires as seen on the left in figure 3-1. The other type seen on the right in figure 3-1 was generated from Arrays of High-Dosage (AHD) nanoislands and gave locally parallel nanowires. In the case of ILD nanowires, the substrate studied was primarily YSZ[100] and briefly YSZ[010] whereas the case for AHD nanowires were analyzed on both STO[100] and silicon substrates. To better relate the findings, the case of ILD nanowires will be explained first, followed by deeper descriptions of how nanowires were generated from AHD nanoislands. Two of the AHD cases were investigated with high resolution TEM and EELS line scans to reveal the crystalline nature of these nanowires. The study of these systems highlights the delicate and surprising nature of mixed valence metal oxide nanowires on insulating substrates by electron beam. The precursor used consisted of lanthanum, strontium, manganese nitrate salts with two percent polyvinyl alcohol which gave LSMO thin films once annealed. The spin coating conditions were six thousand revolutions per minute for two minutes to produce a film of two hundred nanometers in thickness. The electron beam conditions were a working distance of ten millimeters, a potential of five kilovolts, an aperture of thirty micrometers, and a beam current of 150 pA. The annealing conditions in all these experiments, unless noted, was three hundred milliliters per minute of oxygen with a ramp rate of three degrees a minute until a hold of four hours at one thousand degrees.

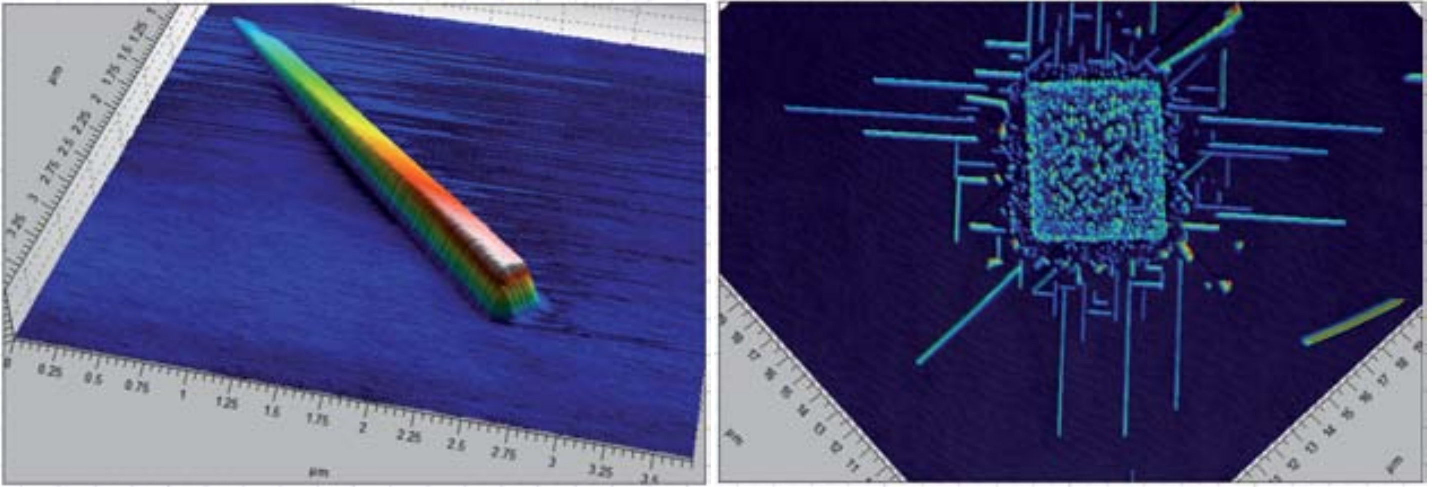

Figure 3-1 *Left: example of nanowire grown by ILD method on YSZ from a dosage of 0.3 pC. Right: example of locally parallel nanowires by AHD method on STO from 10 x 10 array each at 1500 pC.*

The discovery that the LSMO precursor could produce nanowires at all came unexpectedly. At least, the two methods in which nanowires grew were unexpected. Originally it has been hypothesized that nanowires should simply grow from writing a very fine line into the precursor film, developing it, and finally annealing the substrate. Theoretically, a one dimensional written structure should have had the same final morphology as before it was annealed. However this proved not to be the case as can be seen in figure 3-2. When a line was written onto the thin LSMO nitrate-based precursor film, the written line simply turned into a long series of polycrystalline nanodots. Regardless of the electron beam writing conditions such as exposure time, distance between waypoints, length, or width, the end product produced everything but nanowires.

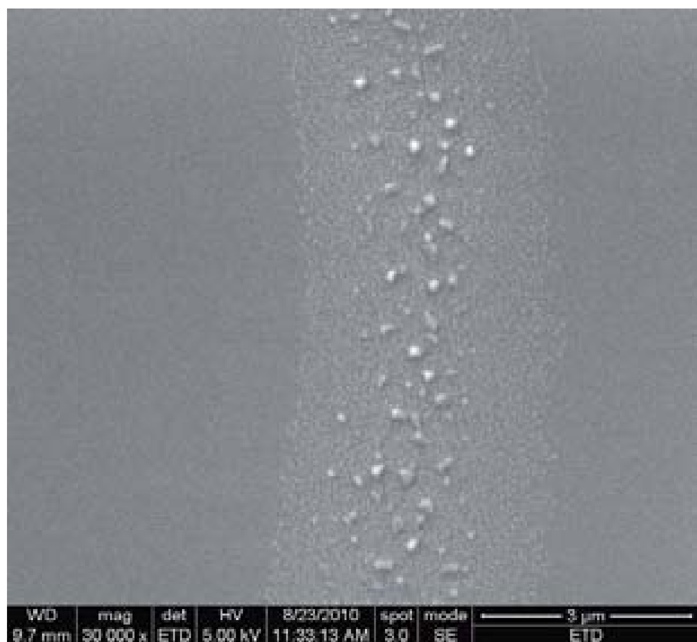

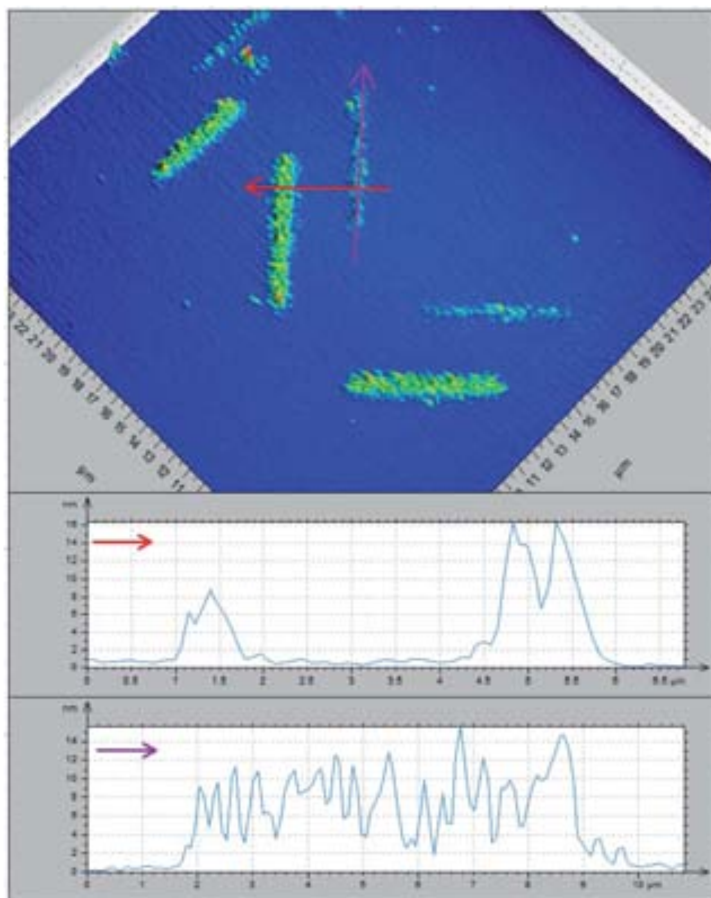

Figure 3-2 *Failed nanowire growth after writing thin lines and annealing on YSZ. Left: SEM image of failed nanowire from 0.15 pC with pitch 100 nm. Right: AFM image of failed nanowires from 0.15 pC and 0.05 pC with pitch 100 nm.*

3.1 ILD Nanowire Growth

The first glimmers of nanowire growth were observed when writing low dosage single-sites on YSZ. These irradiated spots, instead of turning into vertical structures, grew oriented anisotropic structures. The method to obtain these films of nanowires punctuated by nanodots have been ascertained to be dependent on an imperfectly focused electron beam. A perfectly focused electron beam creates vertical isotropic nanostructures as has been seen in the previous chapter. The reason to think beam defocusing is responsible for nanowires is that for highly insulating substrates, focusing consistently over many samples is impossible. So when attempting to focus correctly over many samples, high variation in final output was observed. This focusing variation caused this particular outlier seen on the left of figure 3-3.

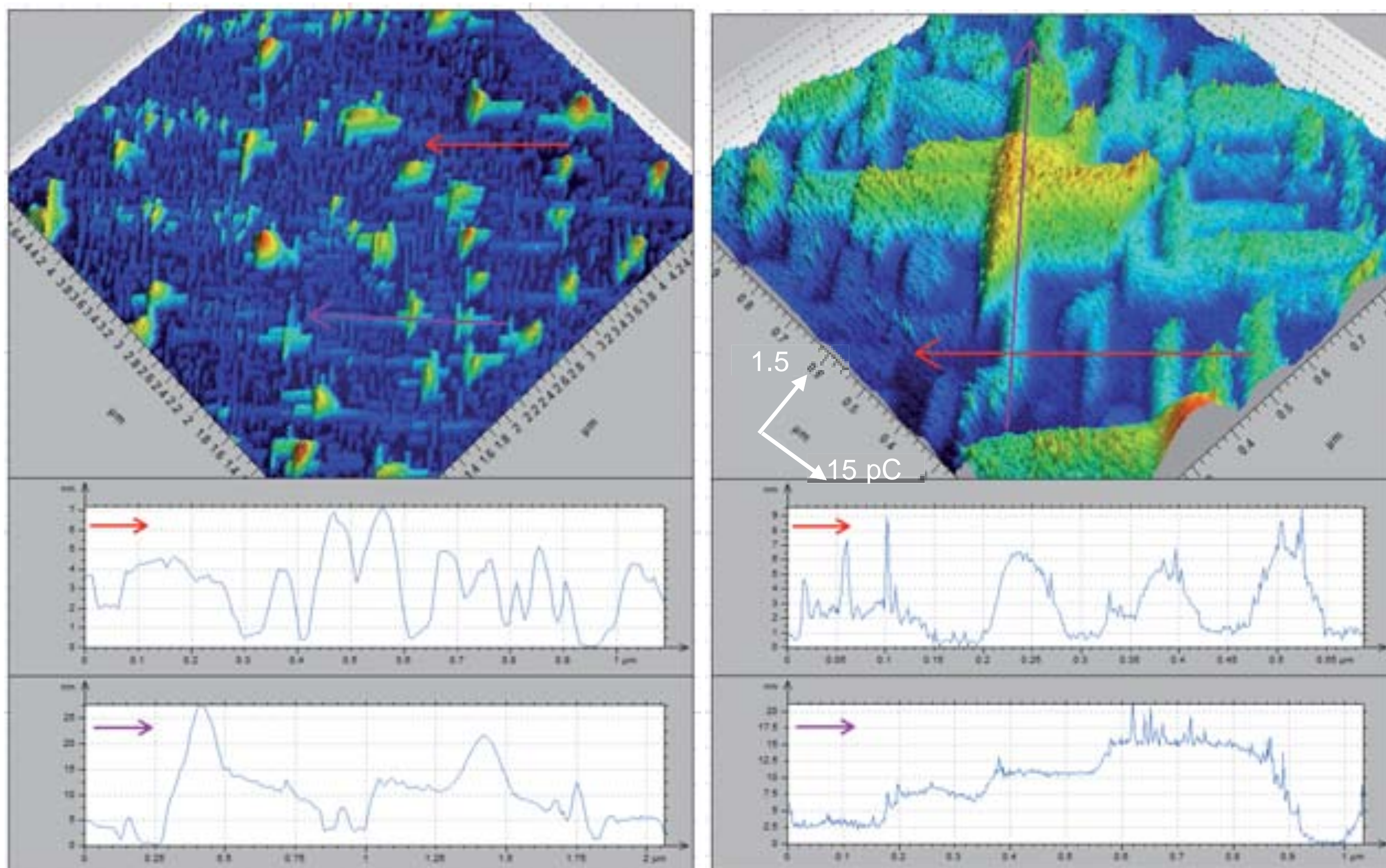

Figure 3-3 *Left: nanowires grown on YSZ[100] after annealing by EBL with dosage 0.1 pC with pitch of 1 μm. Right: zoom of area.*

The particular nature of these nanowires can be seen on the right in figure 3-3; where the central structure was the intended nanodot site. The pitch here was one micrometer with an individual dosage of 0.15 pC. The nanowires are seen to have grown as small as four nanometers and as long as several hundred nanometers. As can be seen in both AFM images, the nanowires have encompassed not just the local area around the nanodot site, but between individual nanodots. This sample led to an earnest effort to alter the way the electrons were focused on the precursor by changing beam parameters so as to create nanowires. Unfortunately this initial type of nanowire growth remained elusive to recreate; however two other variations on this isolated low-dosage approach proved more repeatable.

3.1.1 Defocused ILD Nanowire Growth on YSZ

In this manner, purposely defocusing the electron beam generated the following morphology of non-annealed nanosites as seen on the left of figure 3-4. The parameters used to write these nanoislands were 0.03 pC in the left most column and increased evenly to 0.15 pC on the right most column. On the right of figure 3-4 one

can see the result of annealing the defocused nanoisland with 0.03 pC. Key characteristics to this growth mode were a small number of nanowires per written site, small feature size, and lack of nanowires between sites. That is, an individual irradiate zone broke into several oriented small nanowires once annealed. The region which grew nanowires was approximately two micrometers.

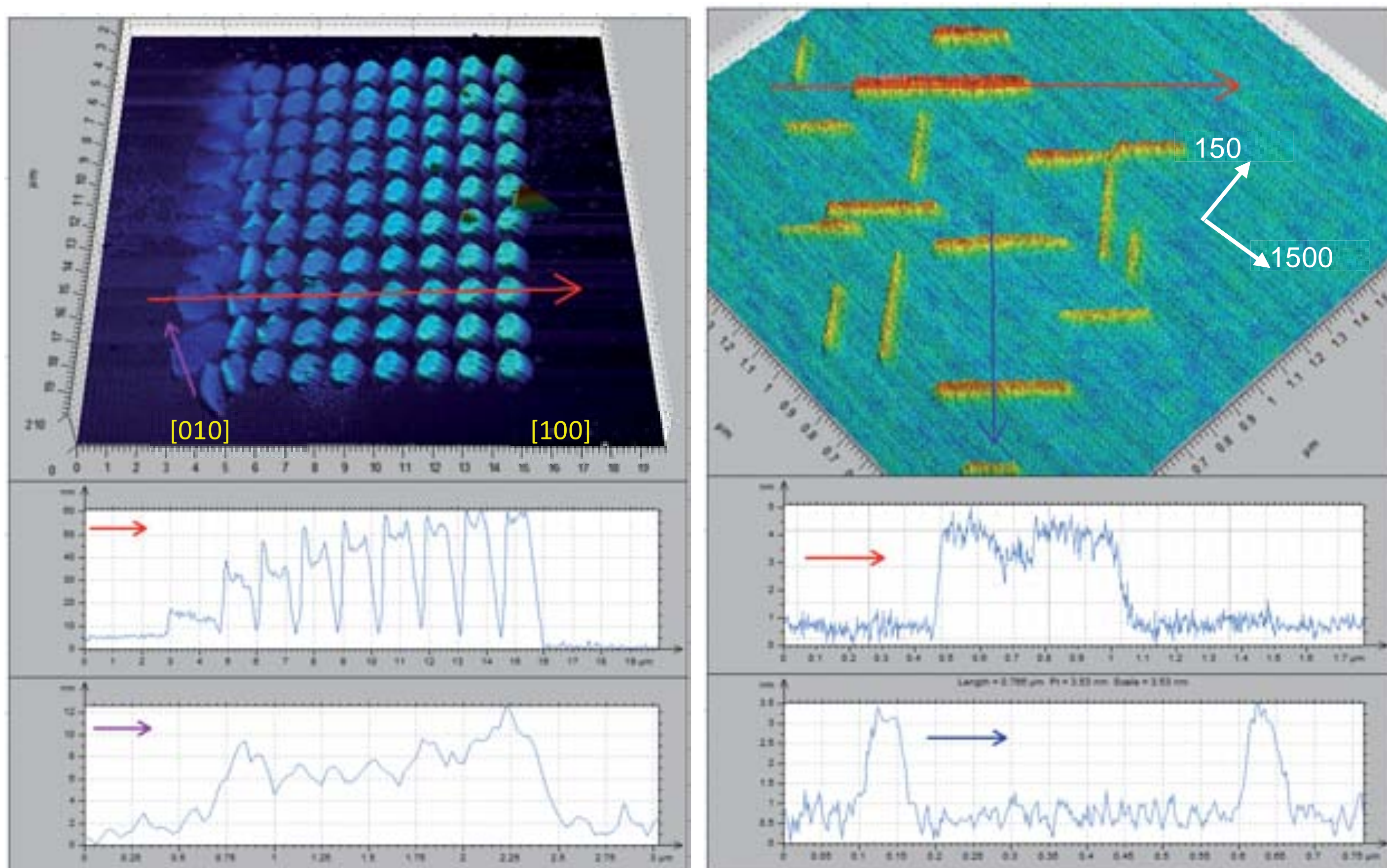

Figure 3-4 *Right: defocused nanoislands before annealing showing a range of dosages from 0.03 pC to 0.15 pC on YSZ. Left: site of lowest dosage 0.03 pC after annealing on YSZ[100] showing ILD nanowires.*

The average length of these nanowires was generally around five hundred nanometers. This contrasts sharply with the other methods discussed next which produced nanowires on YSZ a few micrometers in length and those nanowires on STO which were up to ten micrometers long. The height of the nanowires here was consistently around four nanometers whereas the other nanowire types showed large variations in height and were almost an order of magnitude larger. The width of these nanowires was also quite small relatively at around fifty nanometers. It is unclear if these nanowires are fundamentally different crystaligraphically from those of the other cases, because no TEM analysis was made unfortunately.

The method used to generate these nanowires was to purposely defocus the electron beam moderately. This caused the electron beam to cross-link an area in a more diffused manner than by sharply focusing. The method thereby lessened the amount of material cross-linked and did it in a much larger area than a correctly focused electron beam. It is thought this changed the density of nanoislands so as to promote isolated individual nanowire formation when annealed. However, the procedure was highly variable and consistent growth of nanowires on a single substrate was therefore difficult. Over a range of seven substrates grown in this manner, only three showed nanowire growth and then only in certain areas.

Nonetheless, this may be due in part to the observation method of these nanowires depends solely on the AFM and not entirely due to the nature of these nanowires. The inability to observe the structures with a SEM stems from the large surface charging on the highly insulating YSZ substrate as well as the very small feature size. The sub five nanometer feature size meant even gold coatings – used to increase surface conduction and thus observability with the SEM – of twenty nanometers would largely obscure the nanowires. Hence, possibly there existed more occurrences of this particular type of nanowire growth, but the slow process of randomly scanning small areas with an AFM limited the scope of the search. In the end, it was difficult to definitely determine how much defocusing was optimal and impossible to predict with any certainty if any given nanoislands would eventually yield nanowires.

Another consideration to contend with is the morphological dependence on the dosage used in forming the proto-nanodot. There appeared to be a range of dosages wherein individual nanowires grew, then as the dosage increased, more polycrystalline nanodots would form. This can be seen from the following images in figure 3-5, that is as dosage increases, so does the amount nanodots grown. The dosages seen in figure 3-5 are 45 attocoulombs in the top left hand corner, 0.075 pC top right, 0.105 pC bottom left, and 0.15 pC on the bottom right. Eventually, a saturation point was reached in which the dominate feature was the nanodots and not the nanowires. This fact has two possible explanations: one is that the as written cross-linked area had heterogeneities which led to this dual feature growth; the other is that this area was homogeneous to begin with and when annealed formed pockets of excess material which due to energy considerations preferred nanodot growth rather than nanowire growth. Clearly, the larger the dosage for individual sites, the larger the physical size of the nanoisland. Thus, to achieve an area devoid of nanodots once annealed, it is critical to be under a certain threshold of size. However, there is a limit to the how small the nanoisland may be. Below a certain threshold, the nanoislands do not have a sufficient footprint, and subsequently are ripped away from the substrate when developed.

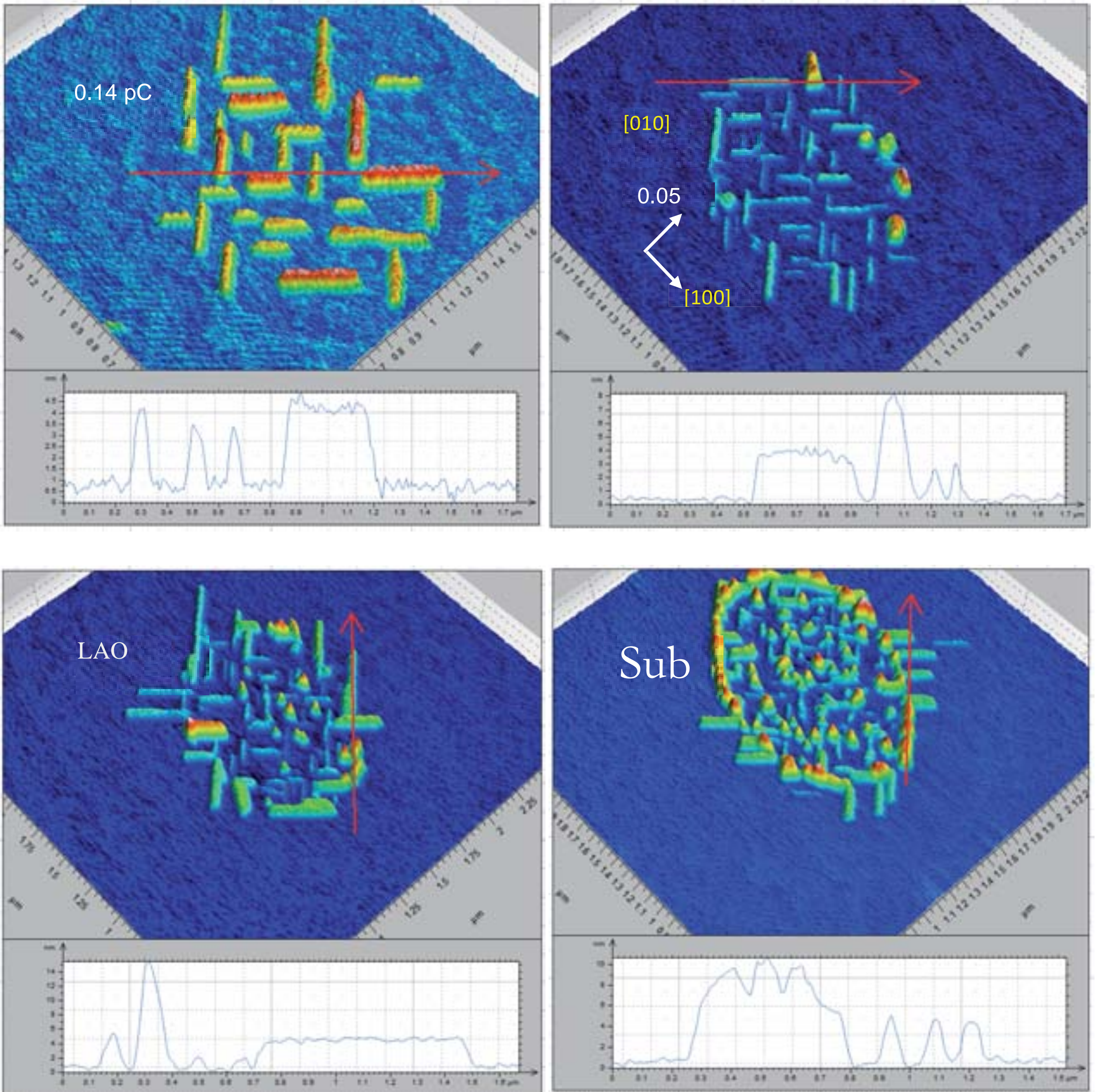

Figure 3-5 *Increasing dosage from top left at 0.045 pC to bottom right at 0.15 pC shows two growth modes on YSZ [100].*

3.1.2 Astigmatic ILD Nanowire Growth on YSZ

Due to the difficulty in systematically reproducing nanowires grown by defocusing the electron beam, other techniques were explored. One technique that was found when the stigmatism was also altered in a

significant way from what would produce normal nanodots, large individual nanowires were grown. When the electron beam is altered to be purposely astigmatic, the beam becomes elliptical if the focal plane is not at the surface. In other words, when a beam is focused at the center but astigmatic and the sample is not completely perpendicular to the beam, the resulting nanodots when written across the entire substrate will be round in the center and very elliptical towards the edges. An example of this can be seen in figure 3-6.

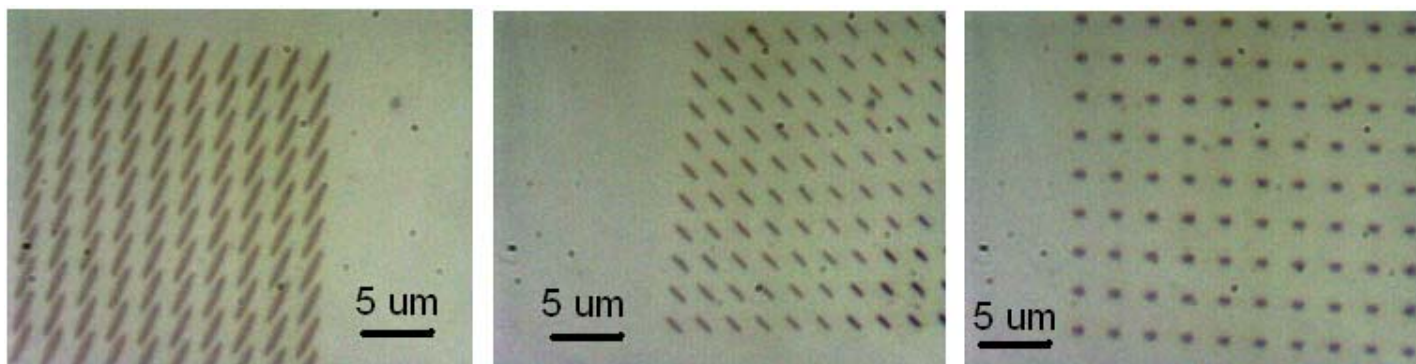

Figure 3-6 *Optical image of a series of nanoislands with differing degrees of ellipticity. Left: highly elliptical nanoislands for ILD nanowires. Center: moderately elliptical. Right: non-elliptical nanoislands.*

Hence with this method, one could systematically produce nanowires on very small sections of very large written areas as seen here figure 3-7. The dosage used for all these sixteen sites in this figure was 0.3 pC. This figure is meant to illustrate the large variation for a given dosage. These nanowires differ drastically from the defocused nanowires in that they have more of a propensity to form large and long isolated nanowires. Another characteristic which differs from the solely defocused methodology is there exists overlap between nanowires whereas previously there was no overlap.

The mechanism behind why these highly elliptical nanoislands grew nanowires remains nebulous. The mechanism is thought to have something to do with a small edge of these elongated nanoislands becoming crystalline before the rest of nanoisland. This small crystalline section might be able to force the rest of the nanoisland into an ordered structure after continued heating. Although, one might suspect if that were to be true the nanowires would all be aligned in the same direction after annealing due to all the nanoislands being written in the same direction. This is however not what one finds when analyzing with an AFM. One finds that the number of nanowires going in the plus forty five degree direction is the same as those going at minus forty five degrees.

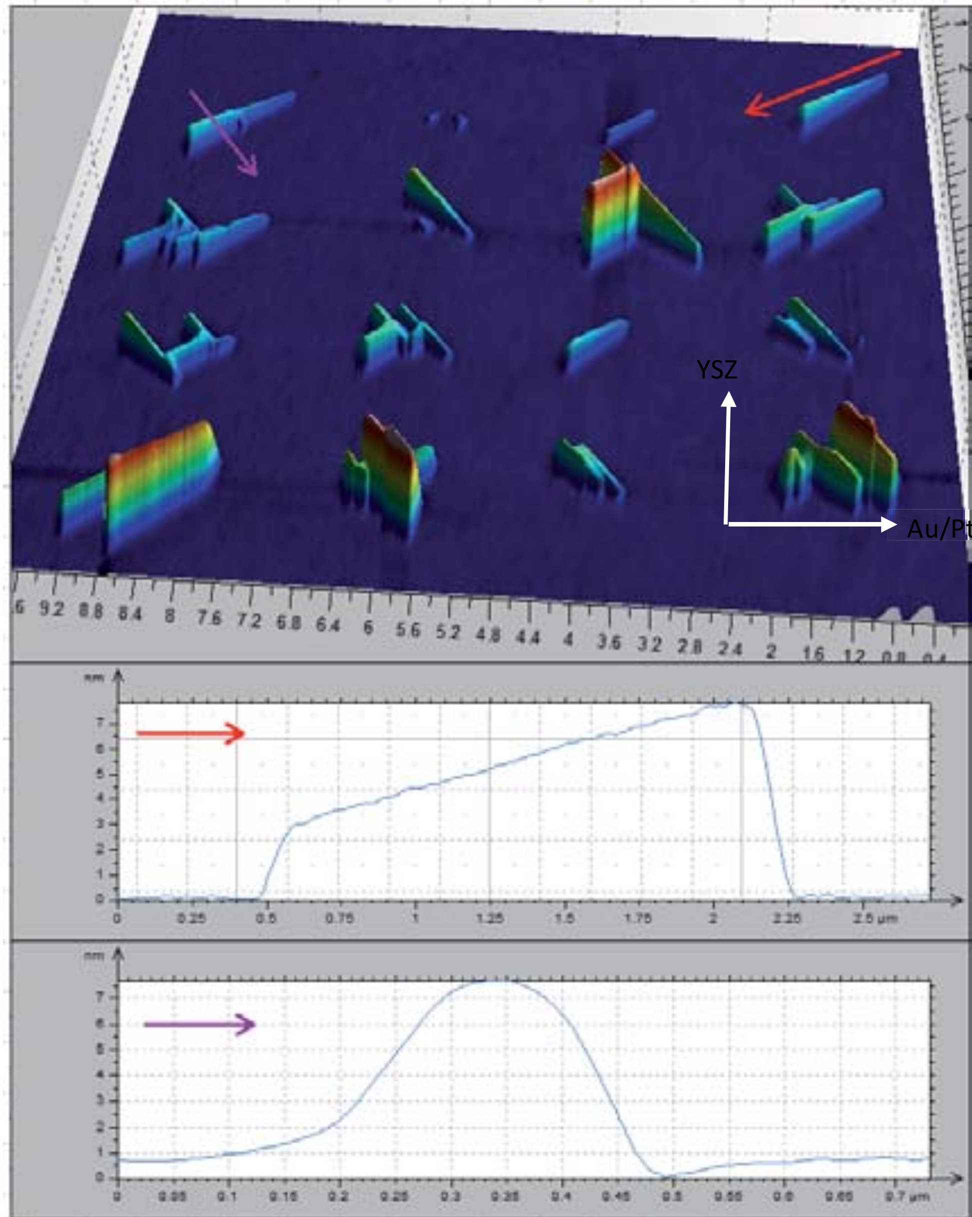

Figure 3-7 *Variation in nanowire growth for ILD method on YSZ[100] at 0.3 pC and pitch of 2 µm.*

As can be seen in figure 3-8, the direction of growth of the nanowires changed depending on the substrate in which they grew upon. One can see in both images an alteration in dosage in the form of four columns ranging from 0.6 pC in the left hand column and 0.15 pC in the right hand column. Even though both the right and left images in figure 3-8 have the same dosage, there exists a variation when isolated nanowires grew. Also what is observable in both AFM images is the distinct absence of some nanostructures. This is due to the odd phenomena of at the critical dosage where nanowires would form, a fraction of the nanowires did not adhere to the surface and subsequently popped off.

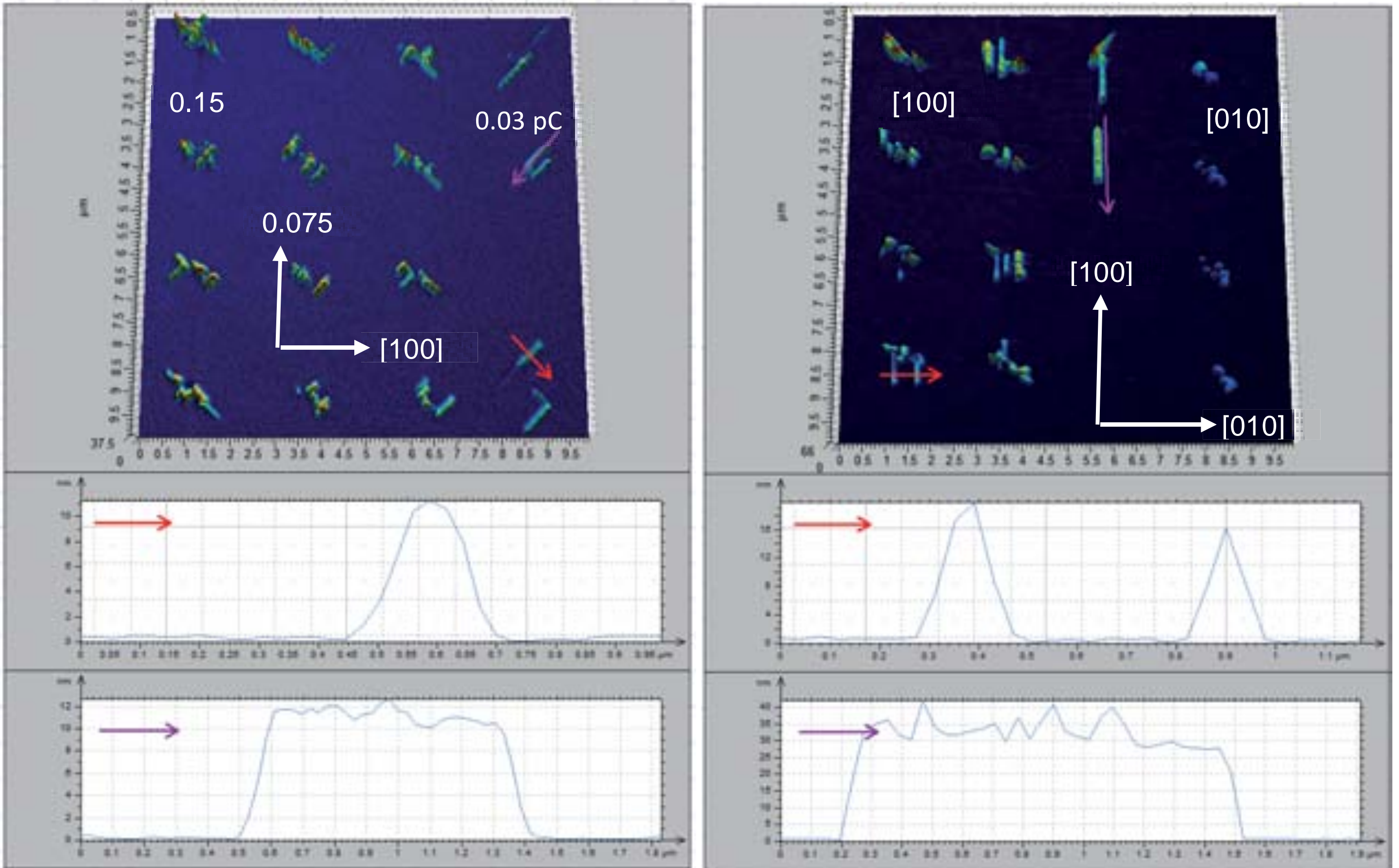

Figure 3-8 *Left: ILD nanowires on YSZ[100]. Right: ILD nanowires on YSZ[110]. Dosages decrease incrementally from 0.6 pC to 0.15 pC.*

Occasionally the ideal morphological conditions were met however and a perfect single nanowire was produced subsequently in an oxygen annealing step, as can be seen in figure 3-9. Another interesting observation was the two types of perfect isolated single nanowires. One nanowire which had a gentle sloping nature is seen in on the left in figure 3-1 and the other having no slope at all as seen in figure 3-9. This also contrasts to the nanowires produced by the AHD method which formed pointed nanowires as seen in figure 3-28.

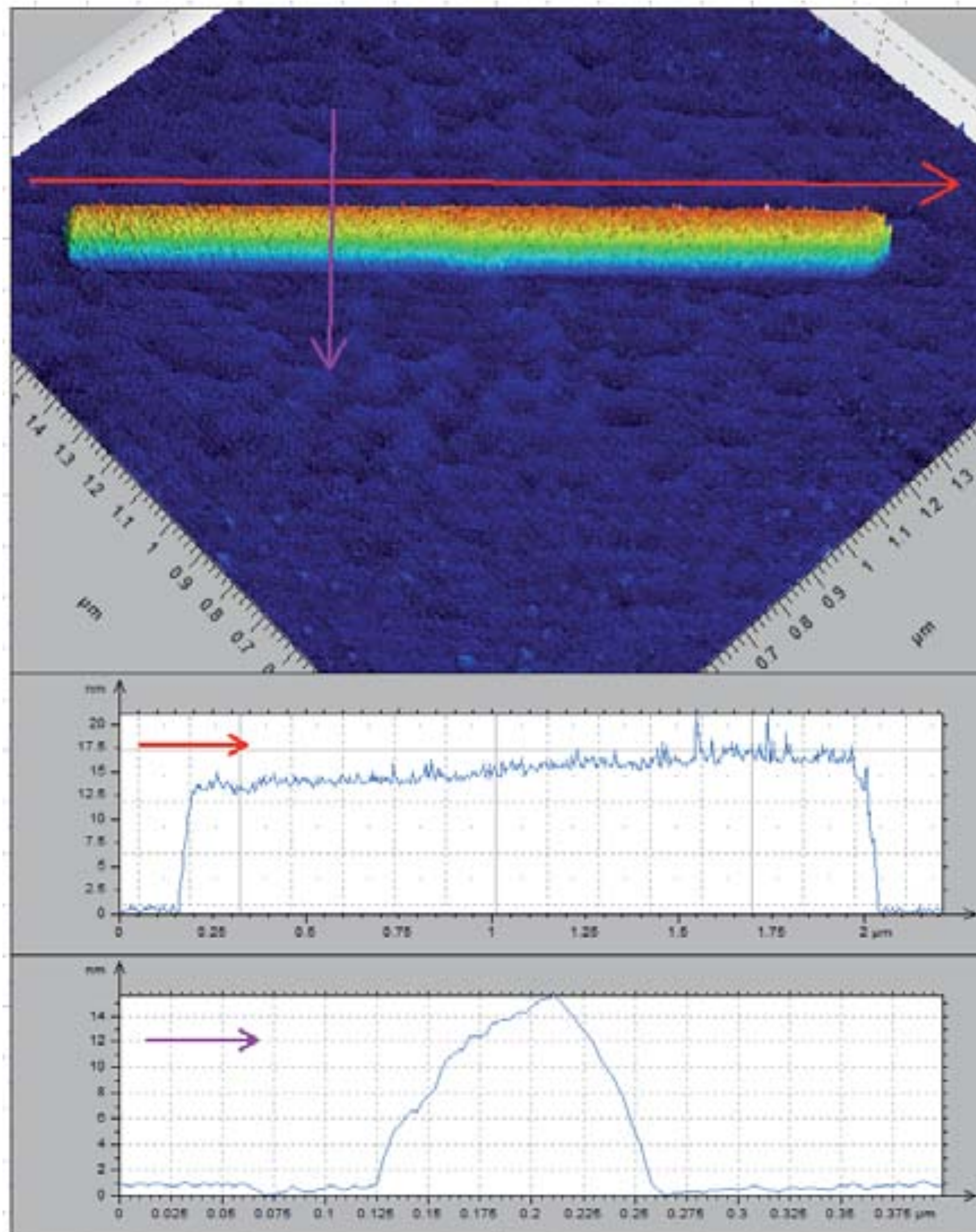

Figure 3-9 *Solitary nanowire produced ILD method on YSZ[100] from dosage of 0.3 pC with annealing at 1000 °C 4h.*

The morphology of this mode of ILD nanowire growth was such that the height ranged from seven to forty nanometers. While the width ranged from 175 to 300 nanometers. Another difference between these types of nanowires and the purely defocused type was if the dosage was lower or higher than a certain dosage window, the nanoisland would produce non-desired polycrystalline nanodots. This can be seen in figure 3-8. This proved a very frustrating aspect of fabricating these nanowires, in the sense that when a particular dosage was found to produce nanowires, another sample on another day might suggest a slightly different dosage window. This proved difficult to thereby write a large area all with the same dosage and then grow nanowires across the entire substrate. Coupled with the inexact focusing and alteration of the stigmatism, this method proved not well defined enough for continued investigation.

3.2 Nanowires Grown from AHD Nanodots

While running a routine high dosage and density test for morphology of LSMO nanodots on STO, it was discovered that at very high dosages and medium densities, oriented nanowires formed after annealing. An example of this AHD growth mode can be seen in figure 3-10, which consisted of a hundred nanodot array (ten by ten) spaced 750nm apart and each written with a dosage of 1500 pC. These nanowires grew along the [010] and [001] directions on the [001] cut substrate, seemed to be surrounded by a dark region as seen with the SEM, had lengths up to ten micrometers, as well as characteristically grew at the edge and perpendicularly from the area that was irradiated.

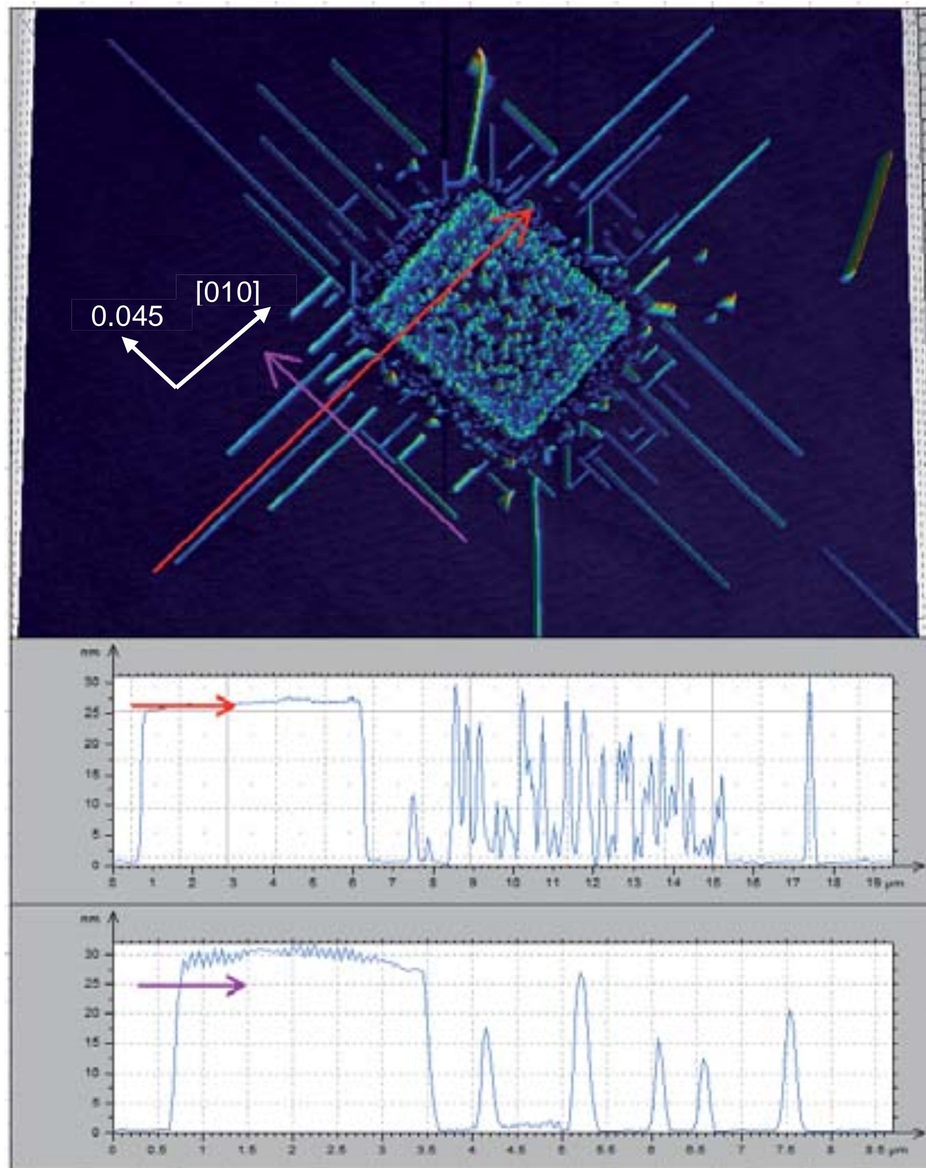

Figure 3-10 *Nanowires produced by high dosage array after annealing on STO. Array size 10 x 10 with each site receiving 1500 pC and 750 nm pitch.*

What can be observed with the SEM after annealing is a complex interplay between the thermodynamics of crystal growth and the physical barrier to further growth, mainly the nanodot array in figure 3-11. At the top of the left SEM image in figure 3-11 is an area being eliminated of any remaining annealed film by the growth of these nanowires. One can see a variation in contrast in the area at the top which was not completely cleaned when developed and the subsequent wave-like envelope being pushed by the growing nanowires. This area extends for approximately six micrometers, but it is by no means uniform across this edge. What is also visible in the left hand side of this SEM image is there exists both small orientated nanowires whereas further away from the edge only long perpendicular orientated nanowires are found.

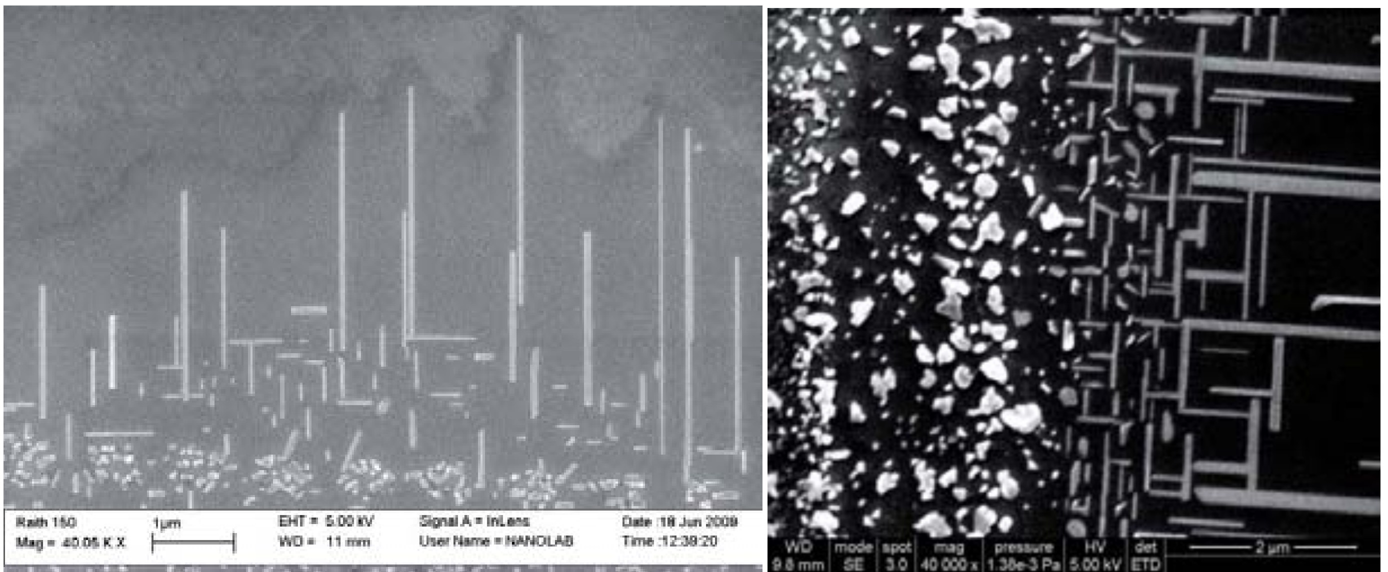

Figure 3-11 *Interface between AHD nanowires and nanodots on STO. Left: array size 10 x 10 with each site receiving 1500 pC and 800 nm pitch. Right: same conditions but 400 nm pitch.*

Looking at the image on the right in figure 3-11, one can see that the reduced distance between neighboring nanoislands as compared to left hand image produced more interplay between smaller and larger nanowires. Specifically the pitch on the left was eight hundred nanometers whereas on the right it was half this amount, at four hundred nanometers. Both SEM images in the figure were generated by arrays of ten by ten nanodots with an individual dosage of 1500 pC. Looking from left to right across this image on the right, one can see polycrystalline nanodots have abruptly become very fine, small nanowires. The nanowires which grew parallel to this edge were unable to overcome the nanowires which grew perpendicular to this edge. Also the width of these nanowires tends to increase as the nanowires begin further away from the edge. Another aspect is the growth of nanowires starting at several micrometers from the location of the irradiated array.

3.2.1 AFM on Corner of AHD Nanodots on STO

In order to understand the transformation of this array of large dosage nanodots into nanowires more precisely, a detailed study by AFM image was made. As can be seen in figure 3-12, one of these corners of the irradiated square after developing in water and then the same corner after annealing were imaged.

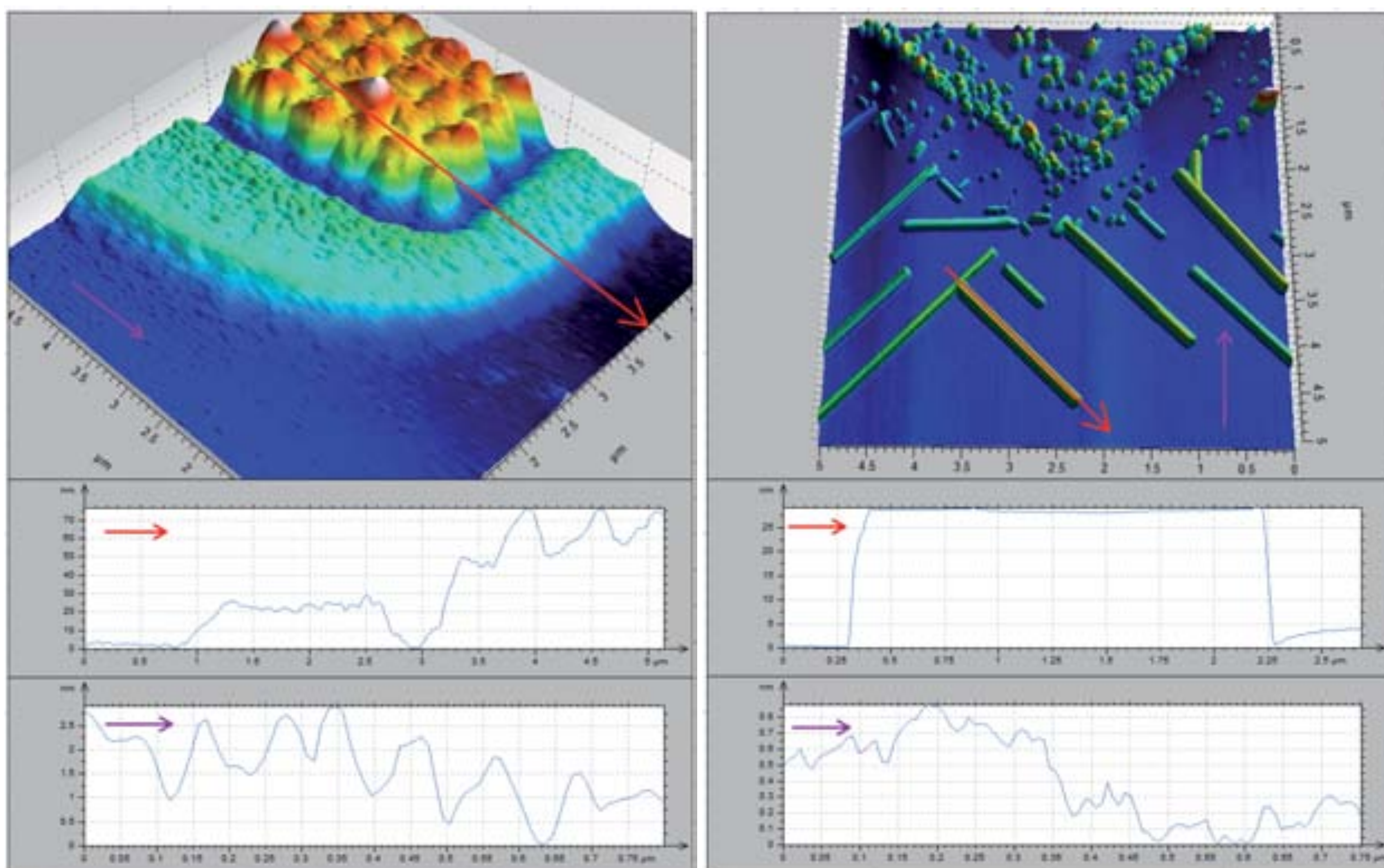

Figure 3-12 *Left: corner of AHD square before annealing. Right: same corner after annealing. Array size 10 x 10 with each site receiving 1500 pC and 750 nm pitch on STO.*

The corner here consisted of a 10x10 array with a pitch of seven hundred and fifty nanometers with a dosage of 1500 pC per site. The left image clearly shows several distinct areas of cross linked precursor. The red-orange area is the area that was initially irradiated directly with electrons and formed the thickest layer. Surrounding this is an area with no cross-linked film. Continuing away from this primary irradiation zone, an area in teal indicates a raised film of twenty-five nanometers. This area is thought to correspond to an area which was irradiated with enough secondary electrons and prevented substantial material loss when washed in developer. The inherent aspect of writing with electrons on to insulating substrates was explored in the work of Zarbout et al, where they found that affected area to much larger for glass substrates than copper ones [20]. This surrounding teal area will be of importance in the following discussions and hence will be called the secondary zone. Finally, an area surrounding everything is indicated by a dark-blue color, signifying a lack of film and hence a generally exposed substrate floor. This area is not completely cleaned down to the substrate and shows a high roughness of three nanometers.

In the AFM image on the right in figure 3-12, one can see the same corner after annealing. A crystalline layer is seen at the top, formed after annealing, along with a defined assortment of nanodots. Adjacent to this area

is a zone largely devoid of nanowires and small nanoislands, approximately one micrometer in width. Surrounding that area, one can see where the majority of nanowires start to grow and that they do so at right angles to one another. In this area smaller nanodots are not found but small nanowires at odd angles are. Interpreting these two AFM images, one could conclude that the teal-colored area in the non-annealed image became the nanowires. This is due to an apparent mass loss seen in this area after annealing. If nanowires had not grown, one would expect that this secondary zone would crystallize into an random assortment of nanodots in that particular area. Hence, one would expect larger number of nanodots in that area and nothing surrounding it. That is not what one finds after annealing however, one finds there a very sparsely populated area. The corollary to this, the mass gained by the nanowires in an area was from the film which was cross-linked by non-primary electrons. Looking closely at the topography of the annealed AFM image on the right in figure 3-12, one sees a marked decrease in surface roughness. It appears that the nanowire mass gain was at the expense of a loss in free particles on the annealed surface. This might also explain the contrast difference seen in the SEM image on the left in figure 3-11.

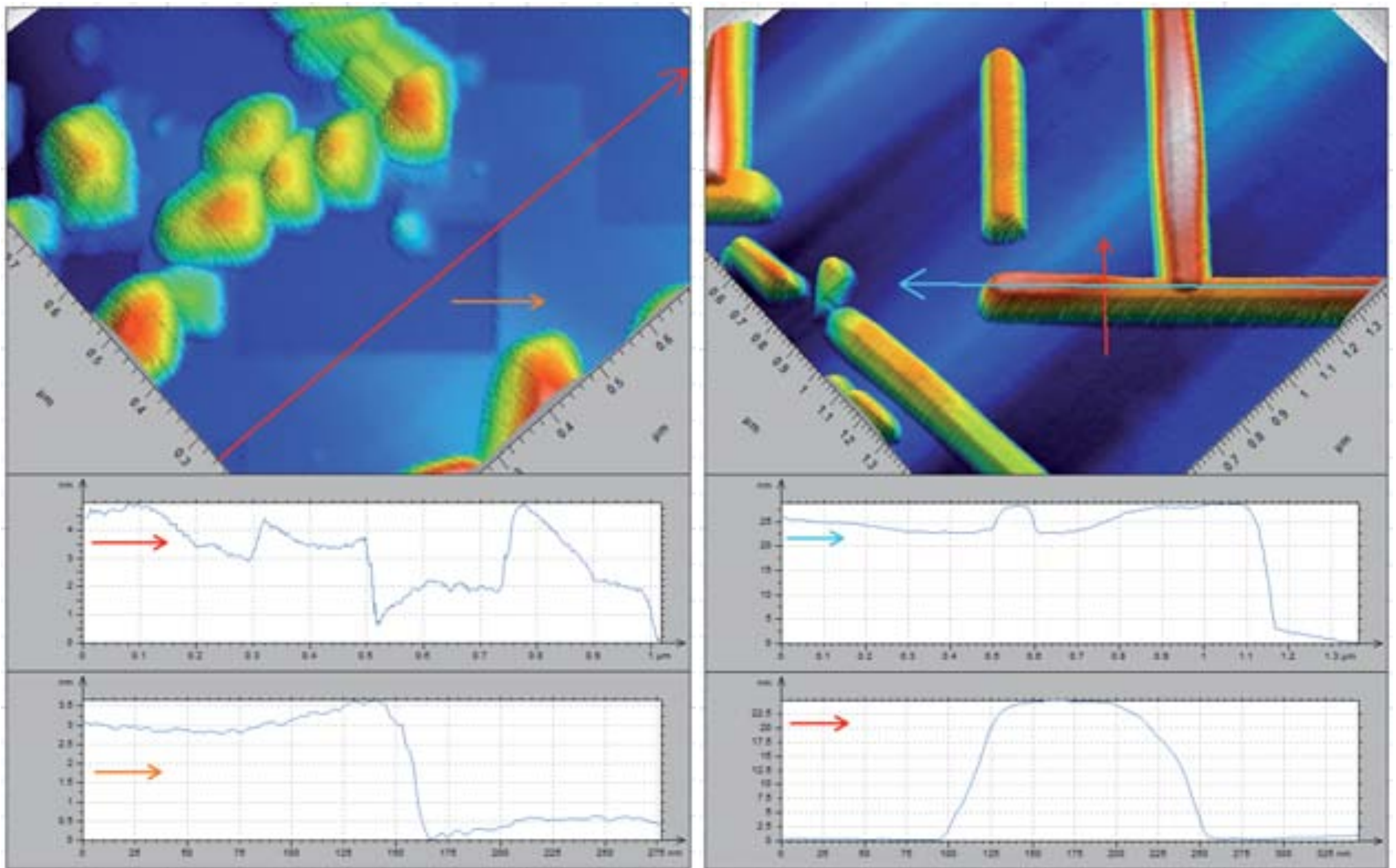

Figure 3-13 *Left: monolayer inside the AHD square. Right: nanowires outside square. Array size of 10 x 10 with each site receiving 1500 pC and 750 nm pitch on STO.*

A closer look at the area inside this primary radiation square is seen on the left in figure 3-13. Here one can observe the monolayer formed here, where the main feature is the square nature on top of an assortment of nanodots. The square film forms this four nanometer monolayer in some places where as in others places no monolayer is found. It is unclear what is the crystalline nature of this monolayer due to a lack of a TEM lamella; perhaps it differs from the nanowires found growing next to it. However this dewetting phenomenon is typical of excessive thermal treatment in films [21].

The nanowires that grew were much larger than the other nanowires grown with other techniques in this work as can be seen on the right of figure 3-13. The AFM profile of these nanowires shows some distinct characteristics which differ from the nanowires grown by the ILD method. One difference these nanowires are uniform in height along their lengths whereas the ILD ones only occasionally showed such morphology. This length-wise height uniformity disappears when annealed for extremely long times as seen in figure 3-28. The twenty-five nanometer height of these nanowires was significantly larger than the four nanometer reached by the defocused ILD nanowires. The greatest difference is the length of the nanowires by the AHD method, reaching up to ten micrometers. The width of these nanometers was one hundred and fifty nanometers and is on par with the widths of the other modes of nanowire generation seen in the ILD case.

3.2.2 Pitch Dependence for AHD Nanowires on STO

After running more experiments centered on the parameters in which the nanowire grew, it was observed that the there existed a condition space in which nanowire growth was promoted. This key parameter was the pitch or the distance between adjacent nanodots. The pitch had to be between two limits whereas another parameter of dosage had to be above a limit. This can be seen in figure 3-14. Numerically this was less than 1000 nm and 250 nm at a dosage of 1500 pC.

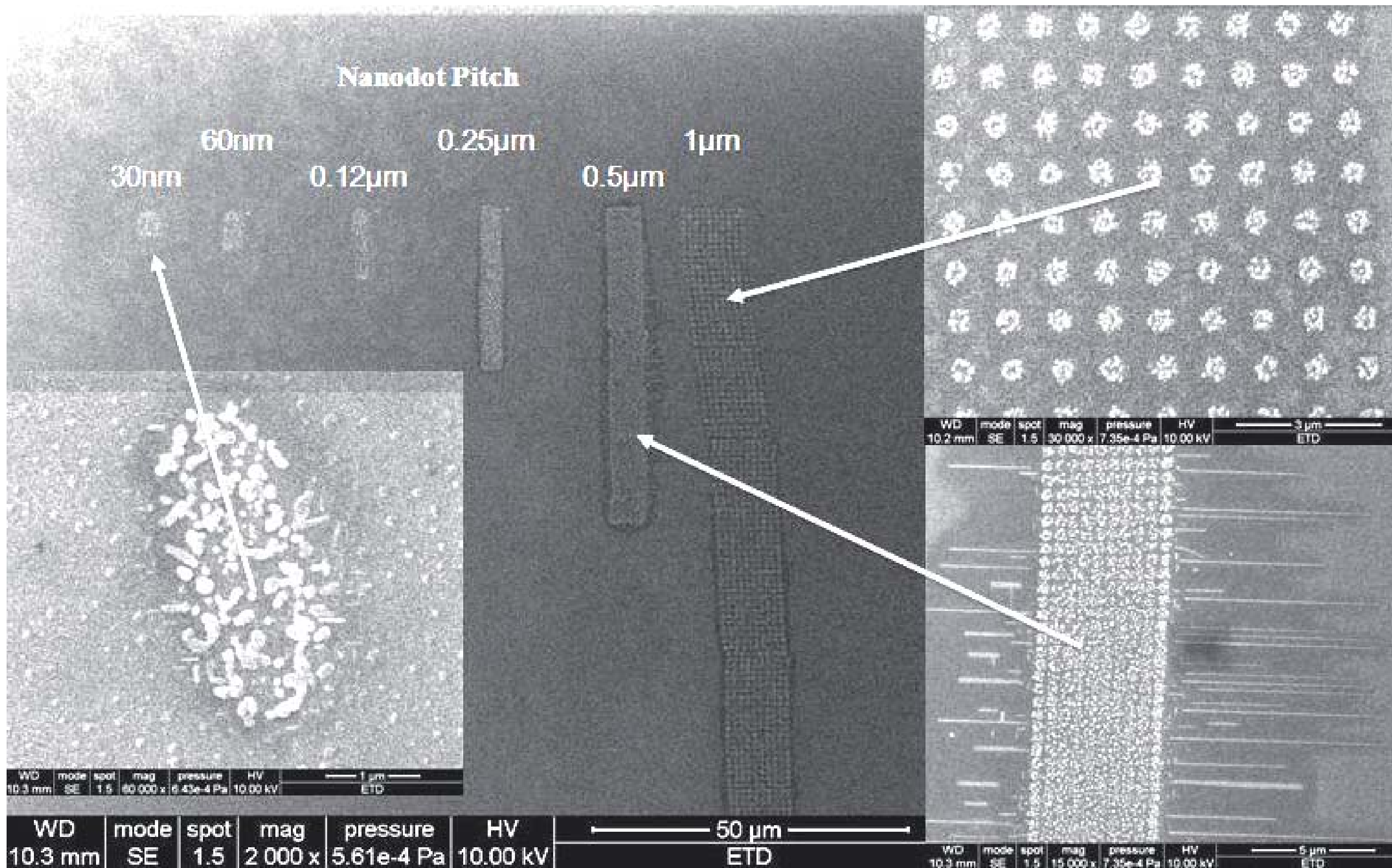

Figure 3-14 *Six columns of different pitch, each arrays of 10 x 100 high dosage annealed nanodots on STO with dosage 1500 pC. Pitch variation consisted of 30 nm, 60 nm, 125 nm, 250 nm, 500 nm, and 1000 nm.*

By altering one of the variables used in promoting nanowire growth, one is able to gain a deeper insight into the underlying mechanism. Here in figure 3-14 the dependence to pitch can be seen clearly due to each column consisting of exactly ten by one hundred nanoislands each with the same radiation dosage of one nanocoulombs. Hence the only parameter changing between the columns was the distance between irradiated dots; it ranged from one micrometer to thirty nanometers. This caused variation in the final annealed structures. This can be seen in the inset SEM images. The lowest density column produced isolated polycrystalline nanodots and the highest density produced a singular polycrystalline clump. However, in between these two extremes, nanowires were observed to grow. Specifically, the nanowires grew here when the pitch was five hundred nanometers. Other dosages will alter this particular dependence on pitch slightly, however it has been observed for AHD growth, the pitch ranges from eight hundred to two hundred nanometers.

The local region surrounding the nanodots has been altered and can be seen in the close-ups of the three columns figure 3-14. The two lowest density columns show dark secondary regions surrounding the nanodots

whereas the highest density column shows no dark secondary zone. When individual nanodots are too far apart, a continuous cross-linked region is also not formed, and hence nanowires are not promoted. Interpreting these results suggests that when too much charge is transmitted to an area, the surrounding cross-linked region found in figure 3-12 is destroyed and hence there is no feed material for nanowires once annealed. Hence, a balance is needed to generate nanowires, which is enough feed material by cross-linking an area around the primary nanoislands, and high dosage nanodots which act as seed sites.

3.2.3 TEM Lamella of AHD Nanowires on STO

In order to analyze the crystalline nature of these nanowires, a TEM lamella was made by FIB. This lamella was made specifically to observe the crystallographic structure and the chemical composition of the nanowires. An array of nanoislands was written so as to produce long uniform nanowires for this lamella. The nanowires were then covered with a twenty nanometer thick gold layer followed by a localized platinum layer as can be seen in figure 3-15. These metallic layers were to protect the nanowires from amorphization during the cutting process and increase surface conductivity. The cut of the lamella was chosen to be cross-sectional so as to increase the likelihood of encountering a nanowire. It is also possible to see here the anisotropic nature of the individual nanowires. This asymmetry was unable to be detected with AFM as one can see from figure 3-13. This particular sample was further polished to the point where it was approximately one hundred nanometers in thickness.

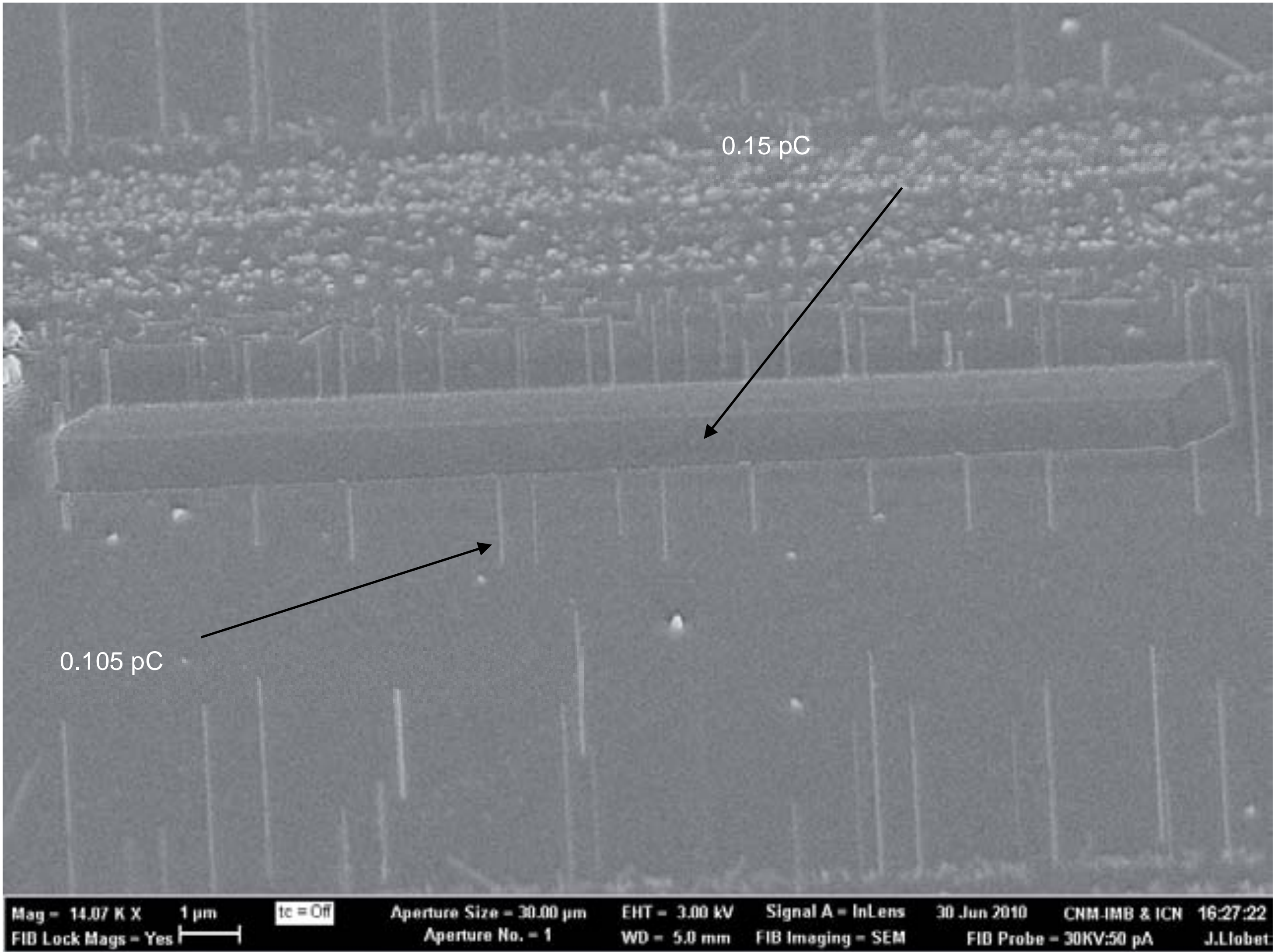
0.15 pC
0.105 pC
Mag = 14.07 K X
1 µm
FIB Lock Mags = Yes
tc = Off
Aperture Size = 30.00 µm
Aperture No. = 1
EHT = 3.00 kV
WD = 5.0 mm
Signal A = InLens
FIB Imaging = SEM
30 Jun 2010
FIB Probe = 30KV:50 pA
CNM-IMB & ICN
16:27:22

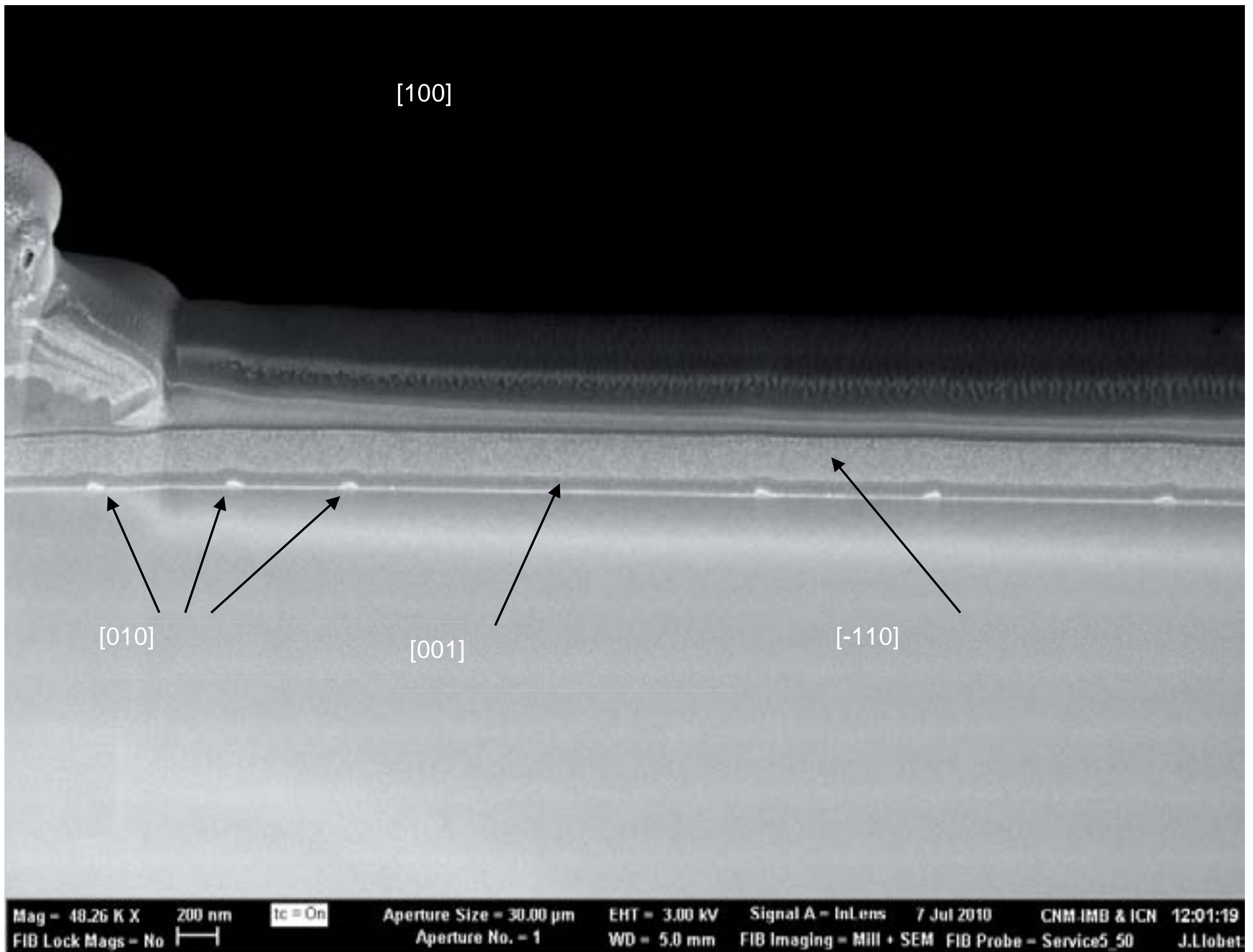

Figure 3-15 *Left: AHD nanowires being coated by platinum. Right: cross-section showing six nanowires on STO.*

3.2.4 TEM Results of AHD Nanowires on STO

A single nanowire was observed with high resolution TEM in figure 3-16 and revealed an epitaxial growth of a single crystal upon the STO substrate. This hetroepitaxy can be seen be noting that the frequency of It showed the nanowire grew as an obtuse triangle with angles fifteen and forty-five. What was not observed was any thin film underneath the nanowire or an inclusion in the STO substrate. This is different than recent TEM analysis of similar oxide systems where it was showed manganese inclusions underneath where nanostructures were [22]. Looking closely at the HRTEM image, one can see the epitaxial interface between the STO and nanowire. The Fourier transform showed an atomic plane spacing of 0.83 nanometers. Unfortunately, the knowledge to construct the unit cell of this crystal would require two more lamella be made of the nanowire.

In order to determine which elements were present in the nanowire, an EELS line scan was performed as can be seen in figure 3-17. When scanning the nanowire the elements lanthanum and oxygen were detected, however manganese and strontium were not. Scanning the substrate, it revealed titanium and oxygen. The fact that strontium was not detected in both the nanowire and substrate came as no surprise due to limit of low energies for the electrons impinged upon the lamella; a higher energy level is necessary to observe this peak. The lack of detection of manganese remained more troubling however. Despite the fact that manganese was introduced into the precursor solution and was confirmed to grow LSMO as a thin film on STO, the nanowires seemed to be devoid of any manganese. This fell in line with the other crystals made from this precursor with electron beam lithography except the observance of a LSMO wetting layer beneath the nanodot [23].

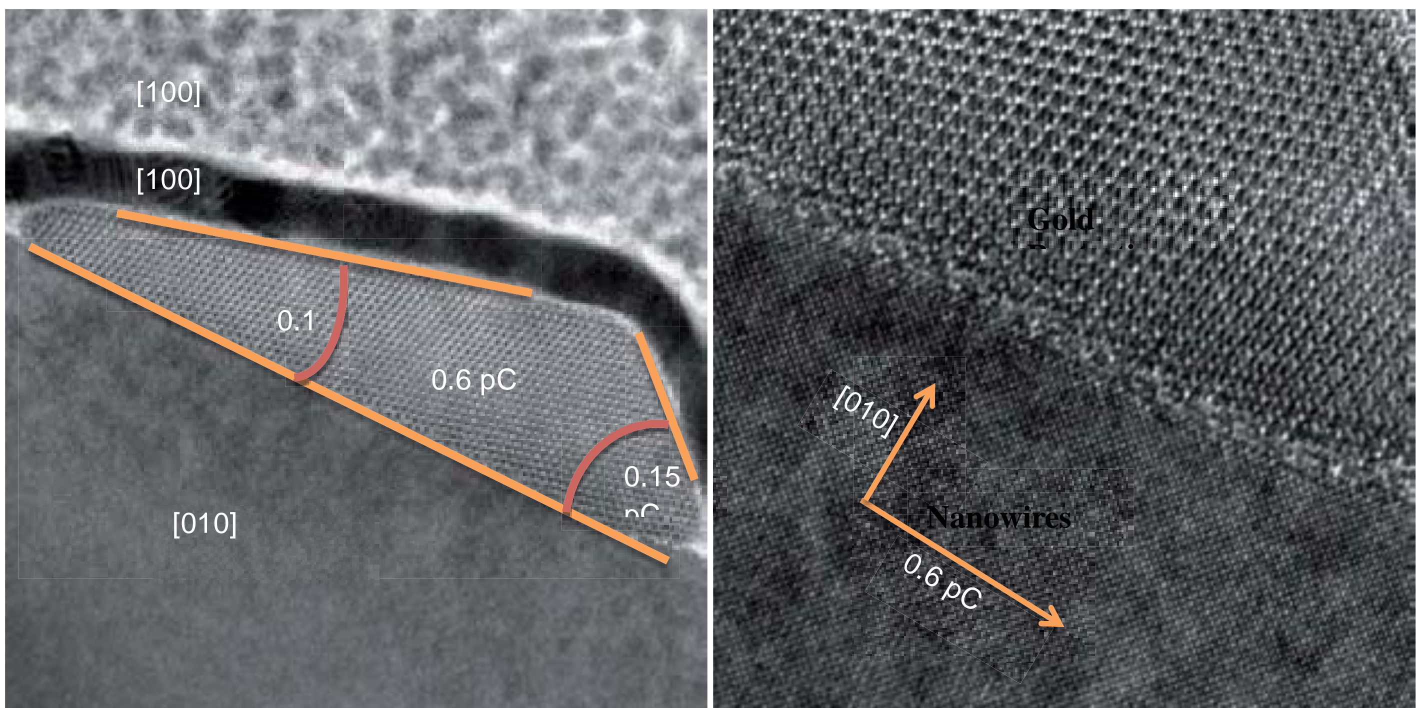

Figure 3-16 Left: HRTEM image of cross section of AHD nanowire on top of STO and the crystals facet angle. Right: zoom of interface.

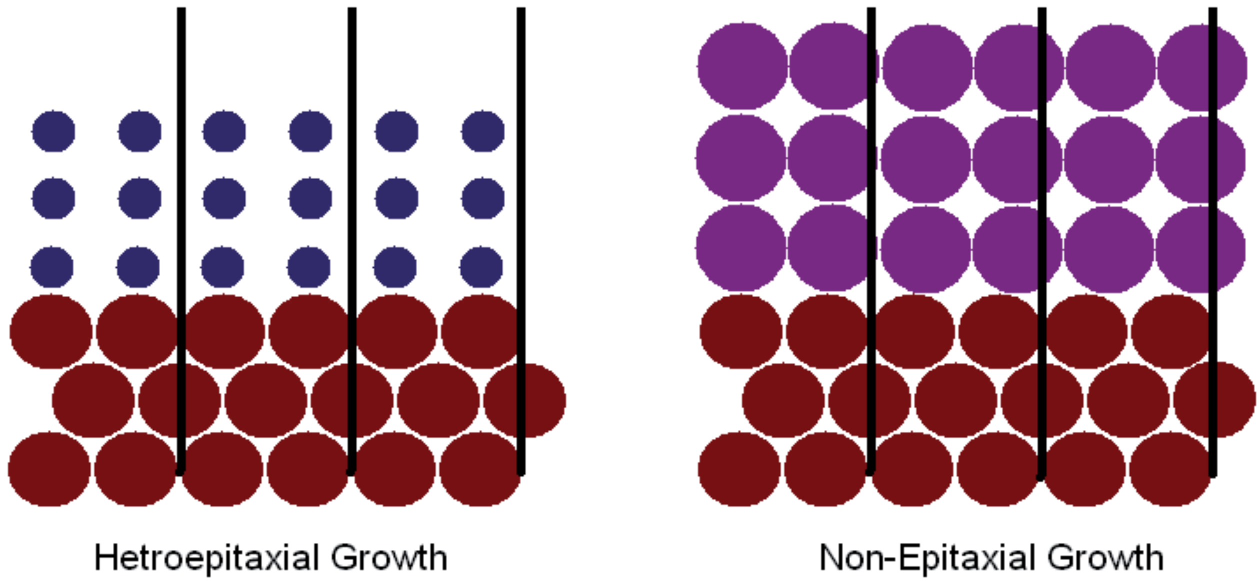

Figure 3-17 *Left: schematic of hetreoepitaxial growth. Right: schematic of non-epitaxial growth.*

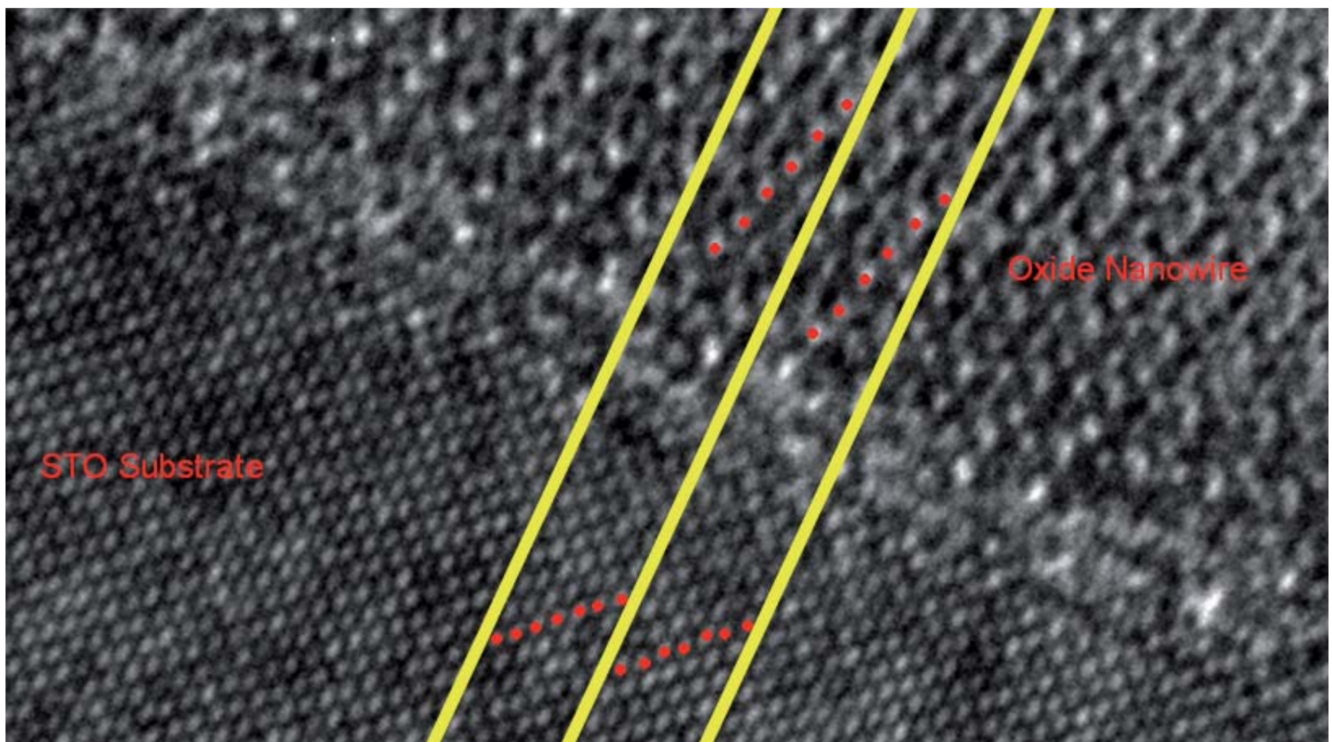

Figure 3-18 *Zoom of interface between STO and oxide nanowire showing hetroepitaxy.* \

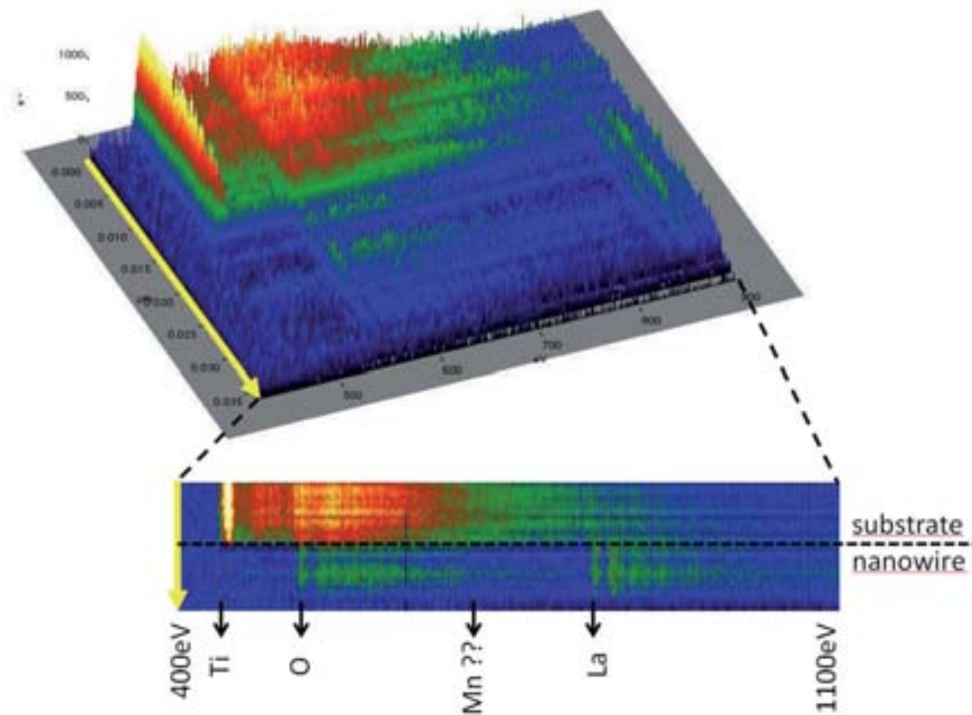

Figure 3-19 *EELS line scan showing the elements detected in the substrate and nanowire on STO.*

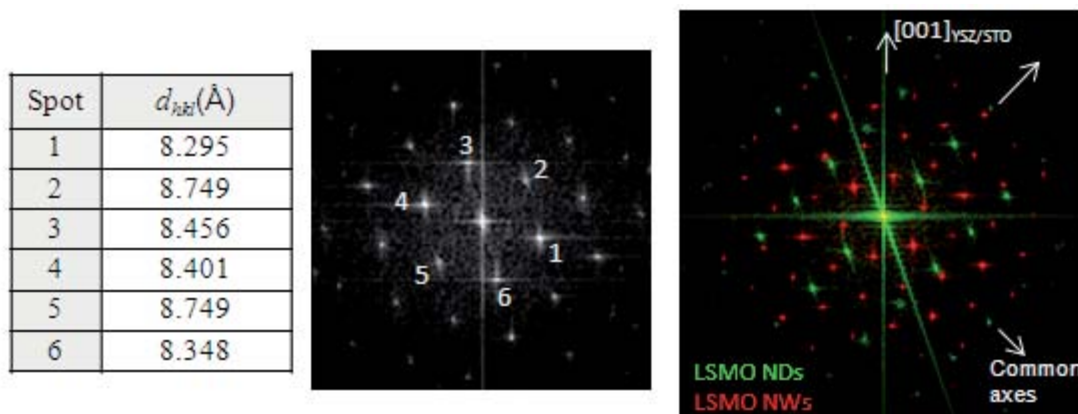

Spot	d_{hkl}(Å)
1	8.295
2	8.749
3	8.456
4	8.401
5	8.749
6	8.348

Figure 3-20 *Left: atomic planes seen by taking Fourier transform of nanowire grown on STO. Center: Fourier transform. Right: composite image showing discrepancy between nanowire on STO and nanodot on YSZ.*

3.2.5 Orientational Relationship of AHD Nanowires

Initially all the sides of the high dosage arrays were oriented parallel to the cut of the crystal. This provided ideal conditions due to the nanowires growing perpendicular to these sides. However, it was unclear if the actual orientation of the arrays played any real part in the nanowire growth. That is, if the array were rotated

forty five degrees to normal, would the nanowires conform to this new arrangement and grow still along the (010) and (100) directions. The experiment was quickly performed at the same conditions as used to make the array in section 3.2.1 and seen in figure 3-21. A square array written at forty five degrees to the cut of the substrate was made and then annealed; subsequent nanowires grew largely in the same direction as in previous experiments.

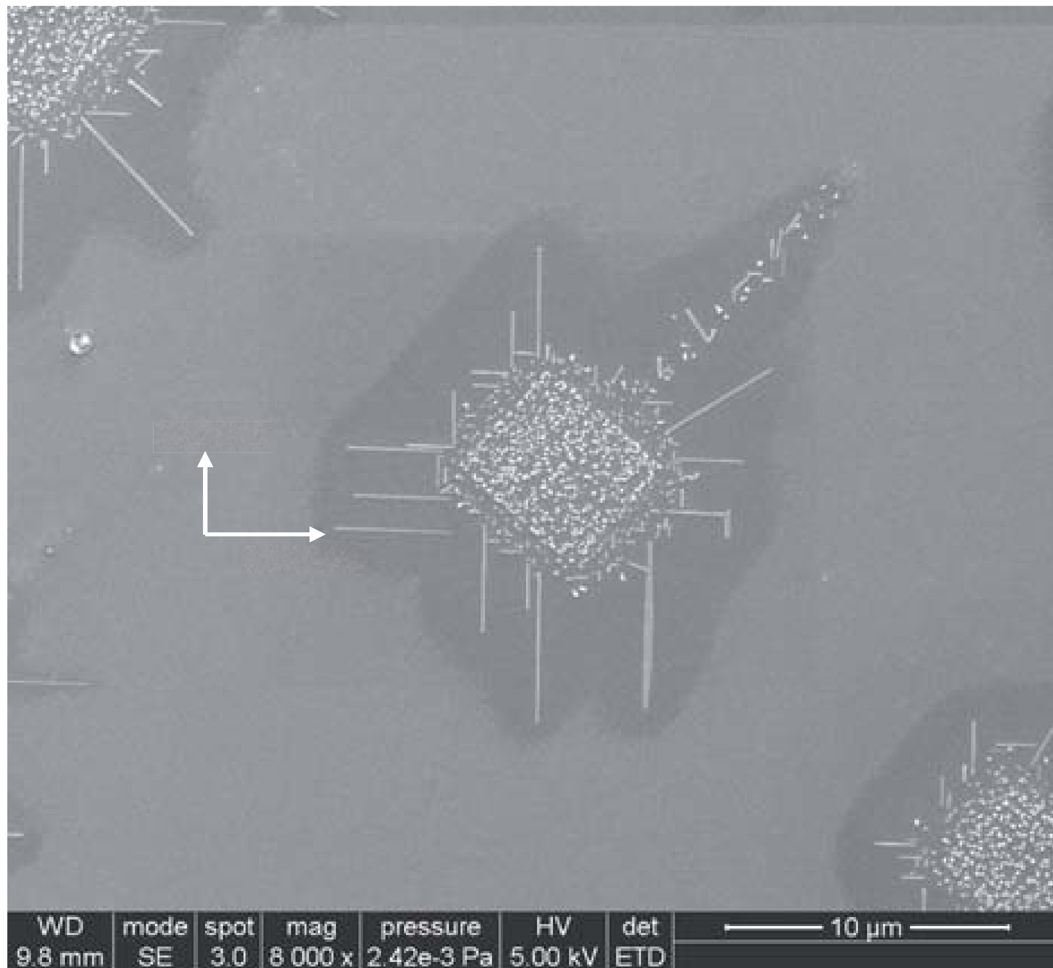

Figure 3-21 *Annealed square array rotated forty-five degrees from normal growing oriented nanowires. Array size 10 x 10 with each site receiving 1500 pC and 750 nm pitch on STO.*

There appears to be no change in the number of nanowires grown from the array either. The led to the conclusion that the nanowires are growing in those directions due to mainly substrate constraints and not due to the physical barrier of an angled array-edge. This also suggests that the nanowires may be grown with a less rigid definition of an array. In other words, the only true necessity for nanowire growth so far is the dosage, pitch, size of array but not its shape.

3.2.6 Number of Neighbors Dependence for AHD Nanowires on STO

The number of nearest neighbors is also a dependent variable in nanowire growth on STO. When controlling for dosage and pitch, while varying the number of nanodots in the array, there appears to be limit of how small the array may be. An experiment was made consisting of a series of nanodots with a similar pitch of 750nm between neighbors as seen in figure 3-22. The controlled variables were the horizontal axis dosage while on the vertical axis the number of neighbors increased. This showed that increasing the number of neighbors increased the likelihood of spontaneous nanowire growth. This can be seen between the 4x4 and 5x5 squares at 500 picocoulombs.

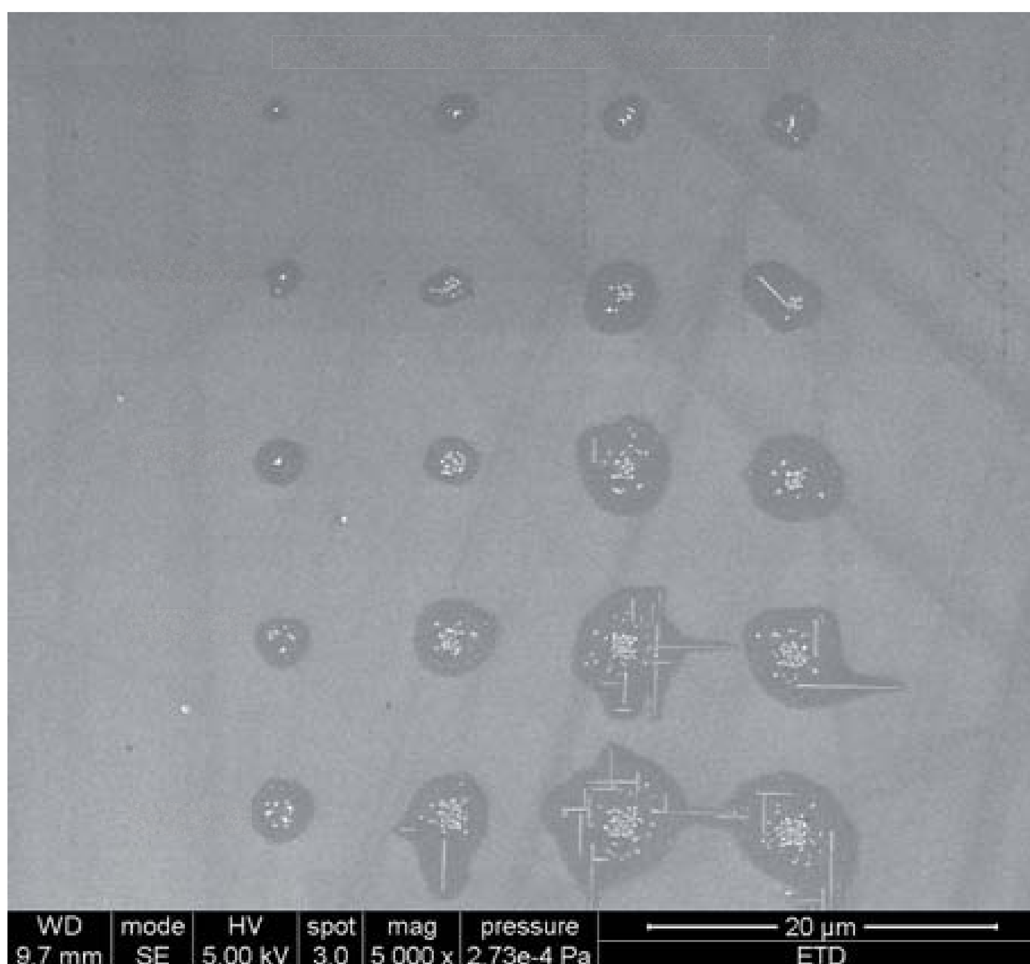

Figure 3-22 *Alteration in number of neighbors and dosage in array on STO. Arrays of varying sizes from 1x1 to 5x5 with varying dosages from 250 pC to 2000 pC all with 750 nm pitch.*

Interpreting these results gives insight into the nature of this type of nanowire formation. Simply having a nanodot with sufficient dosage to cause nanowire growth for arrays is not enough when isolated. Also

increasing this array up to three by three is still not enough to guarantee nanowires to form. Occasionally single nanowires are seen to have formed when the array is small, but consistent growth is absent. Hence, an area that has a sufficiently large continuous secondary zone surrounding the nanoislands is somehow more prone to promote nanowires. Also of note in these images is the observation that even though a small array may be written, once annealed, these nanodots may coalesce into a variety of nanostructures as can be seen in figure 3-23.

Figure 3-23 *Close-up of a high dosage 2x2 array showing variety of nanostructures including nanowire, nanodots in triangular form and irregular shaped form. Array size received 2000 pC and had 750 nm pitch on STO.*

3.2.7 Dosage Dependence for AHD Nanowires on STO

As one could have determined from the previous section, the growth of nanowires is greatly dependent on the individual dosages of nanodots. The dosage dependence can been seen in the next four SEM images in figure 3-24. The dosage increases from 100 to 1500 picocoulombs, displaying non-nanowire growth until full nanowire growth. The number of nanodots in each array here was 10x10 and the pitch was 200nm in each array. Interpeting these results indicates there exists a lower bound for nanowire growth for a particular array

configuration. Lowering the dosage to 100 picocoulombs, one can see very small nanowires inside the radiated area, however long nanowires are absent. Increasing the dosage to 500 picocoulombs, the first long nanowire is observed but growing at an odd angle. Increasing the dosage still further to 1000 picocoulombs, a multitude of nanowires are seen to have sprung from the array. Finally at 1500 picocoulombs, the array produced an extremely large number of nanowires and no small nanowires are seen inside the radiated area.

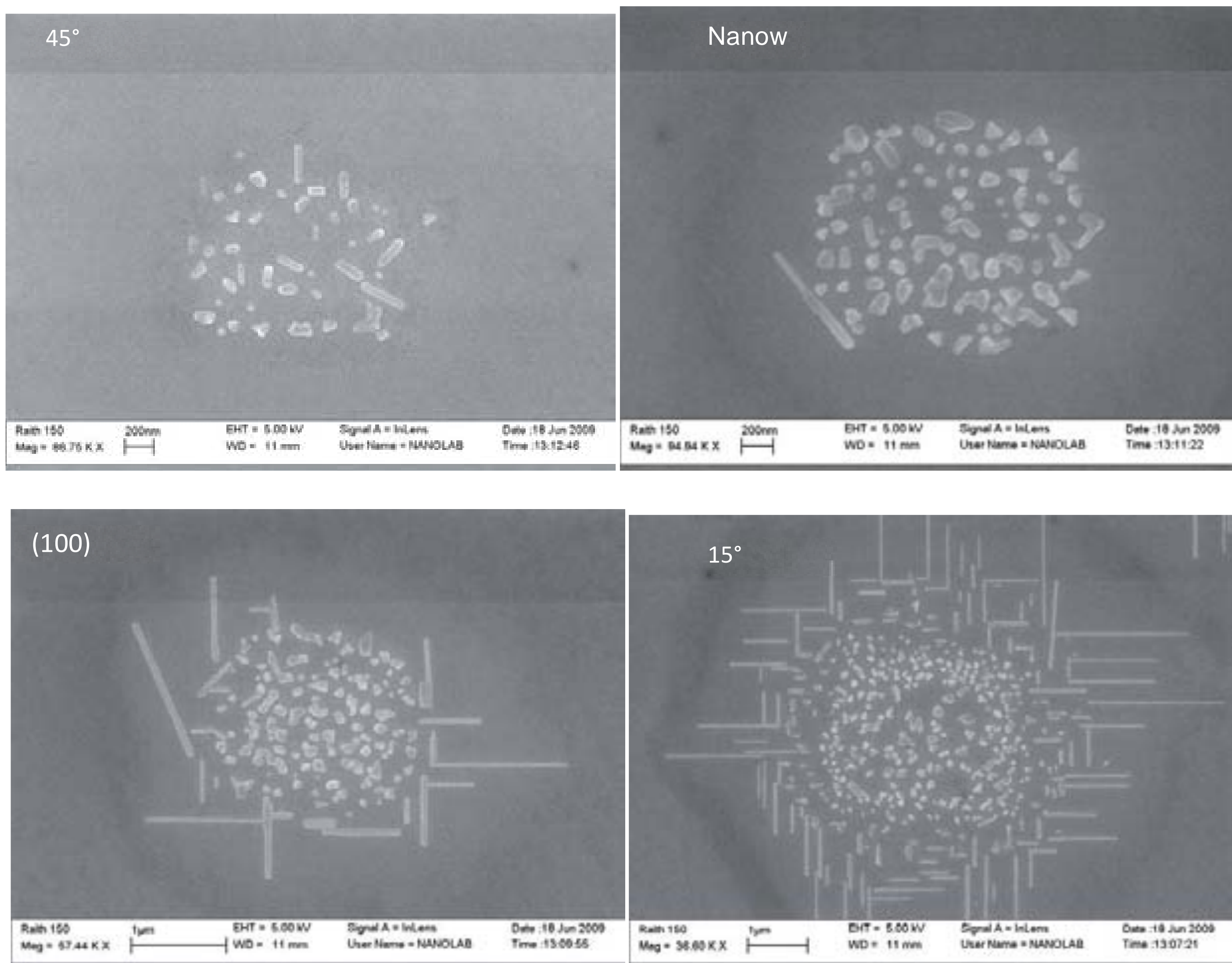

Figure 3-24 *Alteration of dosage on arrays showing nanowire growth changes. Array size 10 x 10 with 750 nm pitch on STO with dosages of 100 pC to 1500 pC.*

3.2.8 Neighboring Effect on AHD Nanowires on STO

It has been observed that arrays can have influence on each other as far as nanowire growth is concerned. This can be seen when arrays are close to each other, the nanowires grow differently than when no neighboring array is near. When between two close arrays, the nanowires grow noticeably shorter in length.

Also the space between the arrays is evenly and homogeneously filled with these short nanowires. If the two large squares are relatively far from each other, the nanowires grow to full length. This can be seen in the SEM image of figure 3-25 and 3-26 where the gap is five and ten micrometers respectively. The nanowires do not grow off of the edge of the array, rather they may grow practically anywhere between the two arrays. When one interprets these results, one comes to the conclusion that entire space between the two arrays must have been somehow primed to growing nanowires prior to high temperature annealing. A close-up of this phenomenon is seen in figure 3-31.

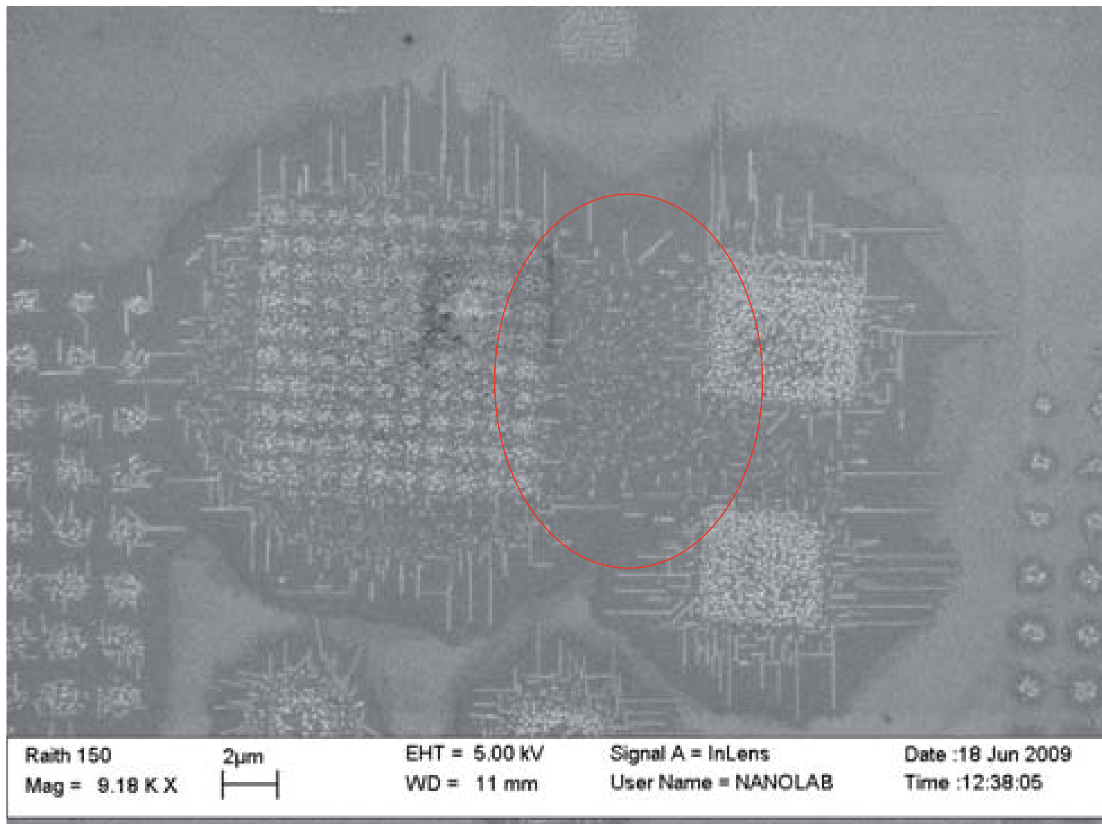

Figure 3-25 *Stunted nanowire growth between close arrays of distance five micrometers on STO.*

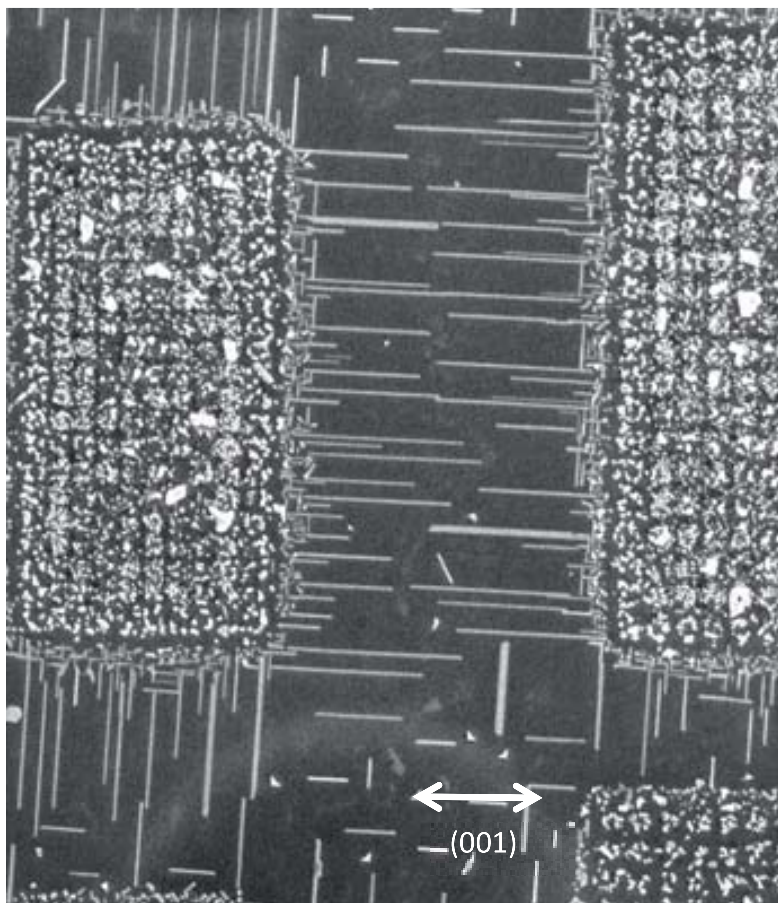

Figure 3-26 *Normal nanowire growth between widely separated arrays of ten micrometers on STO.*

3.2.9 AHD Nanowire Growth as a Function of Temperature

In order to understand the nature of the nanowires, the irradiated zones were observed with SEM at various temperatures. The objective was to observe when nanowires began to form and how their constituent nanostructures evolved. In order to perform this experiment, a characteristic array of nanoislands was written in order to be easily identified after subsequent annealings. This was a 3x20 array with dosage 1000 pC and pitch 800nm. A general observation of how a particular array evolved was of interest here. In the left hand SEM image in figure 3-27, one may see the location where the nanowires grew before any crystallization occurred after 60min at 600 °C. One can see that initially there exists a dark layer surrounding the donut shaped nanoislands, which has previously been shown with AFM to be a layer of polymer before annealing in figure 3-12.

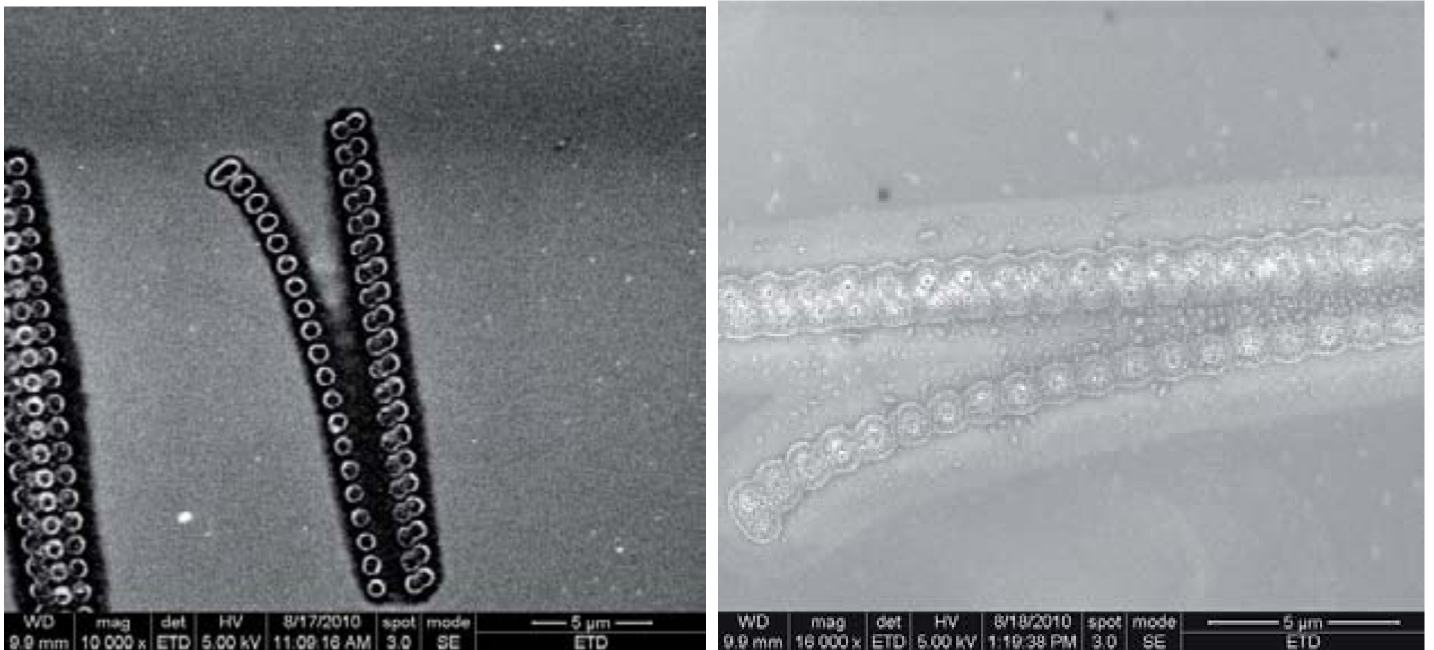

Figure 3-27 *Left: nanodots annealed at 600 °C for 60min. Right: same nanodots after 800 °C for 60 more minutes. Array size 2 x 20 with each site receiving 1500 pC on STO.*

On the right of figure 3-27, it can be observed after 60 more minutes at 800 °C, the first occurrences of crystal formation in the written structures. The general morphology of the written structures is preserved in some instances, while in others the structure has broken down already. What is also seen in the area that was cross-linked is the formation heterogeneities. Also of note is the occurrence of small triangles in between the two strands of nanoislands which is absent when the two strands start to come apart.

In figure 3-28, the nanowires can clearly be seen to have formed at the edge of this secondary zone and not at the site of the written structures after 60 more minutes at 1000 degrees. The nanowires seem to have affected the surroundings in the sense that there exists an area far away from the written structures which appears non-uniform, whereas surrounding this zone the film appears uniform. Immediately next to the nanowires one can see that the film has been cleared by their formation. Interpreting these three SEM images at different stages of nanowire formation, one can see the how the nanowires started at the edge of the secondary zone and that they grow by consuming the remaining film.

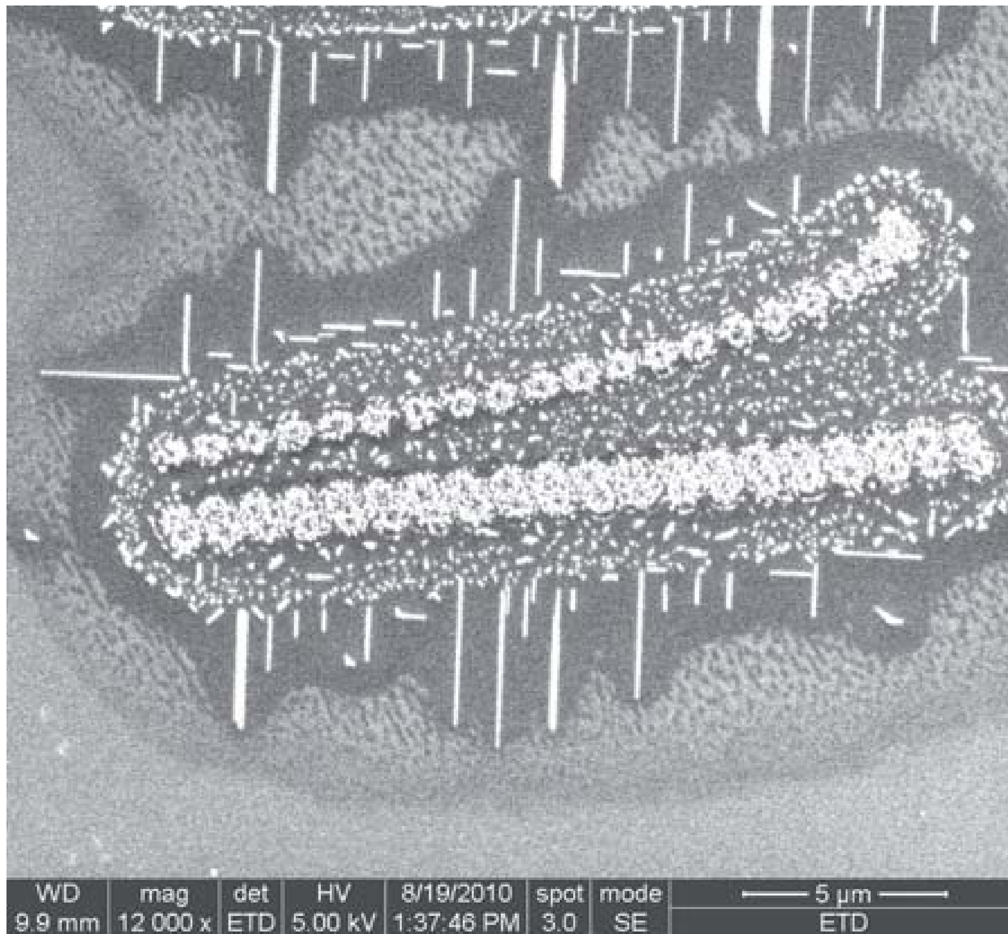

Figure 3-28 *Nanodots annealed at 1000 °C for still 60 more minutes. Array size 2 x 20 with each site receiving 1500 pC on STO.*

3.2.10 Unconstrained Growth as a Function of Annealing Time

In an attempt to refine our understanding of nanowire growth, two arrays were observed as a function of annealing time. The two arrays differ in that one is written very close to another array, leading to constrained growth such as in section 3.2.9, and the other is written with any neighboring arrays, leading to normal growth. In order to perform this experiment, a sample had a series of high dosage nanoislands written as an array. The sample was then annealed at one thousand degrees for one hour, then four more, and finally sixteen hours more. What is observed in general is a fast growth initially and then a ceasing of growth at long times. One can see the behavior of the nanowires beginning at the edge of the cross-linked area as previously seen. Furthermore, one can see the cleaning of the substrate from the nanowires as they consume the unorganized particles in order to grow, known as ripening. This can be seen as a difference in the contrast in the SEM images.

The lengths of the nanowires after one hour at one thousand degrees range from one to four micrometers as seen on the left of figure 3-29. Also of note is that the location where the nanowires grew seems to be random

along the edge of the cross-linked area. Observing this grouping of nanowires as a function of time shows a non-uniform growth for individual nanowires. This could be due to the longer nanowires consuming sufficient material as to prevent growth in the shorter nanowires. This possibly could cap the nanowire and prevent any further nanowire growth even though at high temperatures and long times there is a high mobility of particles on the substrate.

When looking at the center of figure 3-29 one can see the nanowires after annealing for four more hours, one can see that the lengths have increased. The nanowires which grew did so to just under eight micrometers. One glaring aspect is the lack of growth from some of the nanowires. While some of the nanowires doubled in length, others failed to grow at all. Also seen is the secondary zone is much less cluttered than in the image after one hour of growth. It appears that this region coalesced into larger triangular nanoparticles.

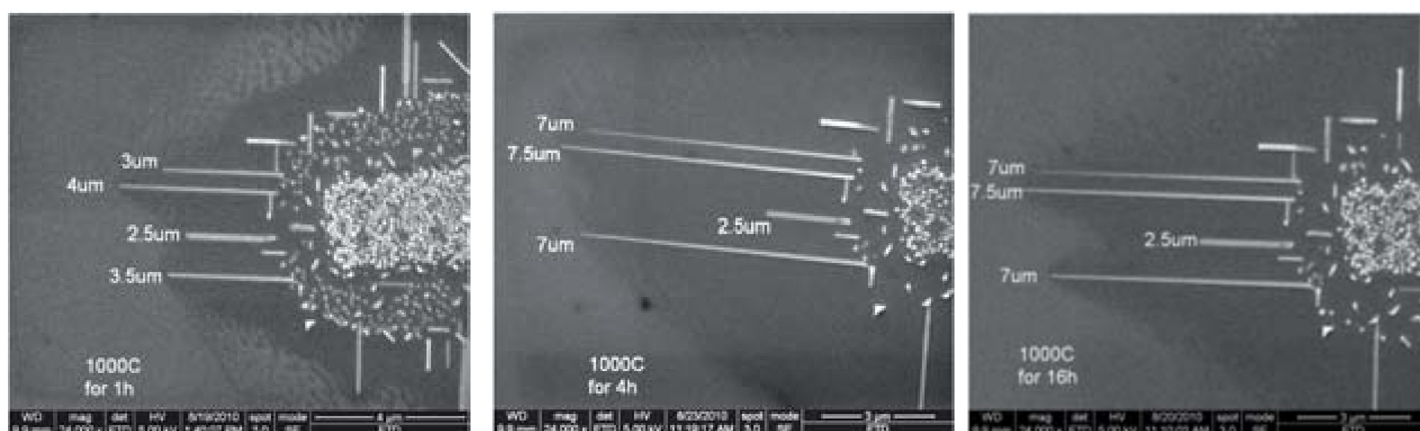

Figure 3-29 *Growth of specific nanowires as a function of time for initially one hour, then four more hours, then sixteen more hours. Array size 3 x 10 with each site receiving 1500 pC and 750 nm pitch.*

Finally after sixteen more hours of growth as seen on the right of figure 3-29, it does appear that the nanowires have stopped growing in a discernible way. The contrast change surrounding the nanowires appears to be wider along their lengths as opposed to directly at the tip of the nanowire. It also appears that the nanowires tend to be narrower where they have grown when compared to their bases which are wider. One of these nanowires came almost to come to a point after a total of twenty-one hours at one thousand degrees. This phenomenon would suggest that as the nanowire grows, its cross sectional area decreased slowly until it is not possible for further growth. This can be also seen in figure 3-30, where an array was annealed for one hundred hours. Here one sees that nanowires have consumed all the feed materials on the surface and have thus stopped growning and some nanowires have come to a point.

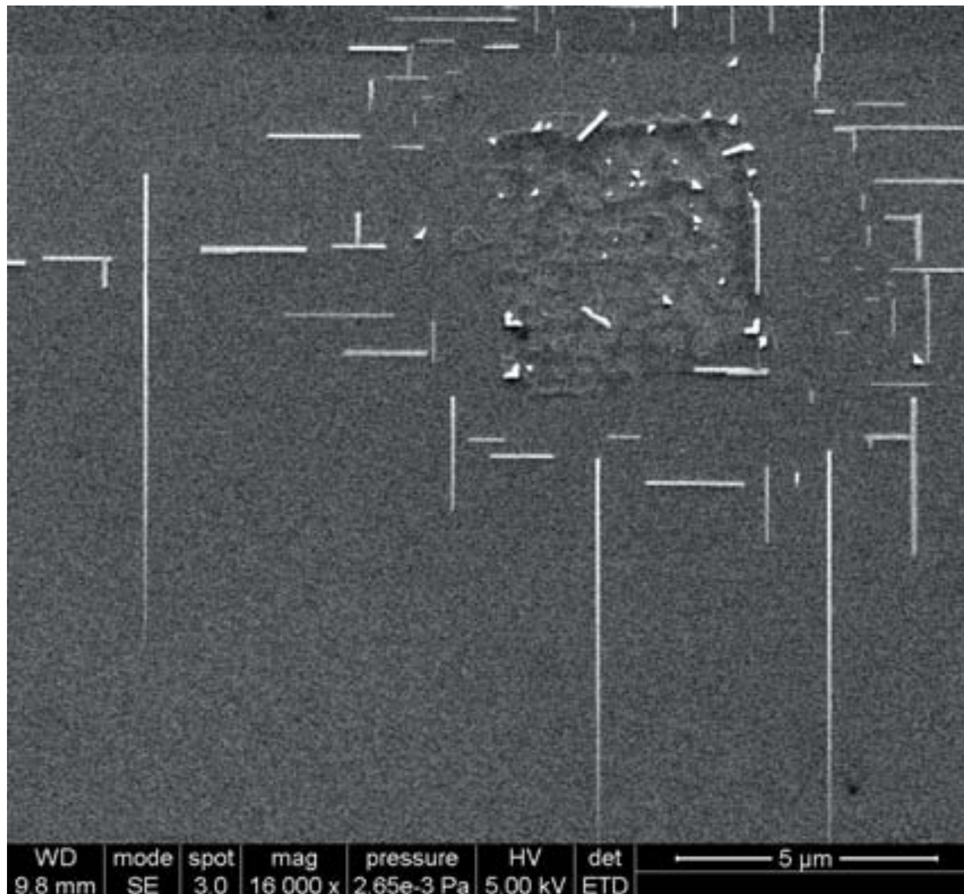

Figure 3-30 *Nanowires after one hundred hours at 1000C. Array size 10 x 10 with each site receiving 1500 pC and 750 nm pitch on STO.*

3.2.11 Constrained Growth as a Function of Annealing Time

It was observed that in image 3-25 that nanowires behave differently when grown between two large arrays of high dosage nanodots. This phenomenon was that nanowires grew shorter than they would grow if between two closely spaced arrays. Another aspect that was observed for these types of nanowires is the homogeneous growth not springing from the array walls. In other words, the nanowires do not grow out from the edge of the irradiated zone, but rather grow homogenously in the space. This is, of course, far different than the typical growth mode observed when unobstructed. In other words, the nanowires do not grow solely from the edge of the secondary zone, they grow without any observable preference between the two close formed arrays.

In order to understand this growth mode more, an experiment was performed in which this nanowires would be subjected to increasingly longer annealing times, as can be seen in figure 3-31. The purpose was to determine if the nanowires were changing in morphology over time and if new nanowires were growing

spontaneously. The same area was observed at one, five, and twenty-one hours of total time at one thousand degrees. The gap where nanowires grew was five micrometers. The first image on the left shows the nanowires after one hour at a thousand degrees. The nanowires here appeared to be arranged in a homogeneous distribution in between the two arrays. The nanowires also tended to be small, on the order of three micrometers at the biggest to less than half a micrometer at the smallest. The nanowires also appear to have a consistent width along their lengths. In all three SEM images one can see that two regions have been circled. This is to highlight the changes to the nanowires as a whole through these two examples.

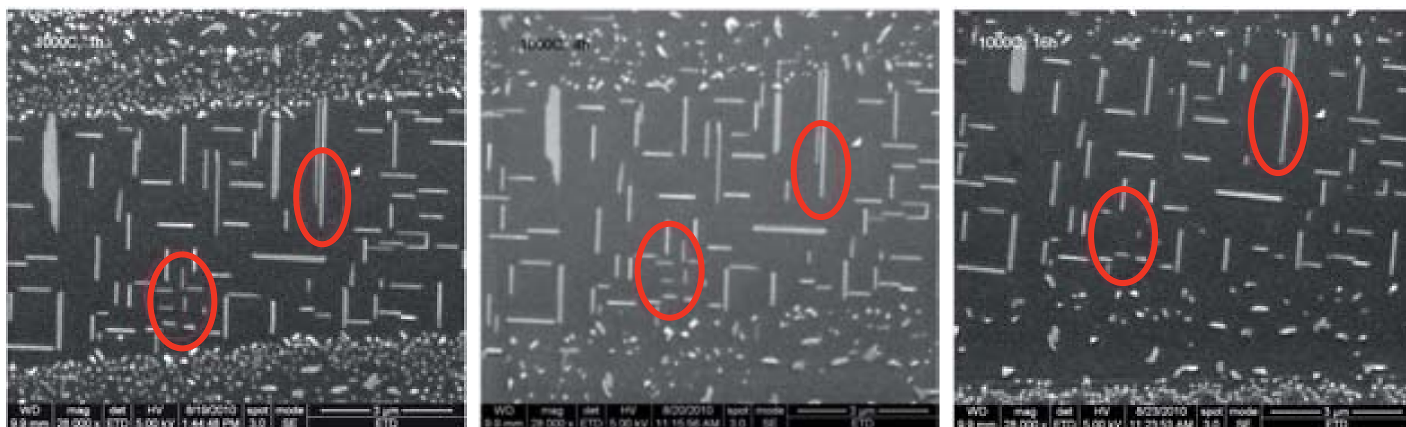

Figure 3-31 *Growth of constrained nanowires at 1000C after one hour, then four more hours, and then sixteen more hours. Array sizes 10 x 10 with each site receiving 1500 pC and 750 nm pitch on STO.*

Looking at the center image in figure 3-31, the substrate has seen four more hours at one thousand degrees. The small individual nanoparticles at the edges of the array have coalesced into larger particles similar to Ostwald ripening. The number and length of the nanowires has not increased. Besides the reduction in the number of small particles at the edges, there appears to be no change in the system after four times more annealing, except for a small reduction in some nanowire lengths. This seems to point to a halt in dynamics with regards to nanowire growth after a certain period of fast growth. This differs starkly with the nanowires which have grown longer after four more hours of annealing when non-constrained. One explanation may lie with the availability of feed stock for unrestricted nanowires growth and a lack of this unorganized material for the restricted nanowires.

Finally, one can see after sixteen more hours at a thousand degrees, no further nanowire growth is observed. In fact, some of the nanowires have oddly disappeared, as marked on the SEM image, as well as reductions in some nanowire lengths. This points to a lack of strong adhesion to the STO substrate with regards to some of the nanowires. Perhaps the long times at high heat were able to dislodge some of the nanowires from the

surface. One of the nanowires is seen to have been reduced to half its original length due to these excessive annealing times. This lack of further growth for the nanowires is similar to that for the non-constricted case.

3.2.12 Long Distance Nanowire Growth due to Markers

Due to the high dosage needed to generate the large arrays which produced nanowires, it took very long times to write these structures. This lengthy process could only produce a few arrays in a given session's allotted time. Also these structures, by their very nature, possess a small footprint. All told, these structures are difficult to find again after annealing with the SEM. A solution was found which allowed for a small amount of the session's time to be allocated to generating markers around the arrays. These markers made it significantly easier to locate said structures later. However, an interesting byproduct of these markers was soon observed.

These markers consisted of a series of medium dosage dots in regular patterns spaced one micrometer apart, specifically fifteen picocoulombs at one micrometer pitch. The parameters used to generate the nanowires where these markers were used were the same as those used in section 3.2.1. These medium dosage nanodots could not by themselves produce nanowires in any configuration with regards to pitch or number of neighbors. However they could be seen easily under low magnification and hence could save a tremendous amount of time in determining where the nanowire arrays were and which array was which. Another point here is that the medium dosage nanoislands cross-link an area in their immediate vicinity. The interesting consequence of making these markers was their interaction with a high dosage array. In fact, these markers became the nucleation points for further nanowire growth as can be seen in the figure 3-32.

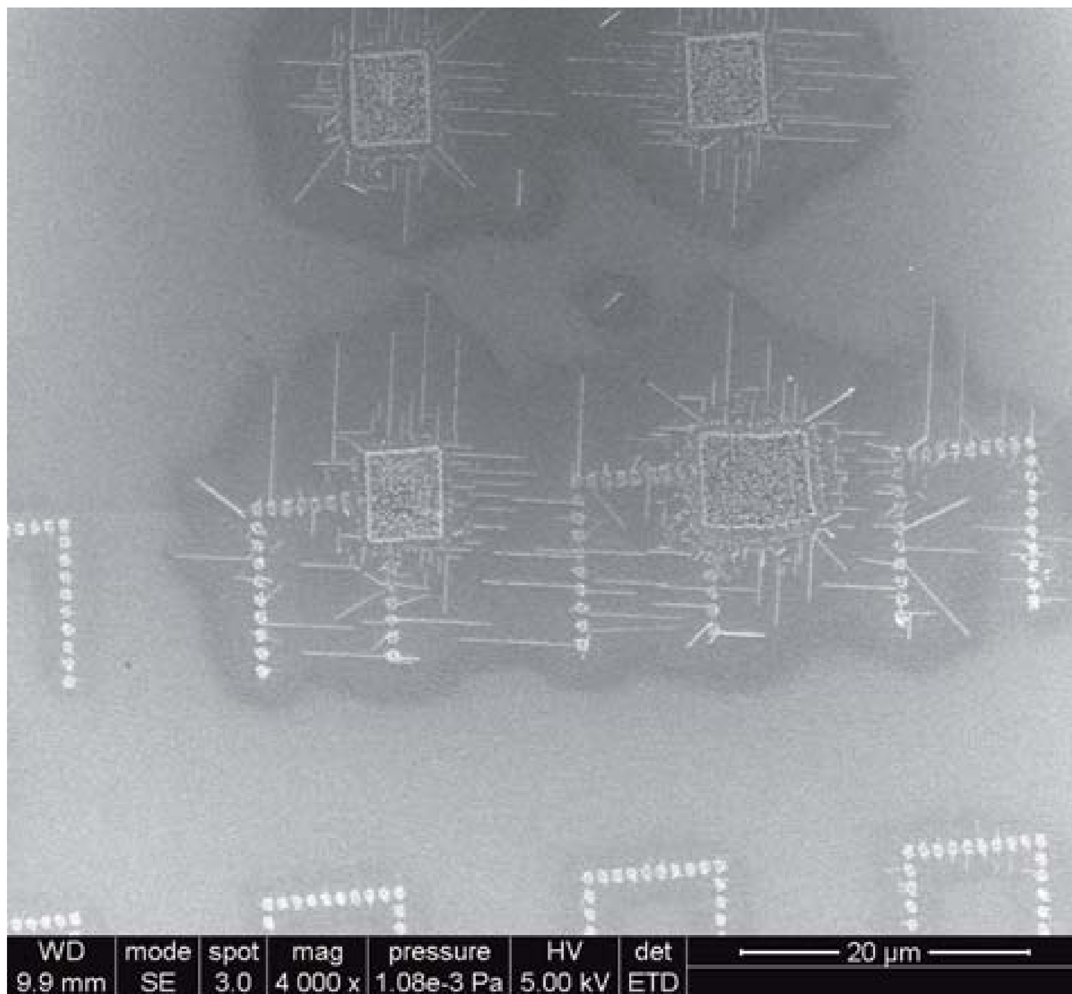

Figure 3-32 *Nanowire growth when interacting with marker nanodots on STO. Squares arrays size of 10 x 10 with each site receiving 1500 pC and 750 nm pitch. Markers had dosage 1.5 pC with pitch 1000 nm.*

In this SEM image, one can see a contrast change around all the markers which indicates this secondary zone. However under closer inspection, one can observe that this contrast difference is stronger for the markers which are somehow connected to the high dosage array. This SEM image also shows that the nanowires grow orthogonally to the edge of the markers, consistent with previous nanowire growth modes. However, the nanowires seem to grow more from the very edge of the marker than the original arrays do. The most curious part of this behavior is of course the ability of the markers, which are quite distant from the original array, to grow long nanowires as if they were part of the array.

Analysis of this growth mode for these nanowires suggests that the square array acts as a catalyst of sorts, transforming the cross-linked area around the markers into a composition prone to nanowire growth. This mechanism would then allow the nanowires to grow from the medium dosage nanodots in an orthogonal manner due to crowding out from parallel neighbors. This action-at-a-distance suggests that the nanowires

simply need to have a cross-linked film and then a nucleation point for nanowires to grow. Also of note is the lengths of these nanowires are on par with those of the non-restricted variety. This intriguing growth mode would suggest that combining an array with a series of nanodots could produce a series of nanowires.

3.2.13 Nanowires Grown at Overlaps between Arrays

The interaction between nanodots and arrays led to the idea that perhaps high dosage arrays were not necessary for this phenomenon to occur. Perhaps all that would be necessary are nanodots with sufficient dosage so as to cross-link a continuous area coupled with nucleation points. In other words, the driving mechanism would be medium dosage nanodots which do not cause AHD nanowire growth but do polymerize a continuous area. Hence above a certain dosage, a polymerization would cause nucleation of nanowires far from the intended target area by simply overlapping it with low dosage nanodots. Some interesting consequences of this behavior can been seen in figure 3-33 where the high dosage arrays were eliminated and a significant overlap between medium dosage X's and low dosage tracks of nanodots was created. The low dosage nanodots here were written and annealed prior to once again spin coating and then writing the medium dosage X's and finally annealing again. No nanowires were observed prior to the second annealing and were simply arrays of nanodots. Here the low dosage nanodots had a pitch of 800nm and dosage of 0.15 pC.

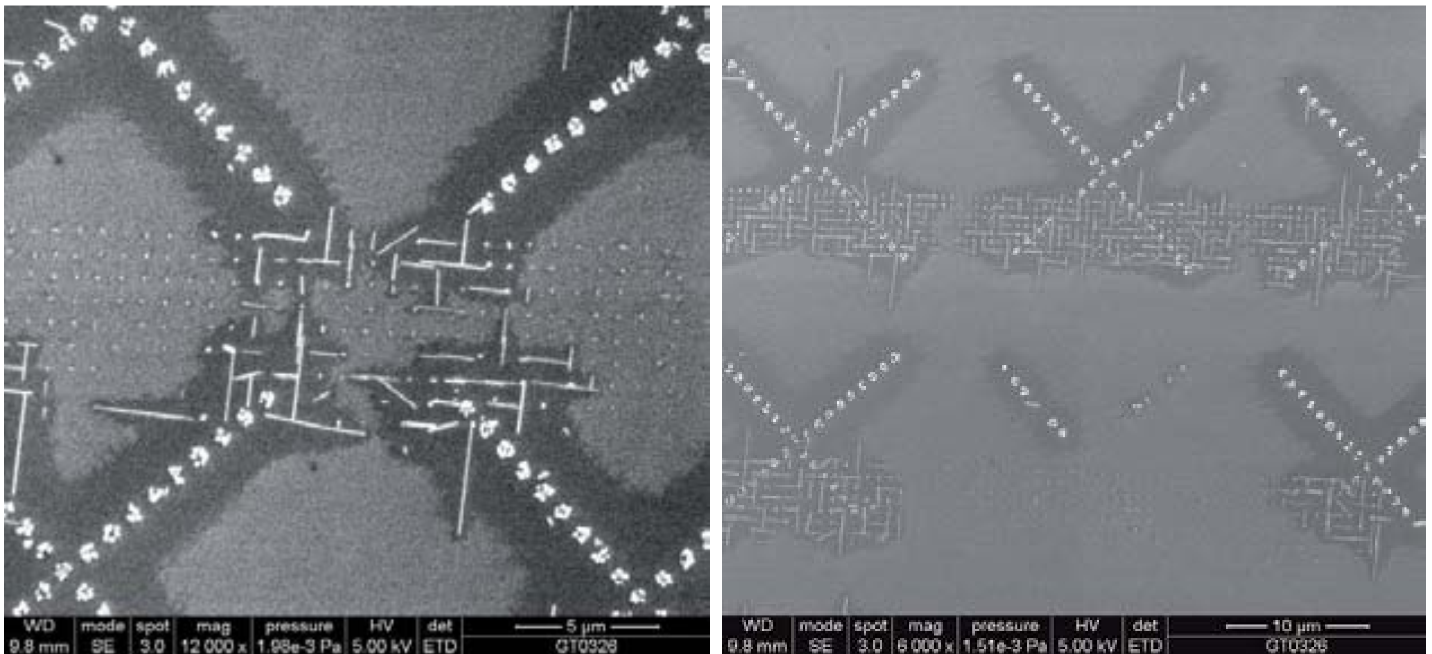

Figure 3-33 *Nanowires grown at the intersection between medium and low dosage nanodots. Array size 10 x 10 with each site receiving 1500 pC and 750 nm pitch on STO. Markers had dosage 0.15 pC with pitch 800 nm.*

In figure 3-33 one can clearly see the phenomena of nanowire growth by overlapping low dosage nanodots and medium dosage ones. When coupled, very small orthogonal nanowires grew from the sites of the low dosage nanodots as long as they started in the region that was cross-linked by medium dosage nanodots. One can see how the nanowire growth is highly controlled at the overlap. The nanowires themselves are short in length, similar to nanowires grown in a restricted space. However at the borders of this secondary zone, some of these nanowires grew longer due to an ample supply of feed stock.

3.2.14 AHD Nanowires Grown on Silicon

In an attempt to better ascertain the cause of the lack of manganese in the EELS line scan of the TEM lamella of nanowires grown on STO, nanowires were grown on silicon as seen in figure 3-34. The idea was that the STO substrate was depleting the nanowires of manganese due reports of elemental migration [22, 23]; hence a substrate which could not readily transfer mass into it would alleviate this problem. Nanowires derived from a LSMO nitrate based precursor were grown by following the same line of reasoning as with the STO derived ones; that is, by the AHD method. This method was successful at a dosage of 2000 pC with an array of 10x100 at a pitch of 400nm. This dosage is similar to that used in the AHD method on STO. An alteration to the surroundings adjacent to the area of radiation was also observed. This alteration appears as a non-homogeneous darkening in a ribbon-like fashion. The nanowires grew however in a very different manner

than the nanowires grown on STO. These silicon grown nanowires grew inside the area that was irradiated also they grew in random orientations.

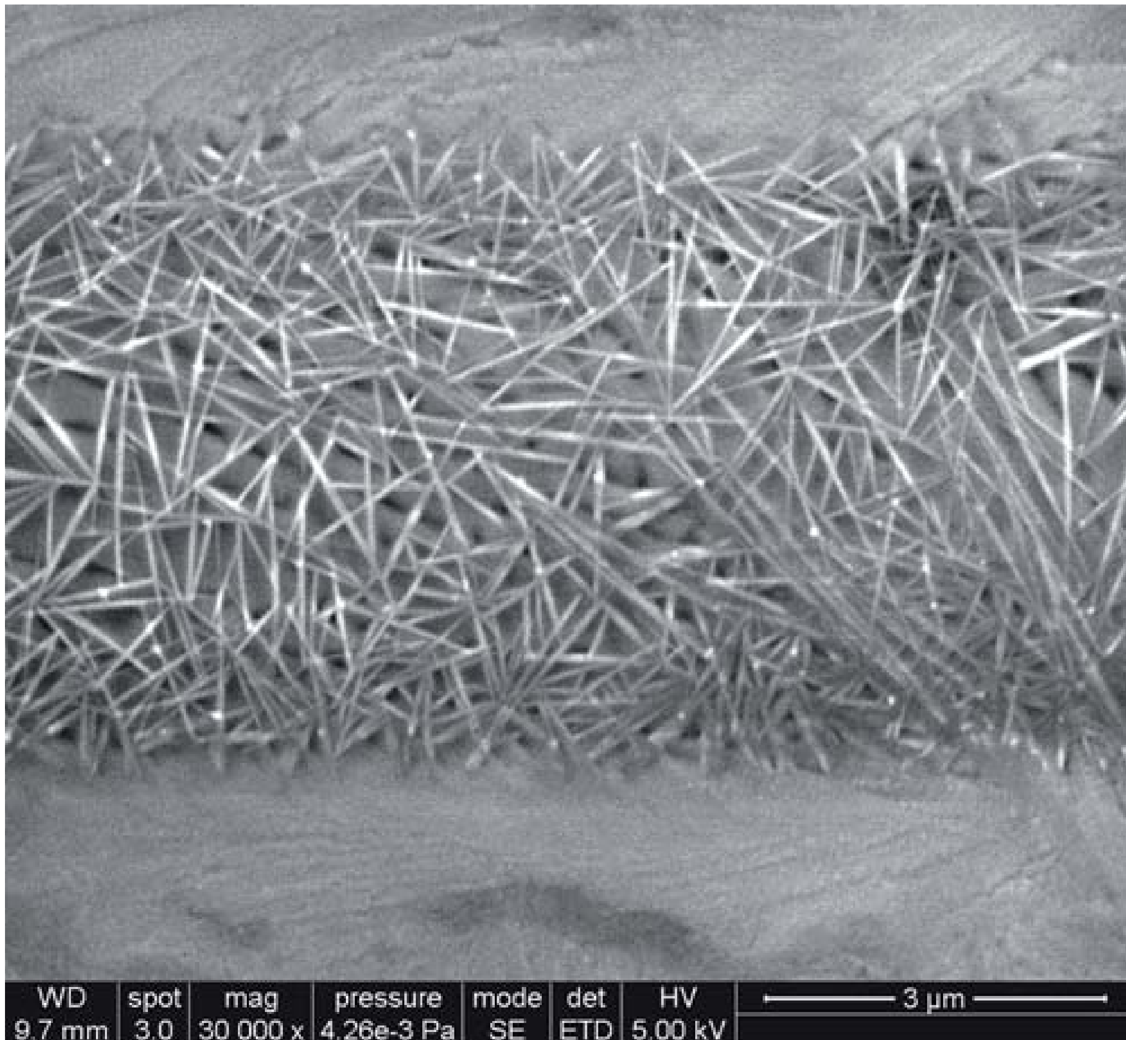

Figure 3-34 *Non-epitaxial nanowires grown on silicon by AHD method. Array size 10 x 50 with each site receiving 2000 pC and 500 nm pitch on STO.*

3.2.15 Analysis of TEM Lamellas of Nanowires on Silicon

When looking at the HRTEM results for the nanowires in figure 3-35, one can see their curious nature; namely the conical like shape. More specifically, one can see where the nanowire is partially surrounded by a silicon oxide layer and partially exposed. Moreover, the shape of the nanowire has a triangular shape directly below the surface of the silicon oxide and then above it the nanowire grows in a more rounded fashion. When fabricating the TEM lamella by FIB, a portion of the nanowire was amphormized and hence does not have a crystalline structure. Clearly this growth mode for the nanowire is very different than for all the other

nanowires grown previously. It must be noted that the silicon was not etched with an acid so to remove the silicon oxide layer prior to spin coating, thus all subsequent steps were performed on this initial layer. Interpreting these results indicates that the silicon oxide is growing up to meet the nanowire. In this case the silicon oxide layer would have to push up until reaching the exact point where the morphology of the nanowire changes to a conical shape. Conceptualizing this process, the nanowire grows length-wise while riding on an expanding bed of silicon oxide. Another point to make is the random directional growth for these nanowires on silicon as opposed to the highly directional growth on STO and YSZ substrates, is to be expected. Although the nanowires grown on silicon obviously are crystalline, they do not grow epitaxially on the silicon substrate floor. Clearly without growing epitaxially along the substrate, the nanowires were not forced to grow in one direction or in another.

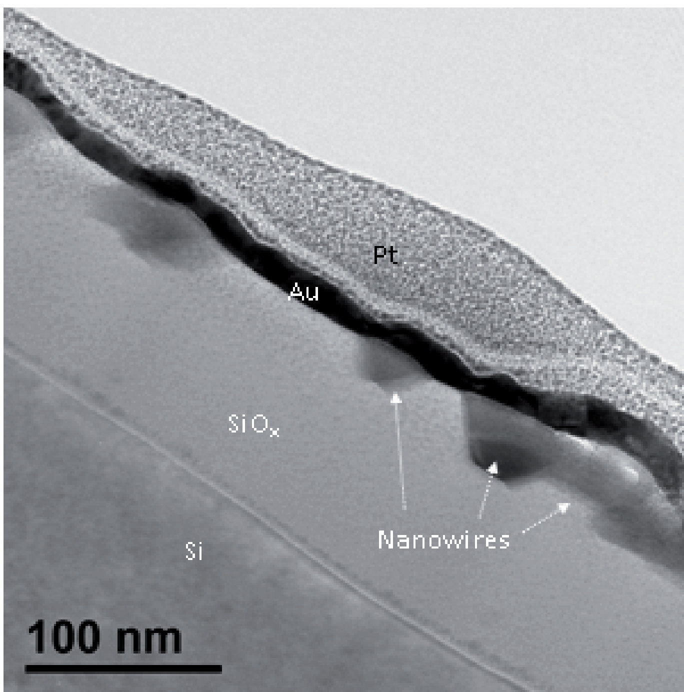

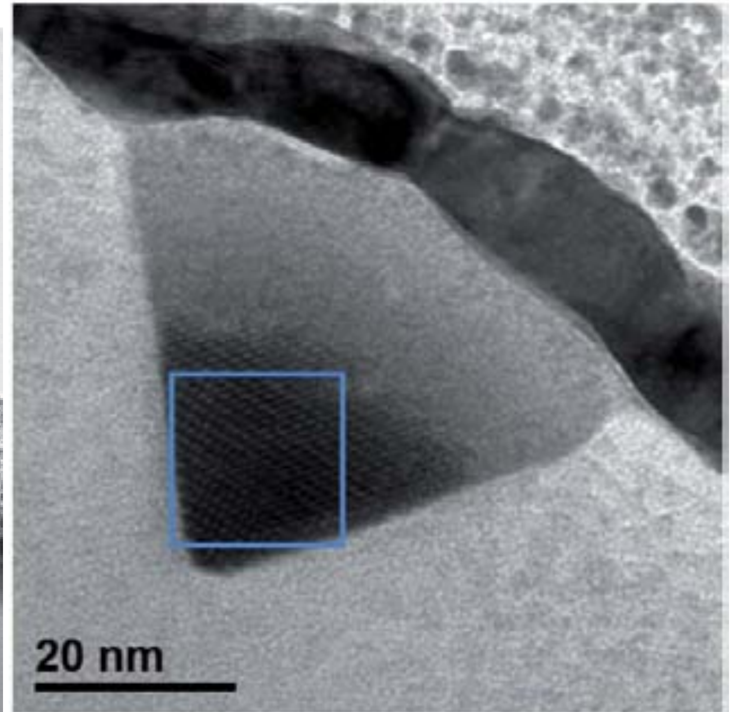

reflection	d_{hkl} (Å)
1	11.4485
2	7.4715
3	9.8766

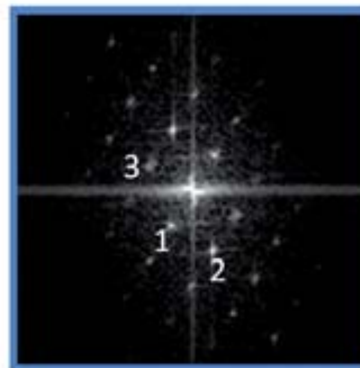

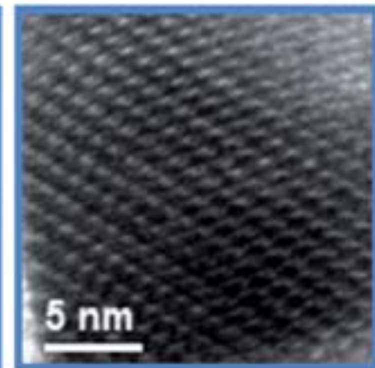

Figure 3-35 *HRTEM image of nanowires grown on silicon and FFT of crystal. Fourier transform showing spacing between adjacent lattice planes to not be similar to any other known crystal.*

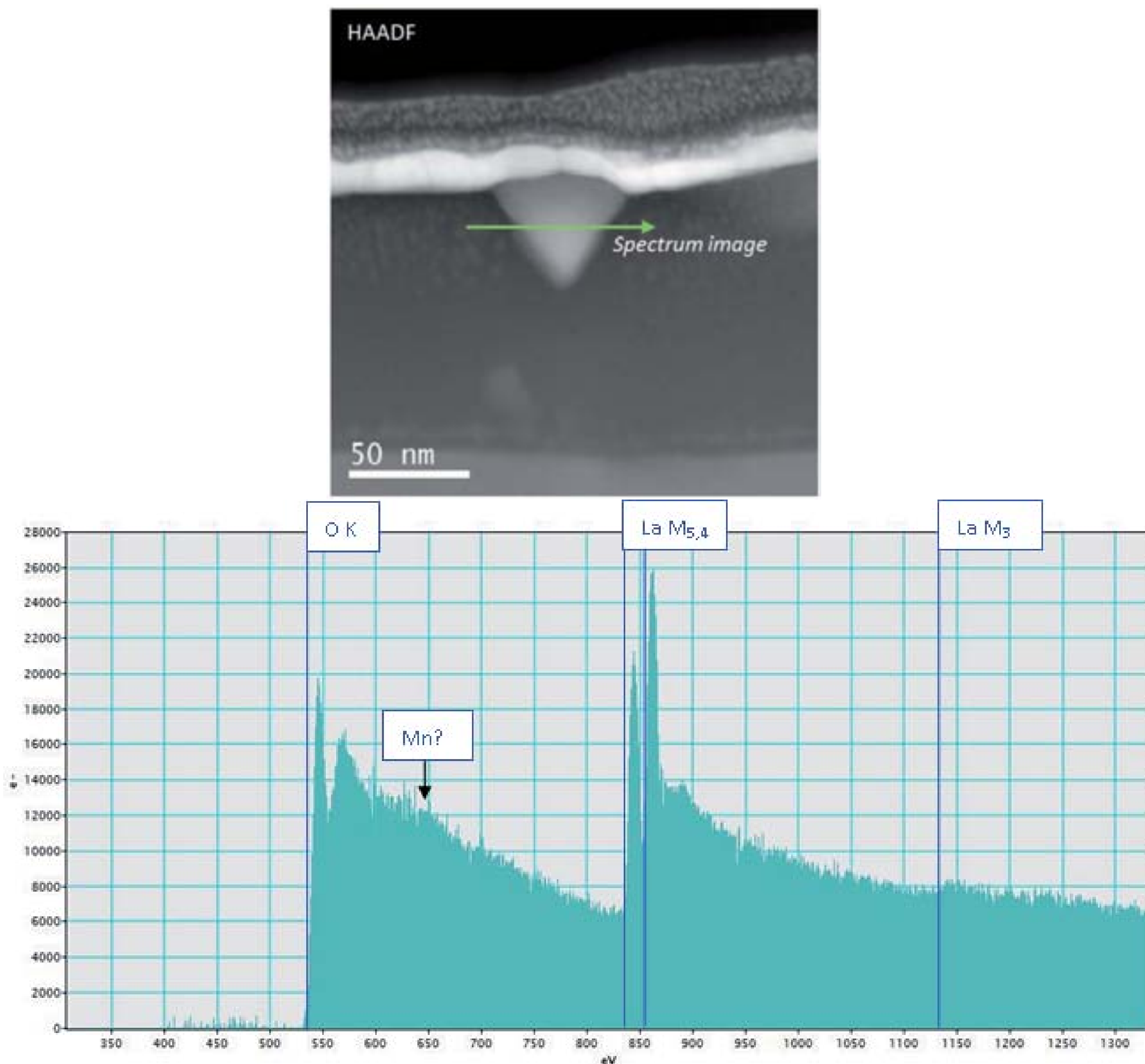

Figure 3-36 *EELS line scan of nanowire grown on silicon showing detected elements.*

Interpreting the results of figure 3-36, one can see the HAADF image showing the inverted conical shape of the sub 50nm wide nanowire. On the right hand side is the EELS line scan of the nanowire showing oxygen and lanthanum, however a signal from manganese is missing. This suggests that the choice of substrate does not affect the absence of manganese once annealed. Thusly, one must conclude that the disappearance of manganese is the result of some other process. Perhaps, this stems from the electron lithography process in the sense that due to high concentrated energy impinged on the thin film, manganese is selectively ablated from the precursor. Another possibility is that the manganese is selectively eliminated from the nanoislands

during the development step. Still another possible explanation is manganese is selectively expelled from the nanoislands during the annealing process.

3.3 Conclusions about Nanowire Growth

One of the goals in this work was originally to write narrow lines with electrons on to a precursor film at a desired angle and length so as to form LSMO nanowires on single crystal substrates when annealed. However this method to make nanowires proved impossible due to these narrow lines decomposing into non-ordered polycrystalline forms. Fortunately, two different principal modes of nanowire growth were discovered from electron beam lithography with the nitrate based LSMO precursor. They came from isolated low dosage nanoislands on YSZ and from high dosage arrays on STO. The morphology of these two principal growth modes differed in many respects. The main over arching characteristic aside, the AHD method proved highly repeatable whereas the ILD manifested itself only occasionally due to the inherent inconsistency when defocusing on high insulating substrates.

For the ILD nanowires, there existed two different growth methods, namely defocusing the electron beam and adding stigmatism. For the nanowires made by defocusing the electron beam, their before annealed nanoislands was very wide and very thin, thus when annealed they formed many small nanowires over a large area. There existed a dependence on dosage where when too much material was cross-linked, nanodots became the dominate feature. For the nanowires made by defocusing while forcing the beam to be astigmatic, the resulting nanowires may become an order of magnitude larger than the only defocused case and may be singular in nature. These nanowires were explored with AFM and not SEM due to the small contrast with the highly insulating YSZ substrate.

As for the nanowires made with AHD method, a multitude of interesting phenomena were observed. Principally, the method calls for writing an array of high dosage nanodots with a spacing sufficient so as to form a continuous cross-linked film surrounding the array. This creates a series of oriented nanowires at the edge of this array and a non-continuous mono layer inside the array. These nanowires form by consuming the continuous cross-linked film as well as the unorganized particles at the edge of the irradiated zone. These nanowires normally grow an order of magnitude longer than those made from the ILD method. However, these nanowires do not grow infinitely long; they stop growing after a period of time and also begin to taper off to a point. When sufficiently close to another array these nanowires grow in a stinted manner and grow evenly distributed though out the region. The arrays must be of sufficient size and dosage, so as to promote nanowire growth. They begin to grow at one thousand degrees and can be seen growing off of the secondary

zone boundary. The nanowires may also be promoted to grow a various nucleation sites, given a sufficiently large continuous cross-linked film. This growth mode can occur at large distances away from the original written array; a consequence of this effect is that nanowires may grow even in the absence of an array. The TEM results of the nanowires grown on STO have shown that they are epitaxially growing on the substrate, are anisotropic triangular crystals, and are devoid of manganese. The AHD method was also used to make nanowires on silicon. These nanowires were inverted and conical in nature, had a morphological change at the silicon oxide boundary layer, and were also devoid of manganese.

3.4 Nanowire References

1. Suh, W.H., et al., *Nanotechnology, nanotoxicology, and neuroscience.* Progress in Neurobiology, 2009. **87**(3): p. 133-170.
2. Liu, A., *Towards development of chemosensors and biosensors with metal-oxide-based nanowires or nanotubes.* Biosensors and Bioelectronics, 2008. **24**(2): p. 167-177.
3. Shankar, K.S. and A.K. Raychaudhuri, *Fabrication of nanowires of multicomponent oxides: Review of recent advances.* Materials Science and Engineering: C, 2005. **25**(5–8): p. 738-751.
4. Burda, C., et al., *Chemistry and properties of nanocrystals of different shapes.* Chemical Reviews, 2005. **105**(4): p. 1025-1102.
5. Xia, Y., et al., *One-dimensional nanostructures: Synthesis, characterization, and applications.* Advanced Materials, 2003. **15**(5): p. 353-389.
6. Sekhar, P.K. and S. Bhansali, *Manufacturing aspects of oxide nanowires.* Materials Letters, 2010. **64**(6): p. 729-732.
7. Comini, E., et al., *Metal oxide nanowires: Preparation and application in gas sensing.* Journal of Molecular Catalysis A: Chemical, 2009. **305**(1–2): p. 170-177.
8. Gaucher, F., et al., *Fabrication of metallic oxide nanowires.* Microelectronic Engineering, 2009. **86**(4–6): p. 820-823.
9. Liu, H.J., S.L. Lim, and C.K. Ong, *Laterally mesoscopic-patterned La0.67Sr0.33MnO3 thin film by pulsed laser deposition on anodic aluminum oxide template.* Materials Letters, 2008. **62**(12–13): p. 2006-2008.
10. Yang, H., et al., *Electron beam lithography of HSQ/PMMA bilayer resists for negative tone lift-off process.* Microelectronic Engineering, 2008. **85**(5–6): p. 814-817.
11. Pedersen, R.H., et al., *Electron beam lithography using plasma polymerized hexane as resist.* Microelectronic Engineering, 2010. **87**(5–8): p. 1112-1114.
12. Arnal, T., et al., *Magnetic nanowires patterned in the La2/3Sr1/3MnO3 half-metal.* Microelectronic Engineering, 2005. **78–79**(0): p. 201-205.
13. Hu, C.-C., et al., *Pulse deposition of large area, patterned manganese oxide nanowires in variable aspect ratios without templates.* Electrochemistry Communications, 2008. **10**(11): p. 1792-1796.
14. Tang, M.-y., T.-h. Ji, and J. Xie, *Scalable Preparation of SrTiO3 Submicro-wires from Layered Titanate Nanowires.* Chinese Journal of Aeronautics, 2007. **20**(2): p. 177-180.
15. Lin, J., et al., *Preparation and characterization of lanthanum borate nanowires.* Materials Letters, 2007. **61**(7): p. 1596-1600.
16. Hu, Z.-A., et al., *Template synthesis of LaMnO3+δ ordered nanowire arrays by converse diffusion or convection.* Materials Research Bulletin, 2006. **41**(6): p. 1045-1051.
17. Vázquez, M., et al., *Preparation and properties of novel magnetic composite nanostructures: Arrays of nanowires in porous membranes.* Physica B: Condensed Matter, 2006. **384**(1–2): p. 36-40.
18. Tagliazucchi, M., et al., *Synthesis of lanthanum nickelate perovskite nanotubes by using a template-inorganic precursor.* Solid State Communications, 2006. **137**(4): p. 212-215.

19. Takai, K. and T. Enoki, *Fabrication of graphitic nanowire structure by electron beam lithography.* Physica E: Low-dimensional Systems and Nanostructures, 2007. **40**(2): p. 321-323.
20. Zarbout, K., G. Moya, and A. Kallel, *Determination of the electron beam irradiated area by using a new procedure deriving from the electron beam lithography technique.* Nuclear Instruments and Methods in Physics Research Section B: Beam Interactions with Materials and Atoms, 2005. **234**(3): p. 261-268.
21. Coll, M., *Stress-induced spontaneous dewetting of heteroepitaxial YBa2Cu3O7 thin films.* Physical Review B, 2006. **73**.
22. Morena, C., *New Features in Solution Derived La0.7Sr0.3MnO3 Thin Films: Spontaneous outcropping and nanoscale reversible resistive switching.* Ph.D Thesis, 2010.
23. Moreno, C., *Spontaneous Outcropping of Self-Assembled Insulating Nanodots in Solution-Derived Metallic Ferromagnetic La0.7Sr0.3MnO3 Films.* Adv. Funct. Mater., 2009. **19**: p. 2139-2146.

4. Oxide Nanoimprinting

$La_{0.7}Sr_{0.3}MnO_3$ nanostructures were fabricated on single crystal substrates by nanoimprinting efforts. Similarly to previous chapters, an aqueous thin film which consisted of La, Sr, Mn metal organics and PVOH was spin coated on to STO, LAO, YSZ, and silicon substrates. A hard stamp a mold replete with nanoscale features was pressed into the oxide precursor film at elevated temperatures for an extended period of time and an array of nanopores was thus generated. The depth of these nanopores did not reach down to the substrate floor, thus a reactive ion etching step was required to remove this residual layer while retaining the nano-sized features. Two different gases were employed in the etching process giving nanoholes for oxygen and nanodots for argon gas. The sample was then annealed in a tube furnace so as to remove any organic components and thereby form oxide nanocrystals. The annealed film was finally cut by FIB and analyzed with TEM and EELS to reveal its epitaxial LSMO nature.

This novel method to generate LSMO nanostructures is of interest due to the convergence of the efficiency of maturing nanoimprint techniques and increased study of nanostructurating multiferroics oxides. Silicon was used predominately in the initial stages of the research to have a less expensive test bed on which optimization studies could be conducted. Single crystal substrates (SCS) were employed for the very same reasons that they were used in the electron beam lithography experiments. Specifically, this was the ability to control strain of the nanocrystals through epitaxial growth and the desire to grow single LSMO crystals. The insulating nature of the SCS did not adversely influence the nanoimprinting process, however when attempting to make TEM lamellas by way of a cutting with a FIB, the charge

build-up hampered the extraction. Part of the enticing feature of this procedure is that it is not limited to only oxide single crystal or silicon substrates and thus this version of nanoimprint lithography may be performed on any substrate.

4.0.1 Current NIL Research

Nanoimprint lithography continuous to be viewed as possible replacement for optical lithography in the fabrication of integrated circuits. This stems from the ever smaller size of the gate transistor as demand continues unabated for even more processing power. The consequence of making these smaller and smaller integrated circuits with optical lithography is the huge up-front cost of making a single fabrication tool, upwards of $100 million [1]. One solution to this problem of large up-front investment is the adoption of cheap low-usage nanoimprinting molds. These small one-off molds can be designed quickly, fabricated with an electron beam in the morning, and then used for imprinting later that day. These would allow small integrated circuit makers to fabricate customer specific devices or to custom make various versions of a device.

Originally developed by the Chou group at Princeton University in 1997, the group pioneered thermal imprinting of nanosized features [2, 3]. This work was then followed up by Lebib et al who first showed that large four inch wafer could be imprinted [4]. That next year the same group reported the first use of an electron beam in the fabrication of silicon molds used in the imprinting process [5]. They subsequently showed a few months later the ability to imprint in precursors with temperatures as low as 50C and the use of molds which did not require an anti-sticking agent [6]. This collection of early work in the field generated the foundation for all other further research. However more importantly they showed that this technology had the potential to move into mainstream integrated circuit fabrication.

In the year 2001, further refinements to this new lithography technique began to take hold. A polymer different from PMMA was used for the first time by Lebib et al due to its lack of etch resistance [7]. They also showed the first demonstration of fabricating magnetic particles by NIL in the form of cobalt nanoparticles. Later it was shown that thin film transistors (TFT) could be fabricated by imprinting into the semiconductor polymers of α-sexithiophene, PDAS and PBAS when combined with interdigitated electrodes [8]. Another polymer film was also used by Malaquin et al in the form of PDMS which allowed for lower pressure and temperature compared to a typical PMMA film [9]. Nanofluidic channel fabrication by NIL was also demonstrated for the first time in 2002 by Pepin et al who also demonstrated the technique using two layers of nanopellets to hot seal an assembly [10]. These early years saw the community experiment with thin films better suited for nanoimprinting as well as the first prototypes of TFT which years later would be of major interest.

In the preceding years several distinctive lines of nanoimprinting research were undertaken by researchers. One new line was the usage of ultraviolet light as the curing agent instead of the thermoplastics, now called UV NIL. These groups attempted to take heat out of the process which would open up nanoimprinting to other more sensitive polymer systems. Block copolymers were also beginning to be used regularly starting with Akbayir et al who used them as donor and acceptors for photoelectric experiments [11]. Soon some necessary work was carried out to determine if the mold was deforming due to the imprinting process and also how much morphological change was occurring at the various steps along the way. Gourgon et al demonstrated that a mold deformation was taking place albeit a small one, so this would have to be taken into account and minimized in the future [12]. The Chou group found that the fidelity of the nanostructuration four times greater after imprinting, etching, and metal lift-off as compared to optical lithography [13]. Another major milestone was reached in the form of using metal stamps in the imprinting process fabricated using proton beam writing. This technique is noted for its ability to produce very small features with very high packing density and coupled with electroplating could yield 3D nanostamps [14].

Another variation of nanoimprint lithography was made possible from the work of Grant Wilson as the ground work for what is now called UV NIL in [15]. Both the thermal and optical versions of NIL have been further refined by scores of groups since 2004 with the notably paper published by Guo et al. They outlined a technique which made use of a UV transparent mold with metal mask which when combined with normal thermal imprinting gave features with higher aspect ratios than what was originally started with [16]. This opened up the field to UV transparent mold fabrication methods and usages. This technique to using UV either combined with elevated temperatures or not, continues to be a leading candidate to break into full industrial production.

Applications started also to be reported for such things as single mode waveguides and patterning bioactive proteins as well as giving more surface area to catalysts [17-19]. An exciting application that came out of research done in Korea in 2005 was the ability to create a photonic bad gap structure on a polymer by careful arrangement of high aspect ratio nanoholes made from NIL [20, 21]. Another exciting application was development of micrometer sized organic light emitting diodes stamped from a diamond mold [22]. These OLED's are seen as very promising with regards to driving down per unit costs as well as allowing for the eventual technology of flexible and foldable computer screens. A combination of thin film transistor and organic light emitting diodes made from nanoimprinting could very well herald in a new generation of electronic devices.

In the last few years there has been a real surge in the number of groups working on nanoimprint techniques. One of the most recent examples of how far NIL has come was reported by the company Beam Technologies who describes a way to generate structures that are less than ten nanometers. They combine electron beam lithography and atomic layer deposition to create the smallest reported structures made from nanoimprinting [23]. Also this year another group also published in the journal Nanotechnology recently told of imprinting magnetic dots 30 nm across on silicon as a demonstration of a possible read/write memory system [24].

Progress has also been made in the roll-to-roll fabrication of flexible displays in the form of color filter arrays for e-ink platforms [25]. Low cost, high performance single mode laser diodes have also been fabricated from InP based imprinted waveguides from a team in Finland [26]. As of the year 2011, certain manufacturing operations have sprung up which use nanoimprint lithography. One such group produces LED's and report that after 8000 uses of a particular mold, that no remarkable deficiencies were observed to have formed [27]. This bodes well for the LED industry specifically and the scientific community in general because if a technology is reliable and robust, continued interest in it is assured. Self switching diodes and side gate transistors were also fabricated by careful employment of RIE insomuch that zinc oxide was patterned selectively by using a combination of methane and hydrogen gas [28].

Blue LED's are highly desirable due to their use in Blue-Ray readers and writers. A method to fabricate high efficient blue LED's has been reported in the journal Microelectronic Engineering where they detail the imprinting of GaN on sapphire substrates and the subsequent increase in photoluminescence [29]. In an effort to bridge to gap between next generation nanodevices and current CMOS technologies, the fabrication of transition metal oxide based memristor cross-bar has been fabricated via NIL which allows for the construction of multi-terminal memristive circuits [30, 31]. Bit-patterned media has become an application longly associated with NIL due to its lost cost per bit of tightly arrayed nanosites. To give an idea of how dense this bit-patterned media has become of late, a group recently reported the fabrication of a sample with 3.3 Tbit/in which approached the limit detectable by MFM [32].

One technique stemming from the traditional nanoimprinting world which is gaining traction is that of roll-to-roll pattern transfer. This idea has been taken up by Hewlett-Packard in an effort to increase the durability of soft stamps such as fluorothermoplastics by introducing nanoparticles which do not fully cure, leaving the stamp semi-porous and thus more gas permeable [33]. One of the major drawbacks of the nanoimprinting process is that the aspect ratio of the features cannot be changed easily after etching. However the group of Harris et al have determined a method whereby through an oxidation process, the nanofeatures will grow in a linear response thus allowing per sample fine tuning [34]. Another important use of NIL is in designing patterns for catalysts. Carbon nanotubes are excellent electron emitters and will grow vertically on iron catalysts, so if those nanoparticles can be arranged in an array over a six inch wafer one

can grown large ordered systems [35]. One of more unconventional new approaches to nanoimprinting comes from a group in Atlanta where they place the entire mold and film on an slant such that only a partial sliver of the polymer is nanostructurated leaving very narrow nanolines [36].

A non-thermal method of curing nanoimprinted structures is currently also being developed in Singapore in that they make numerous oxide species via a polymerization reaction on a silicon mold with MMA and ethylene glycol dimethacrylate [37]. One method being tested now is for the introduction of a hydorofluoroether liquid immediately between a polymer layer and mold. First reported by Meraku et al, it outlines the beneficial reduction in pressure necessary to full imprint polycarbonate from 20 MPa to 5 MPa [38]. One problem often faced by researchers is the build-up of contamination on the stamp. Most use a combination of solvents to remove residuals however it has been reported that the commercial cleaner S-1165 from the company Shipley is more effective at removing inorganic components than traditional methods [39]. Another sub-field which is gaining a lot of attention recently is that of block co-polymer imprint lithography. However one drawback of using block co-polymers is there high affinity to stick to the mold. A group at the Molecular Foundry at Berkeley has reported a solution to this in the form of chemically modifying PS and PDMS to include fluoroalkyl chains which allow defect free separation to occur [40]. A group at Stanford has also found that if the pressure on the mold is gradually lessened, instead of held constant while lowering the temperature before demolding, a more uniform and reliable pattern transfer is observed [41].

One way to create more efficient solar cells is to increase the surface area that could potentially act as a photon receiver. To this end NIL can augment the surface of a P3HT/PCBM bilayer thus increasing power conversion efficiency four-fold through a solvent assisted imprinting process [42, 43]. An interesting application of nanoimprint lithography is attempting to mimic superhydrophobic surfaces of plants by making films with high aspect ratio hairs combined with low aspect ratio microtextures which can be done with a custom mold [44]. With regards to oxide nanofabrication, a group at Osaka University has imprinted a molybdenum layer rendering it porous thus able to act as a mask for pulsed laser deposition so as to grow magnetic and epitaxial $Fe_{2.5}Mo_{0.5}O_4$ on sapphire substrates [45]. Quantum dots have, of late, become another avenue in which nanoimprinting has made in roads. It was reported in the Journal of Crystal Growth that NIL was able to pattern (100) GaAs into nucleation sites for the growth of InAs quantum dots and thus able to double the intensity of emitted radiation as compared to other methods [46]. One group which also used PVOH successfully as an imprinting film was Park et al out of Hanyang University; they reported using SF_6 in the reactive ion etching step on polyimide substrates so as to construct SAM layers [47].

4.0.2 NIL Objectives

One of the original objectives of the project was to generate ordered arrays of oxide nanocrystals over a large area from nanoimprint lithography. Nanoimprint lithography (NIL), unlike electron beam lithography, has the potential to be scaled up in an industrial fashion. Initially, the approach envisioned was to generate holes in a PMMA matrix via imprinting such as on the left of figure 4-1. These holes were then to be filled with an oxide precursor, such that when annealed, the holes would promote vertical nanorod growth of the precursor while the matrix would be eliminated. However, this proved more difficult to accomplish than originally expected. Arrays of nanostructures from nanopores generated in PMMA by NIL and subsequently filled with a propionate LSMO precursor were not observed to have formed. Previous research had produced LSMO nanorods by way of a polycarbonate polymer matrix, and thus it was thought to be a possible technique here [48, 49] . A key difference, however, laid with the narrow aspect ratio of the nanoholes formed by radiation in the work of Carretero-Genevrier et al and the low aspect ratio of the mold readily available for NIL use here, specially their film was up to 1:10 whereas ours was 4:1. This shorter and wider hole did not confine the precursor enough to form a vertical nanorod or even a discernible array of nanodots. Another consideration is that the glass transition temperature of polycarbonate is roughly twice that of polyvinyl alcohol [50].

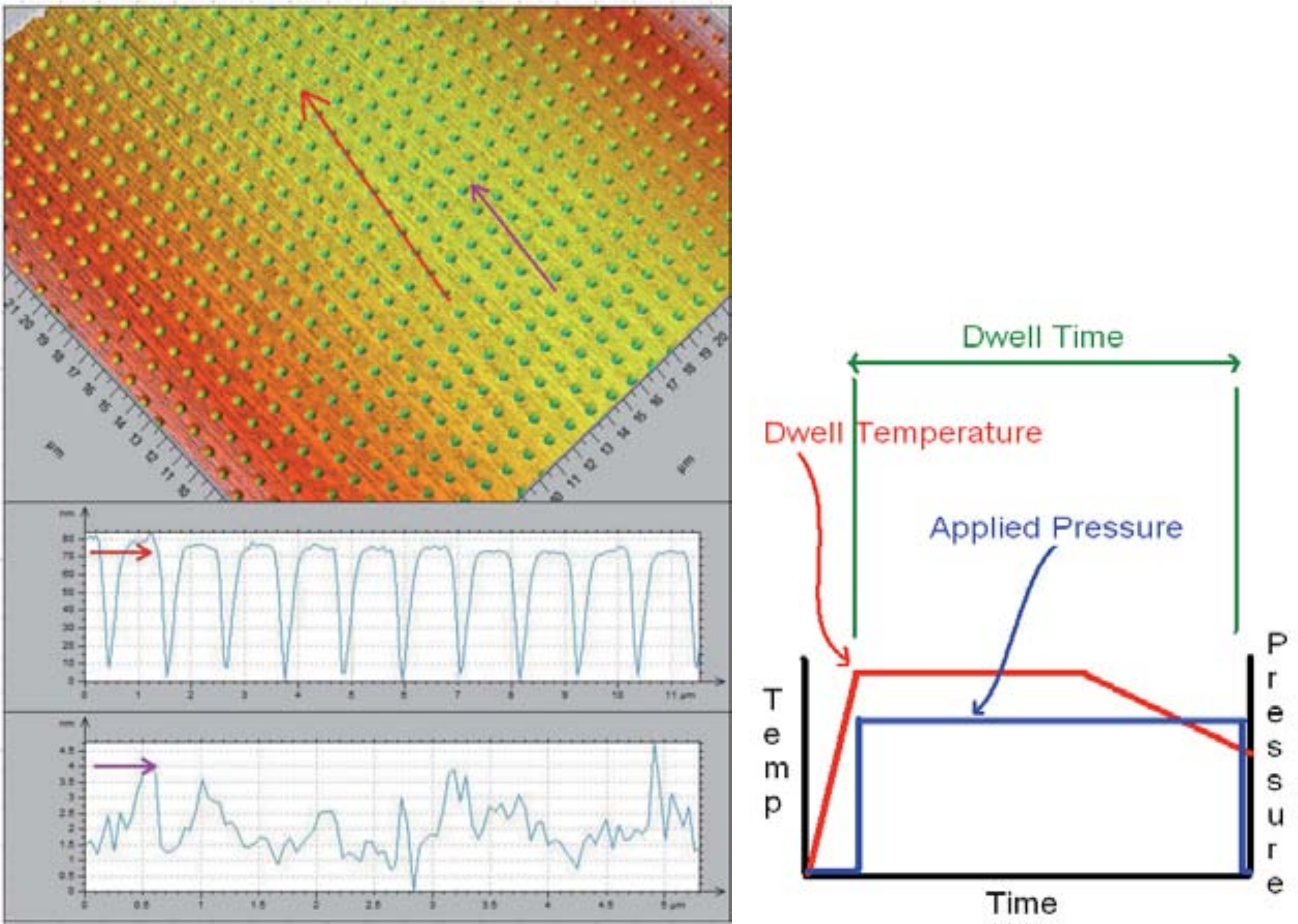

Figure 4-1 L*eft: imprinted PMMA showing large scale nanostructuration. Right: schematic of imprinting conditions. Dwell temperature 160 °C, applied pressure 40 MPa, dwell time 5 min, demolding temperature 80 °C, no etching, no annealing.*

Fortunately, a work-around was found in the form of directly imprinting into a PVOH based oxide precursor. This technique of thermally imprinting into a PVOH based oxide precursor has not been previously reported. The majority of research in the field comes from work done on PMMA or PS [51-53]. The advantage of imprinting directly into the PVOH based oxide precursors is the reduction in the number of steps required to obtain nanocrystal arrays as well as eliminating any possible complications to filling and then eliminating a matrix. This elegant solution to large scale oxide nanostructuration allows for oxide species to be imprinted in one step.

A schematic of the nanoimprinting process as a function of time for temperature and pressure is presented on the right of figure 4-1. There one sees that the temperature of the film is raised to the dwell temperature, then pressure is applied for a duration of time, and finally the temperature is reduced for demolding. The specifics of how changing

these parameters affect the morphology of the imprinted film will addressed here. The basic idea of nanoimprinting a thermoplastic is to raise the temperature above the glass transition temperature, such that the film flows easily. Then a pressure is applied to the mold/film, thereby pressing the nanofeatures into the softened film. This pressure and temperature is maintained for a period of time so that the film relaxes around the nanofeatures. Finally, the temperature is lowered so that the film hardens again and thus enabling the mold to be detached from the film whose surface has been permanently altered.

The objective of the nanoimprinting part of the work became to describe the optimal conditions for lithography using a LSMO precursor. Moreover, it was to determine what imprinting conditions gave good nanopores depth, minimized roughness on the film surface, diminished occurrence of artifacts, and increased percentage of the substrate which was successfully nanostructurated. The tools available to affect the various stages of nanoimprinting included the following: altering the amount of PVOH present in the solution, changing the temperature at which pressure was applied, what pressure would be applied, for how long would the pressure be applied, and what temperature would the sample be demolded. Another series of variables that played in role in the final outcome of imprinting on the oxide layer were the type of gas used in the plasma etching, the power used therein, and the time in which plasma was exposed to the sample. Finally, an important parameter not originally considered a variable, was the type of counter ion used in the precursor. That is, originally the precursor used exclusively nitrates as the counter ion however this was changed towards the end of the experiments to acetates so as to reduce overall roughness after etching.

4.1 Silicon Mold

The design of the stamp was that of a continuous series of one micrometer spaced nano-scale pillars with no gaps or larger repeating pattern. Thus, the smaller chips were completely covered with nano-scale pillars up to the edges of the mold. The pillars themselves were 500 nm in width at the base and tapered very slightly towards their tips where the width was reduced to 250 nm. The height of the pillars was 125 nm, thus the slope of a generated hole was a reduction in width of two nanometers for every one nanometer in depth. Very few of the pillars had been damaged or removed entirely, however occasionally an AFM image showed a lack of a generated hole and thus was reasoned to be the cause. The spacing of the pillars relative to each other was one micrometer peak-to-peak; their arrangement was a square pattern. The wafer was also coated in a non-stick coating such as to allow for facile detachment between mold and substrate film. Nanoimprint molds are made by spin coating PMMA onto silicon, irradiating with focused electrons where the nanopillars would be, developing to reveal holes, then a metallization step, lift off, reactive ion etching to form the pillars, and finally removing the remaining metal.

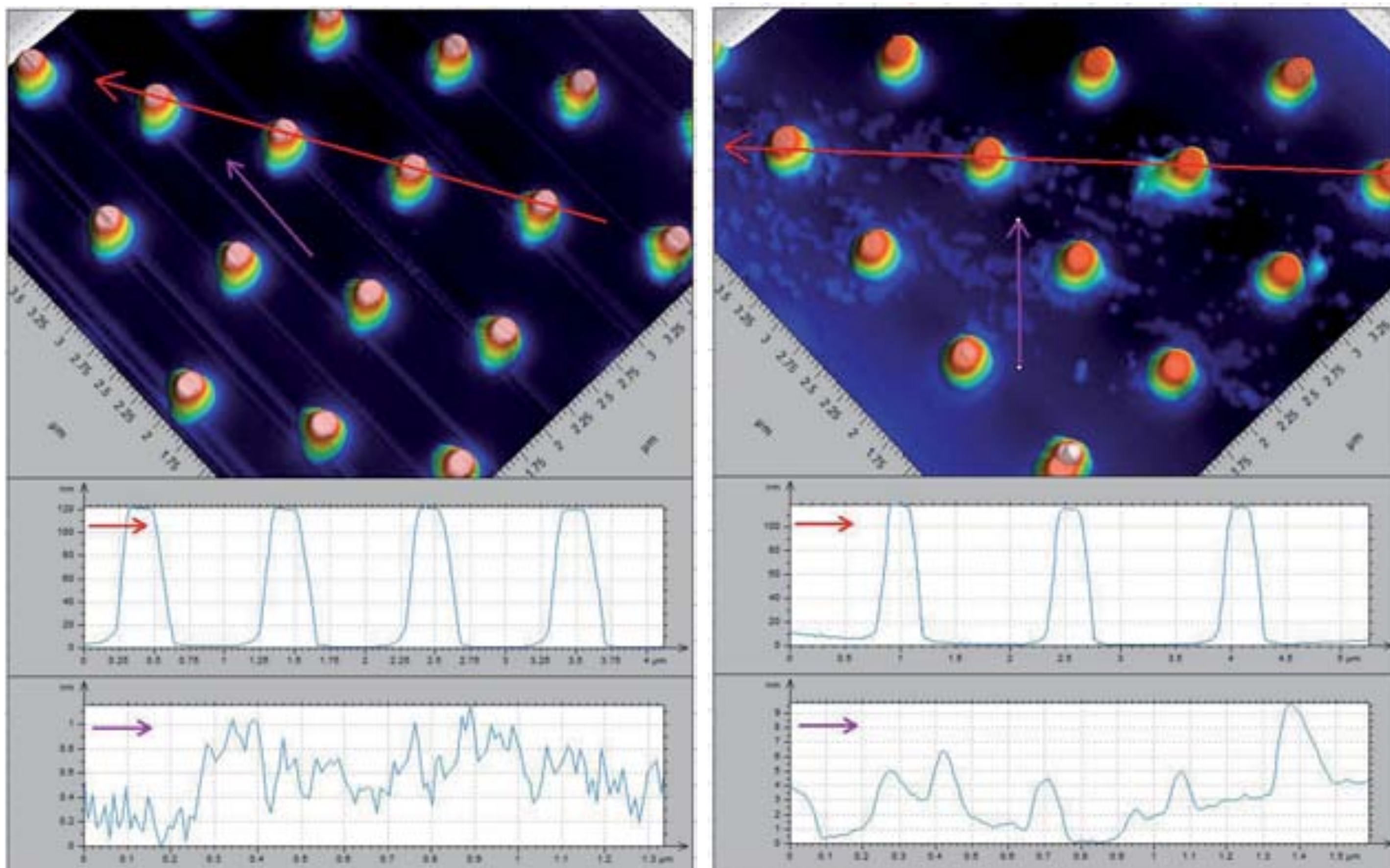

Figure 4-2 *Left: silicon male mold as received. Right: same mold after approximately thirty imprints.*

As a matter of procedure, the mold was cleaned with an equal mixture of water, acetone, and isopropanol in a sonicator after every stamping. The reason for this extra cleaning step was the build-up of debris left on the mold. On the left of figure 4-2 one can see the state of the male mold as it was received. The image on the right of figure 4-2 shows the same mold after approximately thirty uses. One can see in the lower line scan on the right of figure 4-2 debris of several nanometers. Also seen in that image is a rounding of the pillars from continued use. Although occasional debris was retained on the mold as well as a general reduction in the sharp features of the mold, the stamping process was not adversely affected. Of course, to grow single LSMO crystals with NIL, one needs a female mold with very small feature sizes. The reason a male mold was used in these experiments was borne out of inheritance and was used to optimize conditions for future experiments when a female mold could be used.

4.2 Imprinting

A typical result of the imprinting process in a PVOH based oxide precursor is seen in figure 4-3. On the left hand side of the figure one can see the large scale to which the nanoimprinting process can affect the precursor film. Also visible is

the scale to which small alterations to the perfectly nanostructurated surface are present in an imprinted sample. On the right hand side the pitch and depth of the imprinted holes are seen more clearly. The roughness of the remaining film is also seen to be on the scale of four nanometers. This zoomed in area was an ideal area because of the absence of defects or aberrations.

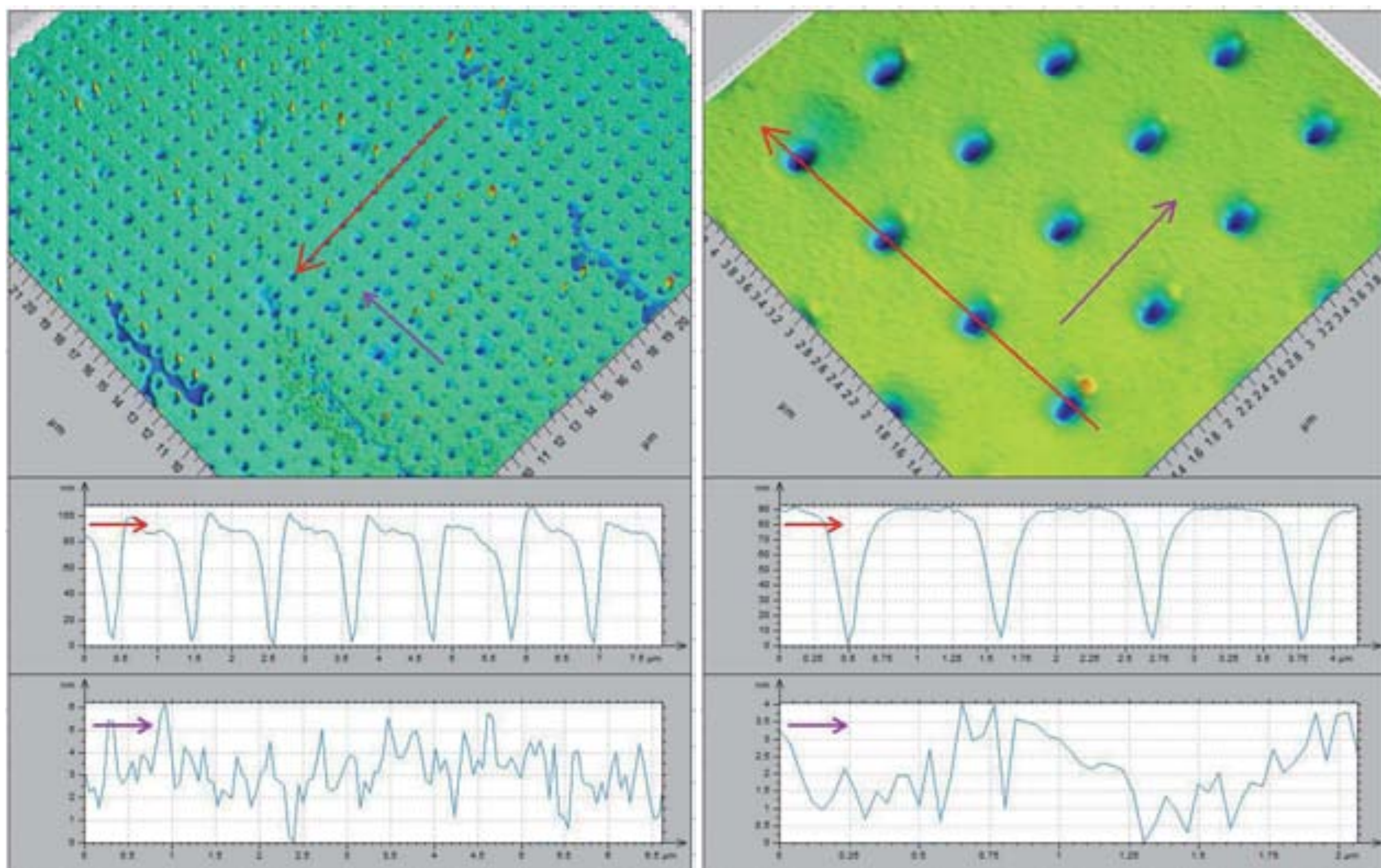

Figure 4-3 *Left: a large area imprinted with a female mold. Right: zoom of area. Dwell temperature 160 °C, applied pressure 40 MPa, dwell time 5 min, demolding temperature 80 °C, no etching, no annealing, nitrate based LSMO precursor with 2 wt% PVOH.*

The thickness of the film is of the utmost importance in the nanoimprinting process. This is due to several factors influencing the final morphology of the nanoholes which are directly tied to the thickness of the film prior to imprinting. The most obvious factor is that the thicker the original film relative to the nanosized features of the mold, the thicker the residual layer and thus the more etching will be required to remove it. The more time or power necessary to undertake a successful etching, the more damage will be done to the remaining nanostructures. Another factor in which thickness plays a role is with regard to local density variations. These density augmentation directly underneath the nanopillars as can be seen when etching with argon plasma. There, a relatively thick precursor film, it is thought,

was able to be compressed locally by the nanopillars to the point that they were able to withstand an argon etching treatment a bit longer than the surrounding uncompressed film. This resulted in positive nanoisland structures surrounded by a bare substrate. Due to the usage of two different precursors in the following experiments, one with 2 wt% PVOH and the other with 15 wt% PVOH, the films wetted the substrates in different thicknesses. Specifically the 2 wt% PVOH solution had a thickness around 200 nm whereas the 15 wt% PVOH solution has a nominal thickness of 250 nm. The minimum thickness that a film should have is at least twenty nanometers more than the feature size of the mold, thus insuring that the delicate nanopillars will not directly contact the substrate if fully emerged.

In order to determine the thickness of a film prior to imprinting, a dull plastic knife was rubbed along the surface of the film so as to expose the underlying substrate. This created a mound directly at the edge of where the knife was rubbed along the film and where the unmolested film was. Hence to determine the true film thickness, one must ignore this artifact of exposing the substrate and take only into account the unaffected film height and bare substrate floor. On the left hand side of figure 4-4, one can see the film height of non-imprinted fifteen percent by weight PVOH LSMO after being scraped by a plastic knife. One can therefore infer from the line scan that this film unaffected by is 250 nm. On the right hand side of figure 4-4, it can be observed the film height of a two percent by weight PVOH LSMO imprinted precursor film. This imprinted film was also exposed by a scratch and shows the overall film height to be around 140 nm.

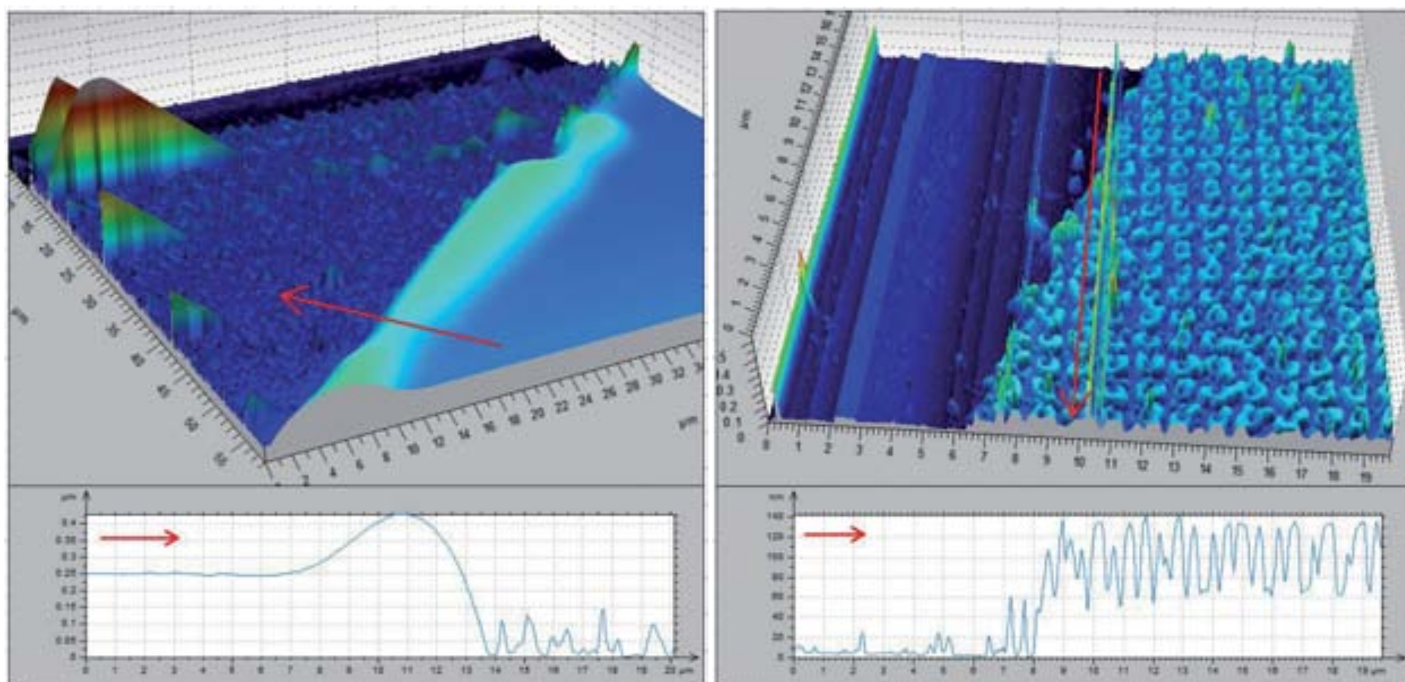

Figure 4-4 *Left: thin film thickness before imprinting of 15 wt% PVOH. Right: imprinted 2 wt% PVOH film showing thickness. Conditions of dwell temperature 160 °C, applied pressure 40 MPa, dwell time 5 min, demolding temperature 80 °C, no etching, no annealing, from nitrate based LSMO precursors.*

A general note about the amount of the films which were nanostructurated after imprinting; initially, the precursor film used to prove the concept of imprinting into polyvinyl alcohol had two percent by weight PVOH. Contrary to typical imprinting patterns, this resulted in only a portion of film becoming nanostructurated. Specifically, this portion was restricted to the edge of the area which was in contact with the mold. Along with this edge, there existed a few isolated small round portions randomly distributed which also were nanostructurated. When the percentage of PVOH by weight was increased to fifteen percent the entire imprint area was nanostructurated. This is thought to stem from the greater degree in which the film could flow around the mold when above its glass transition temperature.

Another consideration to this non-uniform nanoimprinting was the small but impactful meniscus generated at the edges of the substrate after spin coating. In other words, the film at the center was thinner than that towards the edges. This would not be a problem with regards to uniform nanoimprinting if the substrate were much larger than the size of the mold used. However, when the mold was the same size as the substrate, this slight extra thickness along the edges would be imprinted preferentially to that at the center. This was not a difficulty when doing experiments with silicon substrates due their sizes being much larger than the small molds at hand. However, when doing imprinting on the single crystal substrates, which had roughly the same 25 mm^2 area as the mold, this edge effect was amplified. This effect was most apparent when using the 2 wt% PVOH solution and less so with the 15 wt% PVOH precursor. A possible

explanation to this phenomenon is that the 15 wt% PVOH solution has more of an ability to flow and thus is able to relieve local inhomogeneities more easily.

The films, after being nanoimprinted, regardless of the percentage by weight of PVOH present or the counter ion used, all displayed a much higher amount of inhomogeneities when compared to a PMMA film. This can be seen in figure 4-5 from the two representational optical micrographs shown. On the left hand side one sees white spots indicating inhomogeneities. On the right hand side one can see small point defects present randomly throughout the sample whereas dark places were not imprinted at all. All three images are meant to illustrate that every sample was imprinted has a relatively large amount of defects and that any AFM or SEM images were far from these areas. Relative to spin coated PMMA, which is highly regular, the nanoimprinted LSMO precursor would normally contain roughly ten times the amount of aberrant locations. This could be due to the outgasing occurring in the heated film or possibly due to the small PVOH particles which failed to be filtered. These defects did not appear to originate on the film due to dust as the spin coated films were highly homogeneous.

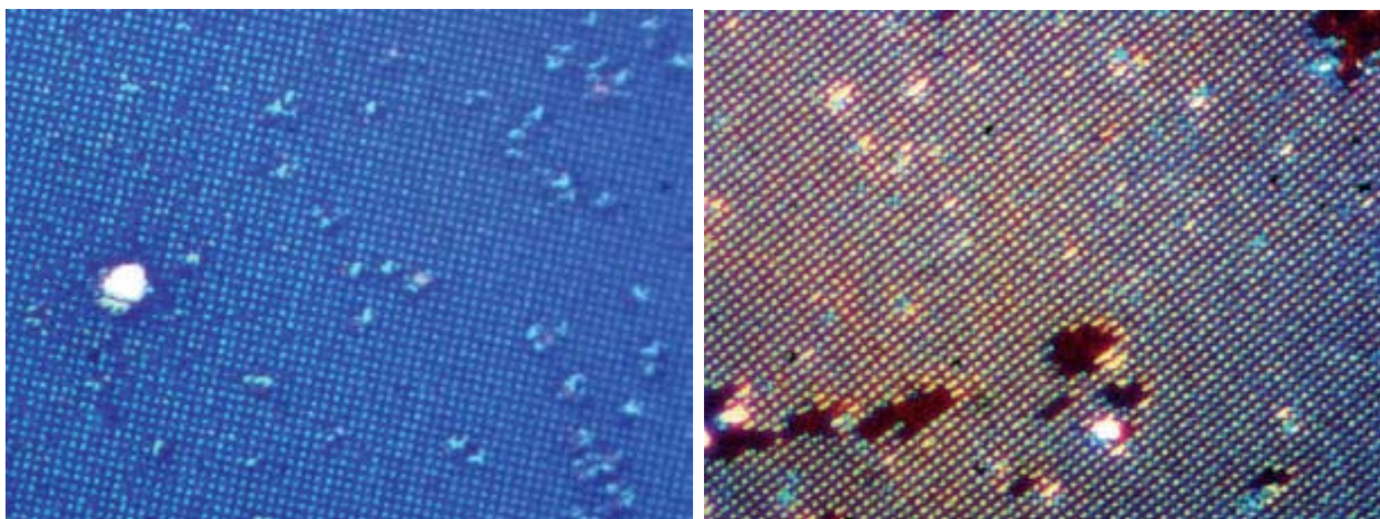

Figure 4-5 *Nanopores with pitch of 1 µm on imprinted LSMO precursor showing point defects and inhomogeneities. Dwell temperature 160 °C, applied pressure 40 MPa, dwell time 5 min, demolding temperature 80 °C, no etching, no annealing, nitrate based LSMO precursor with 2 wt% PVOH.*

In order to imprint a mold into a precursor film, the correct application of heat and pressure along with their temporal components must be realized. These elements come together in what can be visualized as a ramp profile as seen on the right of figure 4-1. That is, the mold and substrate must be in contact at a sufficient temperature so as to allow the polymer to deform freely under the pressure of the mold. However, it must not be too hot so as to degas the precursor or create artifacts on the surface of the film. The pressure must be high enough to penetrate deeply into the precursor film but not so large so as to force the substrate to move laterally. The time the pressure is applied at that temperature

must be long enough to allow the polymer to relax around the nanopillars. And lastly one must be mindful of the temperature at which the mold and film are separated, for too high of a demolding temperature will not allow the nanopores to form correctly and too low of a temperature bring the process to a stand-still.

4.2.1 Dwell Temperature

The temperature applied to the film before the full pressure was brought to bear was found to be ideally at 160 degrees. This temperature was used due to it being well above the glass transition temperature, thus insuring a free polymer flow when fully engaged. Specifically, the higher heat allows the individual polymer chains to start translating throughout the film as opposed to rotating on a short range order [54-56]. The exact glass transition temperature was not determined, however, it was thought to be more than 85 degree and less than 160 degrees [50, 57]. The minor reason why the temperature was not increased higher than 160 degrees was the to avoid the release of gases from the precursor film would lead to possible elemental inhomogeneities. One can see the effects on the quality of the film as well as the depth of the generated holes in figure 4-6 when temperature is varied.

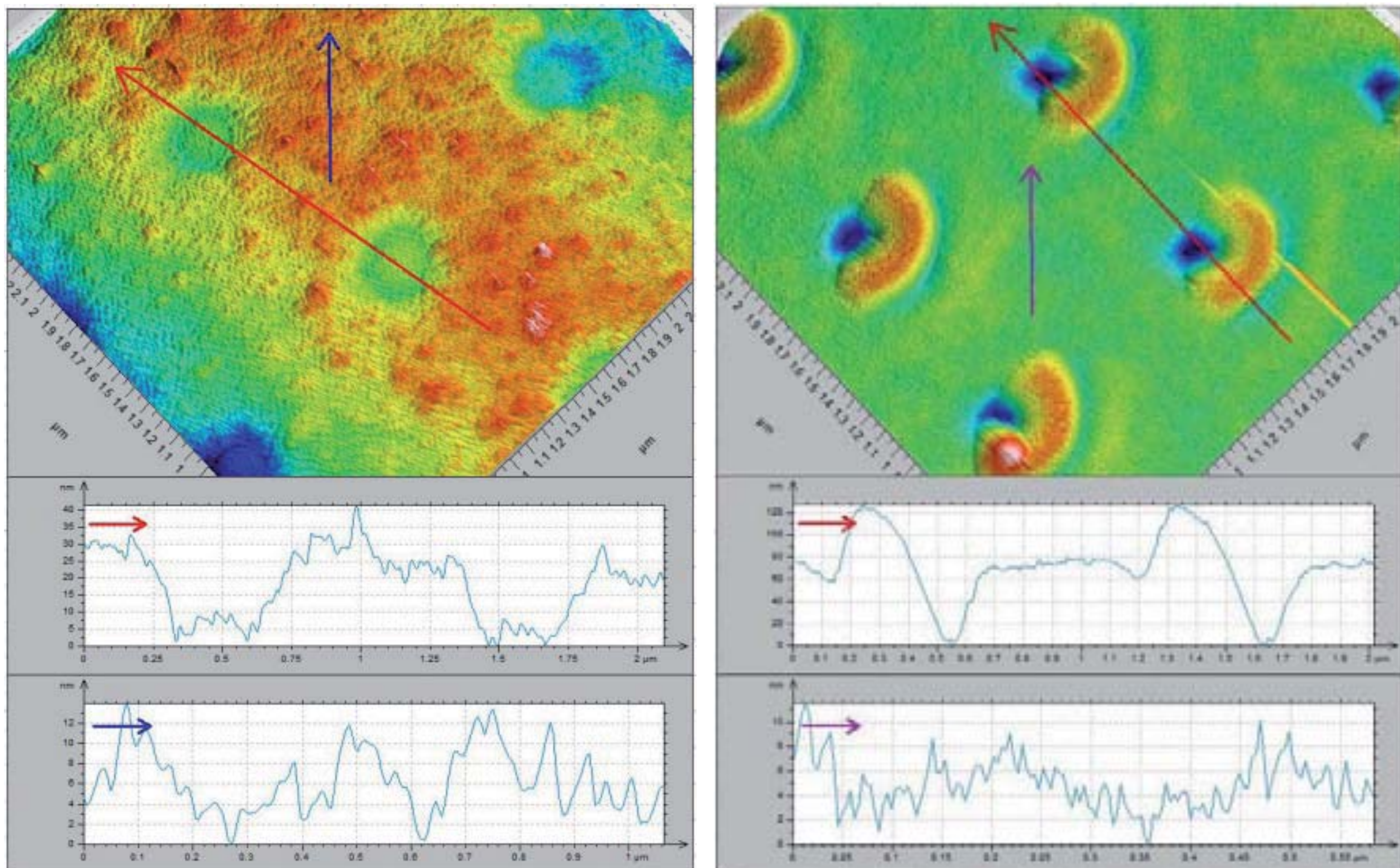

Figure 4-6 *Nanopores at two different dwell temperatures. Left: 100 °C. Right: 220 °C. Applied pressure 40 MPa, dwell time 5 min, demolding temperature 80 °C, no etching, no annealing, acetate based LSMO precursor with 15 wt% PVOH.*

Specifically, one can see that at temperatures of 100C, the nanopores were too shallow, and at 220C undesired artifacts were generated. Specifically, the depth of the nanopores reached around 30 nm in the 100C case, which does not accurately correspond to the shape of the mold used. The reason for this is simply that the precursor film was not heated to a sufficiently high temperature so as to fully relax the polymer. The mold simply could not penetrate completely into the film due to its high viscosity. At the other end, at 220C the polymer was heated too much, causing donut like outcroppings to appear next to the nanopores. Perhaps the cause of these outcroppings was that the polymer was sufficiently heated so as to harden locally near the nanopores, thus pushing against the mold and creating both positive and negative structures. The optimal temperature appeared to lie around 160C due to a relative low roughness, a fully engaged mold, and a low occurrence of artifacts as can be seen on the right of figure 4-3.

4.2.2 Applied Pressure

Once the thin precursor film reached a temperature where the polymer film began to flow freely, a uniform pressure had to be applied so that the nano-scale pillars entered easily. This pressure had to be high enough to overcome the surface tension of the viscous film and displace the volume of millions of nanopillars simultaneously. The pressure which was determined to be optimal for nanoimprinting purposes was four megapascals or forty bars. If assuming a mold equal to 25 mm^2, then the number of newtons applied to the thin film was around one hundred, or roughly the weight of ten kilograms. This increased pressure applied to the system caused a combination of density augmentation along with a mass extrusion out the sides. The amount of displacement when the mold fully engages to the volume of nanopillars in the film is roughly equal to the volume of a grain of sand.

One can see that in figure 4-7 that the resultant effect on nanopore quality when the pressure was pushed to lower limit of 1 MPa and increased to the maximum of 7 MPa. Here, one can observe how the nanopores have not reached their full potential depth when under the lowest pressure conditions. One can additionally observe that at 1 MPa the roughness of the demolded fifteen percent PVOH LSMO precursor film is very high. When increasing the pressure too much, however, one sees how the nanopores have become more elliptical in shape. This is thought to be due to the sliding of the substrate under such high pressures. While this elongation of the nanopores is undesirable, the increased depth of the nanopores is. This increase of thirty nanometers of depth at seven megapascals can be attributed to the increased pressure applied to the film. The optimal depth of the nanopores should be just less than 120 nm due to the mold being that dimension. The amount of pressure applied on the right of figure 4-3 was 7 MPa. This trade-off between depth and elongation of the nanopores is something which should be optimized further if this technique were to be industrialized.

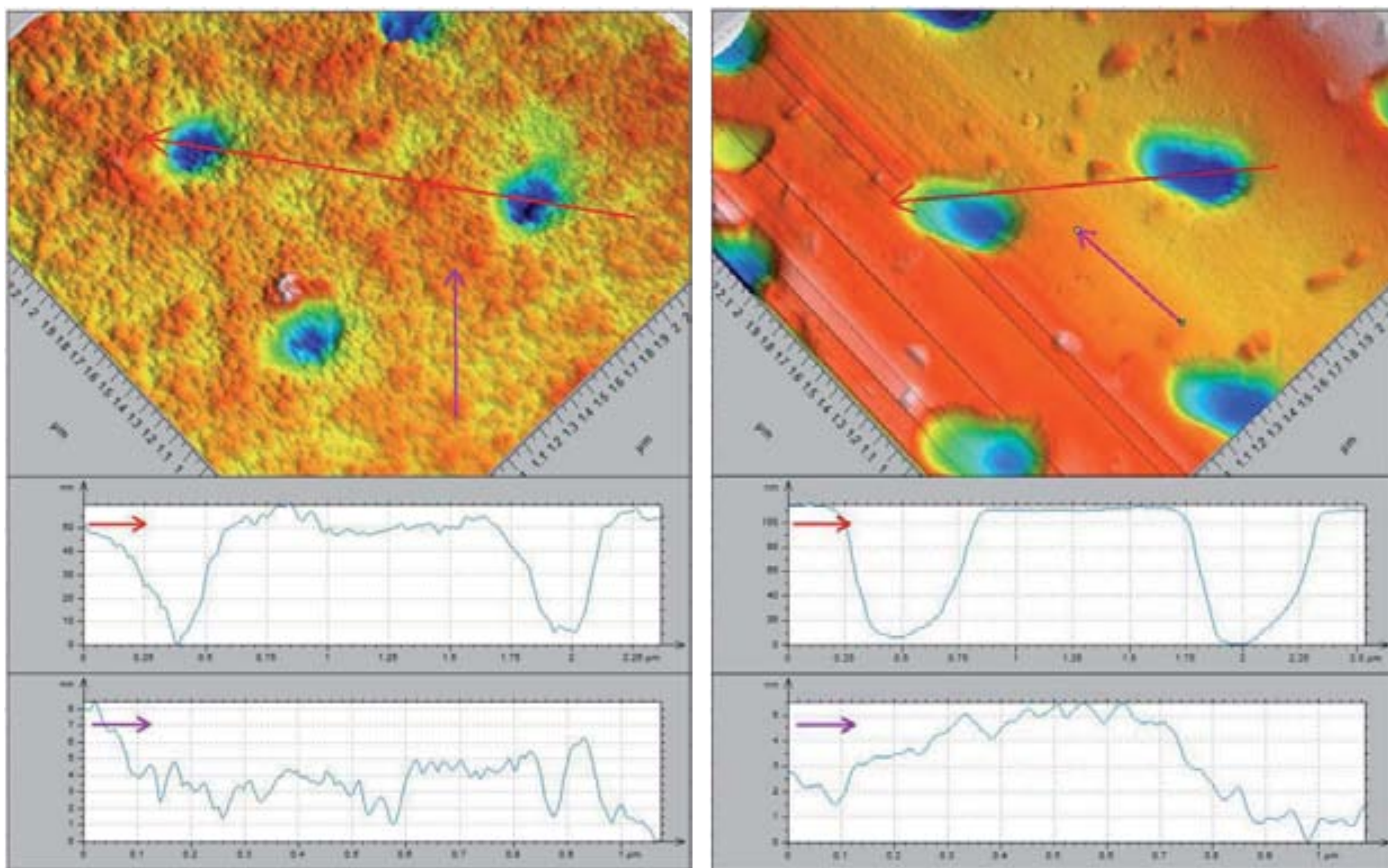

Figure 4-7 *The effect of pressure on the resultant nanopores. Left: 1 MPa. Right: 7 MPa. Dwell temperature 160 °C, dwell time 5 min, demolding temperature 80 °C, no etching, no annealing, from acetate based LSMO precursor with 15 wt% PVOH.*

4.2.3 Dwell Time

The time in which the pressure is applied to the thin film via the mold at an elevated temperature is referred to as the dwell time. This time can range from mere seconds up to hours. The point of having an appropriate dwell time is to give the individual polymer strands enough time to translate into a more relaxed configuration under the presence of the volume displaced from the nanopillars. For a polymer film imprinted with the conditions described herein, this time frame is on the order of a few minutes. Anything shorter than that and the polymer will not flow properly out of the way and not form well defined nanopores. Anything longer than that and a point of diminished return is reached yielding not significantly better formation but with significant longer turn-around time.

As can be seen in figure 4-8, altering the time in which the thin film is pressed at high temperature and pressure, affects the overall film quality as well as the depth of the nanopores. When reducing this dwell time down to zero, there is

insufficient time in which the silicon mold may press into the film. Subsequently, the nanopores depth is less than the height of the nanopillars, and thus does not correspond to the desired morphology. The amount of time the pressure was applied on the right of figure 4-3 was thirty minutes.

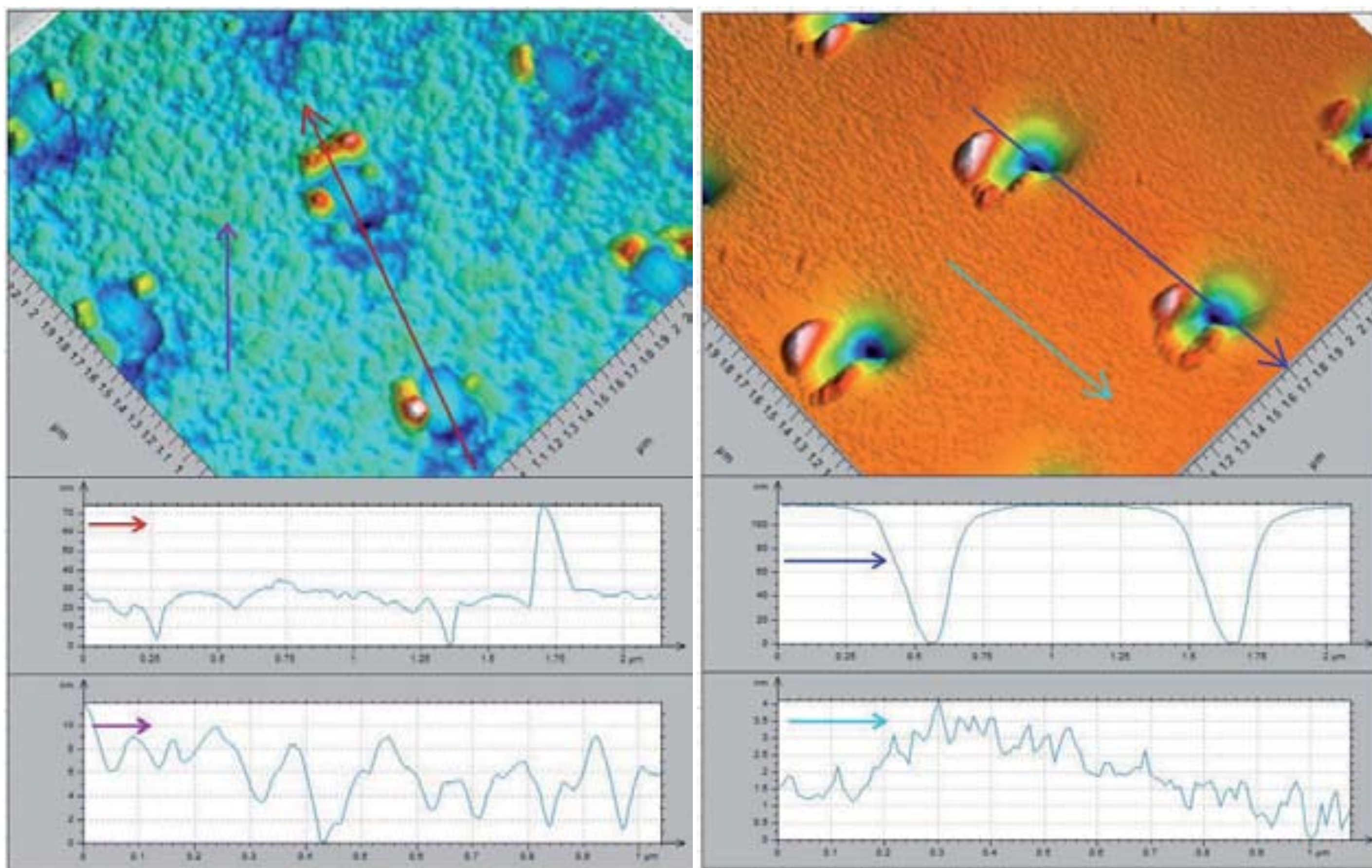

Figure 4- 8 *Altering the dwell time. Left: one second. Right: thirty minutes. Dwell temperature 160 °C, applied pressure 40 MPa, demolding temperature 80 °C, no etching, no annealing, from acetate based LSMO precursor with 15 wt% PVOH.*

.

4.2.4 Demolding Temperature

The demolding temperature refers to the point at which the mold and the film are separated. This separation temperature can be either the same as the dwell temperature, indicating no cooling off of the system before demolding, or it can at a significantly lower temperature. This indicates waiting several minutes for it to reach the desired demolding temperature. The higher the demolding temperature, typically the more the nanopores will revert back to their original shape, which is back to a flat film. This is because the system is still highly mobile at this point and thus will

fill the void left by the absent nanopillars. On the other hand, waiting too long, while insuring a good nanopore morphology closely resembling that of the nanopores, can lead to inefficient allocation of time per unit made.

On the left of figure 4-9, one is able to note the incompletely formed nanopores due to a lack of any cooling before demolding. These nanopores possess outcropping artifacts along their edges which may be due to the still soft polymer film being pulled away from the mold. This would have formed a small meniscus at the interface between the mold and the film, which would have remained after cooling. Another feature these nanopores have is a partially collapsed nature, or in other words, the pores shape partially reformed into its originally pre-imprinting shape. This is also attributed to the lack of any hard structural support in the form of a mold immediately after temperature has been reached. Thus, these nanopores, while being above the glass transition temperature and therefore highly non-viscous, partially reverted back to the more relaxed configuration of a smooth thin film.

On the right of figure 4-9, one can see the resultant nanopores after demolding at 25C. This process of allowing the system to cool down to room temperature took almost three hours compared to thirty minutes with a 80C demolding temperature and instantaneous when demolding at 160C. One observes from the image on the right that the depth of the nanopores is deeper than the sample demolded at 80C as seen on the right of figure 4-3. Perhaps the cause for this non-perfect reflection of the mold in the sample demolded at 80C is also due to a relaxation away from the high aspect ratio hole after demolding. Obviously, for production purposes a balance must be struck between the time given to decrease the films temperature and acceptable morphology of the resultant nanopores.

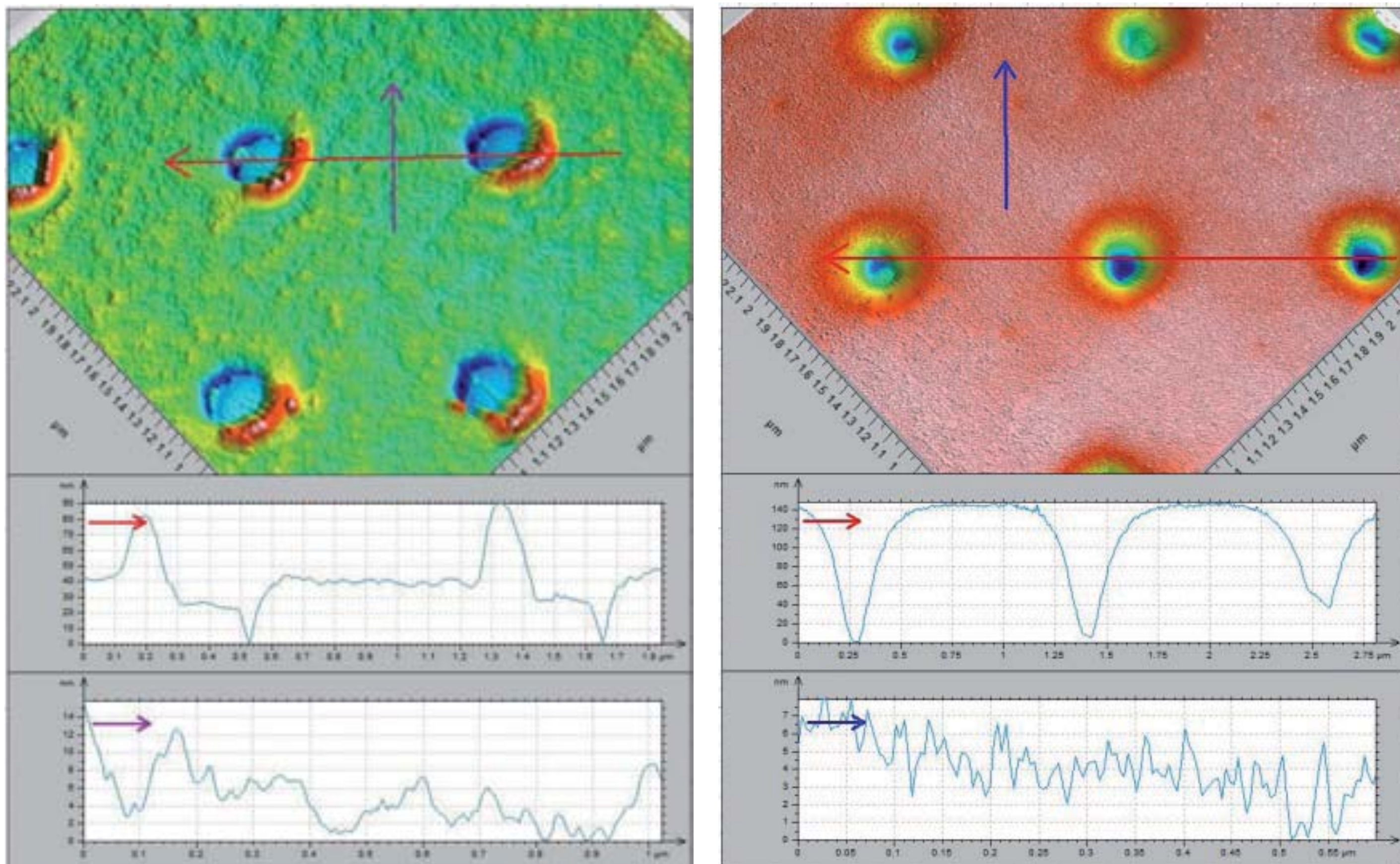

Figure 4-9 *The effect of altering the demolding temperature on the nanoholes morphology. Left: 160 °C. Right 25 °C. Dwell temperature 160 °C, applied pressure 40 MPa, dwell time 5 min, no etching, no annealing, from acetate based LSMO precursor with 15 wt% PVOH..*

4.3 Etching Residual Layer

The removal of a residual layer of nanostructurated precursor film requires the use of a reactive ion etcher. This etching allows for the film to be removed in an anisotropic fashion. This means that the material at the bottom of the nanopore is preferentially removed before the material on the walls of the nanopores. Any material which is perpendicular to the plane of the substrate is removed quickly and material parallel to the plane is removed slowly. Thus, precursor film between the nanopores is also removed. The end result is that the aspect ratio of the nanopores is left relatively unmolested in the etching process whereas the overall thickness of the film is reduced.

Several different gases were used in the residual layer etching process. Including oxygen, there exists argon as well as the fluorine based gases, hydrogen bromide, and litany of others. As well as using solely one type of gas in the plasma etching process, it is common practice to use combinations of gases at various ratios. Clearly the possible combinations

are large to say the least. However that may be, argon was chosen in these following experiments due to it being chemical inert. Argon allows the imprinted film to be removed mechanically as opposed to the chemical etching obtained with oxygen plasma.

Several parameters had to be controlled in the reactive ion etching process. These included the amount of time the plasma is ignited, the type of gas used, the atmospheric pressure inside the vesicle, the power used transmitted in the plasma, and the reflective power. In this work two different gases were used, namely oxygen and argon. The time and power used to etch the imprinted film for oxygen plasma was 150 watts for 5 minutes for nitrate based 2 wt% PVOH and 1200 watts for 120 seconds for acetate based 15 wt% PVOH. For argon plasma etching, 150 watts for 15 minutes was used for nitrate based 2 wt% PVOH. The gas flow was not a parameter which was adjusted in the etching and remained at 200 sccm throughout the experiments.

The procedure for determining the optimal power for a respective gas was such that the time was initially set at two minutes and then the power was altered. The initial power used was set extremely high so as to remove the imprinted film completely. The power was then lowered gradually in an incremental way and the film was inspected optically. When an optical inspection showed that not all of the imprinted film had been etched, the power was lowered slightly so as to leave a very thin residual film. The reason why the time was set at two minutes as opposed to fifteen seconds, for example, was to assure that the amount of etching would not be subject to small aberrations in the plasma strength which is characteristic at short working times.

Another aspect of importance in the etching process when using male molds, is reducing the resultant film's roughness between nanopores. The film should ideally be very smooth after etching due to the annealing process normally roughening the surface up. This smooth surface after etching, while not only being aesthetically more pleasing, allows for a more homogeneous signal from such instruments as an AFM when probing the surface. This in turn allows for a better determination of the depth of the etched nanoholes due there being a more consistent reference level in which to gauge. The roughness of the etched film also signified that the ratio of organic material to inorganic material was too low. Inorganic material will not be etched in an aggressive manner as compared to organic material for an oxygen etching. Because of this, a rough film might indicate that the organic components in the film are lying deep underneath the inorganic molecules and are thus less readily accessible to etching. This inaccessibility had caused the power necessary to etch the imprinted film to rise to relatively high levels.

Initially the gas used in the plasma etching process was oxygen. This was due to the ability of oxygen as a plasma gas to consume an organic layer very quickly. However, the film quality was reduced significantly when using two percent PVOH in conjunction with oxygen plasma. The roughness was observed to be very high when using a precursor with two percent PVOH and less rough when using the more viscous fifteen percent PVOH. This is thought to stem from the increased amount of organic material by weight in the fifteen percent PVOH precursor.

In an attempt to retain the smoothness of the original imprinted film after etching, argon gas was used instead of oxygen. The resultant film was very different from expectations. This film had nanoislands at the same location that there should have been nanoholes as well as being highly reduced in overall film amount. These nanoislands, herein called nanocaps, derived from imprinting with a male mold into a two percent PVOH film and then etched with argon plasma. These nanocaps however defied an easy explanation. One idea was that the male mold was actually compressing the film locally thereby locally increasing density and thus able to withstand the argon etching. This portion of the film, directly underneath where the top of the pillar pressed in, would be more resistant to the argon plasma and thus everything else would be etched except the nanocaps.

The effect on the quality of the film after etching can be seen in figure 4-10. Here the objective is to reduce the film by etching by not adversely affect the roughness of the precursor after being etched with argon or oxygen. The precursor used in the example is two percent by weight polyvinyl alcohol. After etching it is clearly observed that the roughness increases dramatically under the presence of an oxygen plasma as compared to the argon plasma. Numerically one can see this difference by comparing the more than five-fold increase in roughness from 2.09 to 10.3 when etched with oxygen plasma as compared with argon. This roughness is critical to controlling the end film quality once annealed. It was later observed that if the precursor had fifteen percent by weight PVOH, then the oxygen plasma etching did not result in an adversely affected film.

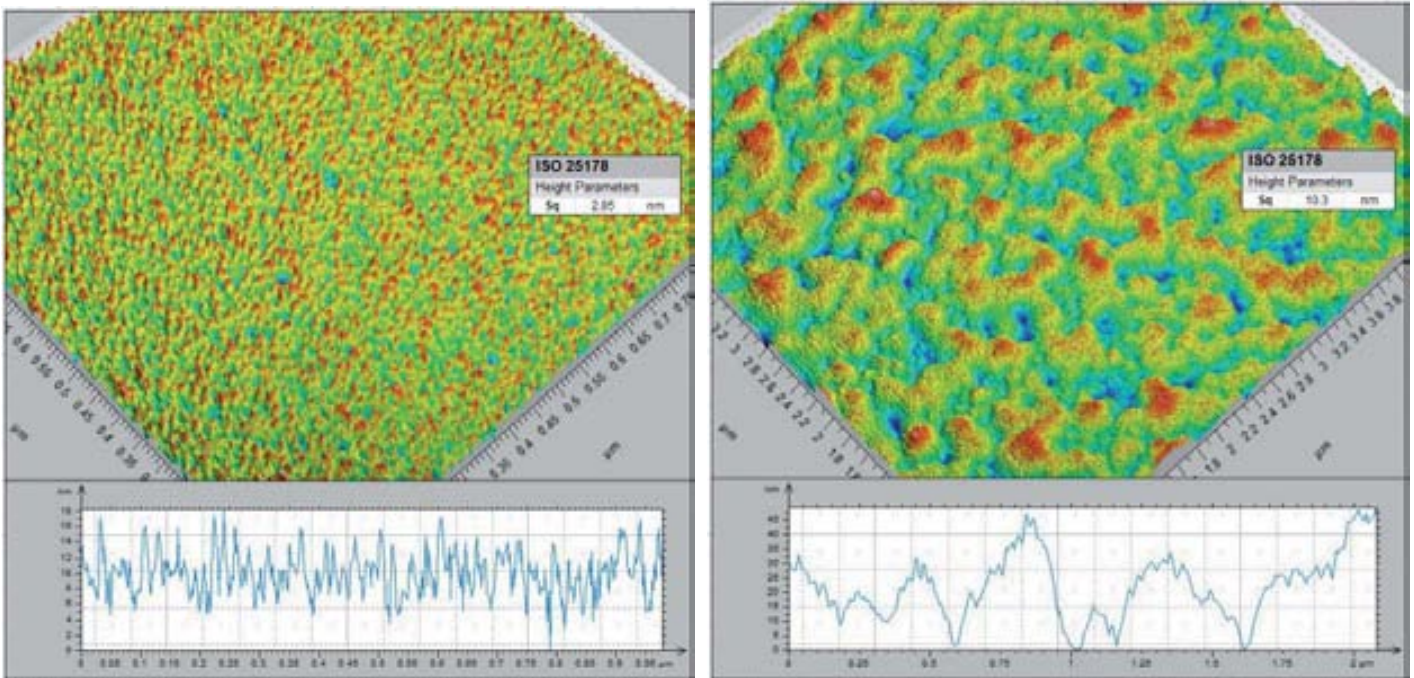

Figure 4-10 *Effect of different gases on surface roughness of nitrate based LSMO precursor with 2 wt% PVOH. Left: etched with argon. Right: etched with oxygen. No annealing occurred. 150 W, 200 sccm, 300 seconds of plasma.*

.

4.3.1 Oxygen Plasma

In figure 4-11 one can see a series of nanoholes imprinted into the LSMO precursor on top of YSZ and then etched with an oxygen plasma. On the right hand side of the image one can see the residual layer has been removed down to the substrate floor. The actual nanoholes are rectangular in shape here due to high demolding temperature coupled with a slight diagonal separation. What one also notices is the high granularity of the material between the nanoholes.

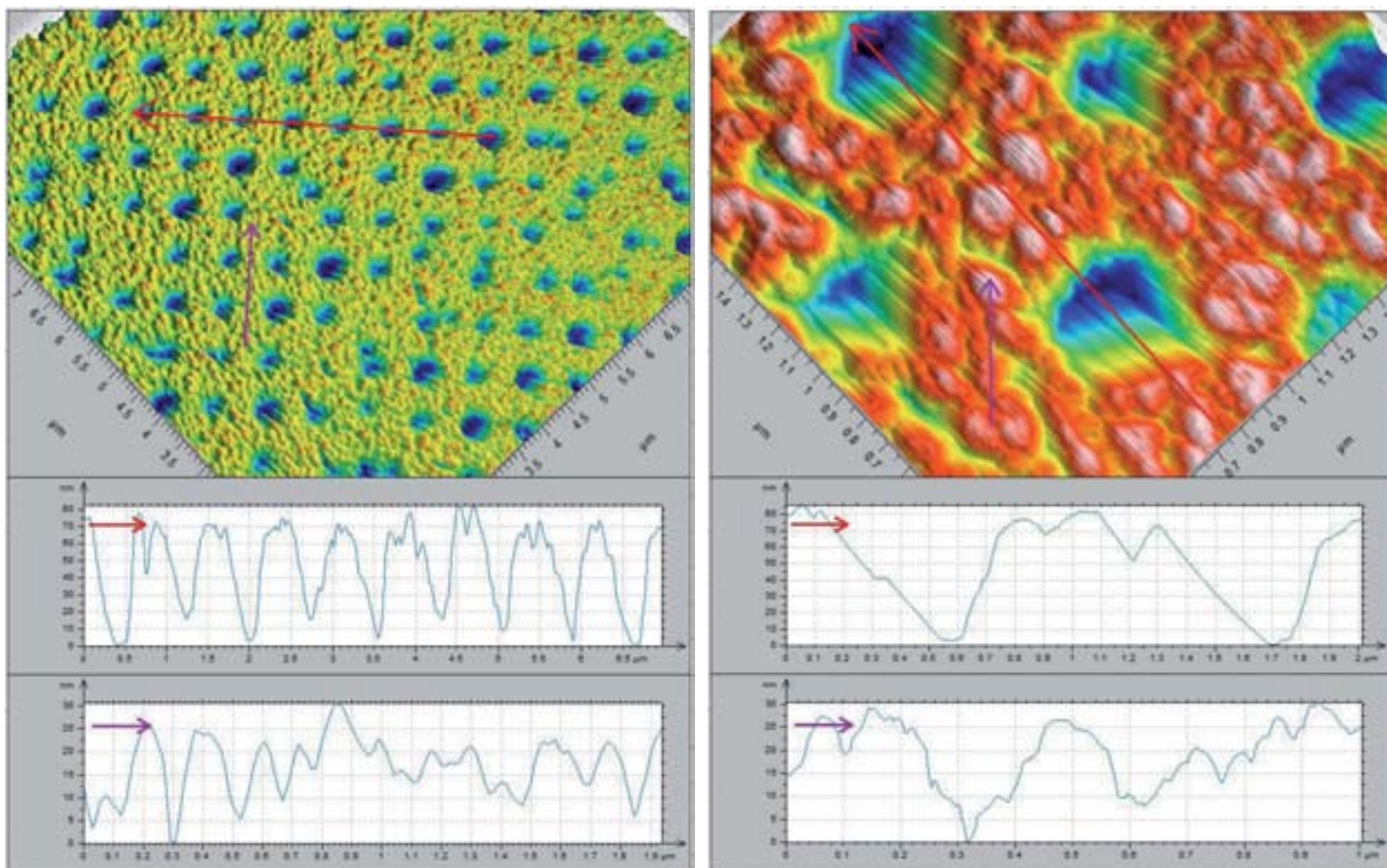

Figure 4-11 *Left: oxygen plasma etching of 300 seconds at 150 watts to generate nanoholes on YSZ. Right: zoom of area. Dwell temperature 160 °C, applied pressure 40 MPa, dwell time 5 min, demolding temperature 80 °C, no annealing, from nitrate based LSMO precursor with 2 wt% PVOH.*

.

The main difficulty with the procedure of using oxygen as the plasma gas on a 2 wt% PVOH residual layer is that the film quality degrads rapidly. This consequence of roughening when using ionized oxygen is unavoidable however lessened with an increase in the amount of polymer as a precentage of precursor weight. Another contributing factor to the degradation in film quality after etching with oxygen is if the counter ion to the metal salts is nitrate. Originally nitrate was used exclusively as the counter ion for the lanthanum, strontium, and manganese salts. This was mainly due to a previously reported successful usage of nitrates as counter ions in a polyvinyl alcohol aquaeous solution [58-60]. A work around was to use acetates instead of nitrates as the counter ions.

The goal was to reduce the volatile reaction of the oxygen plasma and the organic components leading to a deeply scarred film. The introduction of acetates instead of nitrates was observed to reduce the roughness of the imprinted film in the presence of oxygen plasma. One can clearly see a smooth surface after two minutes of oxygen plasma at twelve hundred watts in figure 4-12. This two minutes of high energy oxygen plama would have roughned the film surface greatly if the counter ion would have been nitrate, but in the case the morphology of the nanohole and

surrounding film was preserved. The imprinted film was observed here to have been etched down to the single crystal substrate and the height of the remaining film was on the order of 160 nm. The reason for this was that the 15 wt% PVOH film initial was around 250nm previous to nanoimprinting. The precursor film used here had a relative high percentage of PVOH by weight, that is fifteen percent. This combination of high polymer content and acetates as the counter ion, yieled films with relatively little roughness, on the order of a single nanometer whereas for the low polymer nitrates produced roughness values of thirty nanometers. This elimination of roughness is important in the annealing step where the organic components are completely removed and thus the roughness increases greatly.

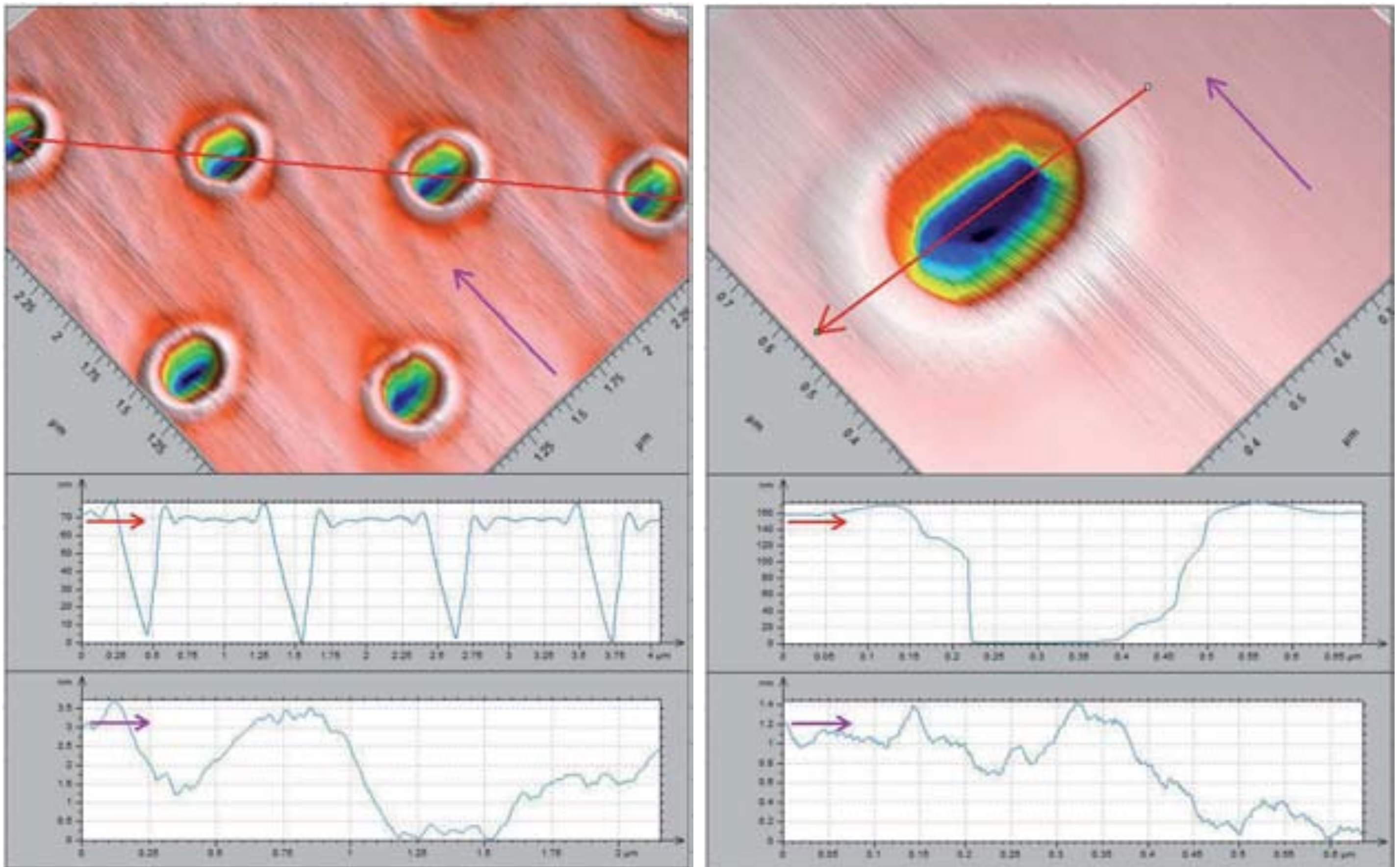

Figure 4-12 *Nanoholes generate in acetate-based precursor from 1200 W, 200 sccm, 120 seconds of oxygen plasma. Dwell temperature 160 °C, applied pressure 40 MPa, dwell time 5 min, demolding temperature 80 °C, no annealing, LSMO precursor with 15 wt% PVOH.*

.

4.3.2 Argon Plasma

When argon was used in lieu of oxygen in the plasma etching step, nanocaps were formed as can be seen in figure 4-13. This particular example was not etched fully enough so as to reach the substrate floor as can be seen in the line scan.

The original spin coated film thickness for the sample used in figure 4-13 was 250 nm and had fifteen percent by weight PVOH. The resulting height of the nanocaps averaged 100 nm above the film floor but was etched down 70 nm more than that at certain places. One can also clearly see the spacing of the nanocaps corresponds to the arrangement of the nanopillars on the mold. That is, the pitch of the mold was one micrometer and the pitch of the nanocaps is also one micrometer. Also the width of the nanocaps is in line with the width of the male mold used in the imprinting process.

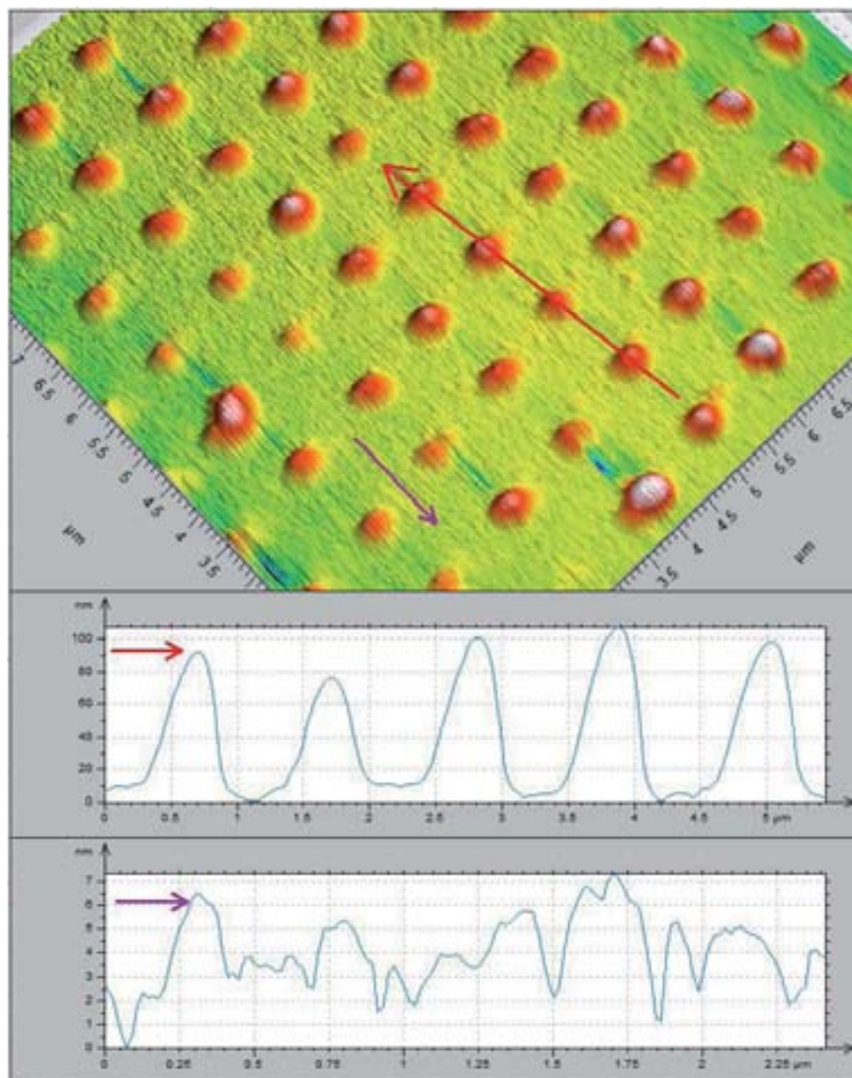

Figure 4-13 *Nanocaps formed after argon plasma etching from male mold. Dwell temperature 160 °C, applied pressure 40 MPa, dwell time 5 min, demolding temperature 80 °C, no annealing, 150 watts for 15 minutes at 200 sccm*, *from nitrate based LSMO precursor with 2 wt% PVOH.*

The hypothesis that the nanocaps are being formed from a compression of the precursor film is difficult to confirm however. This is due to a lack of other molds of varying patterns and a way to check the density of uncompressed film and that of the nanocaps. However, one may observe the evolution of these nanocaps as in figure 4-14. Here, the

central portion which ends up becoming the nanocaps can been seen surrounded locally by a concave shaped etched region. This half completed etching shows that below the nanopores are a series of hardened nanocaps. This series of nanocaps, it is thought, were made of a higher density than the surrounding film, thus making it more impervious to removal by argon. Hence when the amount of power and its applied time was correctly optimized, a row of exposed nanocaps could be generated.

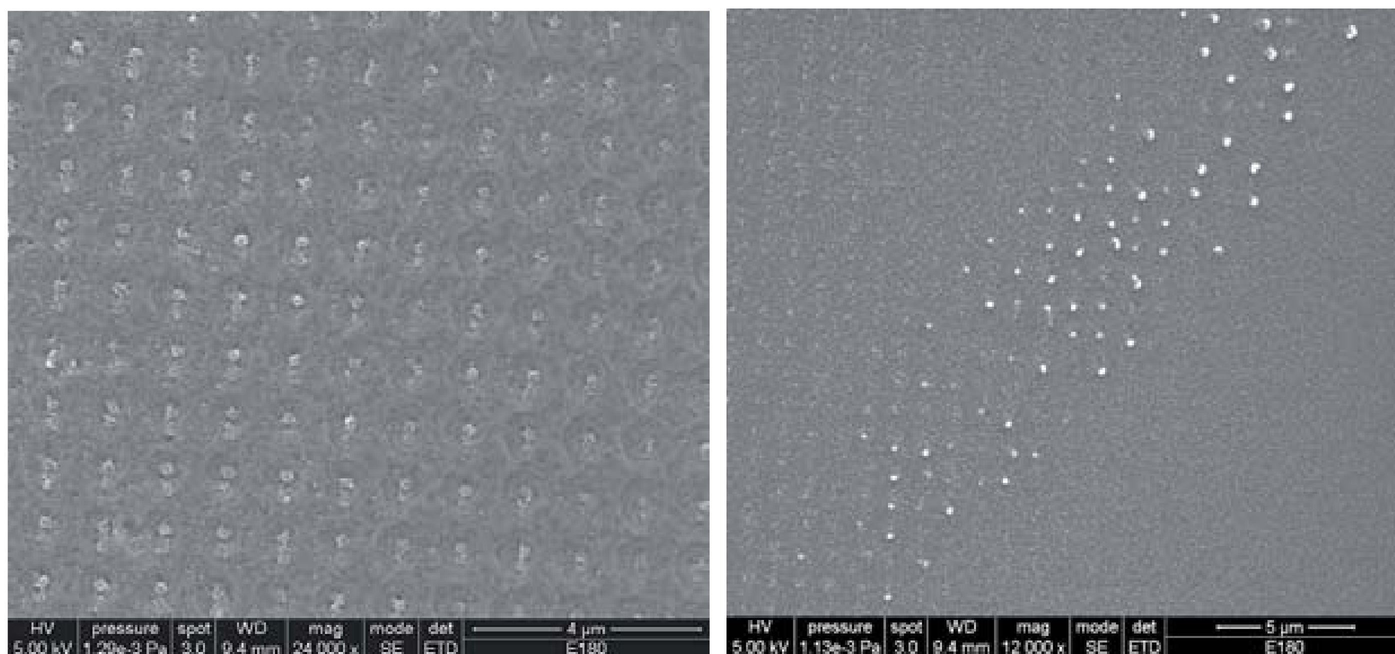

Figure 4-14 *Left: nanopores partially etched with argon plasma exposing nanocaps after 300 seconds of etching. Right: fully exposed nanocaps after 15 minutes of etching. Dwell temperature 160 °C, applied pressure 40 MPa, dwell time 5 min, demolding temperature 80 °C, no annealing. 150 watts at 200 sccm*, *from nitrate based LSMO precursor with 2 wt% PVOH, substrate STO.*

4.4 Annealed Structures

Once the imprinted nanostructures were etched down to the substrate floor, they were annealed in a furnace so as to crystallize the structures. These annealed structures differed morphologically from the etched nanoholes and nanocaps. Their overall size was reduced due to a loss of the organic components and density increase that comes from the formation of a nanocrystal. One of the nanocaps was analyzed with TEM to reveal that manganese, contrary to the nanodots formed from EBL, was present. This elucidates a bit the mechanism in which manganese is being lost in EBL made samples, namely that if unmolested by focused electrons, manganese will remain. Thus the manganese is being lost at the point of where electrons polymerizing the LSMO precursor. Other oxide-based nanostructuration should take

this into account and concentrate production efforts on NIL and not on EBL for this very reason. There is tremendous appeal of introducing a stoichiometric amount of several species of metal salts into an aqueous solution of PVOH, and getting a resulting nanostructure with the same ratio of components.

Looking at figure 4-15, one sees an early attempt to refine the etching and annealing process on silicon. The gas used here was oxygen as can be seen from the nanoholes on the left hand side of the figure. One can also see the fragmentation of the material between the nanoholes as the large amount of polycrystalline LSMO was unable to grow epitaxially on the silicon. The substrate floor is also seen there, thus signifying that the etching process was able to eliminate the residual layer.

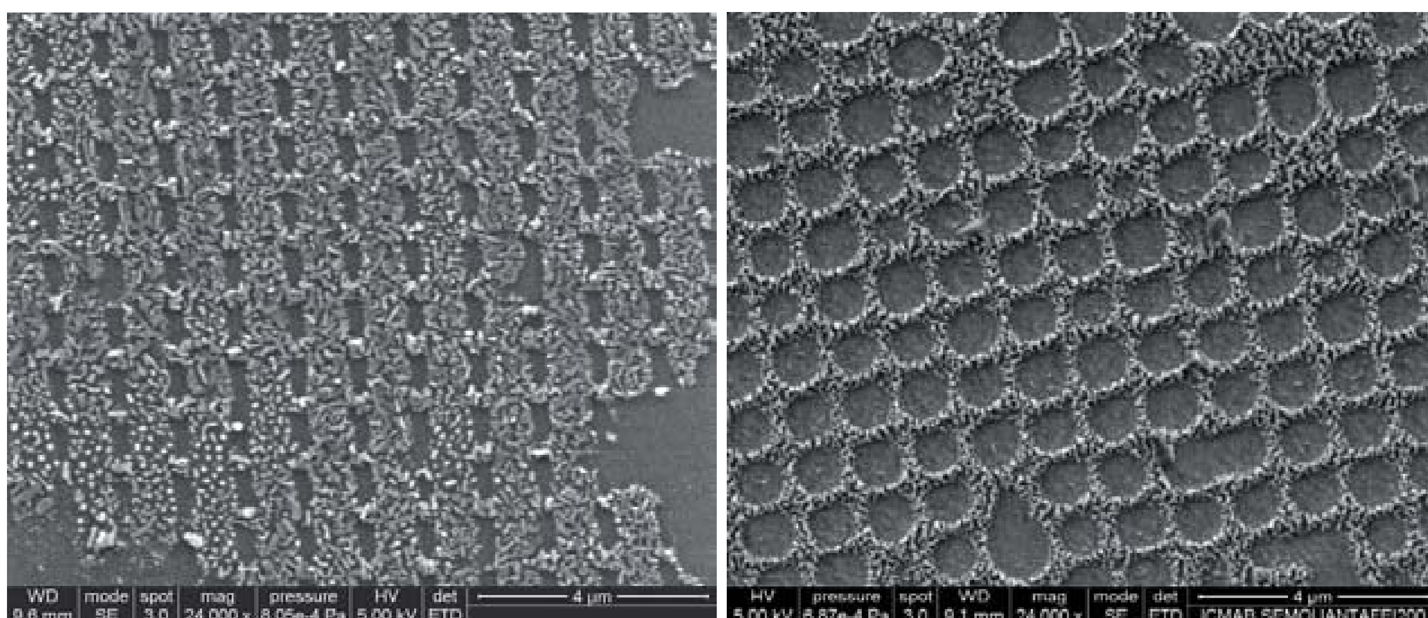

Figure 4-15 *Left: nanoholes after oxygen RIE and annealing on silicon. Right: another area of same sample. Dwell temperature 160 °C, applied pressure 40 MPa, dwell time 5 min, demolding temperature 80 °C, 150 watts for 5 minutes at 200 sccm*, *from nitrate based LSMO precursor with 2 wt% PVOH, 900 °C annealing temperature for 240 minutes.*

In figure 4-16, nanoholes can be seen on a STO substrate made from oxygen plasma etching. What can clearly be observed in the SEM image is that the substrate floor has been reached via etching and that the remaining LSMO material - which makes the form of the nanohole - is not contiguous. This breaking of the remaining crystalline LSMO into tiny pieces is to be expected when growing on silicon and in such a convoluted fashion. Ideally the remaining film would be one continuous crystal on a single crystal substrate. **The resulting film between nanoholes is extremely rough and the boundaries of the nanostructure are not well defined. This roughening caused by oxygen plasma on the two percent PVOH by weight precursor was systematic of this combination.**

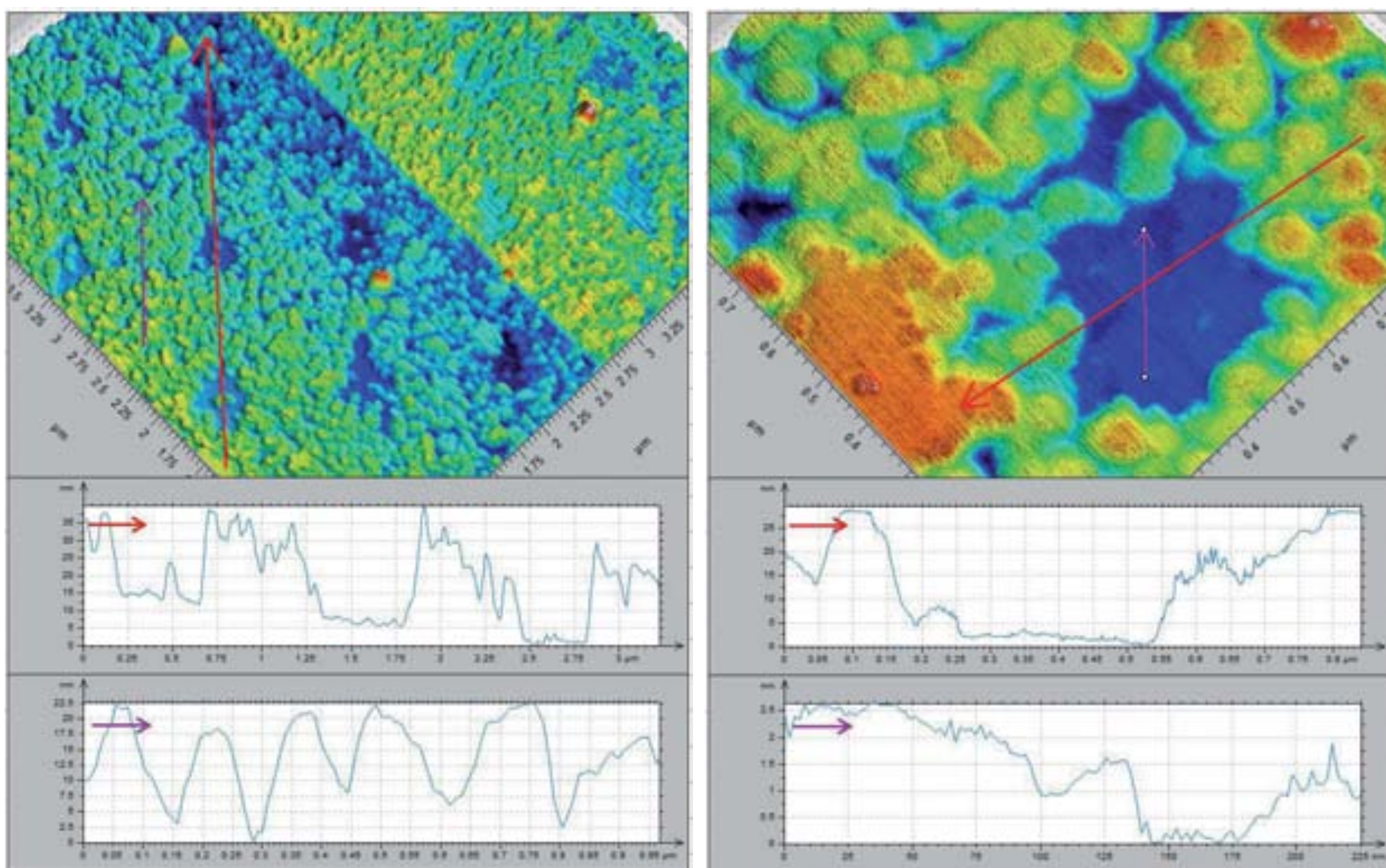

Figure 4-16 *Left: a series of nanoholes etched with oxygen plasma on STO. Right: zoom on one hole. Dwell temperature 160 °C, applied pressure 40 MPa, dwell time 5 min, demolding temperature 80 °C,150 watts for 5 minutes at 200 sccm*, *from nitrate based LSMO precursor with 2 wt% PVOH, 900 °C annealing temperature for 240 minutes.*

In figures 4-17, one finds an array of nanoimprinted structures which have been annealed after being first imprinted with a male mold and then annealed with argon plasma. These nanostructures differ from those produced by the oxygen plasma in that the annealed material is the actual nanostructure and not the absence of annealed material. The annealed nanocaps here are grown on YSZ and do not appear to be single crystals due to their smooth rounded shape. The etching also appears to have roughened the surface between the nanocaps a bit. One can see in figure 4-17 very little reduction in height from the pre-annealed nanocaps compared to the post-annealed ones.

This lack of any real reduction in height of the annealed nanocaps differs from a typical nanostructure. Typically a nanostructure made from the oxide precursor will be a half to a third as large when annealed as compared to before annealing. In the case of the nanocaps, the size is not reduced significantly. This leads to the idea that the annealing process was able to remove any organic components from the individual nanocaps. This would be consistent with the

high amount of elevated thermal contact that took place in the plasma chamber at one hundred and fifty watts for fifteen minutes. Thus, the high heat during the argon plasma annealing process was able to cook the nanocaps such that a further annealing step was unnecessary.

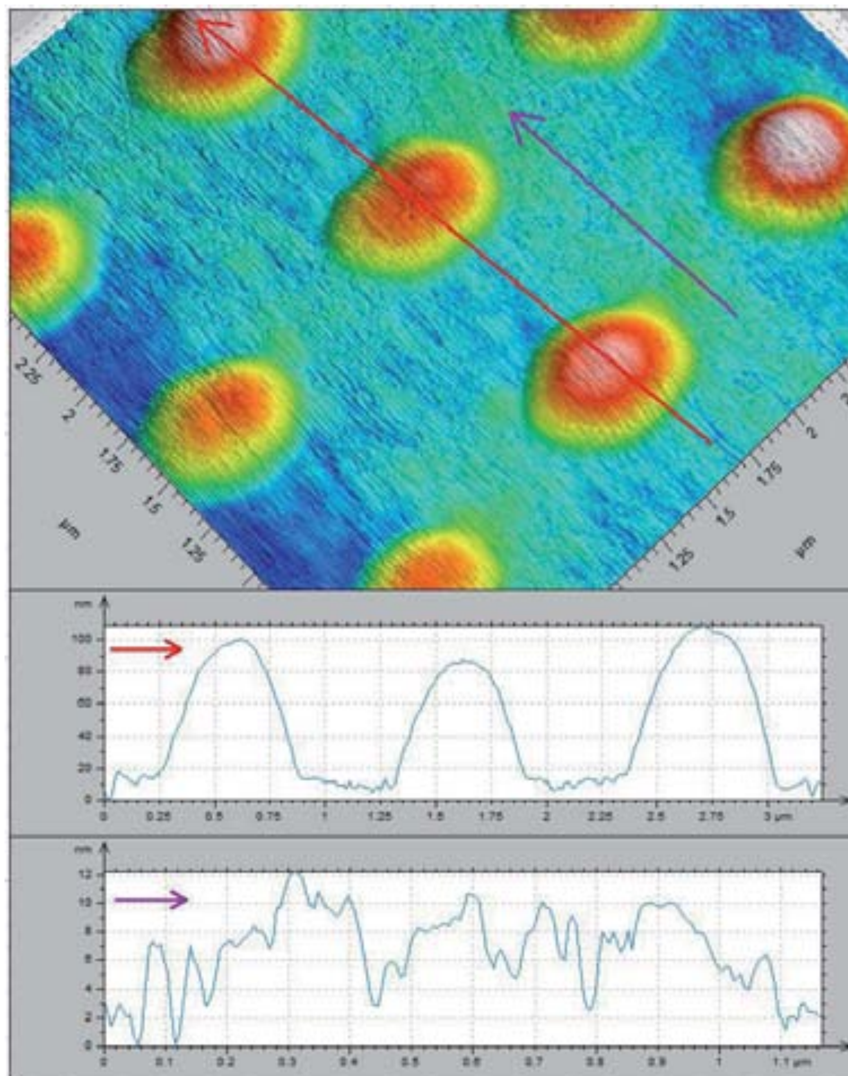

Figure 4-17 *Series nanocaps after being annealed on YSZ. Dwell temperature 160 °C, applied pressure 40 MPa, dwell time 5 min, demolding temperature 80 °C, etching conditions of 15 min at 150W in an argon atmosphere, annealed 900 °C for 240 minutes, from nitrate based LSMO precursor with 2 wt% PVOH.*

One can see in figure 4-18 the effect of nanoimprinting and annealing has on the precursor on a single crystal substrate with and without oxygen plasma etching. On the left hand side of figure 4-18 one can see the result of not etching the residual film, mainly that the nanoholes are still filled with material and that the substrate floor is not exposed. This resulting structure is thicker than the structure on the right hand side of figure 4-18. There the remaining LSMO film is thinned sufficiently enough to allow only a shallow ring around where the imprinted nanopores was. One can see the

morphological differences of the remaining film from the two SEM images, mainly the thicker one on the left has small fracturing running along the ridges of the nanoholes and the thinner one has broken up into individual pieces. The reason why the remaining outline of the nanoholes cannot form a continuous crystal is due to the very large size of the structure involved. The resulting structure without etching is not particularly interesting to the study here due to it giving more of a continuous magnetic signature than that of with a non-ferromagnetic nanohole array. An array or magnetic nanodots or an array of non-magnetic holes surrounded by a magnetic film would prove more interesting technologically than a continuous magnetic film due to the desire to have discrete changeable memory states.

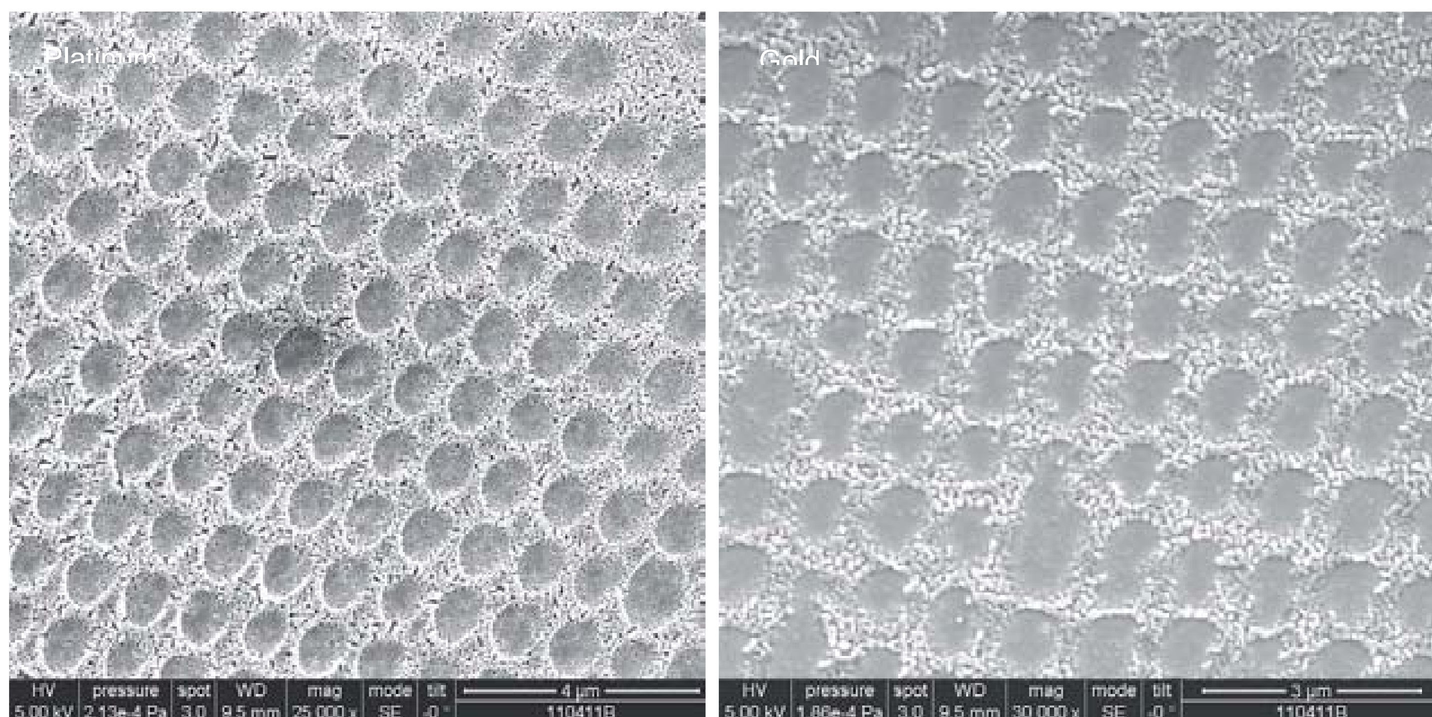

Figure 4-18 *Left: annealed nanoholes without etching. Right: annealed nanoholes after etching. Dwell temperature 160 °C, applied pressure 40 MPa, dwell time 5 min, demolding temperature 80 °C, etching conditions for image on right were 5 min at 150W in an oxygen atmosphere, annealed 900 °C for 240 minutes, from nitrate based LSMO precursor with 2 wt% PVOH on silicon.*

As for the nanocaps that were borne from the argon etching process using a nitrate based LSMO precursor with two percent by weight PVOH, when annealed, the resultant nanostructures broke into small pieces. This can be seen clearly in figure 4-19. The individual nanocaps have been reduced in size due to the volatile organic components being removed during the annealing process. Ideally, the size of the annealed nanocaps should be small enough so that it does not break into smaller pieces but rather stays intact. If a single site has multiple nanocrystals, the discrete magnetic state is harder measure and to control and is thus less useful for applications.

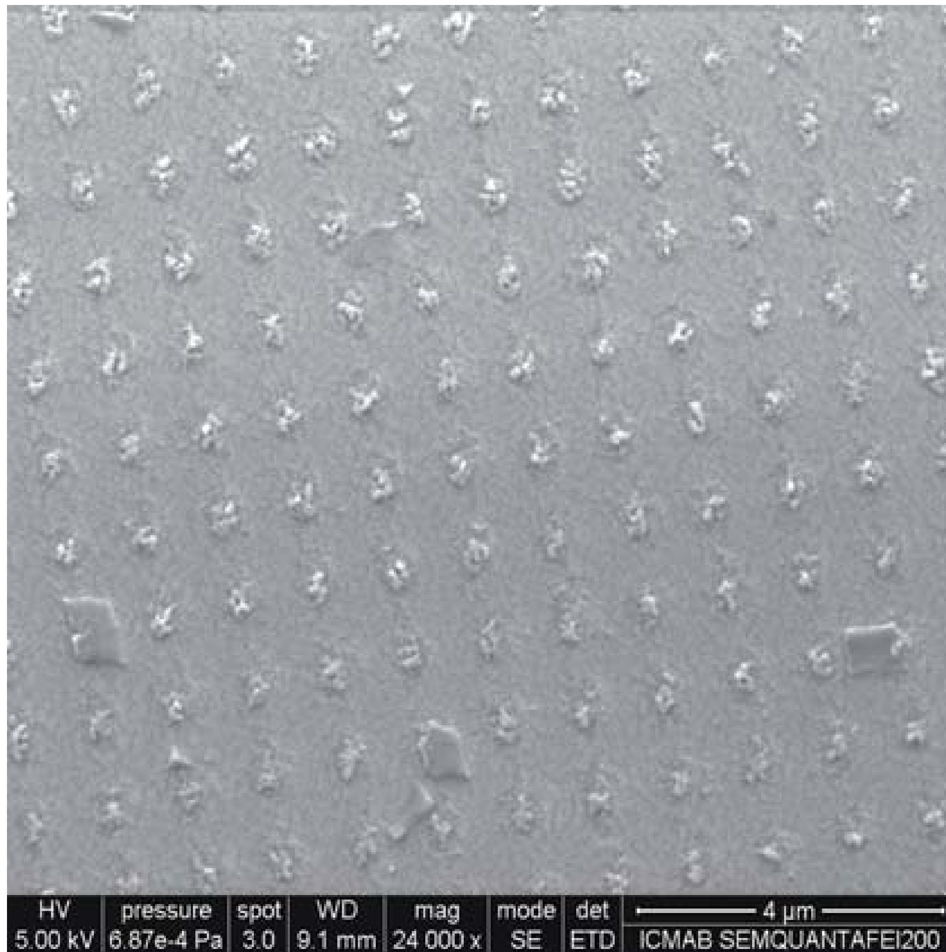

Figure 4-19 *Annealed array of nanocaps on LSMO on silicon. Dwell temperature 160 °C, applied pressure 40 MPa, dwell time 5 min, demolding temperature 80 °C, etching conditions were 15 minutes at 150 W in an argon atmosphere, annealed 900 °C for 240 minutes, from nitrate based LSMO precursor with 2 wt% PVOH.*

A difficulty with scaling up this argon etching process to industrial levels is the fact that the percentage of the surface which retained the nanoholes or nanocaps is low. The amount of well defined nanostructuration varied between ten and twenty percent per substrate. An example of this poorly defined nanostructuration can be found in figure 4-20. Here one can see that the original intended form of nanoholes made by argon has not been fully realized. There exists a large amount of variation over a small section of the film. This particular section of the sample was between a well defined array and an overly etched one.

The reason that on average only fifteen percent of the sample was still nanostructurated after etching and annealing stems from both processes adversely altering the film in some locations. Specifically the plasma etching step excessively etches in some places on the film where they were too thin and insufficiently etches where the film was too thick. Due

to high sample variation, a plasma etching recipe which etched down the majority of nanostructures would simultaneously over and under etch some other parts of the film. The high temperature annealing in the presence of oxygen also destroyed a portion of the remaining nanostructurated film. This exact destructive mechanism is unclear, however what is clear is that more than half of the remaining nanostructures were altered to the point where they were no longer identifiable.

If this process were ever to be fully industrialized, several steps would need to be undertaken so as to improve the overall viability of the process. Homogeneity would be the main objective as every step which was undertaken reduced the total percentage of well defined nanostructuration. Intensively cleaning the single crystal substrate so as to remove any dust particles which might form inhomogeneities on the spin coated film would be necessary. Choosing a SCS that is sufficiently large enough so as reduce the effect of a thin film meniscus when spin coated would be important. Expertly filtering the PVOH solution of colloids so that the precursor when spin coated would give a completely uniform film. Intricately cleaning the dry box of any dust particles which might land on the film and thus adversely affect the homogeneity of the spin coated film. Plasma etching the silicon mold to free it of any residual film from previous imprints. Vigorously cleaning the oven in which the sample is annealed of any aberrant particles which might interfere with the crystal growing process.

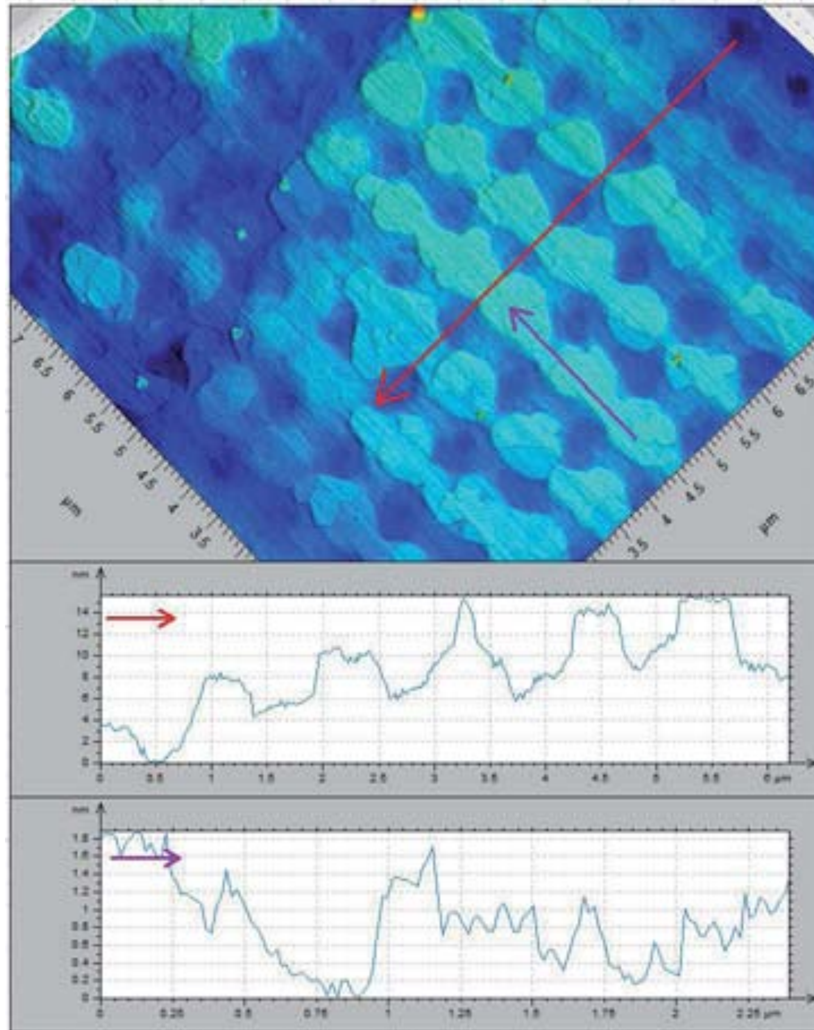

Figure 4-20 *An overly etched film on YSZ. Dwell temperature 160 °C, applied pressure 40 MPa, dwell time 5 min, demolding temperature 80 °C, etching conditions were 300 seconds at 150 W in an oxygen atmosphere, annealed 900 °C for 240 minutes, from nitrate based LSMO precursor with 2 wt% PVOH.*

4.4.1 TEM of NIL Structure

One may observe the morphology of structures produced by the nanoimprinting process by AFM and SEM quite clearly. Although much can be learned about the intermediate and final nanoholes and nanocaps that stem from nanoimprinting on a LSMO precursor by those two microscopes, it is impossible to know their chemical and crystalline nature. That is why observing with a transmission electron microscope (TEM), coupled with the elemental spectral analysis of an electron energy loss spectrometer (EELS), is so critical. By using a TEM with EDX on a lamella which is sufficiently thinned, one is able to definitely determine the crystalline make-up along with a per elemental spectral confirmation that the presence and ratio of inorganic species is correct. Two TEM lamellas were made; one on YSZ

made from argon plasma etching and using nitrates as the counter ion, and one on STO etched by oxygen and using acetates as the counter ion.

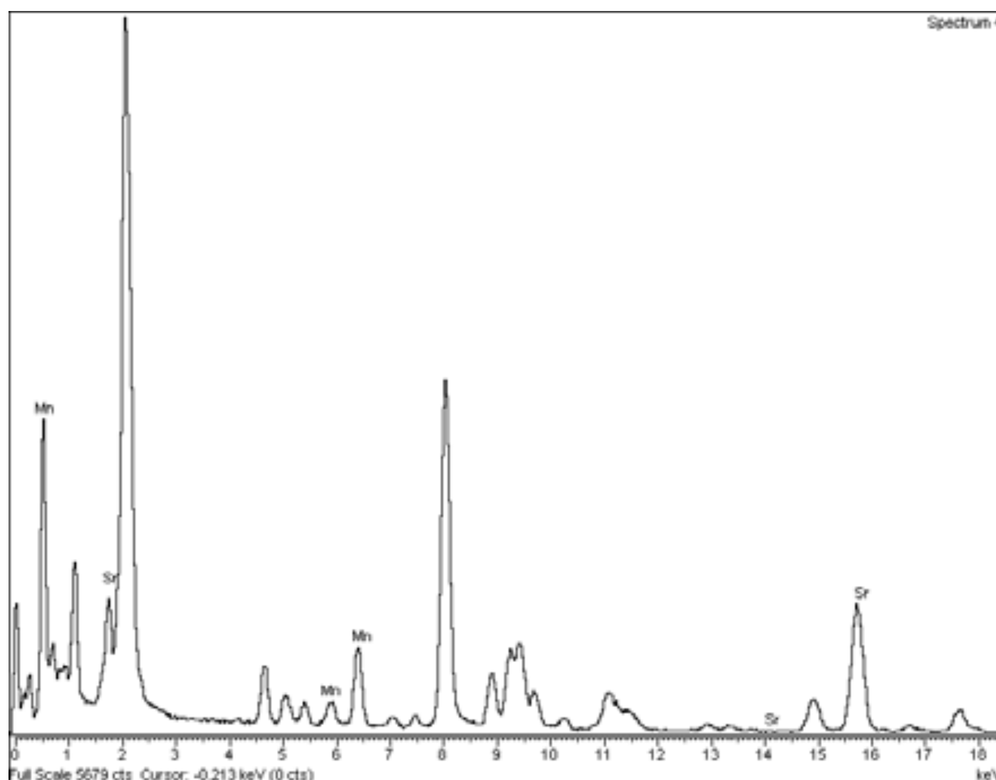

Element	Peak Area	Area Sigma	k factor	Abs Corrn.	Weight%	Weight% Sigma	Atomic%
Mn K	**2813**	**162**	**0.114**	**1**	**63.49**	**12.8**	**73.5**
Sr K	**184**	**101**	**1**	**1**	**36.51**	**12.8**	**26.5**

Figure 4-21 *EDX analysis of nanocap on YSZ showing manganese and strontium in the expected ratio. Dwell temperature 160 °C, applied pressure 40 MPa, dwell time 5 min, demolding temperature 80 °C, etching conditions were 15 minutes at 150 W in an argon atmosphere, annealed 900 °C for 240 minutes, from nitrate based LSMO precursor with 2 wt% PVOH.*

In figure 4-21, one sees an EDX analysis of a nanocap on YSZ made from an imprinted and annealed nitrate based LSMO precursor. There one notes the presence of manganese and strontium in the relative amounts similar to what one would expect from a LSMO crystal. On the right hand side one can see that the ratio of Mn to Sr is roughly 3:1, thus confirming that the ratio of metal constituents is correct for the formation of $La_{0.7}Sr_{0.3}MnO_3$. This particular sample proved that manganese could be retained from the precursor solution as a nanostructure. Also it suggested that the

manganese was being eliminated from the precursor due to the electron beam and not the remote likelihood that the Mn was disappearing at the annealing stage.

Unfortunately, the sample imprinted on YSZ detached from the TEM holder before high resolution TEM analysis could be performed. Another sample was prepared on STO which came from a LSMO solution with acetates instead of nitrates and was etched with oxygen instead of argon. The STO nanostructure appears in the form of a nanodot in figure 4-22 due to geometrical reasons of when a nanohole is cut in half and then thinned it appears to be an isolated object. The high resolution TEM image of this nanostructure epitaxial growth on STO can be seen in figure 4-22. The nanostructure is rounded and is covered with a protecting and conductive gold layer. The crystal LSMO can be seen sitting on the STO substrate and is confirmed from a Fourier transform of the area such that (110)[001]LSMO // (001)[100]STO. What can also be seen is the interface between the crystal and the substrate is slightly mixed.

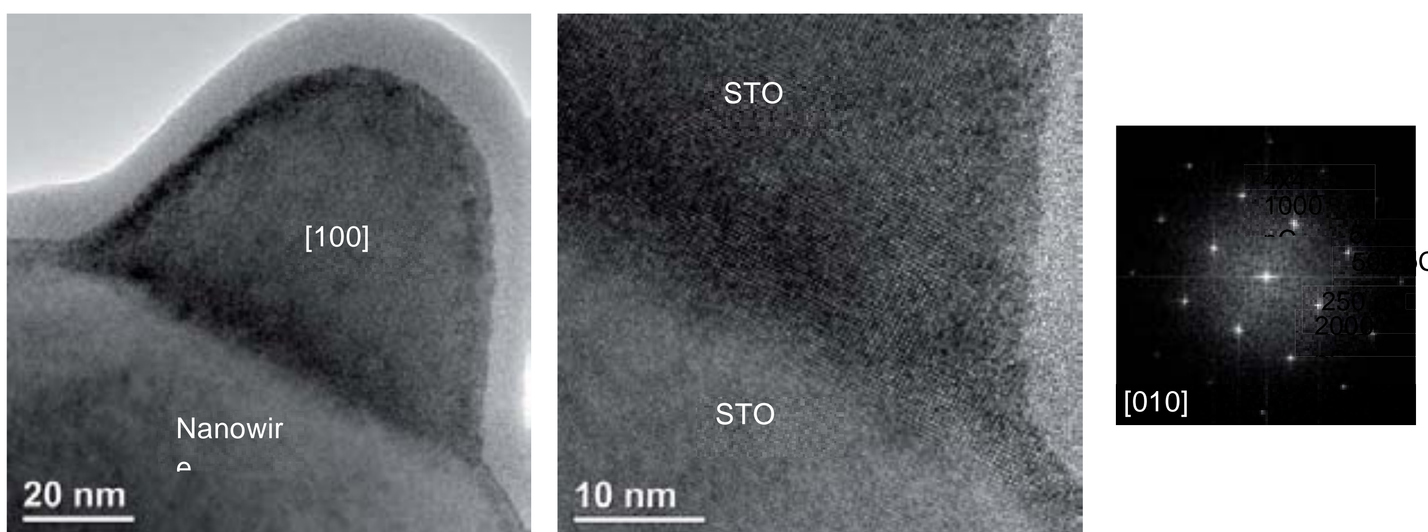

Figure 4-22 *TEM images of LMSO nanostructure on STO and corresponding FT. Dwell temperature 160 °C, applied pressure 40 MPa, dwell time 5 min, demolding temperature 80 °C, etching conditions were 240 seconds at 1200 W in an oxygen atmosphere, annealed 900 °C for 240 minutes, from acetate based LSMO precursor with 15 wt% PVOH.*

This mixture of the LSMO and STO at the interface can also be seen in the EELS line scan of the nanostructure in figures 4-23 and 4-24. Here the individual elements which make up the LSMO can be seen clearly when scanning over the nanostructure. On the nanostructure Mn, Sr, La, and O are easily observed while Ti is absent. At the interface between the nanostructure and the substrate, the presence of Ti is also detected along with spikes in O and Sr and reductions in Mn and La. Scanning on the substrate itself, the elements Sr, Ti, and O are present while Mn and La are not. All of this is consistent with the notion of a LSMO nanodot grown on a STO substrate.

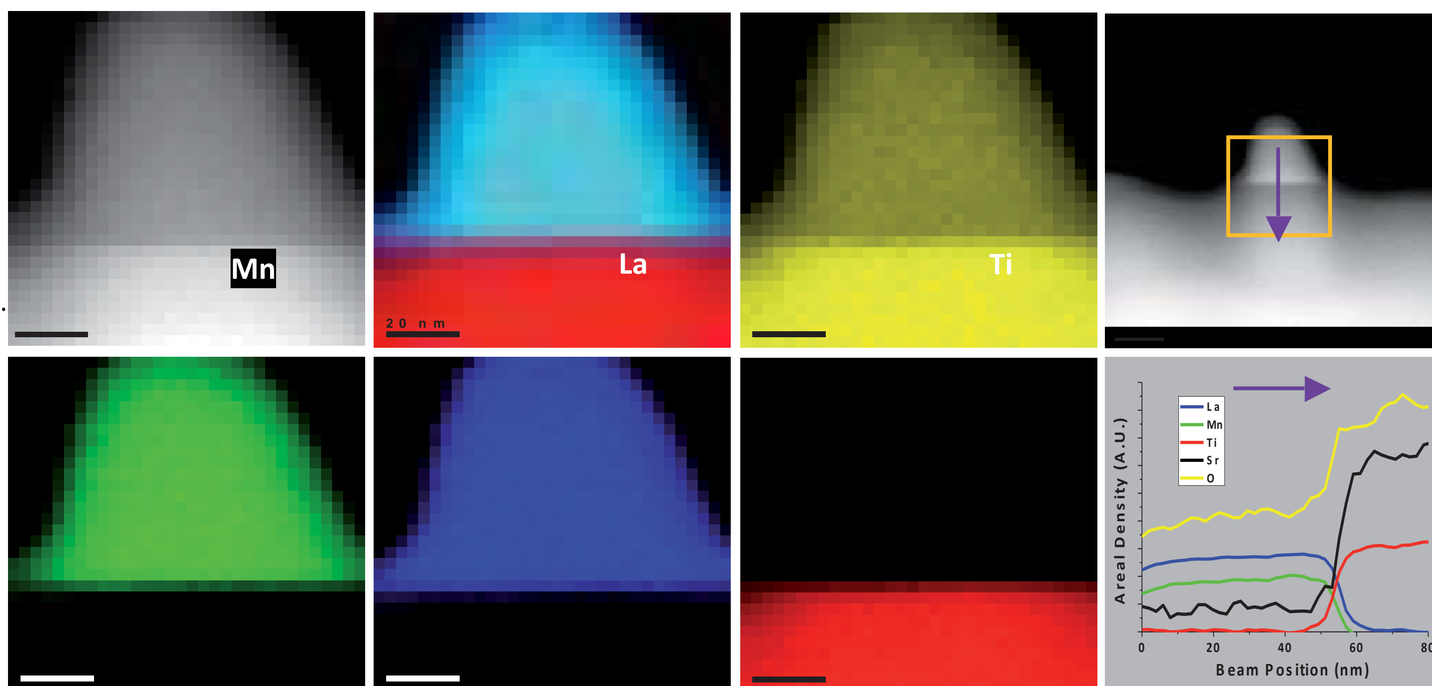

Figure 4-23 *EELS elemental linescan showing silicon, oxygen, manganese, lanthanum, and titanium as a spacial function. Dwell temperature 160 °C, applied pressure 40 MPa, dwell time 5 min, demolding temperature 80 °C, etching conditions were 120 seconds at 1200 W in an oxygen atmosphere, annealed 900 °C for 240 minutes, from acetate based LSMO precursor with 15 wt% PVOH.*

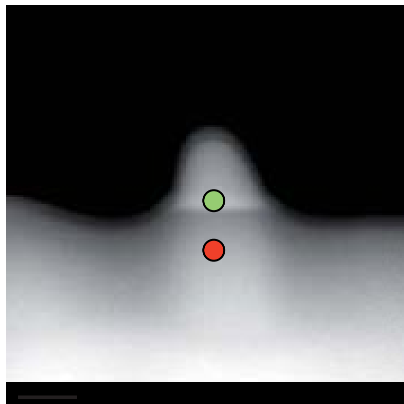

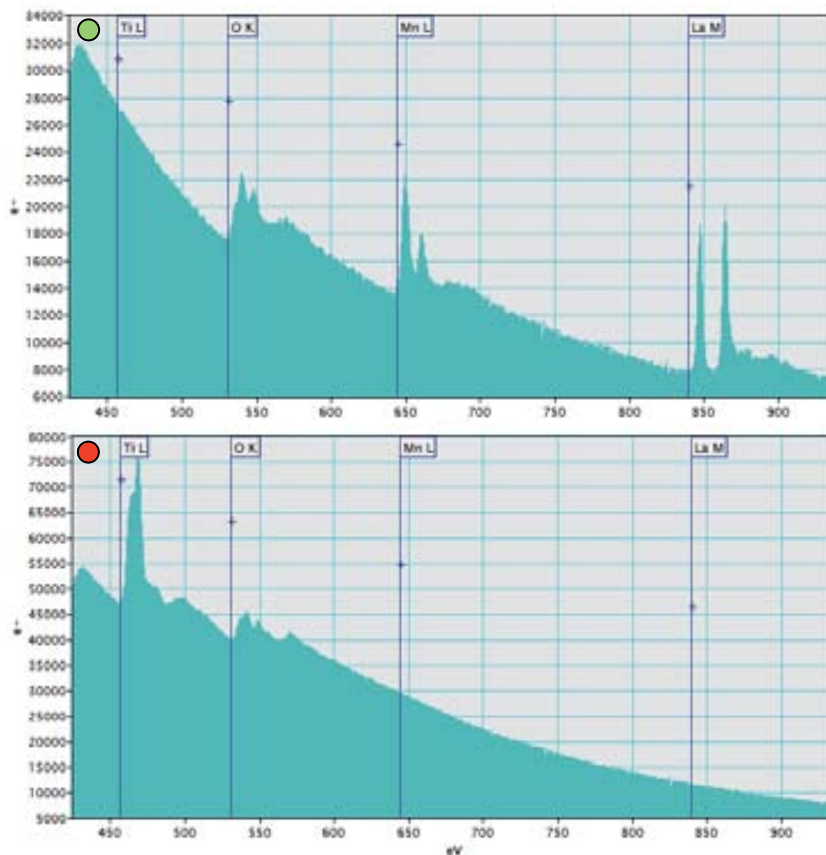

Figure 4-24 *EELS linescan on the nanostructure and substrate showing elemental presence as a function of energy. Dwell temperature 160 °C, applied pressure 40 MPa, dwell time 5 min, demolding temperature 80 °C, etching conditions were 4 minutes at 1200 W in an oxygen atmosphere, annealed 900 °C for 240 minutes, from acetate based LSMO precursor with 15 wt% PVOH.*

One can observe the interface between the LSMO crystal and the STO substrate in more detail in figure 4-25. The location of the elemental atomic planes can clearly be seen in this ultra high resolution image. It shows that La has diffused further into the substrate than Mn and that Ti has also diffused into the nanostructure. The number of atomic planes in which these elements have mixed appears to be on the order of ten. Interpreting this result, the manganese does not preferentially move across the crystal/substrate barrier, nor does the manganese vacate the nanostructure excessively on STO after annealing. This was thought to possibly be an explanation to the disappearance of manganese in the EBL experiments. Conversely, this result shows that the manganese does not migrate more than ten unit cells and certainly is not the cause of all the manganese in the EBL experiments disappearing. Of course, the optimal configuration of the nanostructure would be zero elemental migration due to the subsequent stoichiometric alteration and thus physical property variations. This migration would be lessened if the annealing temperature was lower and annealing time was less.

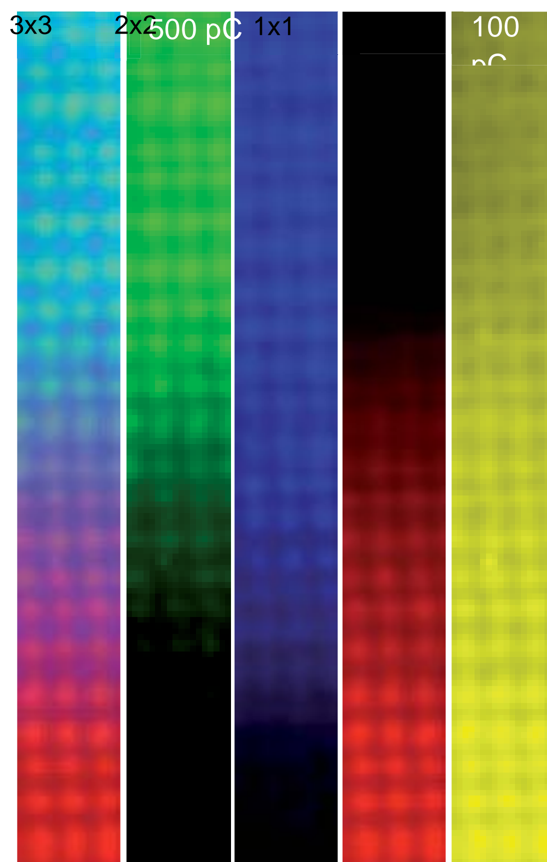

Figure 4-25 *Aberration corrected spectral analysis of interface between LSMO and STO substrate. Dwell temperature 160 °C, applied pressure 40 MPa, dwell time 5 min, demolding temperature 80 °C, etching conditions were 4 minutes at 1200 W in an oxygen atmosphere, annealed 900 °C for 240 minutes, from acetate based LSMO precursor with 15 wt% PVOH.*

4.5 Specific Conclusions

The process used to create the nanostructures is the following: precursor solution consisting of filtered PVOH and the acetate or nitrate salts of La, Sr, and Mn is spin coated on to a substrate, the sample is then imprinted with a male silicon mold at elevated temperature and pressure for a period of time, a reactive ion etching step with either argon or oxygen gas is performed, the sample is annealed at high heat in an oxygen atmosphere for many hours. The morphology of the film before imprinting, after imprinting, after etching, and after annealing is morphologically analyzed with SEM and AFM. A thin lamella is made by cutting with a FIB such that an TEM with EELS can observe the crystalline nature of the nanostructure and relay its elemental composition. The objective of this project was to create a platform in which oxide nanostructures would be grown epitaxially on single crystal substrates.

As far as imprinting of the LSMO precursor is concerned, there are several parameters which must be controlled in order to balance between nanopore depth and efficiency of the process. The parameters necessary to control are the temperature at which pressure is applied, the pressure which must be applied, the length of time pressure is applied, and finally the temperature at which the stamp and film are demolded. The dwell temperature was found to be optimal at 160C, too shallow at 100C, and produced artifacts at the high temperature of 220C. The pressure applied at 160C has been shown to be insufficient at 1 MPa and produce deformation at 7 MPa, therefore 4 MPa was chosen as the optimal pressure. A lack of dwell time does not produce good morphology and has been found that the longer the dwell time, the more the morphology resembles that of the mold. At five minutes a balance was found between recycle time between samples and nanopore depth. Finally, the demolding temperature also found to produce better morphology of the nanopores the closer that temperature was to room temperature. A demolding temperature the same as that of the dwell temperature gave nanopores with artifacts and partially filled while a demolding temperature of 80C was found to be a good balance between efficiency and structure.

The anisotropic plasma etching had a profound effect on the roughness of the film as well as the end nanostructures produced. Specifically, the roughness was drastically increased when etching with oxygen as compared to argon for nitrate based 2 wt% PVOH LSMO. This roughness problem was alleviated largely by increasing the weight percent of PVOH in the solution to 15% and changing the counter ion to acetate. The nanoholes could be etched down to the substrate floor, although the morphology suffered as a result of annealing step due to the high amount of organics involved. The material directly forming the shape of the nanoholes fragmented into many smaller pieces due to the obtuse geometries involved.

As for argon etching, the roughness was not problematic due to the unique nanostructures which were observed to have formed. Typically when using a male mold the end structure is a hole as was the case when etching with oxygen. However, when using argon plasma, an array of positive nanostructures formed where there should have been holes. The evolution of these interesting structures was recorded with SEM at partial etching. It is thought that the nanocaps form from the formation of a higher density region directly beneath the nanopillars and when the non-selective argon plasma is used, these regions are revealed. The size of the nanocaps did not change dramatically from before to after annealing. This could be due to the large energies and long times used in the process which effectively anneal the small structures before they reach the oven.

Both the oxygen plasma nanohole and argon plasma nanocap were cut into electron transparent lamellas on STO and YSZ respectively. These lamellas were investigated with TEM and EELS and discovered many things. The most illuminating observation was that both lamellas had the manganese present and that it was in the correct ratio as per

$La_{0.7}Sr_{0.3}MnO_3$. The result was different that what was observed in the nanowires and nanodots made from electron beam lithography. This suggests that the electron beam is somehow the cause of the manganese loss and future experiments using this procedure with oxides will need to take this into account. The other observation that came from diffraction corrected TEM images was that the interface between the STO and LSMO was a gradual one encompassing over ten unit cells due to elemental diffusion.

Of the two methods in which nanostructures were produced in this study, nanoimprint lithography is the most applicable to industry. Not only is the time per square centimeter nanostructurated less, but also is the cost to buy and run the equipment. The idea of nanoimprinting is a simple one, however there many contributing factors must be taken into account to achieve high final nanocrystal quality and uniformity. The idea of quickly nanoimprinting any oxide film on any substrate and obtaining an array nanostructures is a powerful idea. Hopefully this work has shown that this method is possible by controlling the amount of PVOH present, the counter ions used in the precursor, and the gases used to etch the film away. Future work should be centered on optimizing the process for large wafers and testing other oxide systems than just LSMO.

4.6 Nanoimprinting References

1. Guo, L.J., *Recent progress in nanoimprint technology and its applications.* Journal of Physics D: Applied Physics, 2004. **37**(11): p. R123-R141.
2. Chou, S.Y. and P.R. Krauss, *Imprint lithography with sub-10 nm feature size and high throughput.* Microelectronic Engineering, 1997. **35**(1–4): p. 237-240.
3. Guo, L., P.R. Krauss, and S.Y. Chou, *Nanoscale silicon field effect transistors fabricated using imprint lithoqraphy.* Applied Physics Letters, 1997. **71**(13): p. 1881-1883.
4. Lebib, A., et al., *Nanoimprint lithography for a large area pattern replication.* Microelectronic Engineering, 1999. **46**(1–4): p. 319-322.
5. Carcenac, F., et al., *Fabrication of high density nanostructures gratings (>500Gbit/in2) used as molds for nanoimprint lithography.* Microelectronic Engineering, 2000. **53**(1–4): p. 163-166.
6. Alkaisi, M.M., R.J. Blaikie, and S.J. McNab, *Low temperature nanoimprint lithography using silicon nitride molds.* Microelectronic Engineering, 2001. **57–58**(0): p. 367-373.
7. Lebib, A., et al., *Control of the critical dimension with a trilayer nanoimprint lithography procedure.* Microelectronic Engineering, 2001. **57–58**(0): p. 411-416.
8. Clavijo Cedeño, C., et al., *Nanoimprint lithography for organic electronics.* Microelectronic Engineering, 2002. **61–62**(0): p. 25-31.
9. Malaquin, L., et al., *Using polydimethylsiloxane as a thermocurable resist for a soft imprint lithography process.* Microelectronic Engineering, 2002. **61–62**(0): p. 379-384.
10. Pépin, A., et al., *Nanoimprint lithography for the fabrication of DNA electrophoresis chips.* Microelectronic Engineering, 2002. **61–62**(0): p. 927-932.
11. Akbayir, C., et al., *Nanostructured conjugated polymeric systems for photovoltaic applications.* Reviews on Advanced Materials Science, 2003. **5**(3): p. 205-210.
12. Gourgon, C., et al., *Influence of pattern density in nanoimprint lithography.* Journal of Vacuum Science and Technology B: Microelectronics and Nanometer Structures, 2003. **21**(1 SPEC.): p. 98-105.
13. Li, M., et al., *Pattern transfer fidelity of nanoimprint lithography on six-inch wafers.* Nanotechnology, 2003. **14**(1): p. 33-36.
14. Ansari, K., et al., *Fabrication of high aspect ratio 100 nm metallic stamps for nanoimprint lithography using proton beam writing.* Applied Physics Letters, 2004. **85**(3): p. 476-478.

15. Damle, T.S., S.; Ekerdt, M.; Sreenivasan, J.; Wolfe, S. V.; Willson, J.; Grant. C., *"Patterning curved surfaces: Template generation by ion beam proximity lithography and relief transfer by step and flash imprint lithography,"* J. Vac. Sci. Technol. B 1999. **17**(6): p. 2965-2969.
16. Cheng, X. and L.J. Guo, *A combined-nanoimprint-and-photolithography patterning technique.* Microelectronic Engineering, 2004. **71**(3-4): p. 277-282.
17. Hoff, J.D., et al., *Nanoscale protein patterning by imprint lithography.* Nano Letters, 2004. **4**(5): p. 853-857.
18. Kehagias, N., et al., *Embedded polymer waveguides: Design and fabrication approaches.* Superlattices and Microstructures, 2004. **36**(1-3): p. 201-210.
19. Contreras, A.M., et al., *Fabrication of platinum nanoparticles and nanowires by electron beam lithography (EBL) and nanoimprint lithography (NIL): Comparison of ethylene hydrogenation kinetics.* Catalysis Letters, 2005. **100**(3-4): p. 115-124.
20. Kee, C.S., et al., *Photonic band gaps and defect modes of polymer photonic crystal slabs.* Applied Physics Letters, 2005. **86**(5): p. 1-3.
21. Kee, C.S., et al., *Nanopatterned polymer thin films.* Journal of Nonlinear Optical Physics and Materials, 2005. **14**(3): p. 299-303.
22. Kiyohara, S., et al., *Organic light-emitting microdevices fabricated by nanoimprinting technology using diamond molds.* Japanese Journal of Applied Physics, Part 1: Regular Papers and Short Notes and Review Papers, 2005. **44**(6 A): p. 3686-3690.
23. Peroz, C., et al., *Single digit nanofabrication by step-and-repeat nanoimprint lithography.* Nanotechnology, 2012. **23**(1).
24. Brombacher, C., et al., *L1 0 FePtCu bit patterned media.* Nanotechnology, 2012. **23**(2).
25. Holland, E.R., et al., *An enhanced flexible color filter via imprint lithography and inkjet deposition methods.* IEEE/OSA Journal of Display Technology, 2011. **7**(6): p. 311-317.
26. Telkkälä, J., et al., *Narrow linewidth laterally-coupled 1.55m DFB lasers fabricated using nanoimprint lithography.* Electronics Letters, 2011. **47**(6): p. 400-401.
27. Eriksson, T., et al., *High volume nanoimprint lithography on III/V substrates: Imprint fidelity and stamp lifetime.* Microelectronic Engineering, 2011. **88**(3): p. 293-299.
28. Lee, K.K., et al., *Development of reactive-ion etching for ZnO-based nanodevices.* IEEE Transactions on Nanotechnology, 2011. **10**(4): p. 839-843.
29. Park, H., et al., *Enhancement of photo- and electro-luminescence of GaN-based LED structure grown on a nanometer-scaled patterned sapphire substrate.* Microelectronic Engineering, 2011. **88**(11): p. 3207-3213.
30. Xia, Q., *Nanoscale resistive switches: Devices, fabrication and integration.* Applied Physics A: Materials Science and Processing, 2011. **102**(4): p. 955-965.
31. Xia, Q., et al., *Two- and three-terminal resistive switches: Nanometer-scale memristors and memistors.* Advanced Functional Materials, 2011. **21**(14): p. 2660-2665.
32. Yang, J.K.W., et al., *Fabrication and characterization of bit-patterned media beyond 1.5 Tbit/in2.* Nanotechnology, 2011. **22**(38).
33. Almanza-Workman, A.M., et al., *Fabrication of three-dimensional imprint lithography templates by colloidal dispersions.* Journal of Materials Chemistry, 2011. **21**(37): p. 14185-14192.
34. Bonifas, A.P., R.L. McCreery, and K.D. Harris, *Thermal oxidation as a simple method to increase resolution in nanoimprint lithography.* Microelectronic Engineering, 2011. **88**(11): p. 3256-3260.
35. Chang, W.S., et al., *Fabrication of nano-electrode arrays of free-standing carbon nanotubes on nano-patterned substrate by imprint method.* Applied Surface Science, 2011. **257**(7): p. 3063-3068.
36. Liu, Z., D.G. Bucknall, and M.G. Allen, *Inclined nanoimprinting lithography for 3D nanopatterning.* Nanotechnology, 2011. **22**(22).
37. Ganesan, R., et al., *Direct nanoimprinting of metal oxides by in situ thermal co-polymerization of their methacrylates.* Journal of Materials Chemistry, 2011. **21**(12): p. 4484-4492.
38. Mekaru, H. and H. Hiroshima, *Effect of dropping hydrofluoroether in thermal nanoimprint on polycarbonate.* Japanese Journal of Applied Physics, 2011. **50**(6 PART 2).
39. Meng, F., et al., *Efficient methods of nanoimprint stamp cleaning based on imprint self-cleaning effect.* Nanotechnology, 2011. **22**(18).
40. Voet, V.S.D., et al., *Interface segregating fluoralkyl-modified polymers for high-fidelity block copolymer nanoimprint lithography.* Journal of the American Chemical Society, 2011. **133**(9): p. 2812-2815.
41. Wi, J.S., et al., *Gradual pressure release for reliable nanoimprint lithography.* Journal of Vacuum Science and Technology B: Microelectronics and Nanometer Structures, 2011. **29**(3).
42. Park, J.Y., N.R. Hendricks, and K.R. Carter, *Solvent-assisted soft nanoimprint lithography for structured bilayer heterojunction organic solar cells.* Langmuir, 2011. **27**(17): p. 11251-11258.
43. Scarpa, G., et al., *Patterning poly(3-Hexylthiophene) in the sub-50-nm region by nanoimprint lithography.* IEEE Transactions on Nanotechnology, 2011. **10**(3): p. 482-488.
44. Sharma, C.S., et al., *Biomimicked superhydrophobic polymeric and carbon surfaces.* Industrial and Engineering Chemistry Research, 2011. **50**(23): p. 13012-13020.

45. Cha, N.G., T. Kanki, and H. Tanaka, *Direct fabrication of integrated 3D epitaxial functional transition metal oxide nanostructures using extremely small hollow nanopillar nano-imprint metal masks.* Nanotechnology, 2011. **22**(18).
46. Cheng, C.C., K. Meneou, and K.Y. Cheng, *Effects of nano-pattern size on the property of InAs site-controlled quantum dots.* Journal of Crystal Growth, 2011. **323**(1): p. 180-182.
47. Park, I.S., W.T. Nichols, and J. Ahn, *Nanosize patterning with nanoimprint lithography using poly(vinyl alcohol) transfer layer.* Japanese Journal of Applied Physics, 2011. **50**(6 PART 2).
48. Carretero-Genevrier, A., *Vertical (La,Sr)MnO3 Nanorods from Track-Etched Polymers Directly Buffering Substrates.* Advanced Functional Materials, 2010. **20**(6): p. 892-897.
49. Carretero-Genevrier, A., *Single crystalline La0.7Sr0.3MnO3 molecular sieve nanowires with high temperature ferromagnetism.* Journal of American Chemical Society 2011. **133**: p. 4053-4061.
50. Wilkes, C.E., *PVC Handbook.* Hanser Verlag, 2005. **ISBN 1-56990-379-4**.
51. Choi, P., P.F. Fu, and L.J. Guo, *Siloxane copolymers for nanoimprint lithography.* Advanced Functional Materials, 2007. **17**(1): p. 65-70.
52. Ding, Y., et al., *Polymer viscoelasticity and residual stress effects on nanoimprint lithography.* Advanced Materials, 2007. **19**(10): p. 1377-1382.
53. Ding, Y., et al., *Relaxation behavior of polymer structures fabricated by nanoimprint lithography.* ACS Nano, 2007. **1**(2): p. 84-92.
54. Meskers, S.C.J., et al., *Dispersive relaxation dynamics of photoexcitations in a polyfluorene film involving energy transfer: Experiment and Monte Carlo simulations.* Journal of Physical Chemistry B, 2001. **105**(38): p. 9139-9149.
55. Binder, K., J. Baschnagel, and W. Paul, *Glass transition of polymer melts: Test of theoretical concepts by computer simulation.* Progress in Polymer Science (Oxford), 2003. **28**(1): p. 115-172.
56. Gránásy, L., et al., *A general mechanism of polycrystalline growth.* Nature Materials, 2004. **3**(9): p. 645-650.
57. Nies, C.W. and G.L. Messing, *EFFECT OF GLASS-TRANSITION TEMPERATURE OF POLYETHYLENE GLYCOL-PLASTICIZED POLYVINYL ALCOHOL ON GRANULE COMPACTION.* Journal of the American Ceramic Society, 1984. **67**(4): p. 301-304.
58. Carretero-Genevrier, A., et al., *Single crystalline La 0.7Sr 0.3MnO 3 molecular sieve nanowires with high temperature ferromagnetism.* Journal of the American Chemical Society, 2011. **133**(11): p. 4053-4061.
59. Carretero-Genevrier, A., et al., *Vertical (La,Sr)MnO3 nanorods from track-etched polymers directly buffering substrates.* Advanced Functional Materials, 2010. **20**(6): p. 892-897.
60. Carretero-Genevrier, A., et al., *Single-crystalline La0.7Sr0.3MnO3 nanowires by polymer-template-directed chemical solution synthesis.* Advanced Materials, 2008. **20**(19): p. 3672-3677.

General Conclusions & Future Work

Arrays of $La_{0.7}Sr_{0.3}MnO_3$ nanostructures have been grown on insulating single crystal substrates by nanoimprint lithography and $La_xSr_{1-x}O_y$ nanostructures by electron beam lithography. LSMO was the objective oxide due to it being ferromagnetic at room temperature, has a high magnetic anisotropy, and has colossal magnetoresistance to name but a few of its attributes. The underlying technique behind the creation of thin films herein is chemical solution deposition. This is where an oxide thin film is applied, not by cumbersome vacuum techniques, but by the inexpensive and scalable process of spin coating an aqueous solution laden with soluble metal salts. Two LSMO precursor solutions were made, one with nitrates initially and one with acetates later in the project. The reason for this switch was the observed absence of manganese inside the nanodots and nanowires made by EBL from the nitrate based precursor. The reasoning being that nitrate decomposition is highly exothermic and possibly the electron beam was removing manganese through a volatile decomposition. The metals introduced into the aqueous solution were lanthanum, strontium, and manganese in a ratio such that when annealed would yield crystalline $La_{0.7}Sr_{0.3}MnO_3$. The spin coating was performed in a low humidity environment and accompanied by a thorough cleaning regime so as to reduce thin film inhomogeneities. The substrates used were YSZ, STO, and LAO due to their ability to grow single crystalline LSMO as opposed to silicon which would grow polycrystalline LSMO.

The ratio of the three metals in the precursor solution was measured with ICP and was in accordance with expected values. The roughness of the non-annealed and annealed film was observed with AFM and showed that a high molar concentration gave uneven surfaces. The annealed films were observed with XRD and were

seen to have peaks corresponding to single crystalline epitaxial LSMO. The magnetic nature of the films was also confirmed against bulk values of LSMO by use of a SQUID. The underlying result of the XRD and SQUID measurements was that the precursor produced a LSMO film after annealing. In order to determine the elemental nature of the non-annealed films for loss of manganese after electron radiation and development, XPS was performed. The results do not show a manganese loss after irradiation, however do show a manganese loss from samples annealed at temperatures higher than 500 °C.

The electron beam lithography procedure called for the substrate/film to be moved into a SEM vacuum chamber and then be attached to an aluminum plate by copper tape. This insured that the substrate would be perfectly perpendicular to the axis of the beam and would be able to draw off some excess surface charge. The electron beam would be focused onto the surface of the film where a predesigned patterned would be written by varying the location and time of exposure. This focusing of electrons results in a local deformation in the form of a cavity. The low electrical conductivity of the substrates dictated the usage of a low voltage on the column, an iterative strategy when focusing, and a judicious amount of electrons written at a given location. The substrate was then removed from the vacuum chamber and immersed in water so as to develop the film. This development stage resulted in a cleaned substrate with hardened parts of the precursor film attached where electrons were focused. Finally, the sample was placed into a tube furnace in an oxygen atmosphere so as to anneal the hardened structures and thus form oxide nanocrystals. Numerically the beam conditions used were a 5 kV beam with a 30 μm diameter yielding on average 220 pA in a 1 mT vacuum. This gave between 15 and 40 nm high, 150 nm wide oxide nanodots after annealing an isolated low dosage cross-linked nanosite, as well as nanowires of between 4 and 25 nm high, 500 nm to 10 μm long, after annealing an array of high dosage nanosites.

The intermediate and final nanostructures were observed with SEM as well as AFM. A multitude of subtle morphologies were seen as dosage per site was varied, however two regimes were focused on in this work. The low dosage regime, of 0.05 pC to 1.5 pC, constituted the least amount of electrons impinged upon the film which would result in local polymer cross-linking. The high dosage regime, of 150 pC to 2000 pC, refers to the dosage necessary to cause nanowire growth when configured in tight arrays. A height dependence to dosage at the low dosage regime was observed for recently irradiated spots, those developed spots, and the final annealed nanocrystals. These resultant low dosage nanodots were seen to be conical in shape before annealing and then triangular in nature when annealed. At the high dosage regime, the non-annealed spot showed many non-linear undulations where the central feature might be an already crystallized section. The reason for this hypothesis is that nanowires are seen to grow from the edges of arrays of highly irradiated sites. It is thought that the already crystallized center of the high dosage nanoislands serves as seeds for the nanowire's propagation and the cross-linked surroundings as a feed material. This theory stems in part from the report that the formation of crystals directly from an electron beam on a LSMO PVOH precursor [1-3].

Furthermore, the nanowires have been observed to grow only when a sufficient number of neighboring sites was present and when these neighbors resided neither too closer nor too far from each other. This phenomenon could be the result of the degradation to the cross-linked film when too densely packed, and insufficient heat to cross-link a continuous film when too sparsely packed.

As for nanoimprint lithography, two main LSMO nanostructures were fabricated by altering the gas used in the etching process. The specifics of NIL used in this work was pressing a mold replete with nano-sized pillars into the soft precursor film under high pressure and temperature. The pressure was applied after the temperature was high enough such that polymer could flow around the nanopillars. The temperature was then lowered slowly while retaining pressure so as to prevent the morphology of the newly formed nanopores from returning to a planar state. Specifically, imprinting at 160 °C with a pressure of 4 MPa for 5 minutes with a demolding temperature of 80°C produced nanopores on both 0.1M nitrate based LSMO with 2 wt% PVOH and 0.1M acetate based LSMO with 15 wt% PVOH. After demolding the film from the stamp, the resulting residual layer was selectively removed by reactive ion etching. Nanoholes were created by placing the nanoperforated film in the presence of a highly anisotropic oxygen plasma. The oxygen plasma chemical removed organic species in the precursor film, leaving only metals. This contrasts with the mechanical etching provided by the argon plasma which left a series of nanocaps. Numerically the conditions used were 150 W for 5 min and 15 min in oxygen and argron plasma respectively for 0.1M nitrate based LSMO with 2 wt% PVOH and 1200 W for 120 seconds in oxygen for 0.1M acetate based LSMO with 15% PVOH. A theory explaining this phenomenon is that the film is local compressed during the stamping process, thereby creating areas underneath the nanopores which are more mechanical resilient to the argon plasma with respect to the rest of the film. Numerically, the morphology of the structures after annealing produced by argon plasma etching were 600 nm wide and 80 nm in height, while those produced by oxygen plasma were 500 nm wide and 25 nm in depth.

Nanodots, nanowires, and nanocaps were cut by FIB into cross sectional, electron transparent TEM lamellas. This allowed for analysis on their atomic planes and local elemental presence. The results showed that the structures made by electron beam lithography to be completely devoid of manganese, thus the structures were projected to be lanthanum oxides and quite possibly lanthanum strontium oxides. The growth of the lanthanum oxide nanodots and nanowires on LAO, STO, and YSZ showed epitaxy whereas the nanowires grown on silicon did not. The unit cell of the lanthanum oxide crystal could not be determined due to lack of a more complete TEM analysis. However, the atomic planes of the nanodots and nanowire did not appear to be the same crystal due to differing growth angles. The nanocaps did show the presence of manganese in the expected amount, which led to the conclusion that the act of electron beam irradiation altered the stoichiometry of the film somehow. TEM inspection of the nanostructure also showed that the resulting crystal was truly LSMO.

Future work in this area would center on the assertion that other oxide systems, with different metal salts and stoichiometries, would also be able to be forged into nanostructures following this general procedure. A precursor forming $SrTiO_3$ when annealed as a thin film was already irradiated with electron beam to form nanodots on single crystal substrates as well as nanoimprinted. The advantages of being able to use wet chemical means and quick imprinting to create any oxide nanostructure, is clear. Future work would also center on determining the point at which manganese is removed from the film and what metal salts are impervious to electron bombardment. Computer simulations would also be helpful to form models to explain the intricate interplay between precursor, cross-linking, and an electron beam. Further optimizing the nanoimprint process would also be of use, specifically regarding the increase of yield when etching with argon and increase of structural integrity when etching with oxygen.

As it has been shown, LSMO nanostructure fabrication on insulating single crystal substrates is a complicated, often surprising affair, borne out of as much serendipity as scientific knowledge. However, it is felt that scientific knowledge has been advanced herein with regards to the limitations and possibilities of both electron beam and nanoimprint lithography. As was said in the summary of this work, the individual subtle techniques successful at the nanoscale are what is critical to the eventual introduction of devices based on the umbrella term “nanotechnology”. It is hoped that, however small, some part of the frustration and joy of working at the nanoscale is imparted in these words.

1. Wu, M.C., et al., *Surface potential and magnetic properties of La0.7Sr 0.3MnO3 periodic arrays fabricated by direct electron beam writing.* Journal of Applied Physics, 2008. **104**(2). 024517
2. Wu, M.C., et al., *Fabrication and optical properties of periodical structures based on a water-developable and tunable La0.7Sr0.3MnO3 resist.* Journal of Materials Chemistry, 2008. **18**(7): p. 780-785.
3. Chuang, C.M., et al., *Nanolithography made from water-based spin-coatable LSMO resist.* Nanotechnology, 2006. **17**(17): p. 4399-4404.